LEVEL II

⑧

JANUARY 1979   LMSC-D630807

VORTEX-INDUCED ASYMMETRIC LOADS ON SLENDER VEHICLES

FINAL TECHNICAL REPORT

PREPARED BY:

LARS E. ERICSSON
CONSULTING ENGINEER, ENGINEERING TECHNOLOGY

J. PETER REDING
RESEARCH SPECIALIST, AERO-THERMODYNAMICS

PREPARED UNDER CONTRACT N60921-77C-0234
FOR
NAVAL SURFACE WEAPONS CENTER
WHITE OAK, SILVER SPRING, MARYLAND 20910

Lockheed MISSILES & SPACE COMPANY, INC.
SUNNYVALE, CALIFORNIA

DDC

RECEIVED
FEB 28 1979

D

79 02 23 078

January 1979

VORTEX-INDUCED ASYMMETRIC
LOADS ON SLENDER VEHICLES

FINAL TECHNICAL REPORT

Prepared by

Lars E. Ericsson
Consulting Engineer, Engineering Technology

J. Peter Reding
Research Specialist, Aero-Thermodynamics

Prepared under Contract N60921-77C-0234

for

Naval Surface Weapons Center
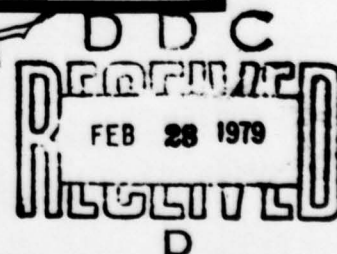
White Oak, Silver Spring, Maryland 20910

9 02 23 078

REPORT DOCUMENTATION PAGE		READ INSTRUCTIONS BEFORE COMPLETING FORM
1. REPORT NUMBER	2. GOVT ACCESSION NO.	3. RECIPIENT'S CATALOG NUMBER
4. TITLE (and Subtitle) VORTEX-INDUCED ASYMMETRIC LOADS ON SLENDER VEHICLES.		5. TYPE OF REPORT & PERIOD COVERED Final technical report,
		6. PERFORMING ORG. REPORT NUMBER LMSC-D630807
7. AUTHOR(s) Lars E. Ericsson J. Peter Reding		8. CONTRACT OR GRANT NUMBER(s) N60921-77-C-0234
9. PERFORMING ORGANIZATION NAME AND ADDRESS Lockheed Missiles and Space Company, Inc. 1111 Lockheed Way Sunnyvale, California 94086		10. PROGRAM ELEMENT, PROJECT, TASK AREA & WORK UNIT NUMBERS 62332N; F32-322; WF32-322-202; WA8209(A).
11. CONTROLLING OFFICE NAME AND ADDRESS Naval Surface Weapons Center, WOL White Oak, Silver Spring, MD 20910 Attn: Code R44		12. REPORT DATE January 1979
		13. NUMBER OF PAGES 240
14. MONITORING AGENCY NAME & ADDRESS(if different from Controlling Office) 237 p.		15. SECURITY CLASS. (of this report) Unclassified
		15a. DECLASSIFICATION/DOWNGRADING SCHEDULE

16. DISTRIBUTION STATEMENT (of this Report)

Approved for public release; distribution unlimited.

17. DISTRIBUTION STATEMENT (of the abstract entered in Block 20, if different from Report)

18. SUPPLEMENTARY NOTES

19. KEY WORDS (Continue on reverse side if necessary and identify by block number)

Slender vehicles
Vortex-induced asymmetric loads

20. ABSTRACT (Continue on reverse side if necessary and identify by block number)

The steady and unsteady vortex-induced asymmetric loads on slender vehicles have been investigated. The study consisted of a review of pertinent two-dimensional and three-dimensional data, the development of analytic means for prediction of the upper limit for vortex-induced asymmetric loads, and the assessment of the importance of these loads to the vehicle dynamics of slender bodies of revolution. The study showed boundary layer transition

DD FORM 1473 EDITION OF 1 NOV 65 IS OBSOLETE
1 JAN 73
S/N 0102-LF-014-6601

to have a dominant influence on static and dynamic vortex-induced loads. The predicted upper limit for vortex-induced asymmetric loads bounds all available experimental data from subcritical to supercritical Reynolds numbers. The most powerful dynamic effect is that of the moving wall at the separation point, which has a wall-jet-like effect on the boundary layer separation and transition. Preliminary experimental results indicate that because of this effect the dynamic stability parameters due to pitching and coning can be one order of magnitude larger than those occurring in attached flow at lower angles-of-attack. One very important effect of the asymmetric vortices existing at high angles-of-attack is to provide a coupling mechanism at zero sideslip between longitudinal and lateral degrees of freedom. As these cross coupling effects are very large, highly nonlinear, often discontinuous and associated with hysteresis effects, with especially large impact on the vehicle dynamics, they are presently of great concern to missile and aircraft designers.

ABSTRACT

The steady and unsteady vortex-induced asymmetric loads on slender vehicles were
~~have been~~ investigated. The study ~~consisted of a~~ review~~ed~~ ~~of~~ pertinent two- and three-
dimensional ~~and three-dimensional~~ data; ~~the development of~~ developed analytic means for
prediction ~~of~~ the upper limit for vortex-induced asymmetric loads; and ~~the~~ assessed
~~assessment of~~ the importance of these loads to the vehicle dynamics of slender
bodies of revolution. The study showed boundary layer transition to have a
dominant influence on static and dynamic vortex-induced loads. The predicted
upper limit for vortex-induced asymmetric loads bounds all available experimen-
tal data from subcritical to supercritical Reynolds numbers. The most powerful
dynamic effect is that of the moving wall at the separation point, which has a
wall-jet-like effect on the boundary layer separation and transition. Prelimi-
nary experimental results indicate that because of this effect the dynamic
stability parameters due to pitching and coning can be one order of magnitude
larger than those occurring in attached flow at lower angles-of-attack. ~~One~~
A very important effect of ~~the~~ asymmetric vortices existing at high angles-of-
attack is to provide a coupling mechanism at zero sideslip between longitudinal
and lateral degrees of freedom. As these cross coupling effects are very large,
highly nonlinear, often discontinuous and associated with hysteresis effects,
with especially large impact on the vehicle dynamics, they are ~~presently~~ of
great concern to missile and aircraft designers.

CONTENTS

CONTENTS (Continued)

ILLUSTRATIONS

ILLUSTRATIONS (Continued)

ILLUSTRATIONS (Continued)

ILLUSTRATIONS (Continued)

ILLUSTRATIONS (Continued)

ILLUSTRATIONS (Continued)

ILLUSTRATIONS (Continued)

ILLUSTRATIONS (Continued)

Section 1
INTRODUCTION

At high angles of attack the flow separating off the leeside of a slender body rolls up into a pair of symmetric vortices. Above some critical, high angle-of-attack the vortices become asymmetric, generating large side forces that can cause an aircraft to spin or a missile to tumble if these vortex effects have not been considered in the control design. Although the phenomenon has been known for some time (Refs. 1-14), it was of little practical interest until recently when both high performance aircraft and missiles began operating at these high angles-of-attack. This renewed interest has precipitated intensive experimental activity, both in regard to aircraft (Refs. 15-24) and missiles (Refs. 25-42), and has also resulted in extensive theoretical efforts (Refs. 43-54).

In spite of all this activity, the present state of the art in regard to forecasting the vortex-induced asymmetric loads is rather poor. The existing theories are founded on the principle of space-time equivalence using either the impulsively started cylinder analogy or a mathematical model where the steady three-dimensional vortex array is related to the nonsteady two-dimensional vortex street. This makes the theories strictly applicable only to the loads generated by vortices that start on the aft body. However, the dominant vortex-induced side loads are caused by the asymmetric vortex pair generated by a slender nose. As most existing missile geometries have slender noses, the developed theories are often not able even to repredict the experiments which were used to determine the empirical constants in the theory.

In regard to the forecasting of full scale asymmetric loads from the existing data base the state of the art is not any better. The extreme sensitivity of the vortex-induced asymmetric loads to Reynolds number, roll angle,

surface roughness, Mach number, etc. makes it difficult to define the maximum
side loads from test data. And if such an extensive data base were to become
available, it would probably not be directly applicable to the full scale
vehicle because of the problem of Reynolds number simulation in subscale tests.
The results for an advanced performance aircraft (Ref. 55 and Fig. 1) illustrate
this. In the subscale model test the large vortices associated with subcritical
flow conditions were generated, with associated large side loads, whereas the
full scale supercritical flow conditions caused much smaller vortex wake with
correspondingly smaller side loads. When the flow conditions are supercritical
both in test and flight, good simulation is obtained in spite of sizeable
Reynolds number differences (Ref. 23 and Fig. 2).

Because of the problem of experimental data scatter, Wardlaw and Morrison
(Refs. 53 and 56) suggest a statistical approach, which Hunt and Lamont (Ref.
57) do not think is practical because of the tremendous amount of wind tunnel
test data that would be needed (at the correct Reynolds number, one should add).
The results obtained on an advanced performance aircraft (Ref. 17 and Fig. 3)
illustrate the problem one faces. It is very difficult to vary tunnel test
conditions, tunnel noise environment, surface roughness, roll position, etc.
to the extent needed to assure oneself that the maximum possible side load has
been measured. And even then one would be faced with the scaling problem
discussed earlier.

Because of the difficulties discussed above, a different approach has been
selected in the present analysis, i.e., to establish the upper bounds for the
side loads that can be generated by asymmetric vortices, and to do that for
the complete Reynolds number range of interest, from subcritical to highly
supercritical flow conditions. Based upon past experience with unsteady separated
flow it is postulated that the unsteady lift to steady drag ratio for a cylinder
normal to the flow provides the upper limit for the steady, sectional side force
to normal force ratio that can exist on an axisymmetric body at high flow inclina-
tions. Available unsteady cylinder data is reviewed to provide the data base
needed for definition of this limiting load ratio.
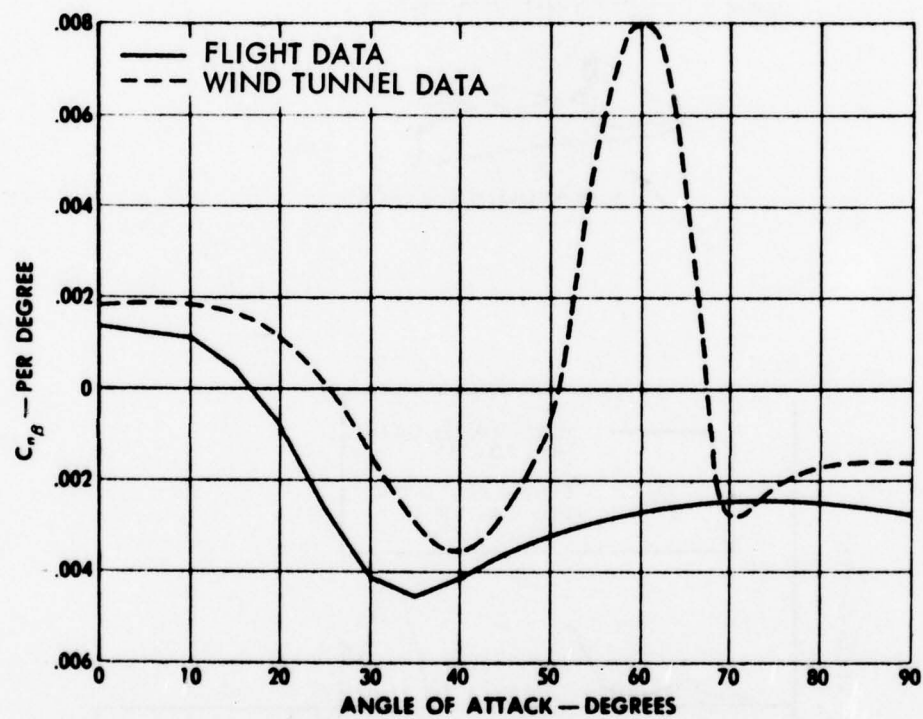
Fig. 1 F-111 Body Axis Directional Stability (Ref. 52)

WIND → LOW ANGLES-OF-ATTACK

WIND → HIGH ANGLES-OF-ATTACK

WIND TUNNEL DATA
(Re = 2.0 x 10^6)

△ FLIGHT TEST DATA
(Re = 6.7 x 10^6)

YAWING MOMENT COEFFICIENT
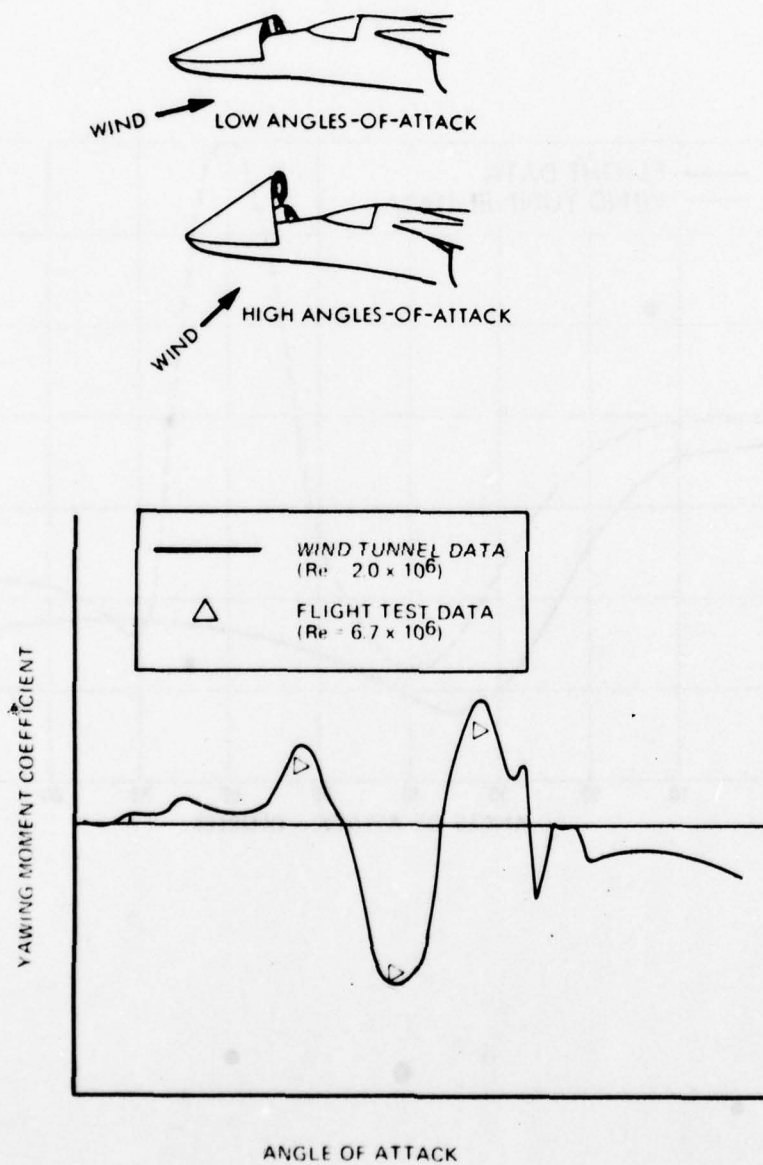
ANGLE OF ATTACK

Fig. 2 Wind Tunnel/Flight Test Correlation for the Effects of
Asymmetric Forebody Vortices (Ref. 24)

1-4
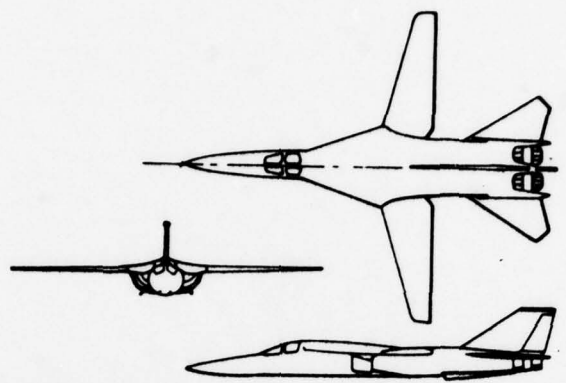
THREE-VIEW SKETCH OF CONFIGURATION WITH LONG
POINTED NOSE
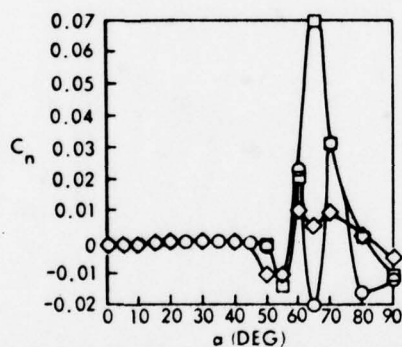
a. VARIATION OF YAWING-MOMENT COEFFICIENT WITH
ANGLE-OF-ATTACK; SYMBOLS INDICATE VALUES OBTAINED
IN SEVERAL REPEAT TESTS
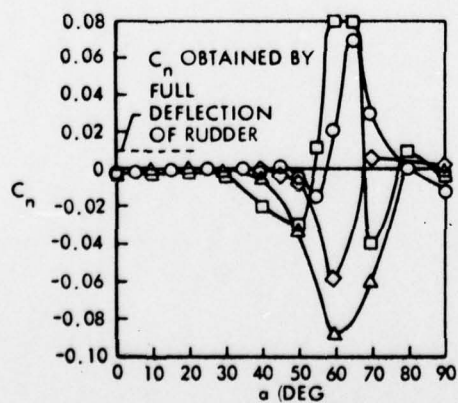
b. VARIATION OF STATIC YAWING-MOMENT COEFFICIENT
WITH ANGLE-OF-ATTACK FOR SEVERAL MODELS OF THE
CONFIGURATION; β = 0 DEG

Fig. 3 Repeatability of Measured Vortex-Induced Characteristics
(Ref. 18)

Section 2

BACKGROUND

As a slender body is pitched through the angle of attack range $0 \leq \alpha \leq 90^\circ$, it experiences four distinct flow patterns that reflect the diminishing influence of the axial flow component (Fig. 4). At low angles of attack ($0 \leq \alpha < \alpha_{SV}$) the axial flow dominates and the flow is attached. At intermediate angles of attack ($\alpha_{SV} \leq \alpha < \alpha_{AV}$) crossflow sweeps the boundary layer to the leeward side where it separates and rolls up into a symmetric vortex pair. At high angles of attack ($\alpha_{AV} \leq \alpha < \alpha_{UV}$), crossflow effects start to dominate and the vortices become asymmetric thereby producing a side force at zero sideslip. Finally, at very high angles of attack ($\alpha_{UV} \leq \alpha \leq 90^\circ$), the crossflow dominates completely and the boundary layer is shed in the form of a von Karman vortex street or a random wake depending upon Reynolds number, Mach number, geometric details, etc. These different flow regions were discovered by Allen and Perkins (Ref. 1), and their gradual development has been described in detail by Fiechter (Ref. 13) using exquisite flow visualization results to illustrate the various flow patterns.

On pointed, slender cones development of symmetric vortices has been observed when the angle of attack exceeds the cone half angle, both for laminar and turbulent flow, and at all speeds from incompressible flow to hypersonic velocities (Refs. 58-61). In laminar flow $\alpha_{SV} \approx 1.1 \, \theta_c$ whereas the turbulent value is $\alpha_{SV} \approx 1.3 \theta_c$. Asymmetric vortex shedding starts when the angle of attack exceeds the total included angle at the apex (Refs. 27 and 29), i.e., $\alpha_{AV} \approx 2 \, \theta_A$.

Whereas the angle α_{SV} seems to be rather insensitive to Mach number (Ref. 62), the angle α_{AV} varies greatly with Mach number (Refs. 27, 42, 63, 64 and Fig. 5). For not so slender noses ($\theta_A > 20^\circ$) α_{AV} is determined mainly by the body fineness ratio (ℓ/d). Fiechter (Ref. 11) observed asymmetric vortex shedding to start at station x when $\alpha = 4.2 \, d/x$. This value of α_{AV} agrees well with
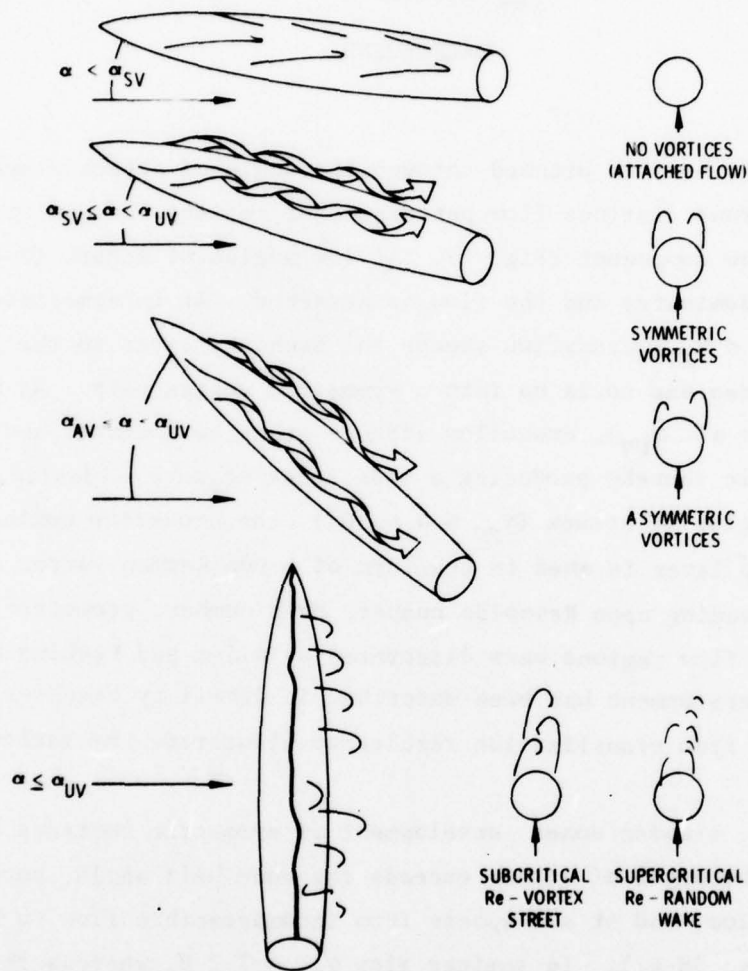
Fig. 4 Effects of Angle-of-Attack on Lee-Side Flow Field
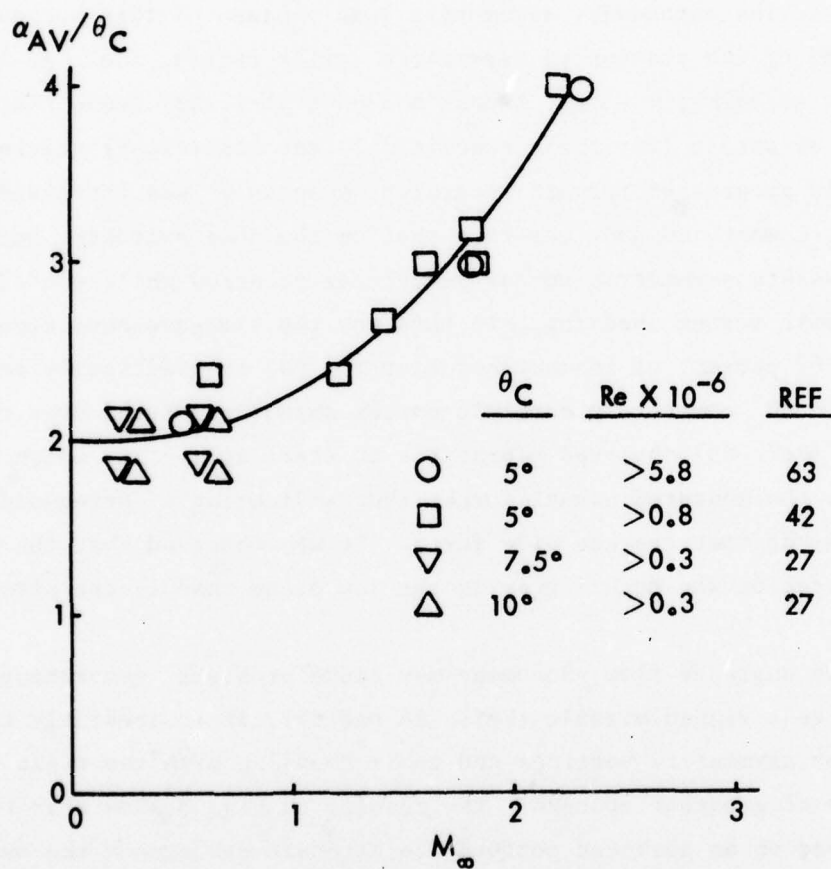
Fig. 5 Angle-of-Attack for Starting Asymmetric Vortex Shedding
on Cones at Subsonic and Supersonic Mach Numbers
(Refs. 58 and 59)

the experimental results in Refs. 27 and 32 for large ℓ/d. According to
several independent tests (Refs. 11, 25 and 29) unsteady vortex shedding starts
at $\alpha_{UV} \approx 60^\circ$.

At incipient asymmetric vortex shedding, $\alpha = \alpha_{AV}$, switching between symme-
tric and asymmetric vortices occurs (Refs. 11, 32 and 33). Through their
unsteady pressure measurements, Lamont and Hunt (Ref. 33) were able to show
that the time-averaged side force measured in a static test at $\alpha = \alpha_{AV}$ was only
60 percent of the instantaneous, asymmetric load because of this unsteadiness.
At the other end of the stationary asymmetric vortex region, i.e., at incipient
unsteady vortex shedding, $\alpha = \alpha_{UV}$, Lamont and Hunt (Ref. 33) found that the
von Karman vortex street (for their subcritical test conditions) started on
the aft body and progressed forward toward the nose as α was increased above
$\alpha = \alpha_{UV}$. Thus, Lamont and Hunt observed that on the nose switching between
the two steady-state asymmetric vortex geometries occurred while the aft body
exhibited periodic vortex shedding. In this way the time-averaged side force
decreased from 62 percent of instantaneous at $\alpha = 60^\circ$ to practically zero at
$\alpha = 75^\circ$. At $\alpha = 80^\circ$ completely harmonic vortex shedding existed over the whole
body. Thomson (Ref. 65) observed vibrations to start at $\alpha = 53^\circ$ which had a
large effect on the measured normal force, thus indicating a correspondingly
large effect on the time average side force. It was observed that the ampli-
tude of the vibration was much larger in the yaw plane than in the pitch plane.

While these unsteady flow phenomena may cause problems, generating significant
unsteady loads on a finned missile (Refs. 66 and 67), it is presently the static
loads induced by asymmetric vortices and their coupling with the rigid body
motion that are of greatest concern. The results in Fig. 3 show that the vortex-
induced side load on an advanced performance aircraft can exceed the available control
capability by an order of magnitude. Results from Ref. 30 shown in Fig. 6 demon-
strate that the side force generated by asymmetric vortices can exceed the normal
force for a missile type geometry. Consequently, the present investigation has
to a large extent been focused on the development of reliable means whereby the
upper bounds for vortex-induced asymmetric static loads can be determined. In
regard to the important problem of coupling between the vehicle motion and the
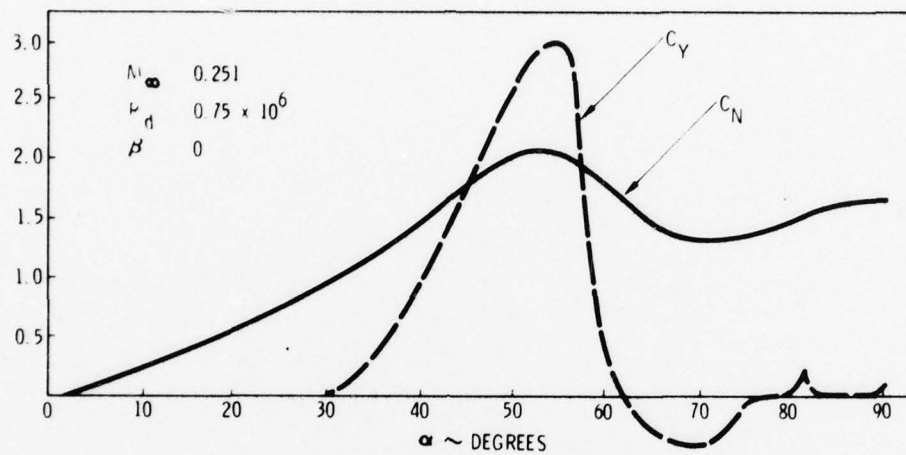
Fig. 6 Normal and Side Force Coefficients for a 3.5 ℓ/d Tangent Ogive (Ref. 30)

generation of asymmetric vortices, a full analysis was beyond the scope of this investigation. However, the problem has been explored to the extent needed for an intelligent evaluation of its importance.

Section 3
DISCUSSION

The standard approach when analyzing vortex-induced asymmetric loads has been to study the unsteady vortex shedding from a cylinder in two-dimensional flow and to apply that experience to the phenomenon of steady asymmetric vortex shedding from inclined bodies of revolution in three-dimensional flow. We are going to follow this classical approach, but will apply the two-dimensional results in a novel manner to determine limiting asymmetric loads in the three-dimensional case.

3-1 ASYMMETRIC VORTICES IN TWO-DIMENSIONAL FLOW

In two-dimensional flow the asymmetric vortices appear in the form of a periodic vortex shedding from bluff bodies. The various facets of the flow around circular cylinders are described in the reviews by Morkovin (Ref. 68), Wille (Ref. 69) and Berger and Wille (Ref. 70). Von Karman (Ref. 71) showed mathematically that only one vortex wake geometry was stable, one in which the vortices were forming an asymmetric vortex wake in which the ratio between lateral and longitudinal spacing is $h/L = 0.28$ (see Fig. 7). Thus the wake Strouhal number is

$$fh/\overline{U}_v = 0.28 \tag{3-1}$$

With $\overline{U}_v/U_\infty = 0.75$ (Refs. 72 and 73) and $h \approx d$ for a cylinder in subcritical flow one obtains $S_{vo} \approx 0.21$, which for $Re > 10^3$ is in good agreement with Rosko's subcritical formula (Ref. 74)

$$S_{vo} = 0.212 \left(1 - \frac{12.7}{Re}\right) \tag{3-2}$$
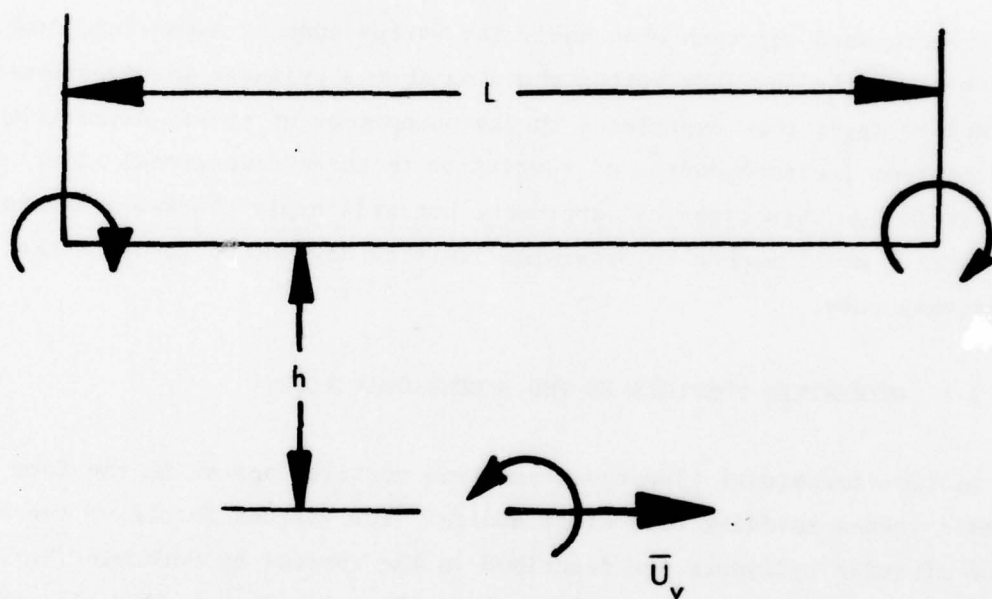
Fig. 7 Von Kàrmàn Vortex Street

3.1.1 Effect of Reynolds Number

Reynolds number has a profound effect on the vortex wake at very low speeds, $Re < 400$, and in the critical range, $10^5 < Re < 3.5 \times 10^5$. Following Roshko (Ref. 75) we show how the dimensionless wake wave length (S_{vo}^{-1}) and the drag exhibit similar Reynolds number trends (Fig. 8). In the subcritical range Roshko (Ref. 74) has already shown how the Strouhal number, Eq. (3-1), can be derived from the pressure at separation, which is equal to the base pressure and, hence, related to the drag. Until Roshko showed otherwise (Ref. 75), it was generally believed that the periodic von Kármán type vortex street could not exist at supercritical Reynolds numbers. Roshko showed that the harmonic vortex shedding reappeared at $Re \geq 3.5 \times 10^6$, with a shorter wavelength, higher frequency ($S_{vo} = 0.27$). Fig. 8 shows that this decrease in wavelength ($\sim S_{vo}^{-1}$) is "predicted" by the fall in drag. As the drag is reduced in proportion to how far past $\theta_s = 90°$ the separation point moves at supercritical Reynolds number one would think that the Strouhal number variation with Reynolds number could be deduced from the separation point movement. Eq. (3-1) gives

$$S_{vo} = 0.28 \; \frac{\overline{U}_v}{U_\infty} \Big/ \frac{h}{d} \tag{3-3}$$

The separation geometry gives

$$\left(\frac{h}{d} \right)_{supercrit} = \sin \theta_s \tag{3-4}$$

The convection velocity $(\overline{U}_v)_{supercrit}$ should be well approximated by the convection velocity in a turbulent boundary layer (Ref. 76), i.e., $\overline{U}_v/U_\infty = 0.8$. This approximation is well justified by the findings in a recent publication by Roshko (Ref. 77), showing that large scale eddies are an integral part of (all) turbulent flow. With $\theta_s = \sin^{-1}(0.8) = 127°$, which is in agreement with experiments (Refs. 78 and 79), Eq. (3-4) gives $(S_{vo})_{supercrit} = 0.28$. Roshko (Ref. 75) measured $S_{vo} = 0.27$, and others have measured $S_{vo} = 0.28$ (Ref. 80).

In regard to the very high frequencies ($.32 \leq S_{vo} \leq .42$) measured by Delany and Sorensen (Ref. 81) at $10^6 \leq Re < 2 \times 10^6$, the following observations can be made. The gaps between the cylinder and the tunnel wall allowed air of free stream
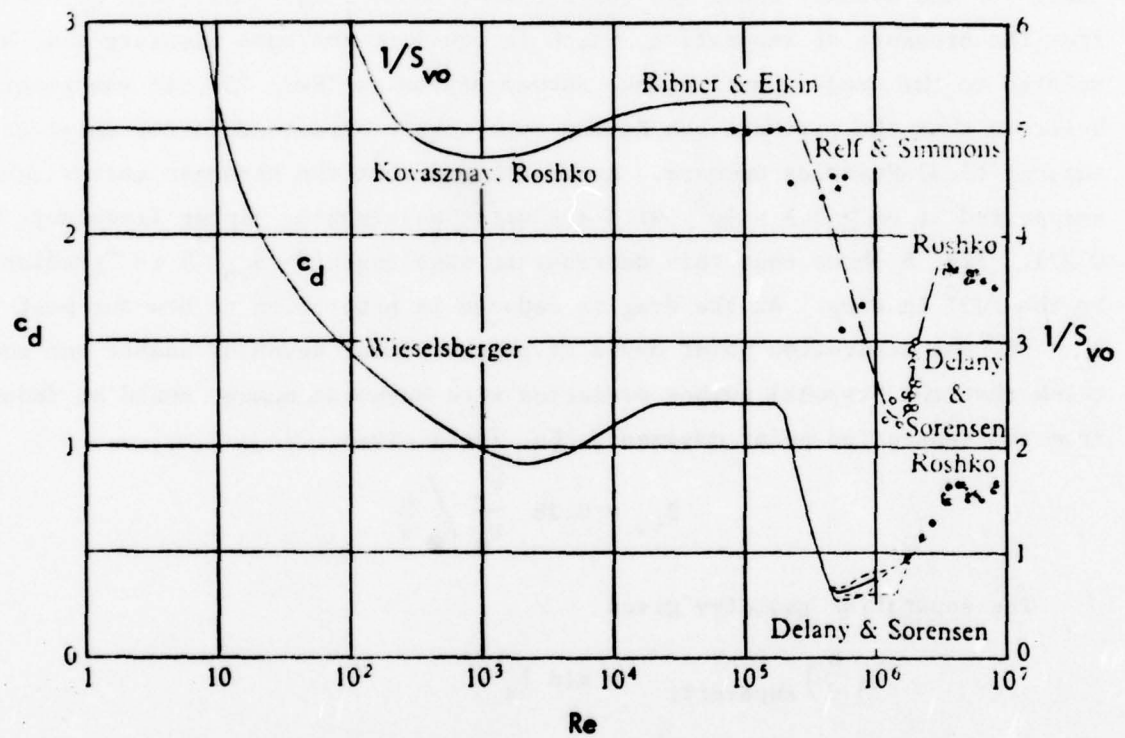
Fig. 8 Drag and Reciprocal Strouhal Number as a Function of Reynolds Number (Ref. 75)

pressure to bleed into the separated flow region. It caused a 20 percent reduction of the subcritical drag and could, of course, through its spanwise action help organize periodic vortex shedding. This is, at least, a possible effect, judging by Theisen's study (Ref. 82). More important, however, is the point brought up by Roshko (Ref. 75): That is, the Delany-Sorensen data are taken in the wake formation region, $x < 2L$ (Ref. 83). They had their probe at $x/d = 1.0$ and $x/d = 1.5$, whereas Roshko make his measurements at $x/d = 3.5$. Detailed measurements by Modi and Dikshit on a 0.9:1.0 elliptic cylinder (Ref. 84 and Fig. 9) show that the vortex wake geometry changes from $h/L = 0.48$ to $h/L = 0.24$ and the wavelength from $L/2a = 1$ to $L/2a = 4$ over this x-region, indicating that the frequency could be more than twice as high at $x/d = 1$ as at $x/d = 3.5$. In regard to the fact that h/L deviates from the von Kármán ratio $h/L = 0.28$, it should be noted that it has been shown by Birkhoff's Invariance Theorem (Ref. 85) that all h/L-values can be stable, and that it is the associated periodicity that may be unstable. This agrees well with the comment made by Delany and Sorensen about their Strouhal data: "At supercritical Reynolds numbers the Strouhal number data presented are for the predominant frequencies encountered, with the exception of the fineness ratio 2:1 rectangle where the disturbances in the wake were periodic and had a value of about 0.4." Also the high Strouhal number data by Bearman (Ref. 86 and Fig. 10) were taken in the near wake region, $x/d = 1.0$.

The high frequency data by Relf and Simmons (Ref. 87) and by Dresher (Ref. 88) shown in Fig. 10 were obtained in water tunnels pushing the speed to reach into the critical Reynolds number region. It is discussed by Varga and Sebestiyen (Ref. 89) how one in this case easily can run into cavitation problems. When cavitation occurs, the shedding frequency is determined by the cavitation number, independently of the Reynolds number. As one can obtain the same cavitation number with different Reynolds number, it is possible to obtain S_{vo} as a multi-valued function of Reynolds number, although it is uniquely determined by the cavitation number. Another way of obtaining a multivalued Strouhal number curve is to measure the second harmonic as well as the first as Loiseau and Scechenyi did (Ref. 90 and Fig. 10). Their spectral data show that at $Re = 10^6$ the second harmonic is better defined than the first (see Fig. 11). It is, therefore,

3-5
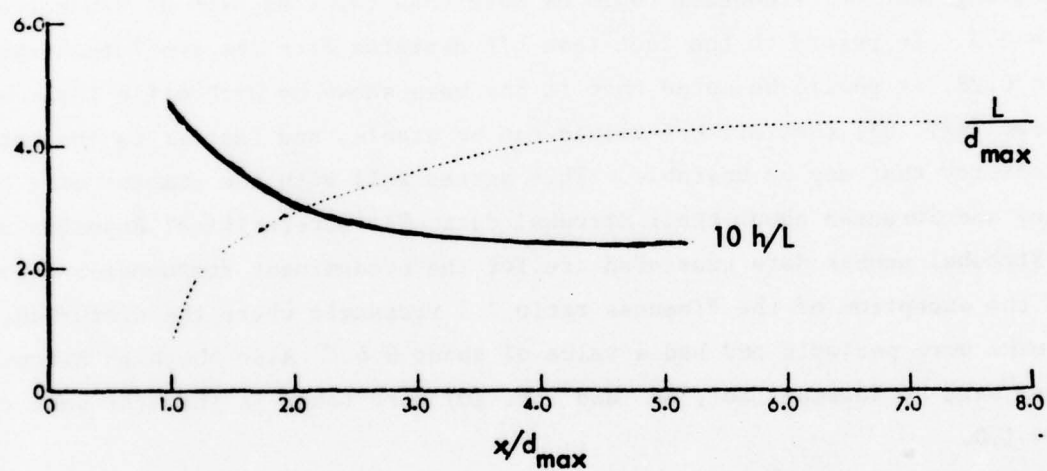
Fig. 9 Wake Geometry Ratio for Elliptic Cylinders as a Function of Downstream Distance (Ref. 84)
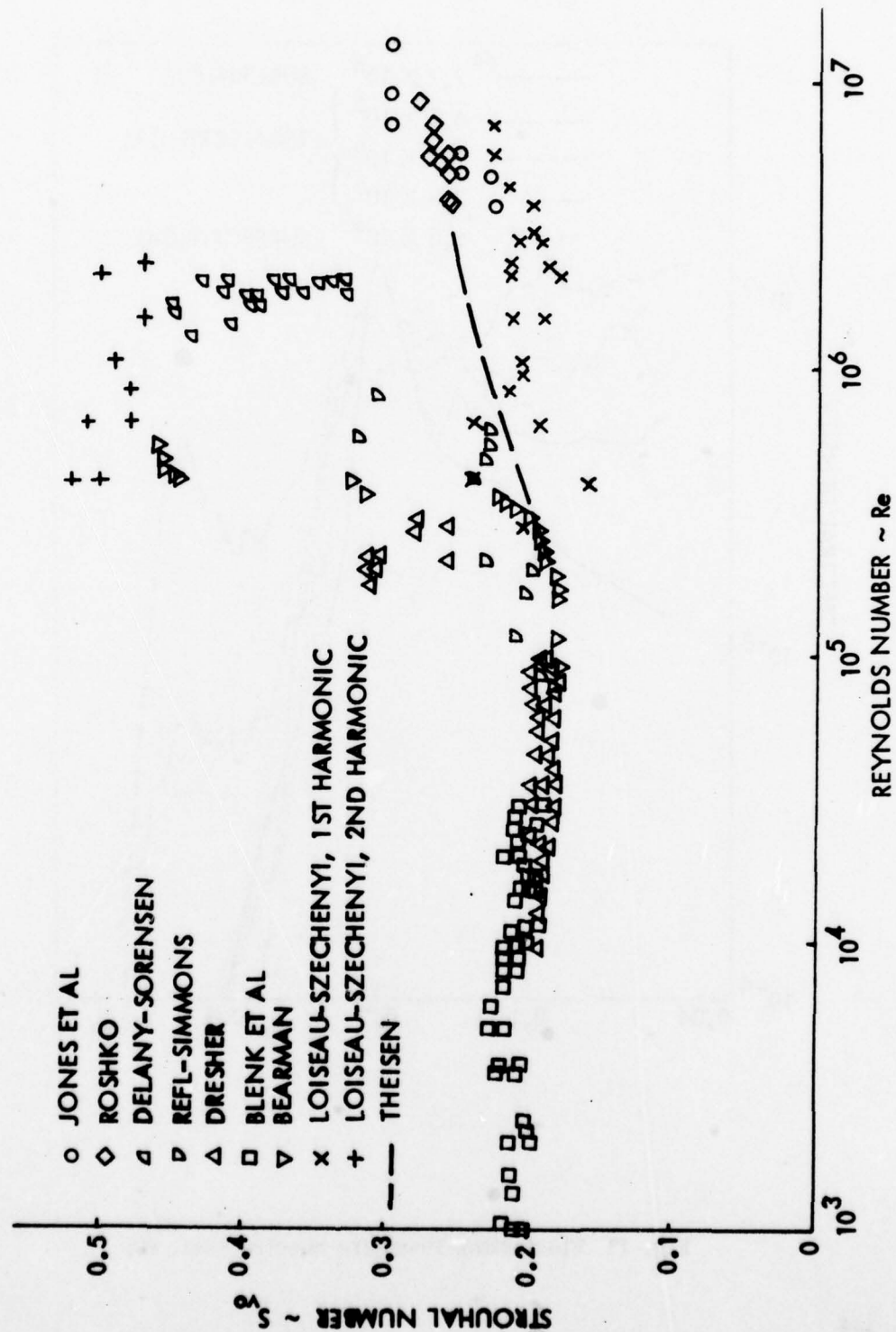
Fig. 10 Strouhal Number as a Function of Reynolds Number
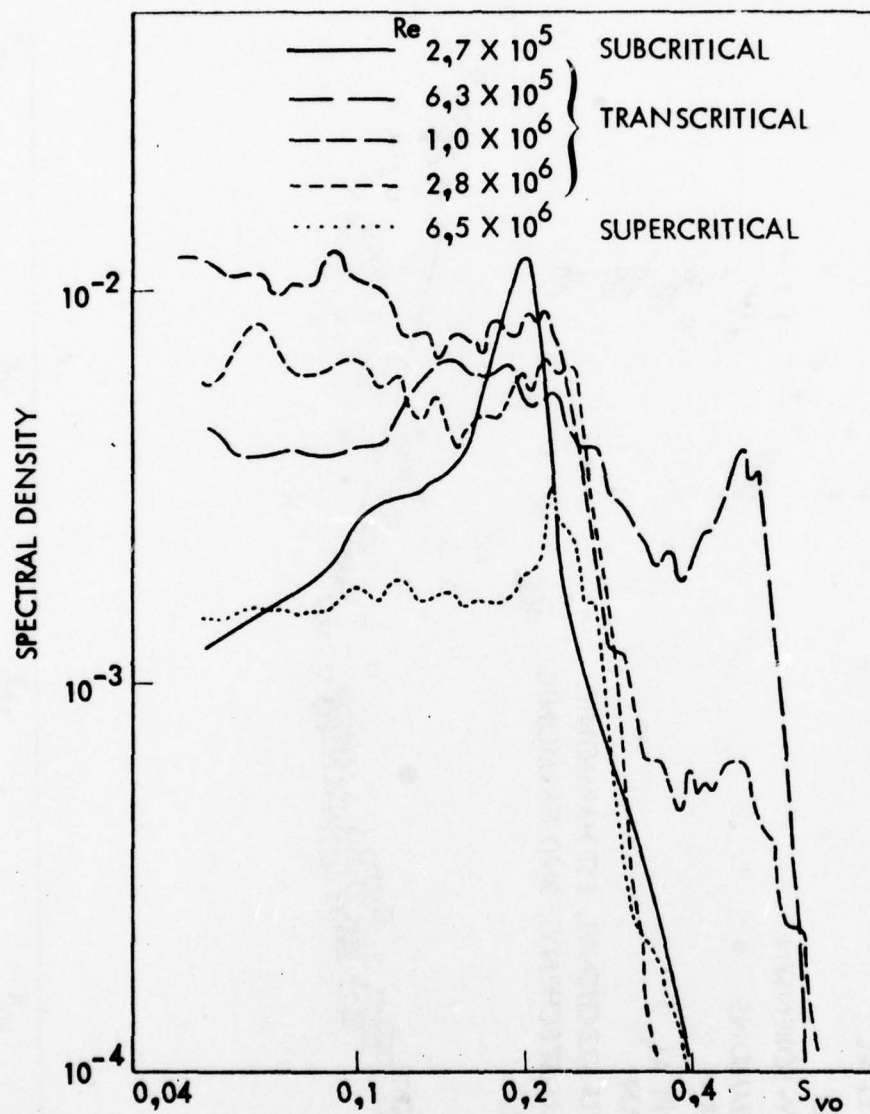
Fig. 11 Fluctuating Pressure Spectra (Ref. 89)

possible to mistake it for the fundamental frequency, thus explaining some of the high Strouhal number values obtained from flunctuating pressure measurements, for example.

In addition to the above speculations about the causes for the measured high Strouhal numbers in the critical Reynolds number region one has to add the following: Humphreys (Ref. 91) has shown that the boundary layer transition process is highly three-dimensional, with a spanwise wave or cell pattern near the cylinder surface playing an important role. Jones et al. (Ref. 92) show that translatory oscillations increase the spanwise correlation length greatly. Thus, model vibration could affect the measurements. Dresher describes his high Strouhal number data as being for very irregular vortex shedding for which it was difficult to assign a fixed frequency. Roshko (Ref. 75) did not find any periodicity in the wake below $Re = 3.5 \times 10^6$, and neither did Jones, et al. (Ref. 92), who probed the wake down to $Re = 1.3 \times 10^6$. The Strouhal number results obtained by Blenk et al. (Ref. 93) at subcritical Reynolds numbers are also included in Fig. 10. Also included is the "center frequency" computed by Theisen (Ref. 82) for the critical Reynolds number region ($0.2 \times 10^6 < Re < 3.5 \times 10^6$) using the spectral characteristics measured by Fung (Ref. 94). It can be seen that this "center frequency" curve provides a smooth transition from subcritical to supercritical Strouhal numbers.

It was shown in Fig. 9 that the wavelength can be up to four (4) times shorter in the near wake region than in the downstream, stabilized, periodic vortex wake. The question one asks oneself is, of course: How is this continuous change of wavelength (and associated frequency) taking place? A recent publication (Ref. 95) explains this phenomenon using a vortex coalescence process.* At the separation point eddies are emitted at a high rate. This emission Strouhal number S_e is determined by the local Reynolds number at separation. After n coalescences the Strouhal number is reduced to $S_{vo} = S_e/2^n$. This coalescence region, which precedes the final stable wake, can be extended by use of a short splitter plate, $L_S/d < 1$, with the result that the final Strouhal number is decreased (Ref. 96).

---

*A similar process was discussed by Roshko recently (Ref. 77).

While the Delany-Sorensen data (Ref. 81) may not be quantitatively correct, they should, as the authors point out, give the correct qualitative effects of cross-sectional shape. Fig. 12 shows an interesting comparison between two isosceles, triangular cylinders, one with the apex forward, the other with the apex aft. In both cases the maximum exposed cross-sectional height is the same, and the Strouhal frequency at subcritical Reynolds numbers is, as a consequence, roughly the same. However, the Strouhal numbers measured at supercritical conditions are widely different. This is the result of widely different flow separation geometries. Assuming that the flow separates close to the flat base for the forward facing triangle, one obtains through the (h/d)-ratios discussed earlier, Eqs. (3-3) and (3-4), the ratio 1.4 between supercritical and subcritical Strouhal numbers, which compares rather well with the measured value. For the backward facing triangle one would expect flow separation to occur at the start of the hemispherical base. This gives the ratio 3.6, which also is in good agreement with the experimental value.

3-1.1.1 <u>Effect of Roughness and Turbulence</u>. Although Reynolds number is a very important parameter, it is not sufficient by itself to determine whether the flow on the cylinder is supercritical or subcritical. Surface roughness can change the effective critical Reynolds number by one order of magnitude (Ref. 97 and Fig. 13). Szechenyi (Ref. 98 and Fig. 14) shows how by the means of this roughness data, correlated via the roughness Reynolds number (R_δ), the smooth cylinder data can be extended more than one decade up to an effective Reynolds number of 2×10^8 (obtained as $Re/(\delta/d)_{smooth}$ where $(\delta/d)_{smooth} = 3.5 \times 10^{-5}$). This reliance solely upon roughness Reynolds number has come under some criticism from others (Ref. 99), who point out that at high Reynolds numbers, $Re > 10^8$, the roughness effect is independent of Reynolds number. However, looking at Fig. 14, one finds that the drag does not change for $R_\delta > 10^3$, i.e., for $Re_{eff} > 3 \times 10^7$, and that the R_δ-correlation therefore is valid for extrapolation up to the supercritical, high Reynolds number level. How the roughness and Reynolds number in combination affect the boundaries between subcritical and supercritical flow conditions is shown in Fig. 15 (Ref. 100).

It is interesting to compare the effect of roughness on drag with that of

3-10
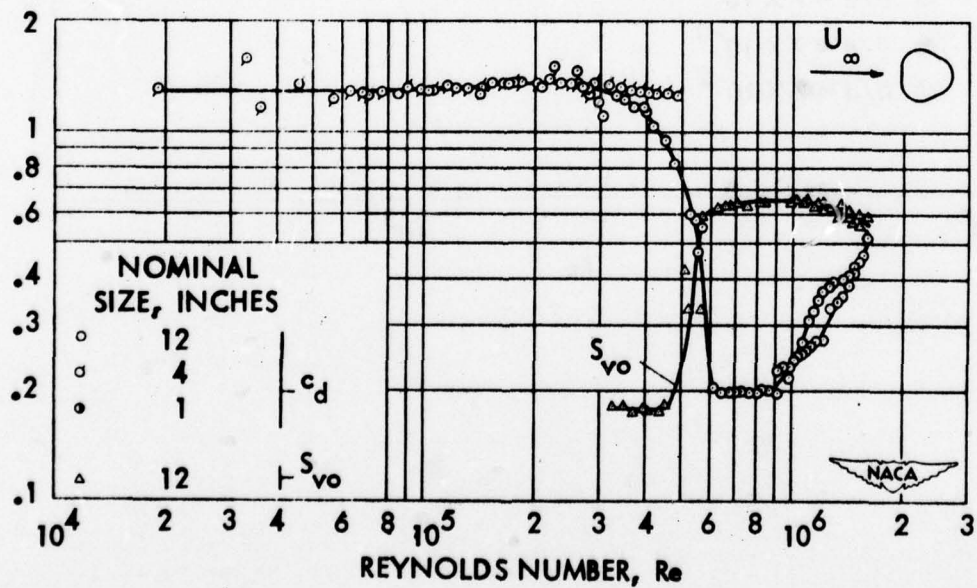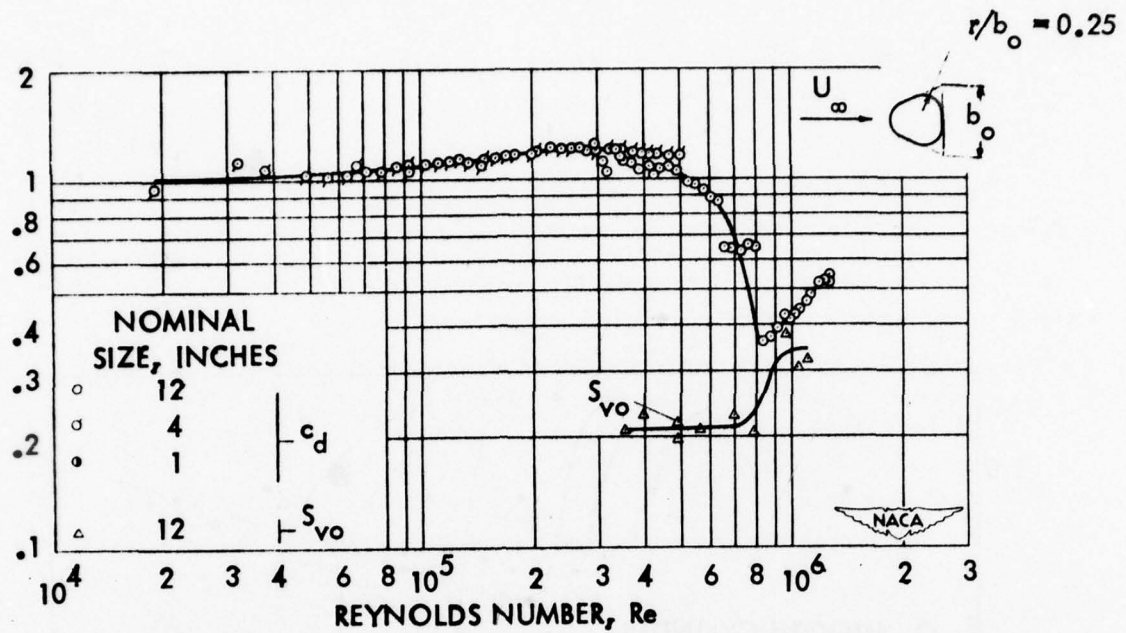
Fig. 12 Strouhal Number for Cylinders with Triangular Cross
Section (Ref. 81)
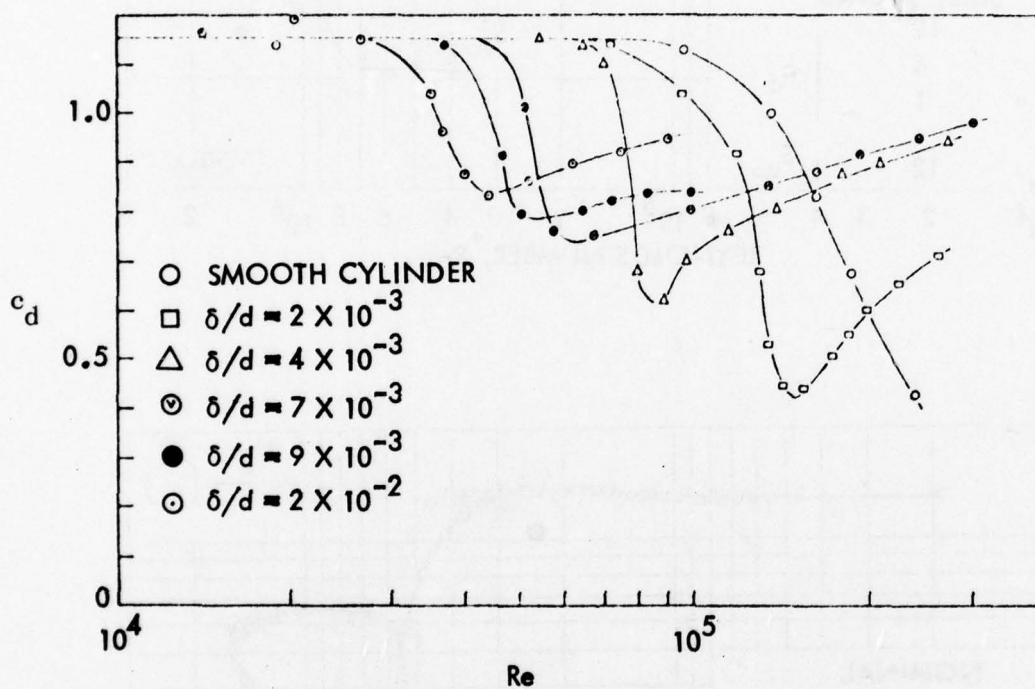
Fig. 13 Effect of Roughness on Cylinder Drag (Ref. 97)
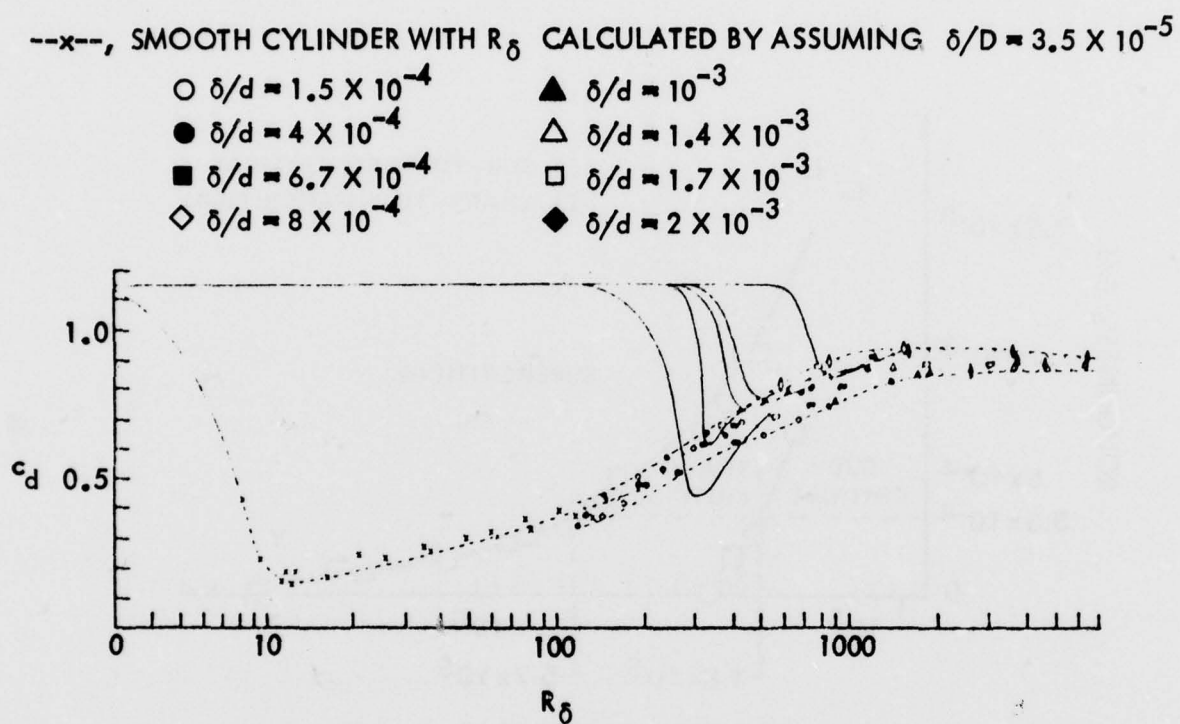
Fig. 14 Equivalence for Roughness and Reynolds Number Effects on Cylinder Drag (Ref. 98)
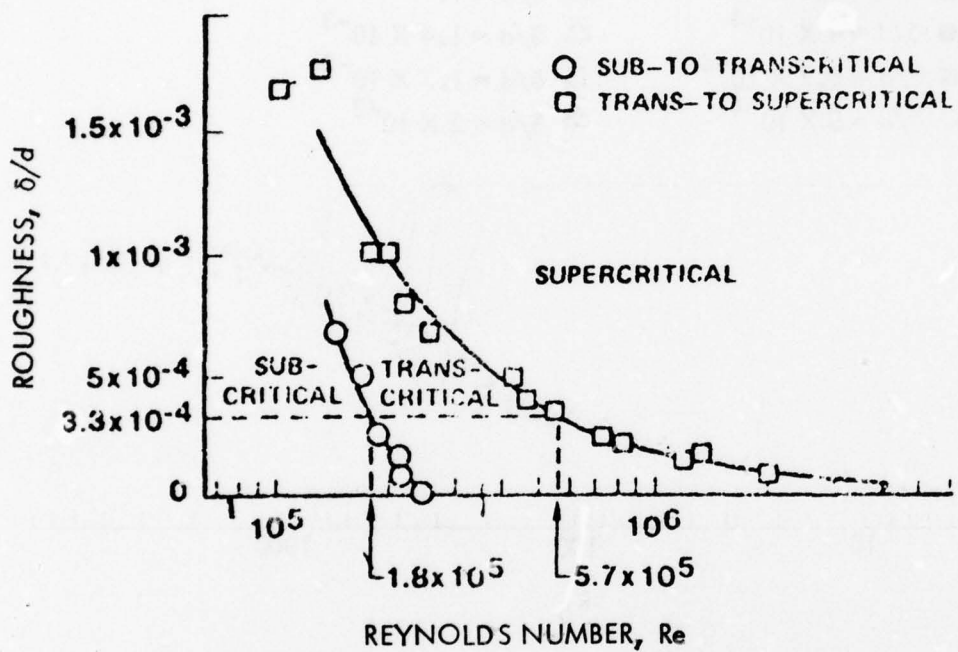
Fig. 15 Limits of Flow Regimes for Different Relative Roughness Sizes
(Ref. 100)

well designed vortex generators, placed in one row at $\theta = 50^{\circ}$ (Ref. 101 and Fig. 16). The vortex generators do not simply move the critical Reynolds number but seem to eliminate the subcritical drag rise altogether. Of course, at supercritical (off-design) flow conditions the vortex generators cause a large drag increase.

The effect of turbulence has been studied by Gerrard (Ref. 102) and many others. However, of more direct interest here are the results published by Humphreys (Ref. 91 and Fig. 17) showing how much the critical Reynolds number can vary between various low speed wind tunnels. The effect of turbulence, wall boundary layer noise, etc. is almost as large as that of roughness, and together the effects can move the critical Reynolds number more than one decade.

3-1.2 Effect of Mach Number

Compressibility has a pronounced effect on the cylinder drag at high Reynolds numbers (Ref. 103 and Fig. 18). The supercritical low drag region is effectively terminated at $M_{\infty} \approx 0.4$, where shock-boundary layer interaction starts controlling the drag until at $M_{\infty} \approx 0.5$ it has reached the subcritical level and is essentially independent of Reynolds number. Of course, the drag characteristics are a great deal more complicated than what Fig. 18 would indicate. The "competition" between Reynolds number and Mach number effects in forming this "drag bucket" is described in great detail in Ref. 104, using flow visualization and measurements, such as those shown in Fig. 19. In the low Mach number end of the "bucket" Reynolds number effects dominate, at the high end Mach number effects dominate. This causes the same problem when evaluating experimental data as has been encountered in regard to static and dynamic stall of airfoils (Refs. 105 and 106).

Figs. 18 and 19 show that the subcritical drag is relatively unaffected by compressibility effects. It is, therefore, no surprise that the corresponding vortex shedding frequency is also relatively insensitive to subsonic Mach numbers (Refs. 43, 107 and Fig. 20). It was also shown recently that the separation points oscillate in very similar manner whether the separation is shock-
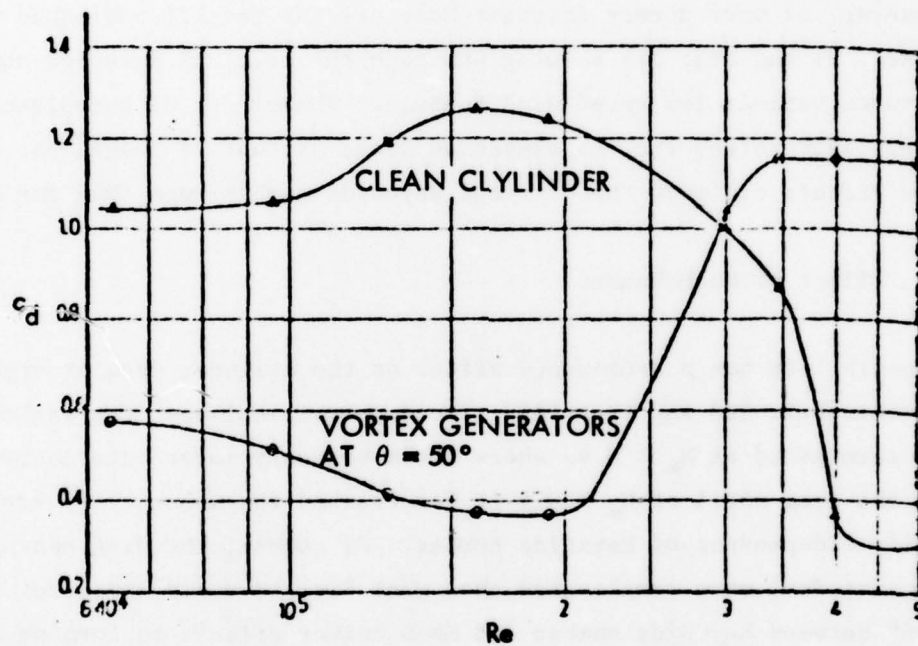
Fig. 16 Drag Coefficient for Cylinder with and without Vortex
Generators (Ref. 101)
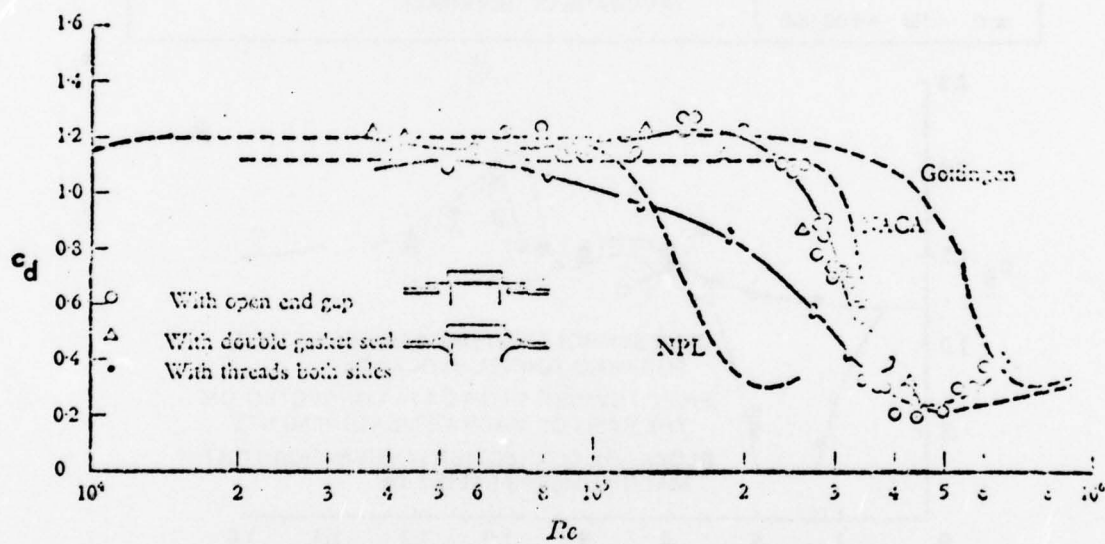
Fig. 17 Drag Coefficient vs Reynolds Number in Different Ground Facilities (Ref. 91)
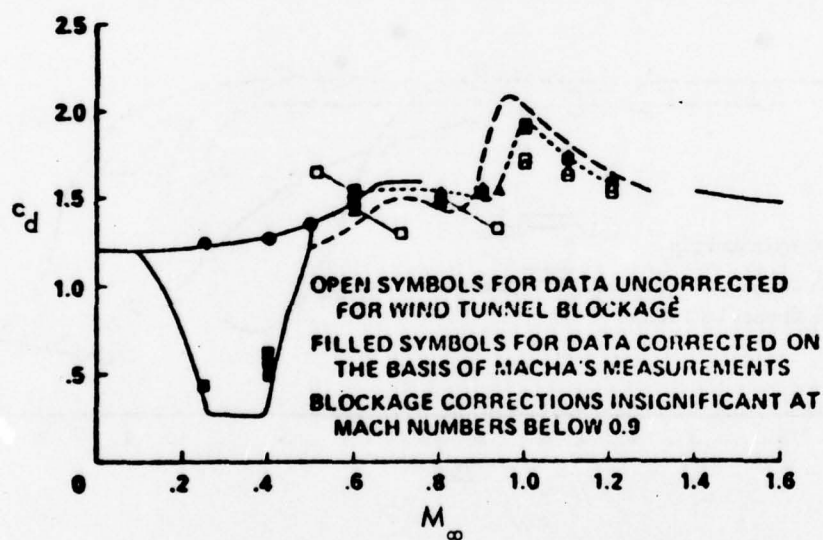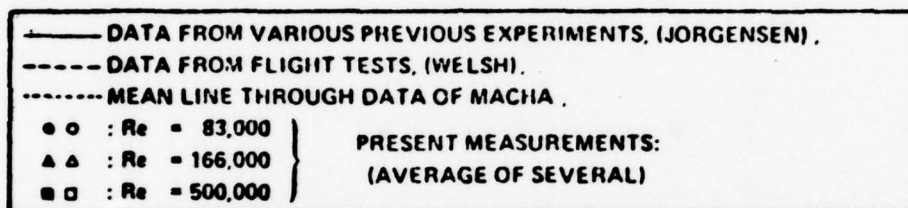
Fig. 18 Effect of Mach Number on Cylinder Drag (Ref. 103)
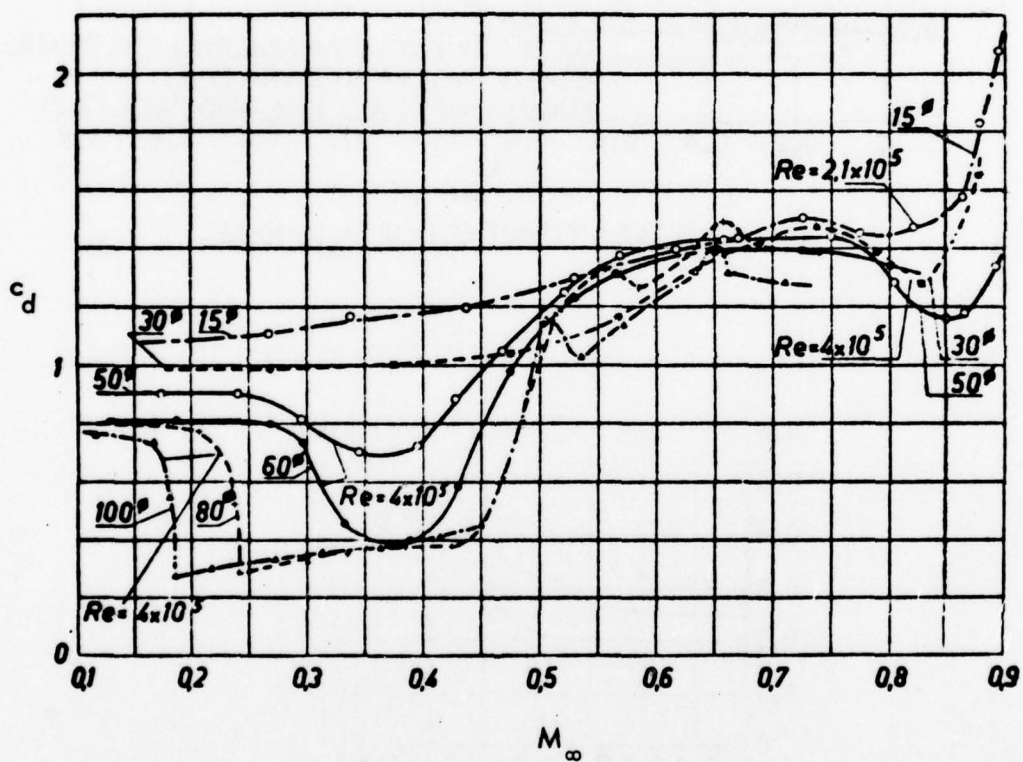
Fig. 19 Effect of Mach Number and Reynolds Number on Cylinder Drag
(Ref. 104)
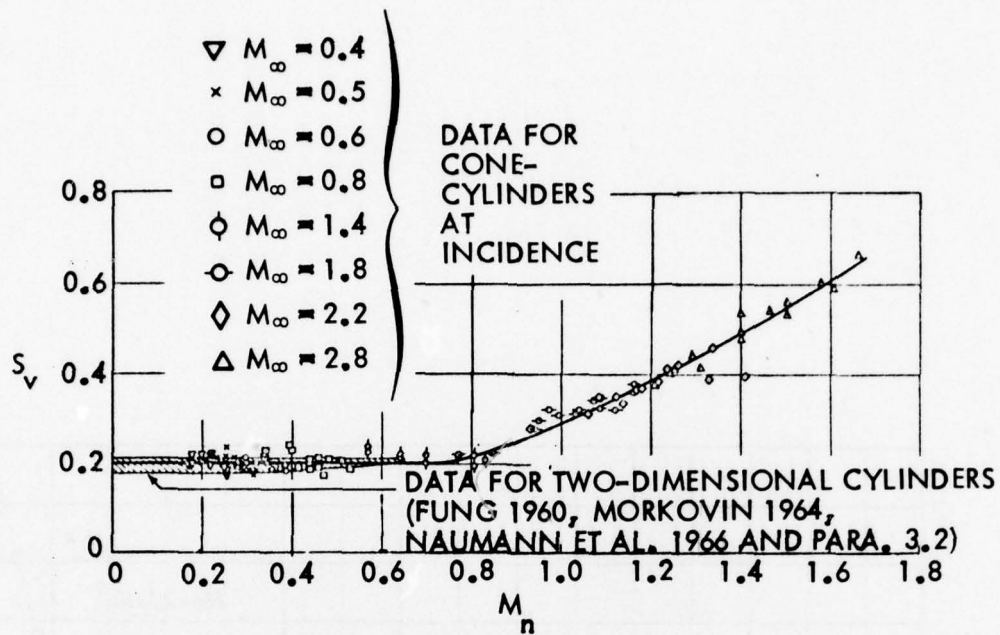
a. S_v AS A FUNCTION OF M_n AND M_∞
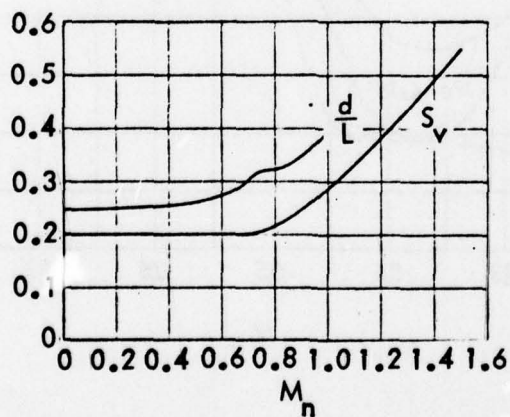
b. S_v AND d/L AS A FUNCTION OF M_n

Fig. 20 Effect of Mach Number on Vortex Wake Geometry and Strouhal Number (Ref. 107)

induced or not (Ref. 95 and Fig. 21). In the transonic and supersonic speed range, however, changes do take place, both in regard to drag (Figs. 18 and 19) and frequency characteristics (Fig. 20). The cross flow Mach number trends[*] in Fig. 20 are, of course, associated with the changing separation location. Using again the concepts expressed in Eqs. (3-1) through (3-4) one obtains

$$\left(\frac{d}{L}\right)_{M_n} \bigg/ \left(\frac{d}{L}\right)_{M_n=0} = S(M_n)/S(0) = \csc \theta_s \qquad (3-5)$$

For $M_\infty = 1$ Fig. 20b gives $(d/L)_{M_\infty}/(d/L)_{M_\infty=0} = 1.53$ and $S(M_\infty/S(0) = 1.45$. The mean value 1.49 gives $\theta_s = 138°$. For $M_\infty = 1.5$ the Strouhal number data in Fig. 20 gives $\theta_s = 158°$ using Eq. (3-5). In contrast to these results by Thomson for 3-D steady asymmetric vortex arrays (Ref. 107) Thomann (Ref. 108) found in his two-dimensional test that the periodic vortex shedding from a wedge ceased when the sonic speed was exceeded.

Macha (Ref. 109) has found that the terminal shocks seem to freeze the cylinder drag at a constant level for $0.6 \leq M_\infty \leq 0.9$, a trend clearly visible also in the data shown in Fig. 18. The terminal shocks have a similar effect on the flow separation on airfoils (Ref. 106 and Fig. 22). The results indicate that the unsteady perturbation of the separation point is restricted by the presence of the terminal shocks. One can expect the effect to be similar for the cylinder, and that, as a consequence, the root-mean-square lift will reach its minimum in this Mach number range. This would explain the observed effect of compressibility on the loads induced by three-dimensional asymmetric vortices (discussed in Section 3-2.2). It has an important implication in regard to our predicted maximum load boundaries. As they are determined using incompressible data they should supply conservative upper boundaries up to near sonic speeds.

3-1.3 Magnus Effects

The Magnus characteristics for rotating bodies in two-dimensional flow have recently been reviewed by Jacobson (Ref. 110). The classical positive

---

[*] The good agreement with two-dimensional data at $M_n = M_\infty < 1$ in Fig. 20a suggests that the M_n-trends at $M_n > 1$ also could apply to 2-D trends at $M_\infty > 1$.

$M_\infty = 0.80 \quad Re = 1.6 \, 10^5$

$M_\infty = 0.30 \quad Re = 0.80 \, 10^5$
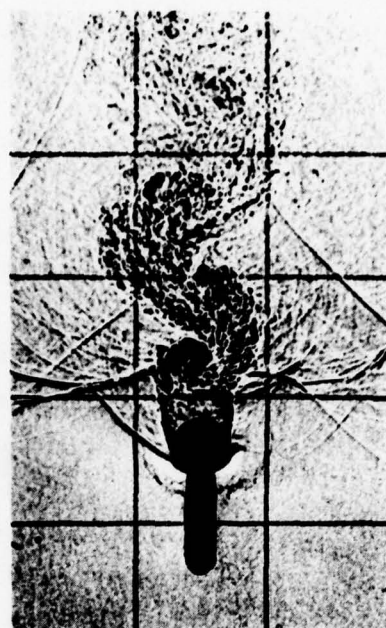
Fig. 21 Flow Pictures of Oscillating Separation Points on Cylinder
at $M_\infty = 0.3$ and $M_\infty = 0.8$ (Ref. 95)
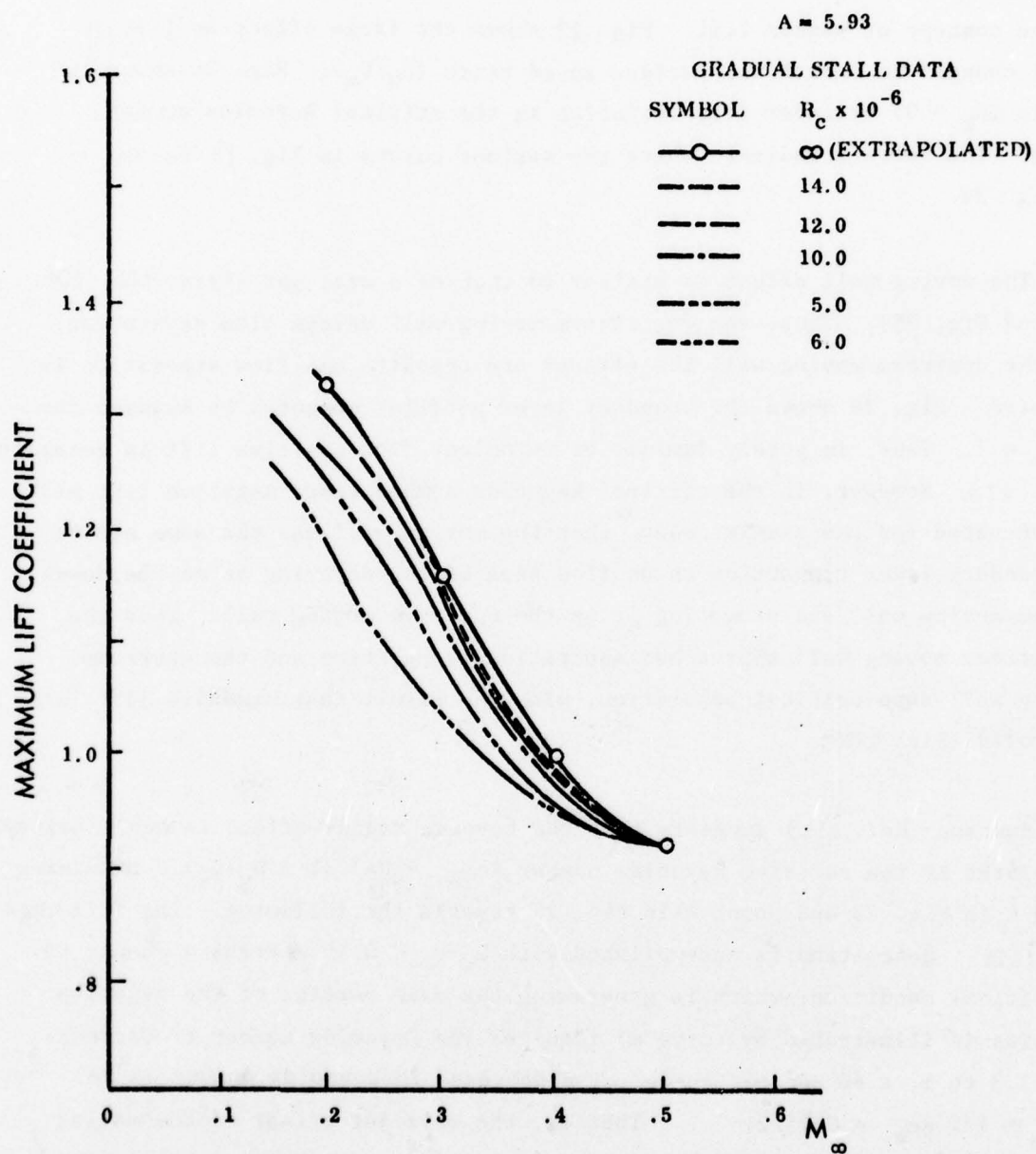
Fig. 22 Maximum Lift as a Function of Mach Number and Reynolds
Number (Ref. 106)

lift is generated when the boundary layer remains laminar or turbulent.
However, when boundary layer transition occurs large reversals of the Magnus
effect are observed, resulting in the generation of negative lift (Ref. 111).
A very thorough investigation of this phenomenon has been carried out by
Swanson (Ref. 112), who also gives a historical account of the development
of the concept of Magnus lift. Fig. 23 shows the large effect on lift of
small changes in rotational surface speed ratio (U_W/U_∞). Fig. 24 shows the
static $(U_W = 0)$ cylinder drag variation in the critical Reynolds number
range. The letters indicate where the various curves in Fig. 23 belong
in Fig. 24.

The moving wall effect is similar to that of a wall jet (Refs. 105, 106,
113 and Fig. 25). Thus, the downstream moving wall delays flow separation.
For the upstream moving wall the effects are opposite and flow separation is
promoted. Fig. 26 shows the boundary layer profiles computed by Swanson for
$U_W/U_\infty = 1$. Thus, in purely laminar or turbulent flow positive lift is generated
(Fig. 27a. However, in the critical Reynolds number range negative lift will
be generated for the simple reason that the moving wall has the same effect
on boundary layer transition as on flow separation, delaying it on the down-
stream moving wall and promoting it on the upstream moving wall. Thus the
downstream moving wall approaches subcritical separation and the upstream
moving wall supercritical separation, with the result that negative lift is
generated (Fig. 27b).

Swanson (Ref. 112) suggests that the reverse Magnus effect is qualitatively
correlated by the relative Reynolds number $Re_{rel} = Re$ $(1 \pm U_W/U_\infty)$. Examining
curve ℓ in Fig. 23 and point ℓ in Fig. 24 reveals the following. The full nega-
tive lift generation is accomplished with $U_W/U_\infty < 0.15$ whereas a change to
subcritical condition, which is generating the main portion of the negative
lift (as is illustrated by curve m) requires the Reynolds number to decrease
from 3.3 to 1, a 60 percent chage. The decrease in Reynolds number is Re
$U_W/U_e \approx 1/2\ Re_\infty = 0.15/2$. That is, the wall jet effect of the moving
wall accounts for 7/8 of the observed negative lift generation. Looking at
curve n reveals that the regular positive lift due to delayed separation is

3-24
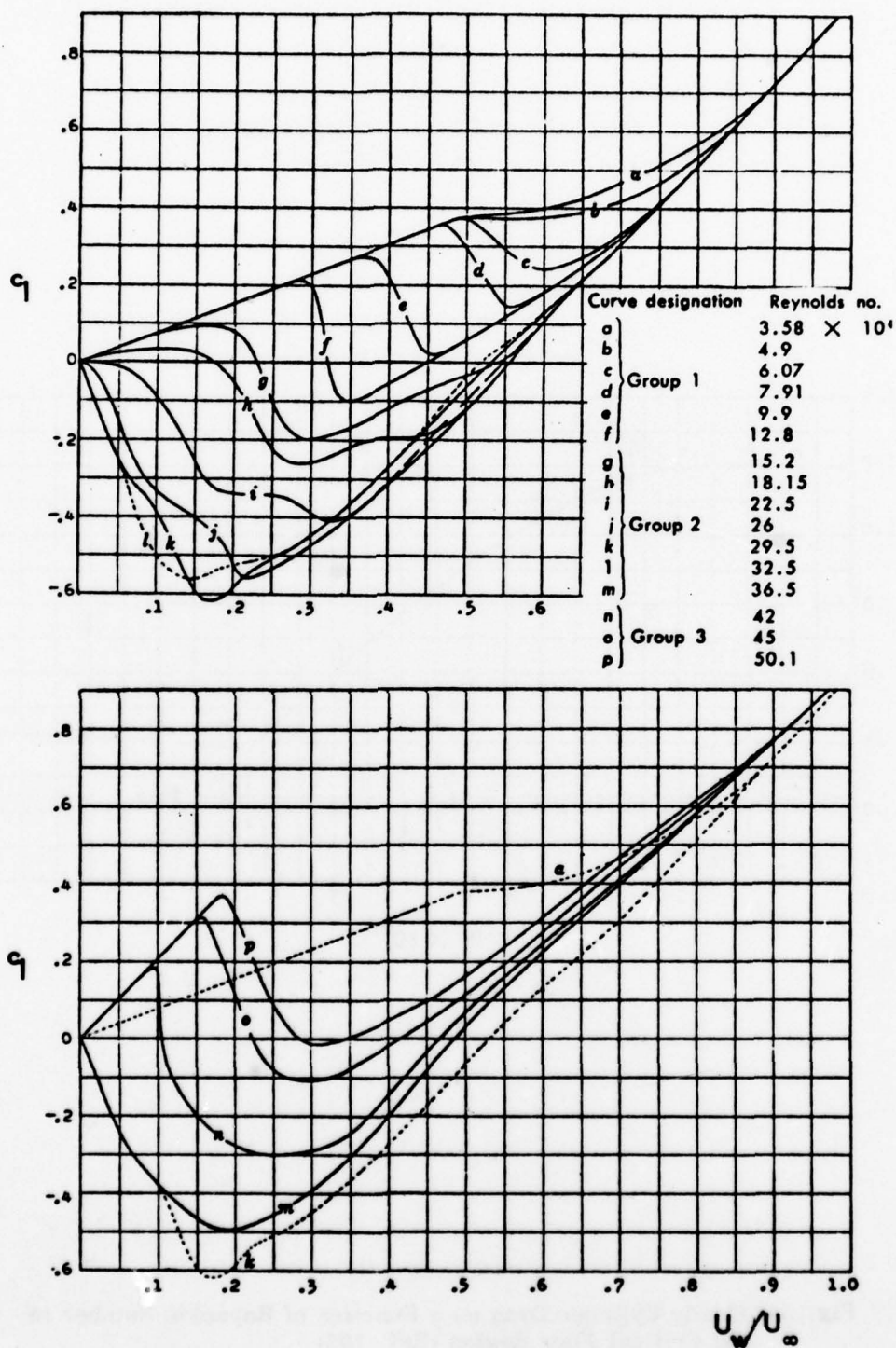
Fig. 23 Magnus Lift as a Function of Rotational Speed Ratio and Reynolds Number
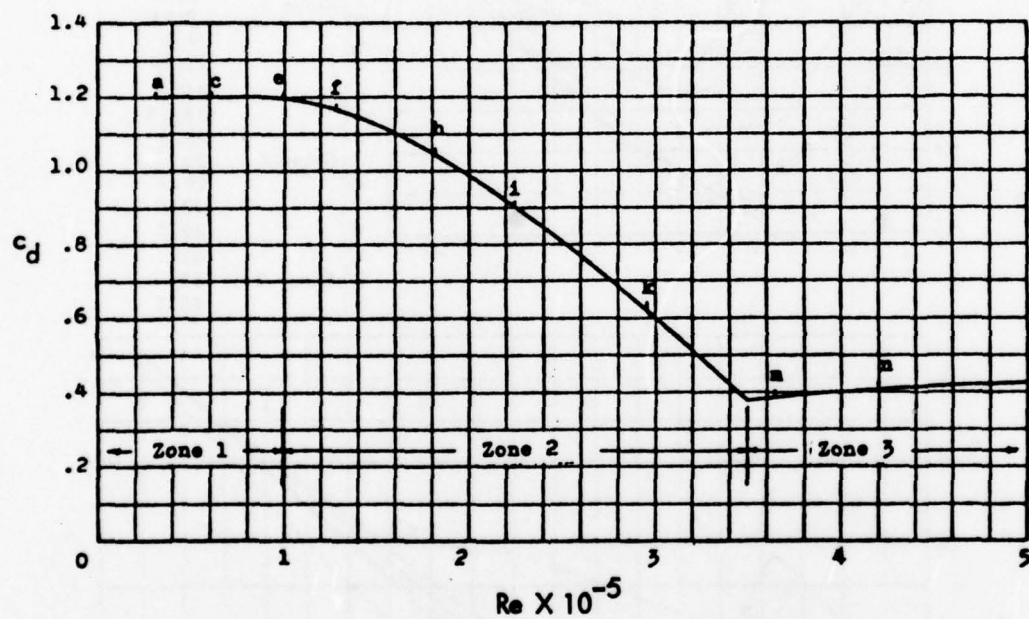
Fig. 24 Steady Cylinder Drag as a Function of Reynolds Number in the Critical Flow Region (Ref. 103)

generated up to $U_W/U_\infty = 0.1$, when the delay of transition on the downstream moving wall causes a more or less discontinuous loss of the positive lift as subcritical flow conditions are established on the top side. The results obtained by Miller (Ref. 114) show that this discontinuous jump can occur intermittently back and forth at the critical condition, in his case Re = 5×10^5 and $U_W/U_\infty = 0.27$.

Swanson (Ref. 112) also measured the drag for the rotating cylinder (Fig. 28). Studying this figure together with Figs. 23 and 24 reveals that the supercritical condition tends to dominate the drag change, which is understandable from geometric considerations. For curve f the rotation effect is completely a change from subcritical to supercritical flow conditions on the bottom side, when the velocity ratio is increased from $U_W/U_\infty = 0.25$ to 0.35. Consequently, the drag decreases greatly. For curve ℓ, on the other hand, the rotation effect is completely a change from supercritical to subcritical flow conditions on the top side, when increasing U_W/U_∞ from zero to 0.2, and the drag is increased. In this case the drag change is small relative to the lift change, again due to the geometric location of the separation point affected by the rotation.

3-1.4 Effect of Translatory Oscillation

Parkinson and Ferguson (Refs. 115 and 116) showed that the von Kármán vortex street could be driven off its regular shedding frequency by oscillating the cylinder transversely to the flow at nearly resonant frequencies (Fig. 29). Stansby (Ref. 117) showed recently that for large oscillation amplitudes this change in frequency could be as large as a 30 percent decrease or a 90 percent increase (Fig. 30). Koopman (Ref. 118) has shown that for very low Reynolds number there exists a threshold amplitude which must be exceeded before vortex "lock-in" occurs (Fig. 31). Mei and Currie (Ref. 119) report that Maekawa and Mizuno found in their test at high subcritical Reynolds numbers, 0.37×10^5 > Re < 2.8×10^5, that the separation points on a stationary cylinder oscillated between 78 and 90 degrees azimuth, while Landweber had found it to remain fixed when the cylinder described small amplitude translatory oscillations. However,
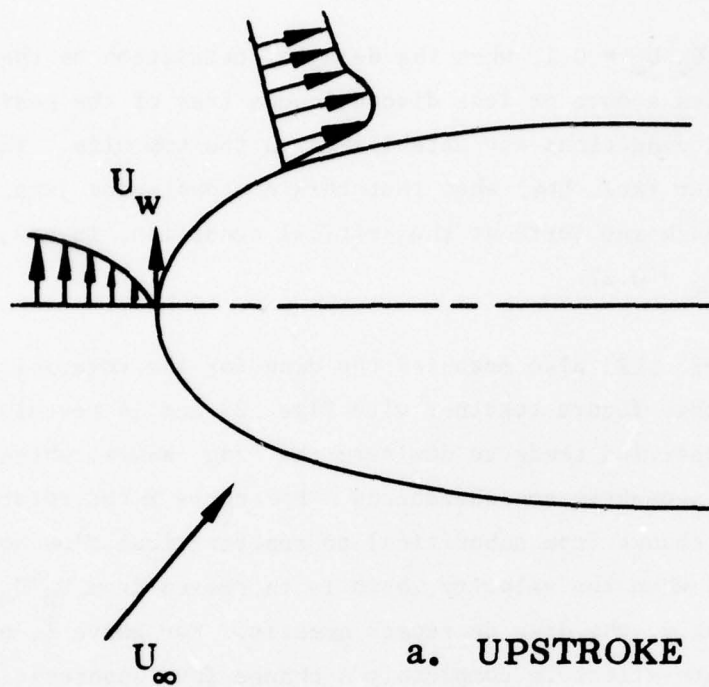
a. UPSTROKE
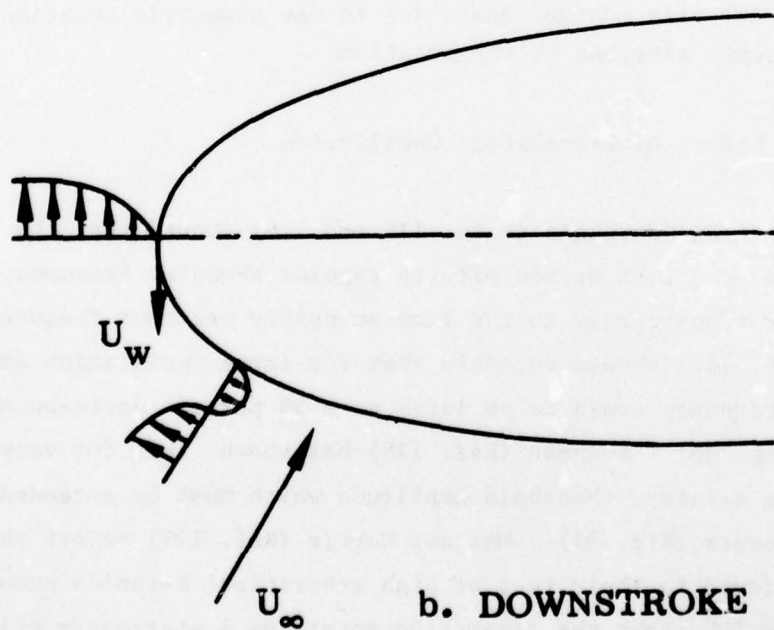
b. DOWNSTROKE

Fig. 25 Pitch Rate Induced Wall Jet Effects
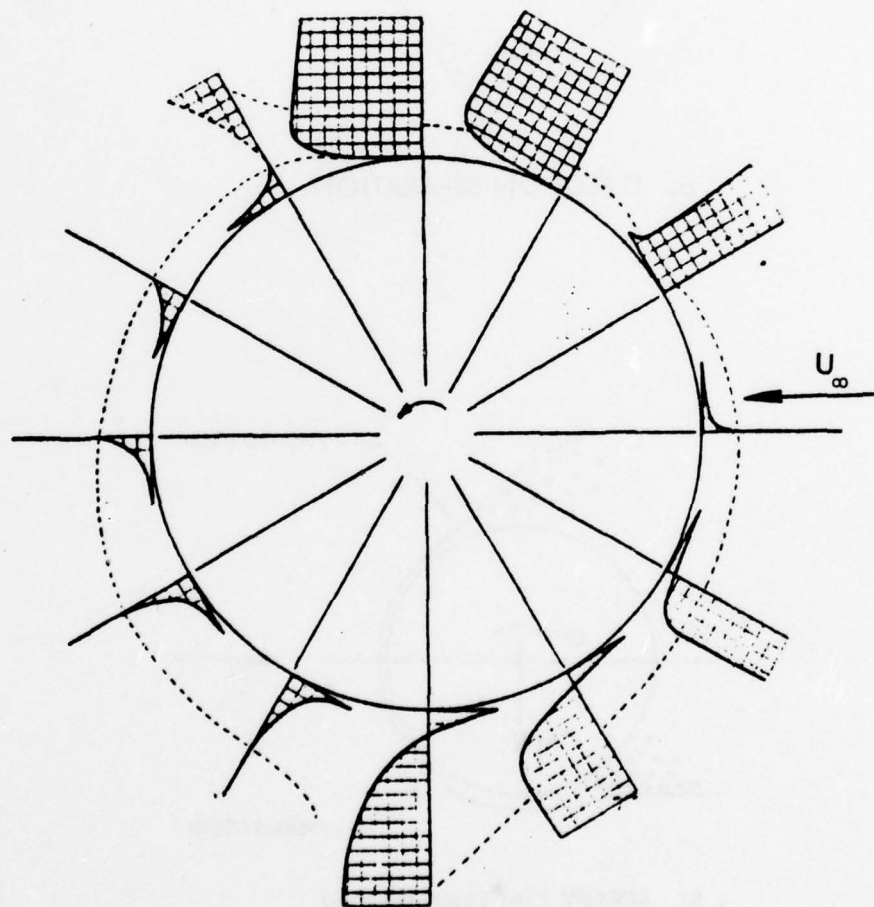
Fig. 26 Boundary Layer Profiles at a Rotational Velocity Ratio of Unity (Ref. 112)
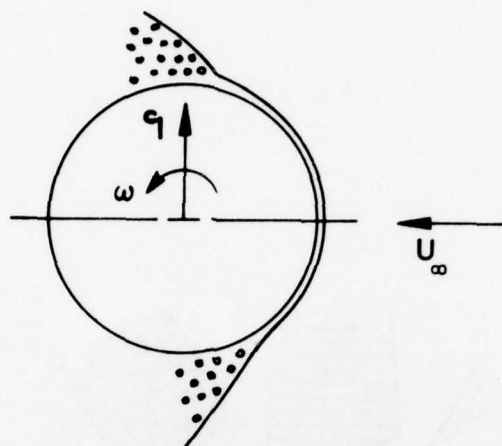
a. EFFECT ON SEPARATION
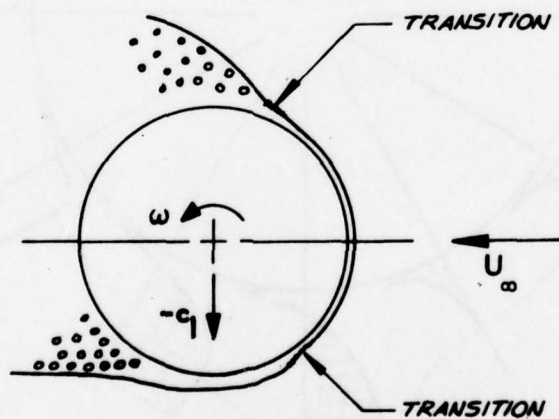
b. EFFECT ON TRANSITION

Fig. 27 Moving Wall/Wall Jet Effect
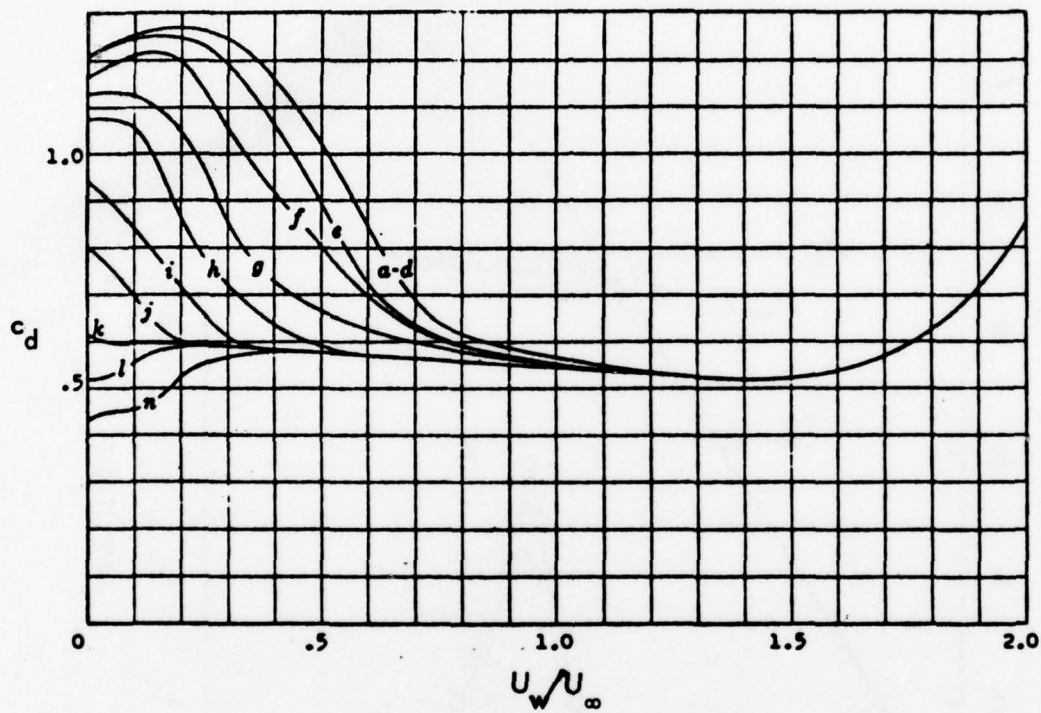
Fig. 28 Cylinder Drag as a Function of Surface Velocity Ratio
(Ref. 112)
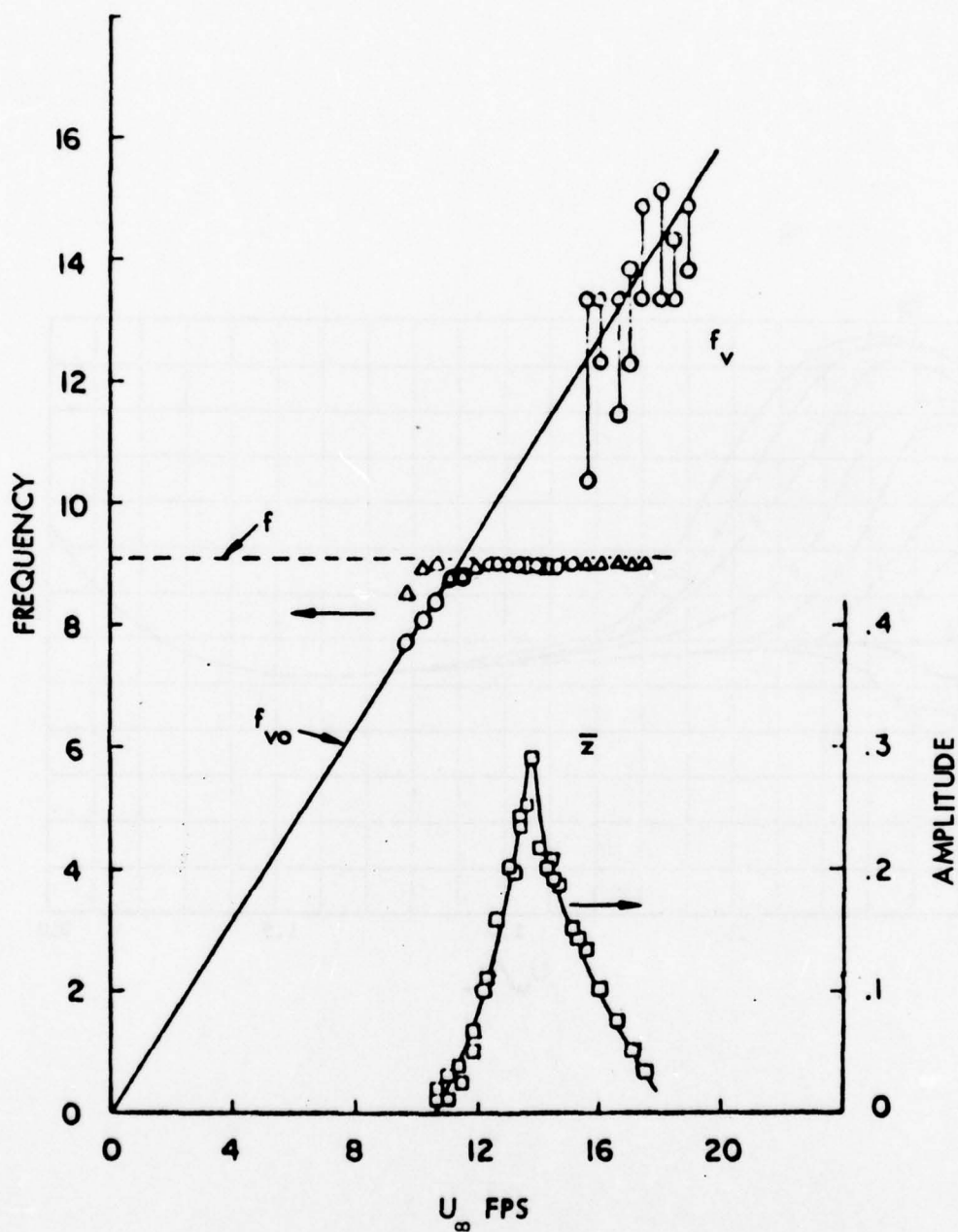
Fig. 29 Effect of Translatory Oscillation on Vortex Shedding
Frequency (Refs. 115 and 116)
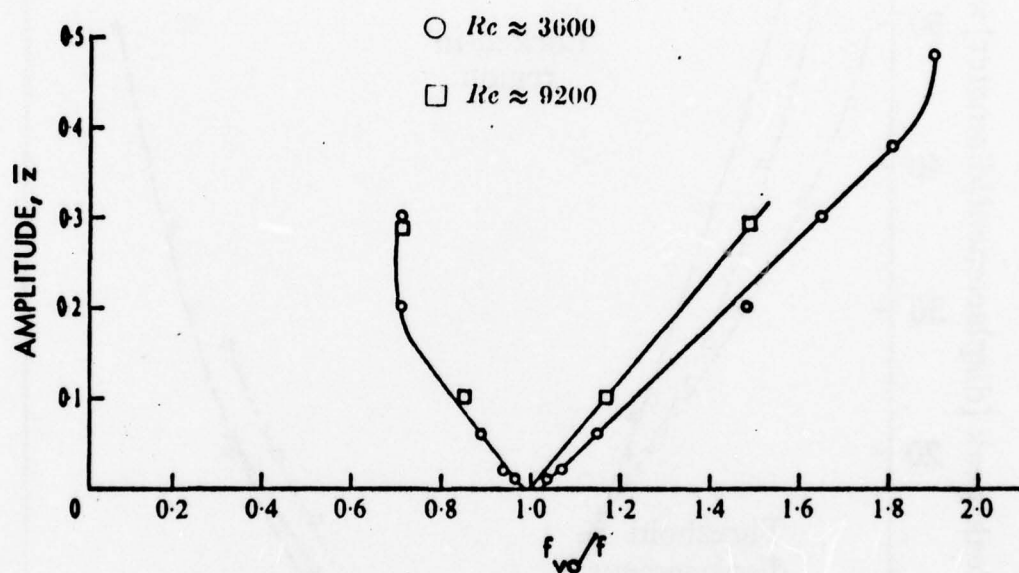
Fig. 30   Lock-In of Vortex Shedding to Translatory Oscillations at
Low Reynolds Numbers (Ref. 117)
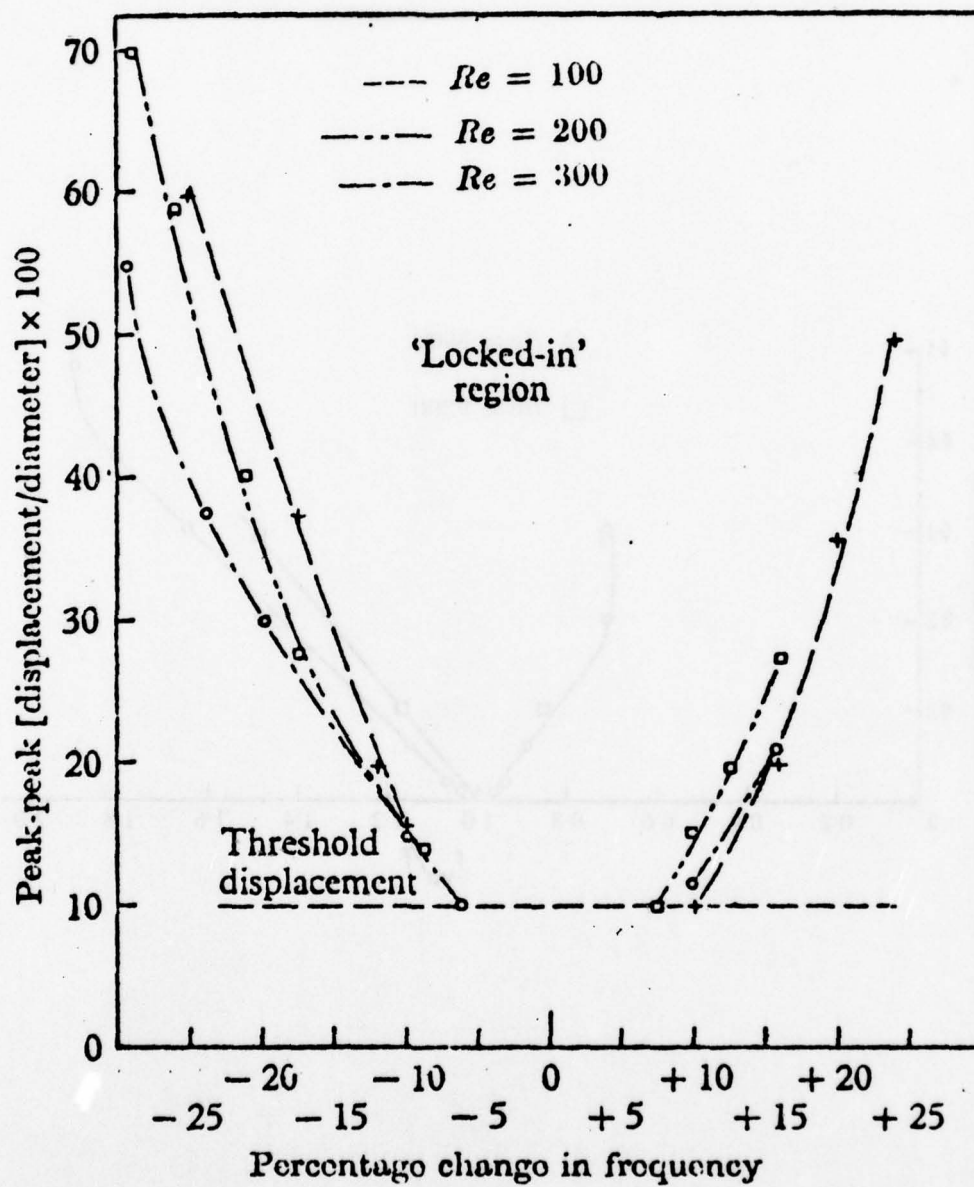
Fig. 31 Lock-In of Vortex Shedding to Translatory Oscillations at
Very Low Reynolds Numbers (Ref. 118)

in their own tests at Re = 1.67×10^4 the separation points did oscillate, in agreement with the findings by Schindel and Zartarian (Ref. 120), and the angular amplitude of the separation movement was approximately proportional to the relative translatory amplitude $\bar{z}$ = a/d (see Fig. 32).

That coupling between the vortex shedding and the cylinder oscillation exists also at critical and supercritical flow conditions was demonstrated by Cincotta, Jones and Walker (Ref. 121) at the same meeting where Parkinson and Ferguson first showed their subcritical results (Ref. 115). In the transcritical Reynolds number region the cylinder oscillation can cause more than a threefold increase of the unsteady lift (Ref. 92 and Fig. 33).

The coupling between translatory oscillations and the vortex shedding off a circular cylinder has received a great deal of attention and has been investigated extensively both theoretically and experimentally. The results in Fig. 32 show the peak separation point displacement to occur at f/f_{vo} = 0.9 and the peak amplitude response at f/f_{vo} = 0.83. Jones, Cincotta and Walker found in their test (Refs. 92 and 121) at supercritical Reynolds numbers, Re > 6×10^6, the maximum response to occur at f/f_{vo} = 0.99 at a Strouhal number of S = 0.28 (Fig. 33). They also found that the phase lag and associated negative damping (causing the large amplitude response) at $f/f_{vo} < 1$ changed to a phase lead and positive damping when f exceeded the natural vortex shedding frequency, f_{vo} (Fig. 34). One important effect of translatory oscillation is to organize the vortex shedding, increasing the spanwise correlation length (Ref. 92).

A question of great practical consequence is the possibility of obtaining vortex lock-in at higher harmonics, f = 2 f_{vo}, 3 f_{vo}, etc. Stansby's results at Re $\approx 10^4$ (Ref. 117) show that this can indeed occur (see Fig. 35). It is interesting to note that tertiary locking-on is well documented, while secondary lock-in is definitely absent for the large amplitude oscillation (a/d = 0.29). All experimental data discussed so far have shown that lock-in occurs more readily the larger the oscillatory amplitude is. Consequently, the "wiggle" in the data for the lower amplitude (a/d = 0.10) cannot have been a sign of
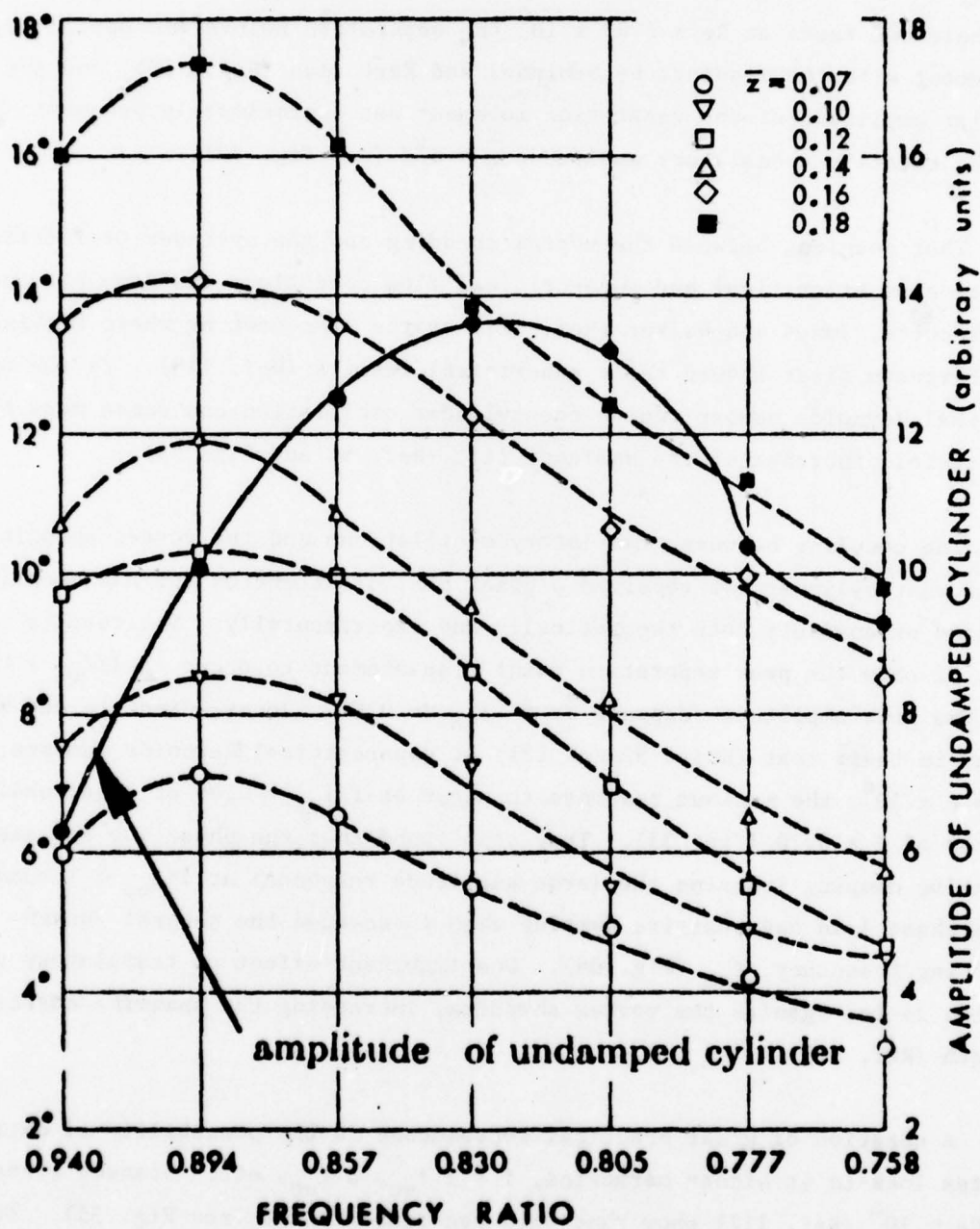
Fig. 32 Effect of Amplitude of Translatory Oscillation on the Lock-In
of Oscillatory Flow Separation (Ref. 120)
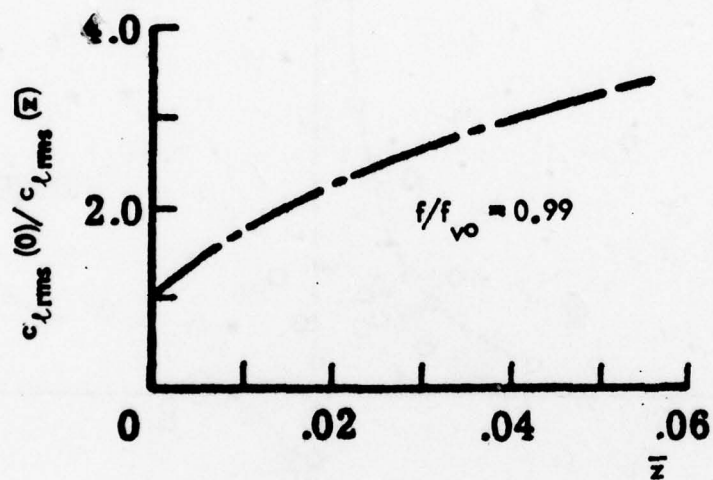
Fig. 33 Effects of Translatory Oscillation on RMS Lift at High
Reynolds Number (Ref. 92)
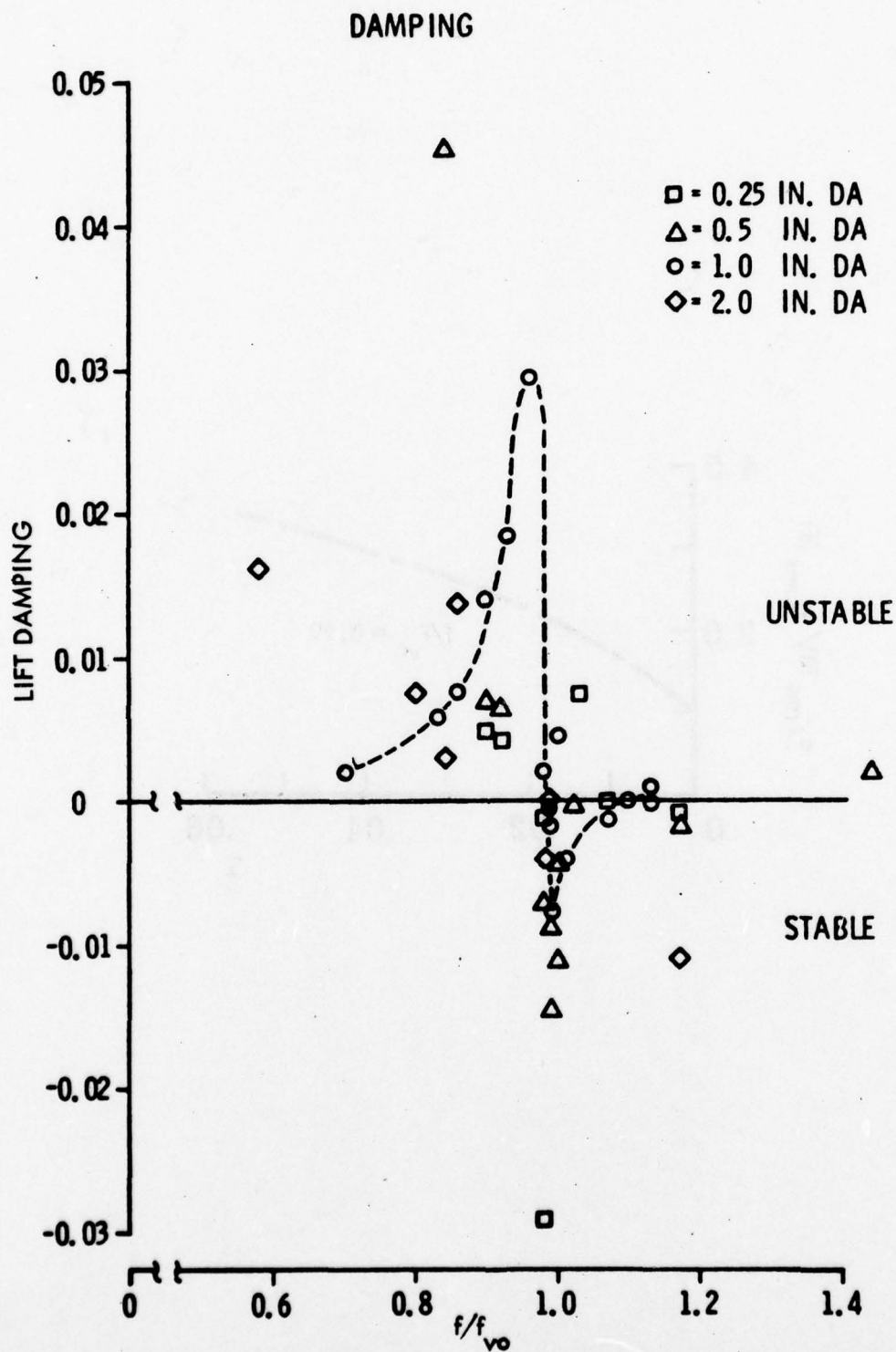
Fig. 34 Damping and Undamping Coupling Between Translatory Oscillation
and the Vortex Wake for a Cylinder at High Reynolds Number
(Ref. 92)

3-38
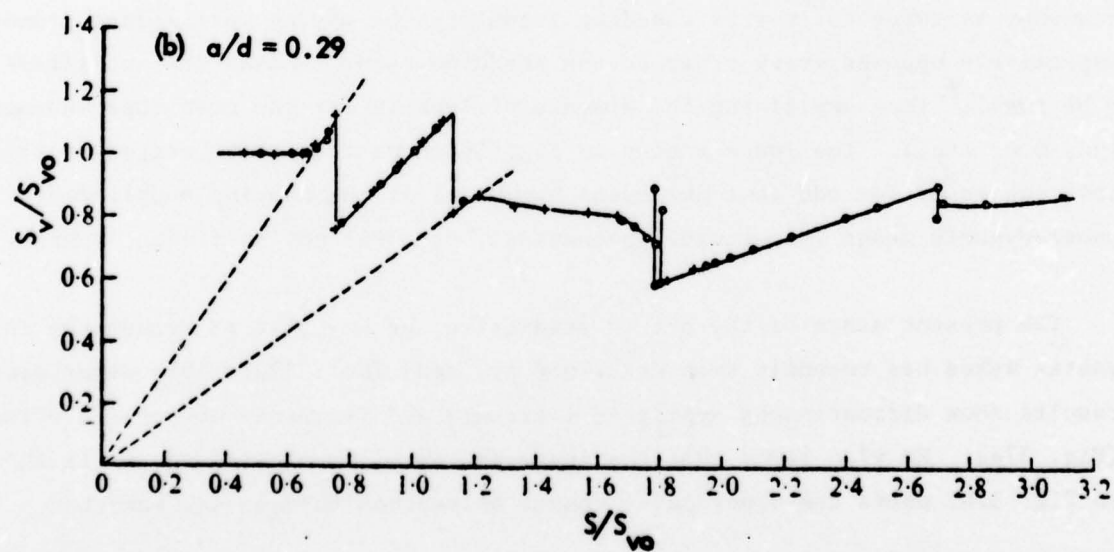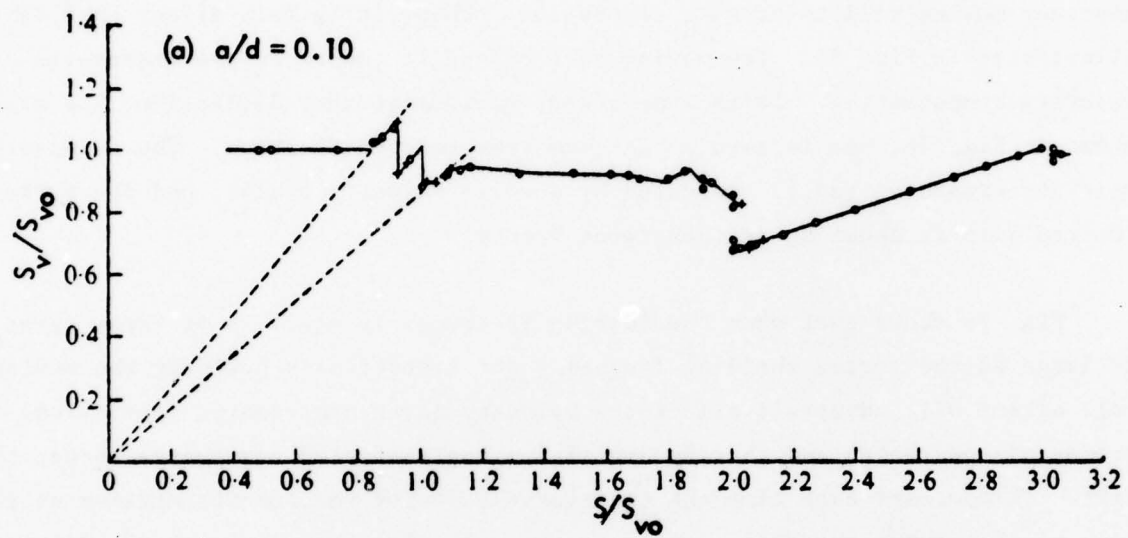
Fig. 35 Locking-On at Superharmonic Frequencies (Ref. 117)

tentative secondary lock-in, as was suggested by Stansby. What can be the reason for this "skipping" of the even super-harmonics in the lock-in phenomenon? Fig. 36A illustrates one physical flow process that can explain this anomalous behavior, i.e., the moving wall effect discussed earlier in connection with Swanson's results (Ref. 112 and Fig. 23). As was shown for the spinning cylinder the adverse effect of the moving wall is the strongest, i.e., the effect of the upstream moving wall to promote separation. Thus, it is this effect that is illustrated in Fig. 36. The moving wall effect is caused by the transverse velocity component, $\dot{z}$. It is, therefore, maximum at zero deflection, the case shown in Fig. 36, and is zero at maximum transverse deflection. The transverse velocity component ($\dot{z}$) is indicated by a solid velocity vector, and the vortex-induced lift is shown by an open force vector.

Fig. 36 shows that when the forcing frequency is equal to or three times as large as the vortex shedding frequency for a stationary cylinder the moving wall effect will adversely affect the boundary layer approaching separation, thus promoting separation and thereby amplifying the generated transverse force, the lift. This occurs each time the transverse velocity reaches its maximum at the time of the vortex shedding event. In contrast, for the case that the driving frequency is twice the vortex shedding frequency the moving wall effect promotes respectively opposes every other vortex shedding event causing the net effect to be small, [#] thus explaining the absence of lock-in for the even super-harmonics (2nd, 4th, etc.). The force vector in Fig. 36 shows that self-excited oscillations can occur for odd (but not even) harmonics if the damping supplied by nonaerodynamic means (structural, mechanical, etc.) is not sufficiently high.

The present state of the art in predicting the response of structures to vortex wakes has recently been described by Landl (Ref. 122). His experimental results show discontinuous amplitude increases and frequency hysteresis effects (Fig. 37a). He also found that the response can be double-valued, as is shown in Fig. 37b, where the upper curve cannot be reached through self-excited

---

[#] Stansby's spectral data (Ref. 117) showed broad harmonic spikes for $f = 2f_{vo}$ both at $a/d = 0.10$ and $a/d = 0.29$, whereas the spikes are extremely narrow for $f = f_{vo}$ and $f = 3 f_{vo}$.

Fig. 36 Translatory Moving Wall Effect on Cylinder Vortex Shedding

a. HYSTERESIS EFFECTS f/f_{vo}

○ Increasing velocity
● Decreasing velocity
Re ≈ 926

b. THRESHOLD AMPLITUDE EFFECTS

△ Large amplitude vibration
▲ Small amplitude vibration
Re ~ 2000
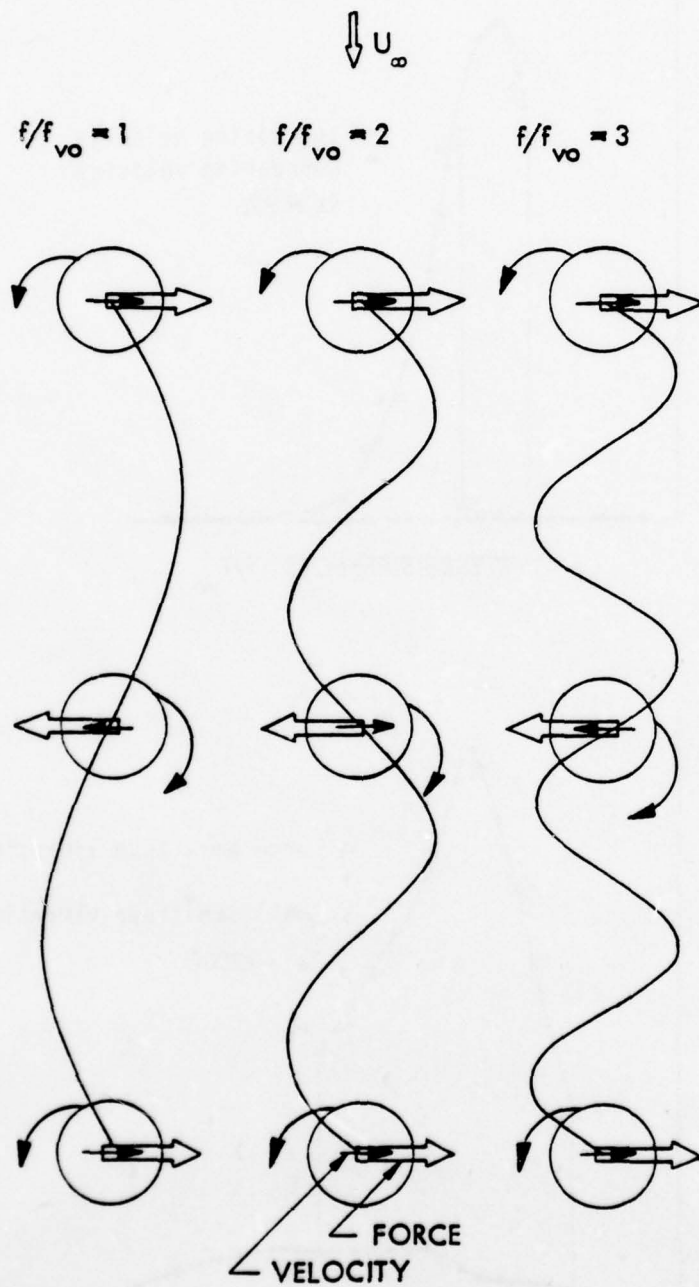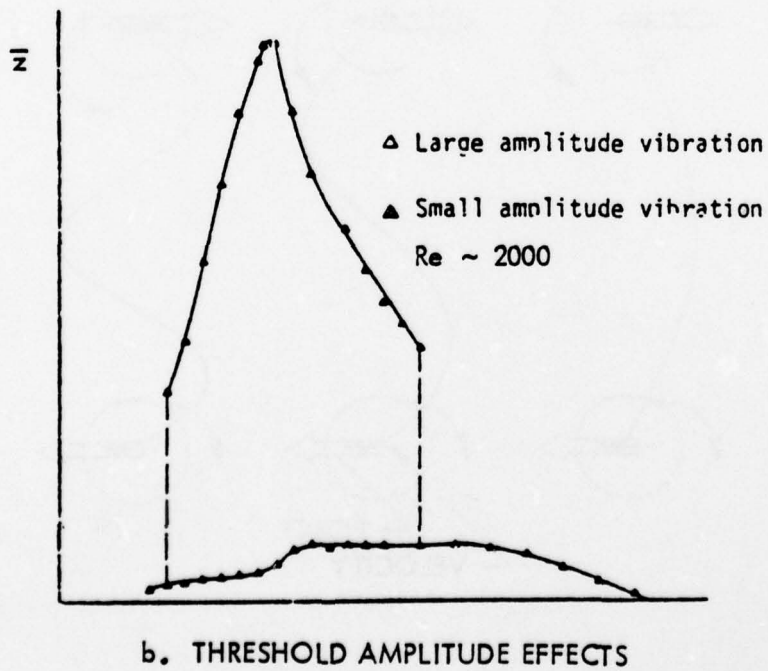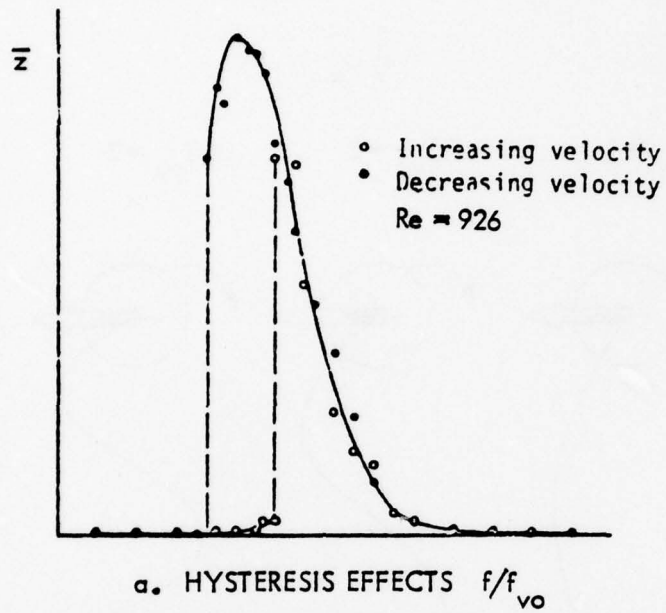
Fig. 37 Vortex Induced Cylinder Vibration (Ref. 122)

oscillations but only after receiving an external disturbance that is larger than that corresponding to the lower curve amplitude level. This jump in response has also been observed by others (Ref. 123).

In regard to the theoretical treatments they all seem to concentrate on solving the nonlinear mathematics needed to reproduce some of the experimentally observed response characteristics. Although some success has been obtained through this approach (Ref. 122), in most cases the agreement with experiment is poor, especially in regard to the response of the circular cylinder, the case studied by the most researchers. The approach discussed in Ref. 23 is typical. The oscillating cylinder is assumed to be represented by a stationary cylinder of diameter $d + 2$ a $\sin \varphi_D$, where $\varphi_D = 2 \pi f \Delta t$ is the phase angle corresponding to the time Δt it takes before the vortex generated by the cylinder enters the stabilized wake region, starting two wavelengths downstream of the cylinder, at $x = 2L$. The double-valued functions obtained for frequency and amplitude by this analysis are in poor agreement with experimental results (Fig. 38), and so are the results obtained by Sallet (Ref. 124) using a similar theoretical approach. However, when lock-in does not occur the effective vortex wake width would be increased by the translatory oscillation, thus explaining the decrease of the vortex shedding Strouhal number (referenced to d rather than to $h > d$) observed in Stansby's test (Fig. 35). Also the effect of amplitude is explained in this manner (compare Figs. 35a and b).

All these theories have one thing in common; viz, a complete disregard for the flow separation process generating the wake. Common sense says that there is a large difference between the wake-body coupling mechanism for a flat-based wedge or plate, where the separation point is fixed by the geometry, and that for a cylinder, where the separation point is free to move. That it does move was (first) demonstrated by Schindel and Zartarian (Ref. 120). The experimental results obtained by Mody and Slater (Ref. 125 and Fig. 39) for a structural angle section indicate that this separation point movement is an important mechanism. Thus, the largest response was obtained when the angle was oriented with its concave section forward, in which case the separation point was free to move on the aft "boat-tail." In contrast, no significant response was seen
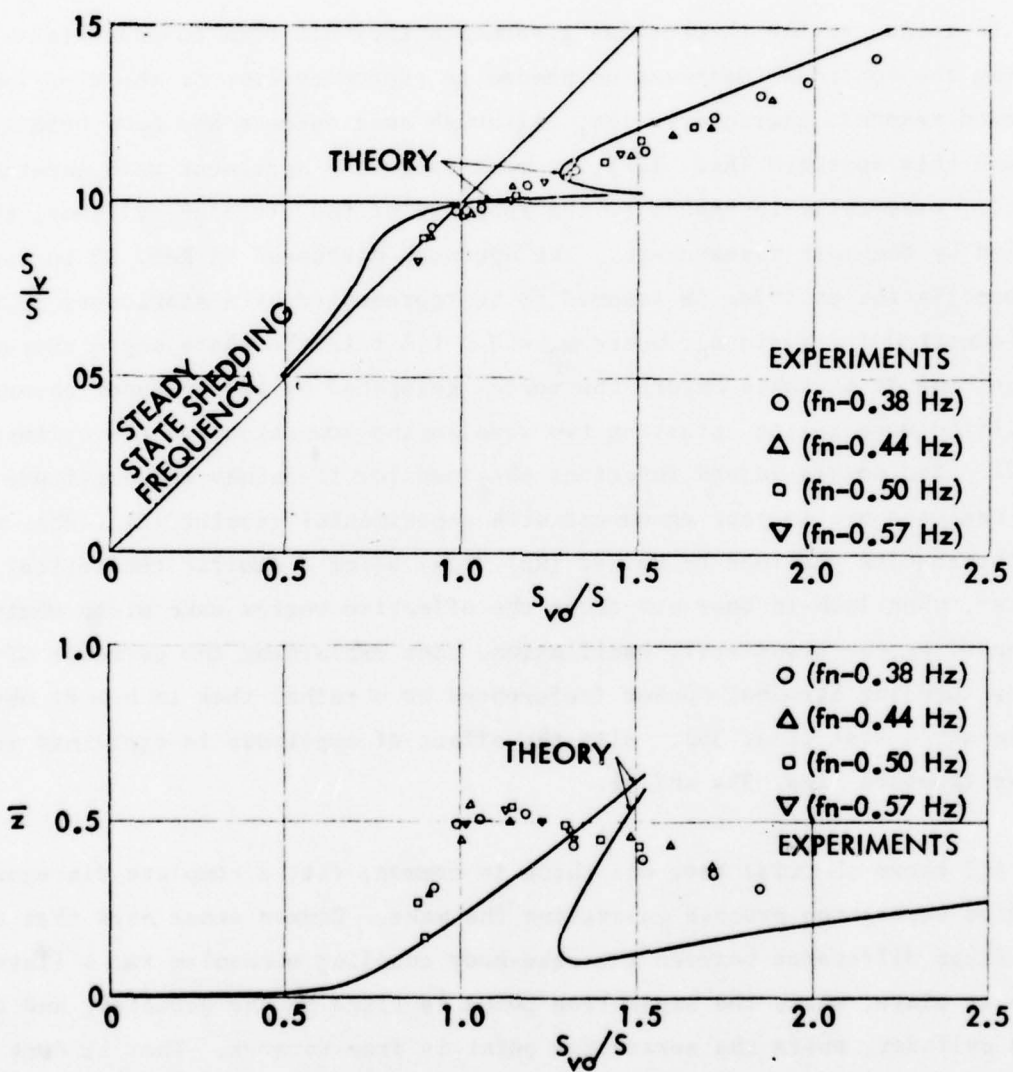
Fig. 38 Comparison Between Theoretical and Experimental Vortex
Lock-In Characteristics (Ref. 83)
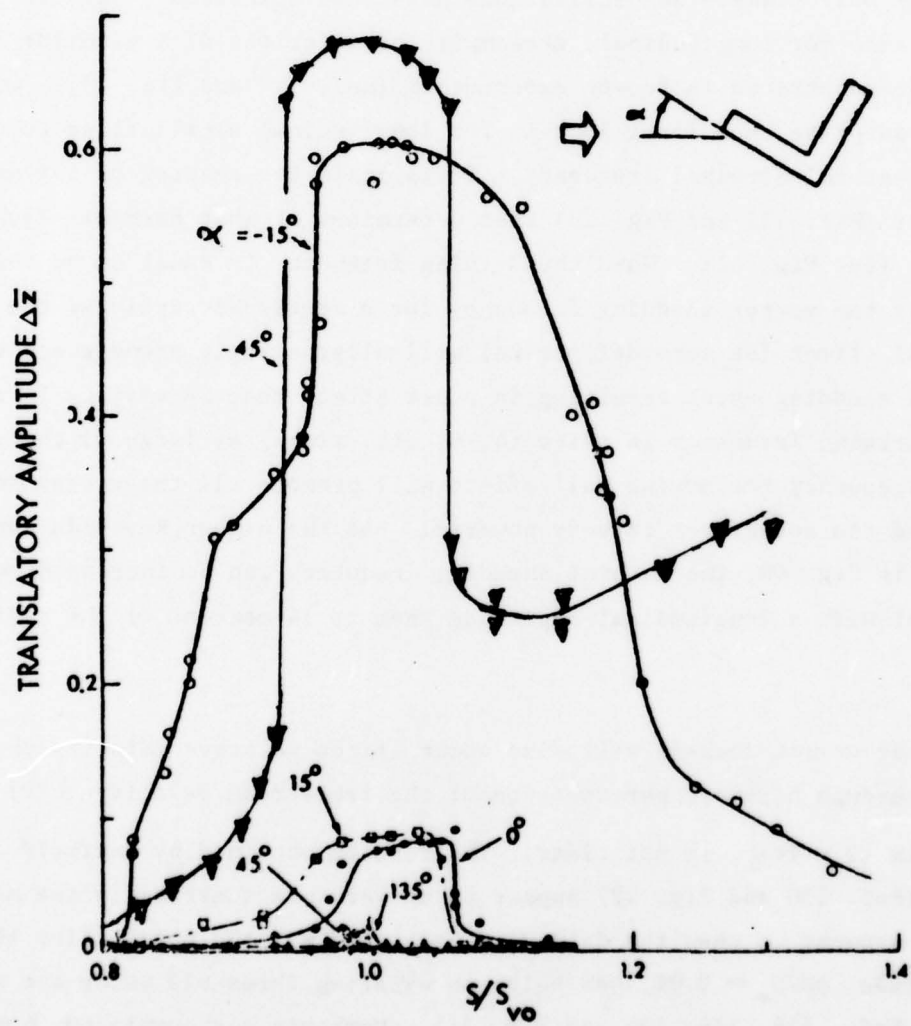
Fig. 39 Effect of Orientation on the Translatory Response of Structural
Angle Cross Section Cylinder to Vortex Excitation (Ref. 125)

for the opposite orientation, when the cavity was facing downstream and the separation points were fixed. Marris (Ref. 126) has pointed out the importance of the moving separation point, and suggests that the cylinder performing translatory oscillations could possibly be analyzed by applying Swanson's Magnus theory (Ref. 112) to oscillatory rotation.

So far only transverse oscillations have been discussed. That vortex lock-in occurs also for longitudinal, streamwise oscillations of a circular cylinder has been deomonstrated in recent experiments (Ref. 127 and Fig. 40). One notes with some surprise that first lock-in for longitudinal oscillations occurs at twice the natural Strouhal frequency. It is again the phasing of the moving wall effect (Ref. 112 and Fig. 23) that determines at what harmonic lock-in will occur (see Fig. 41). When the driving frequency is equal to or three times as large as the vortex shedding frequency for a stationary cylinder the (maximum) moving wall effect (at zero deflection) will alternatingly promote and oppose the vortex shedding event resulting in a net effect that is small. In contrast, when the driving frequency is twice (4, 6, etc. times) as large as the vortex shedding frequency the moving wall effect will promote all the vortex shedding events, and the net effect is very powerful. At the higher Reynolds number, $R_d = 4000$ in Fig. 40, the natural shedding frequency can be increased more than 100 percent with a longitudinal amplitude that is 14 percent of the cylinder diameter.

Whether or not lock-in will also occur if the relative velocity change is obtained through harmonic perturbation of the freestream velocity, $U(t) = U_\infty \left[1 + \frac{\Delta U}{U_\infty} \sin (2 \pi ft)\right]$, is not clear. The results obtained by Hatfield and Morkovin (Ref. 130 and Fig. 42) appear to answer this question in the negative. One point brought up when the data were presented was the possibility that the amplitude, $\Delta U/U_\infty \approx 0.08$, was below an existing threshold value for excitation (see Refs. 118, 119, 122 and Fig. 31). Morkovin was convinced, however, that the used 8 percent amplitude was high enough as it is 3 to 5 times larger than the velocity amplitude corresponding to the pressure fluctuations observed on a stationary cylinder. Figs. 40 and 42 tend to support Morkovin's conclusion, i.e., the reason for the absence of lock-in was not lack of amplitude, but may
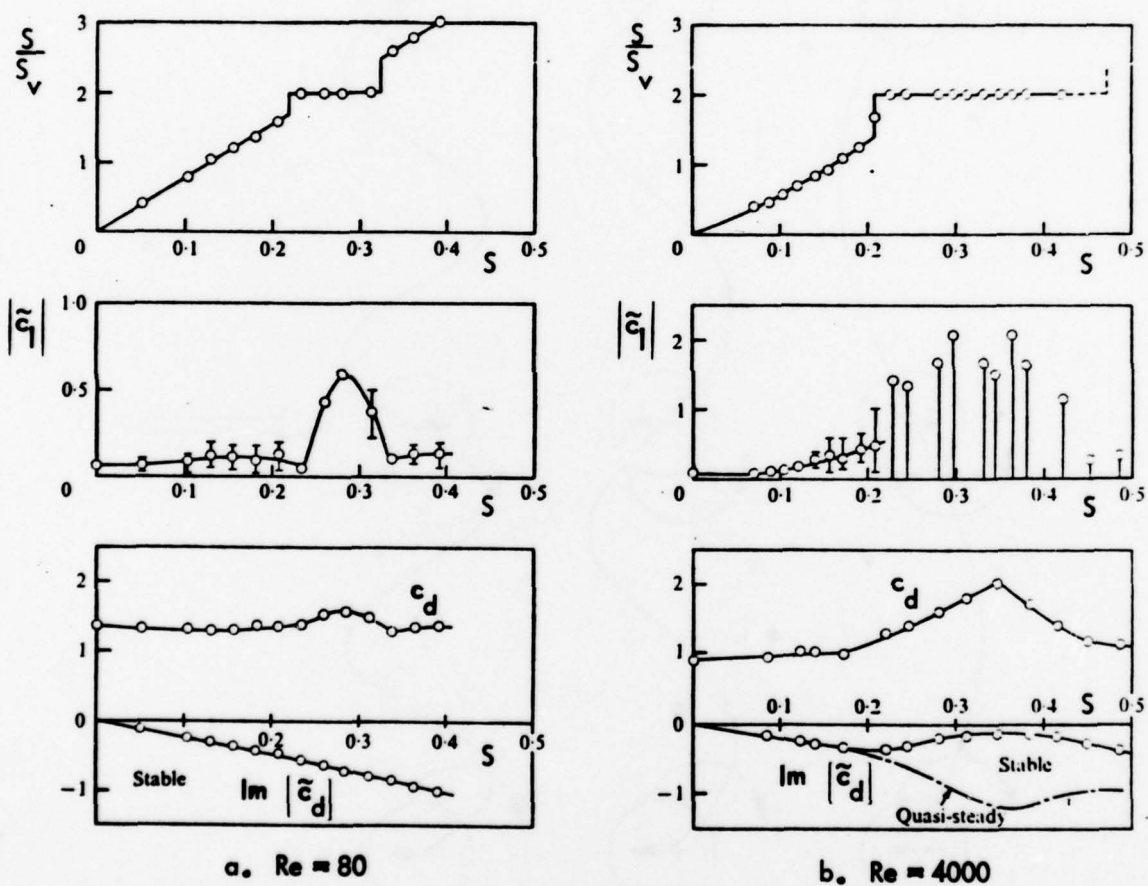
Fig. 40 Lock-In of Vortex Shedding on a Cylinder Describing Longitudinal
Oscillations of Amplitude a/d = 0.14 (Ref. 127)
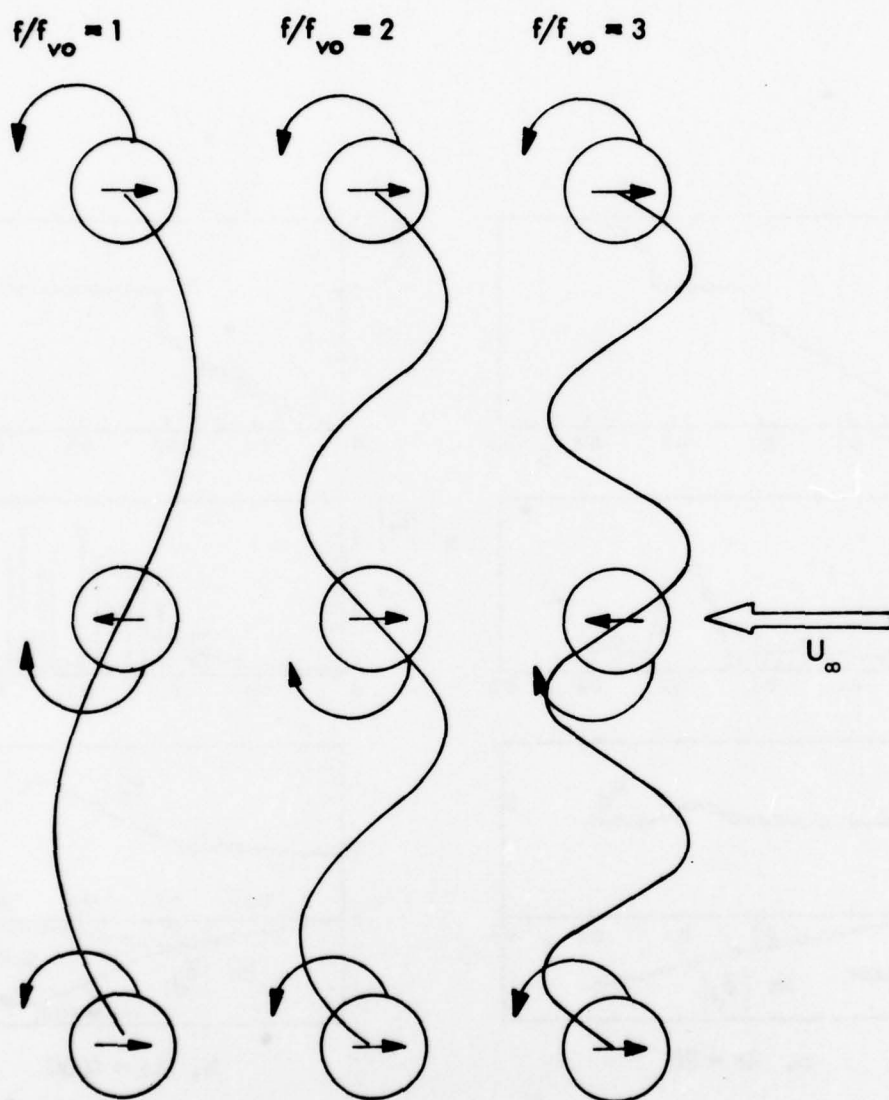
Fig. 41 Longitudinal Moving Wall Effect on Cylinder Vortex Shedding
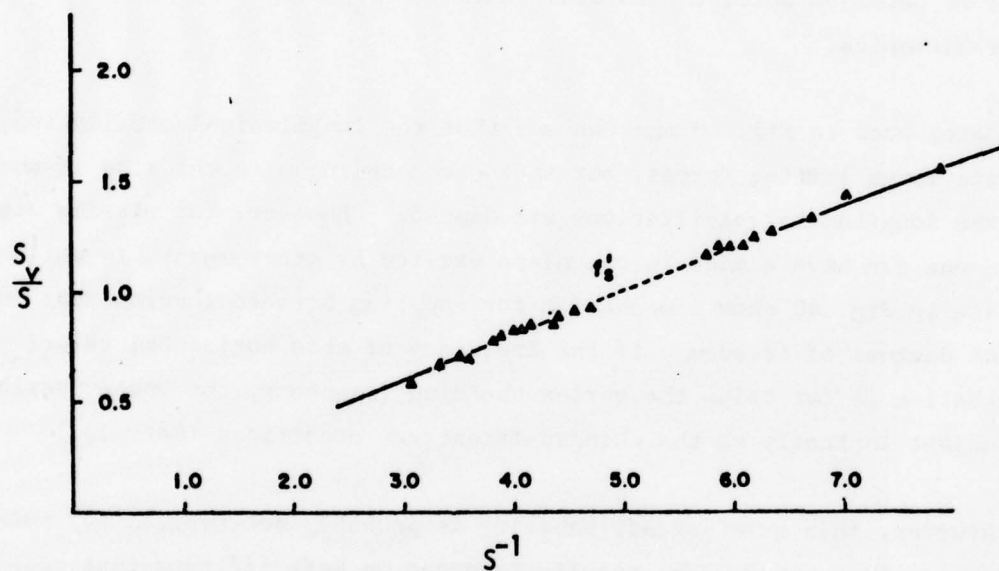
Fig. 42 Effect of Free Stream Oscillation on Cylinder Vortex Shedding (Ref. 130)

have been a lack of frequency. The data in Fig. 42 indicate that the highest frequency used was 60 percent above the Strouhal frequency, which Fig. 40 indicates is not high enough for lock-in. It is not certain that locking-on will occur, as the wall-jet-like effect of the moving wall is absent in the case of the oscillating free stream velocity. However, it is very likely as one has instead the effect of accelerating and decelerating flow. It is discussed in Ref. 113 how the accelerated flow and moving wall effect have similar influence on the flow separation. A definitative answer to the question of locking-on in the case of oscillatory perturbations of the free stream velocity cannot be obtained until the Hatfield-Morkovin experiment has been extended to higher harmonics.

Going back to Fig. 40 one can see that the longitudinal oscillation can generate large lifting forces, but that the coupling with the flow is such that the longitudinal oscillations are damped.[#] However, for missile applications one can have a mode in one plane excited by other means, in which case the data in Fig. 40 show a mechanism for coupling between longitudinal and lateral degrees of freedom. If the frequency of this horizontal velocity perturbation is far below the vortex shedding frequency, the vortex periodicity will adjust instantly to the changed freestream conditions (Ref. 131).

However, this quasi-steady behavior is probably not typical for subharmonic frequencies in general. The results reported in Ref. 132 show that coupling leading to self-excited translatory oscillations of a cylinder occurred when the cylinder natural frequency was one third of the regular vortex shedding frequency, but not when the fraction was one half. Fig. 43 shows the reason for this behavior. It is again a question of the phasing of the moving wall effects. At $f \approx f_{vo}/2$ the translatory velocity - moving wall effect is zero for every other vortex shedding event taking place at maximum deflection. And at zero deflection, where the moving wall effect is maximum, it alternately enhances and opposes the vortex shedding. Thus, no significant coupling can occur at this frequency.

[#]One would not expect any significant effects of Reynolds number in the range $4000 < Re < 200000$.

$f/f_{VO} = 1$ $f/f_{VO} = 2^{-1}$ $f/f_{VO} = 3^{-1}$

U_∞

FORCE

VELOCITY
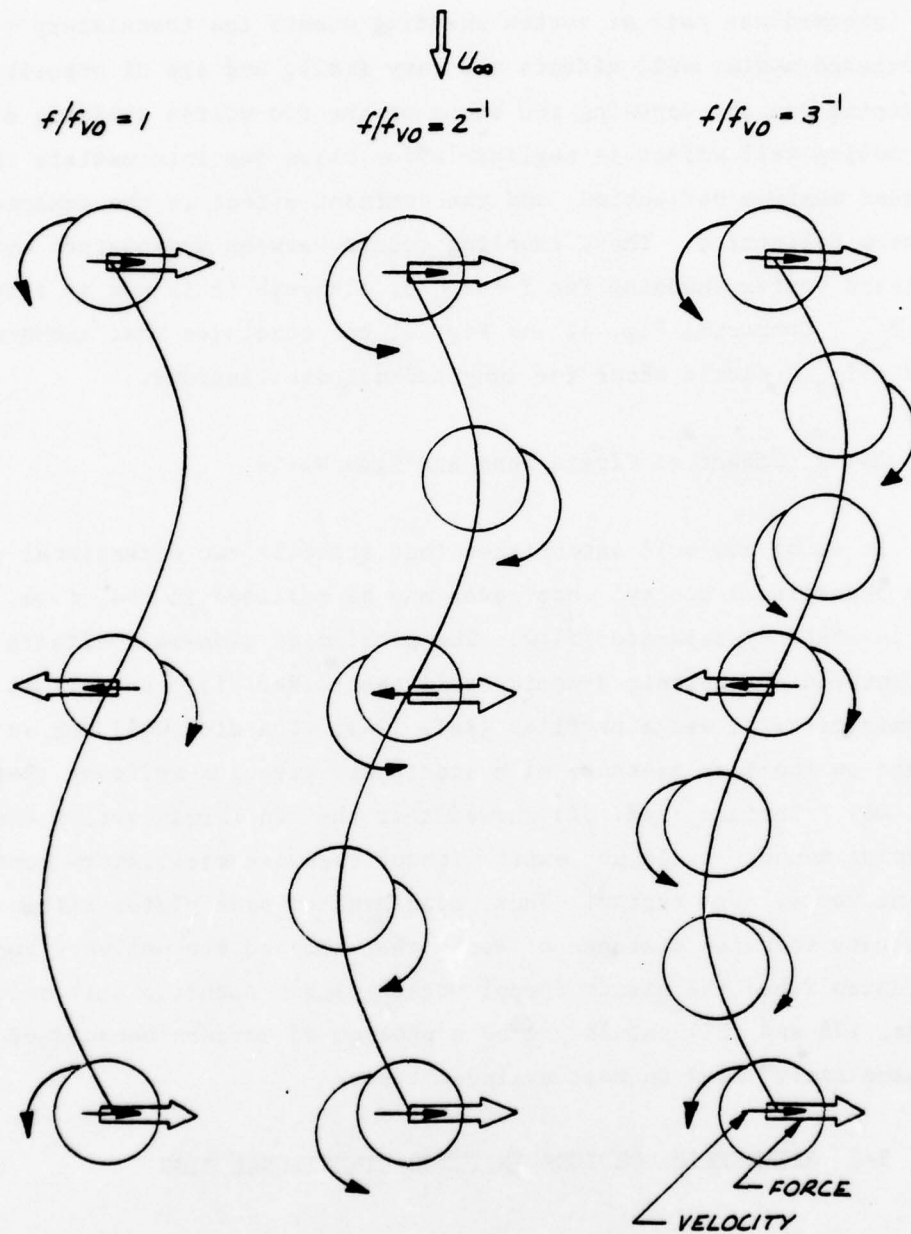
Fig. 43 Subharmonic Translatory Moving Wall Effects

For $f = f_{vo}/3$, on the other hand, the maximum moving wall effect at zero deflection always enhances the vortex shedding, as in the case $f = f_{vo}$. For the intermediate pair of vortex shedding events the translatory velocity and associated moving wall effects are very small, and are of opposite signs, i.e., enhancing one and opposing the other of the two vortex shedding events. Thus, the moving wall effect is negligible for these two intermediate shedding events at near maximum deflection, and the dominant effect is the enhancement existing at zero deflection. Thus, coupling occurs between translatory cylinder oscillation and vortex shedding for $f = f_{vo}/3$, although it is not as strong as for $f = f_{vo}$. Comparing Fig. 41 and Fig. 43 one concludes that subharmonic response at $f = f_{vo}/2$ should occur for longitudinal oscillations.

3-1.5 Effect of Finite Span and Side Walls

It is by now well established that strictly two-dimensional separated flow is a theoretical concept that never may be realized in real flow, especially not in unsteady separated flow. The problem of side-wall effects has been encountered in subsonic dynamic stall tests (Ref. 133) as well as in hypersonic dynamic tests of wedge profiles (Ref. 134). The side wall has an appreciable effect on the base pressure of a stationary circular cylinder (Ref. 135 and Fig. 44). Theisen (Ref. 82) showed that the von Kármán vortex shedding at low Reynolds numbers could not exist without spanwise oscillatory momentum transfer in the vortex core region. Thus, placement of side plates within four (4) diameters spanwise distance of each other stopped the unsteady vortex shedding and established the steady Foeppl vortex pair. Acoustic test section resonance (Refs. 136 and 137) should not be a problem of concern because of the high "aspect ratio" used in most cylinder tests.

3-2 ASYMMETRIC VORTICES IN THREE-DIMENSIONAL FLOW

In three-dimensional flow the asymmetric von Kármán type vortex geometry can be realized in a steady state condition, as has been pointed out by Thomson

a. $Re = 1.6 \times 10^4$

b. $Re = 4.0 \times 10^4$
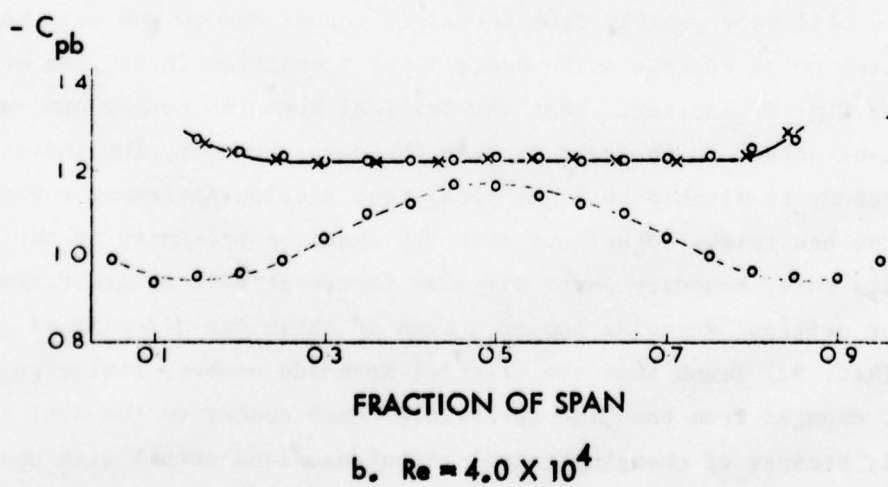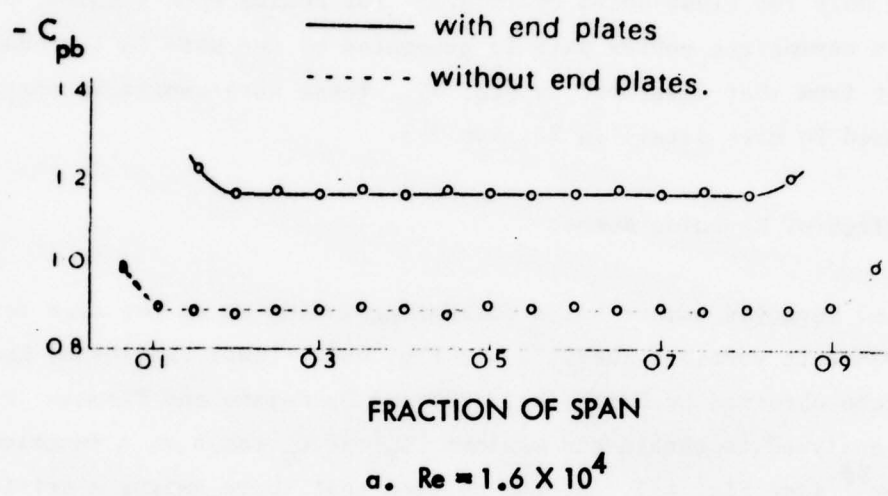
Fig. 44 Effect of End Plates on Cylinder Base Pressure (Ref. 136)

and Morrison[#] (Ref. 43) and by Pick (Ref. 14). Fig. 45 shows the vortex geometry. The axial flow degree of freedom makes this possible. The analogy is, however, strictly valid only for blunt-nosed cylinders. For bodies with slender, pointed noses the first asymmetric vortex pair is generated by the nose in a manner quite different from that described in Fig. 45. These nose-generated vortices will be discussed in more detail in Section 3-3.

3-2.1 Effect of Reynolds Number

As expected Reynolds number has a dominating influence on the side force induced by asymmetric vortices (Ref. 32 and Fig. 46). These results by Keener, et al., and those obtained by Smith (Ref. 28) and by Nelson and Fleeman (Ref. 29) have been analyzed to obtain the maximum $|C_Y|$ to C_N ratio as a function of Reynolds number[##] (see Fig. 47). It can be seen that there exists a critical Reynolds number giving the maximum $|C_Y|/C_N$ ratio. It is also evident that this critical Reynolds number varies from one angle-of-attack to the next and from one test to the next (in a different wind tunnel). We expect, of course, the maximum side force to be realized at a Reynolds number where boundary layer transition can influence the flow separation asymmetry the most (see the discussion of 2-D Magnus effects earlier in Section 3-1.3). It is clear that this Reynolds number will vary greatly from tunnel to tunnel due to the well known problem of tunnel noise effects on boundary layer transition (Refs. 138 and 139) as was shown in Fig. 17 earlier. That the critical Reynolds number can vary from one angle-of-attack to the next is less obvious. However, the vortex-generating forebody is pitched to a new local test section environment when α is changed. One has reason to believe that the changing proximity to the tunnel ceiling with its noisy boundary layer plays an important role in generating this α-affect on the critical Reynolds number. Even in their two-dimensional test, Jones et al. (Ref. 92) found that the critical Reynolds number, giving peak unsteady lift, changed from one "incompressible" Mach number to the next (Fig. 48), presumably because of changing tunnel turbulence (and noise) with changing power demand.

[#] They acknowledge that the idea was suggested to them by Morkovin as a check on the results obtained using the impulsively started cylinder approach.

[##] At $\alpha > 30°$ ($R_{eff} \approx Re$) as will be shown in Section 4.
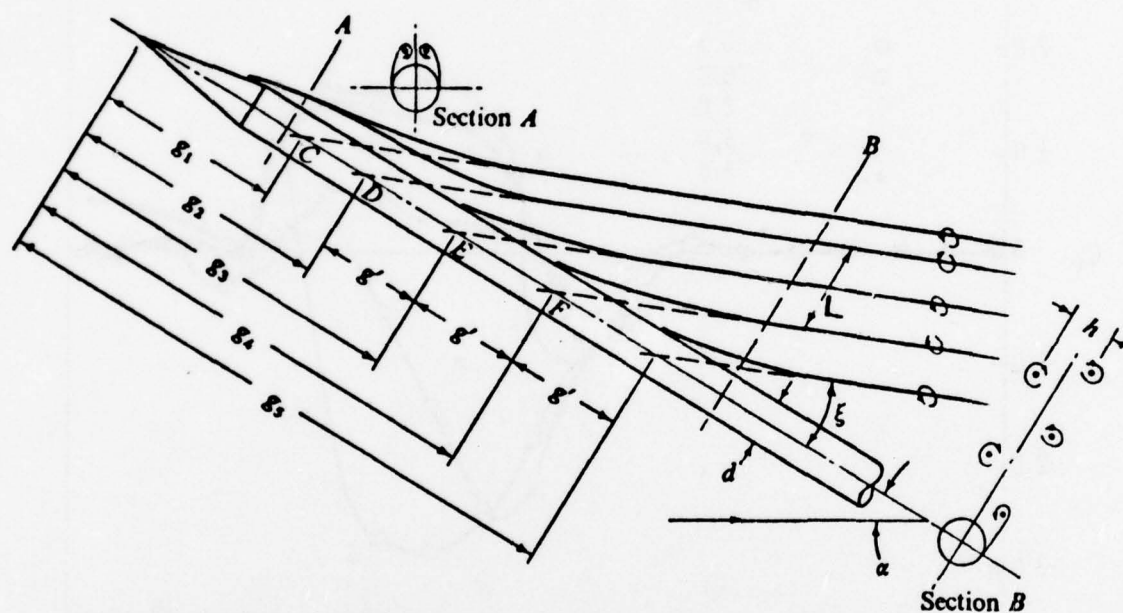
Fig. 45 Asymmetric Steady Vortex Array on an Inclined Body of
Revolution (Ref. 43)
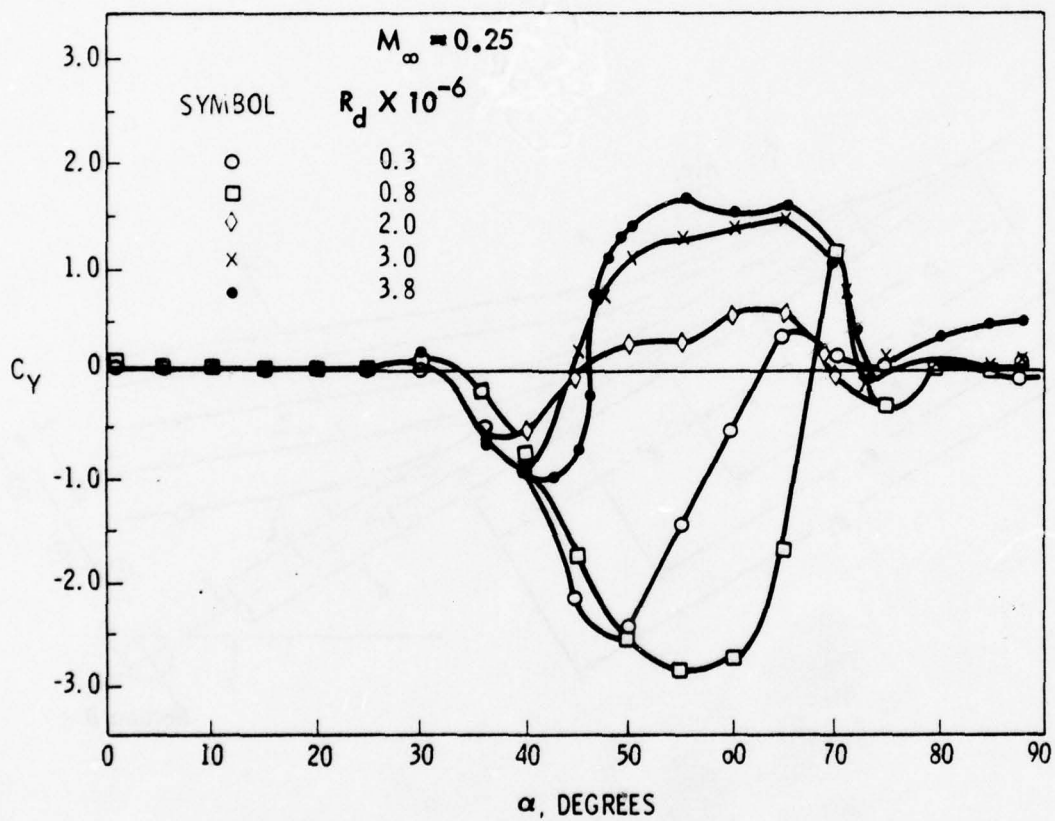
Fig. 46 Effect of Reynolds Number on the Vortex-Induced Side Force
on a $l/d = 3.5$ Ogive (Ref. 32)
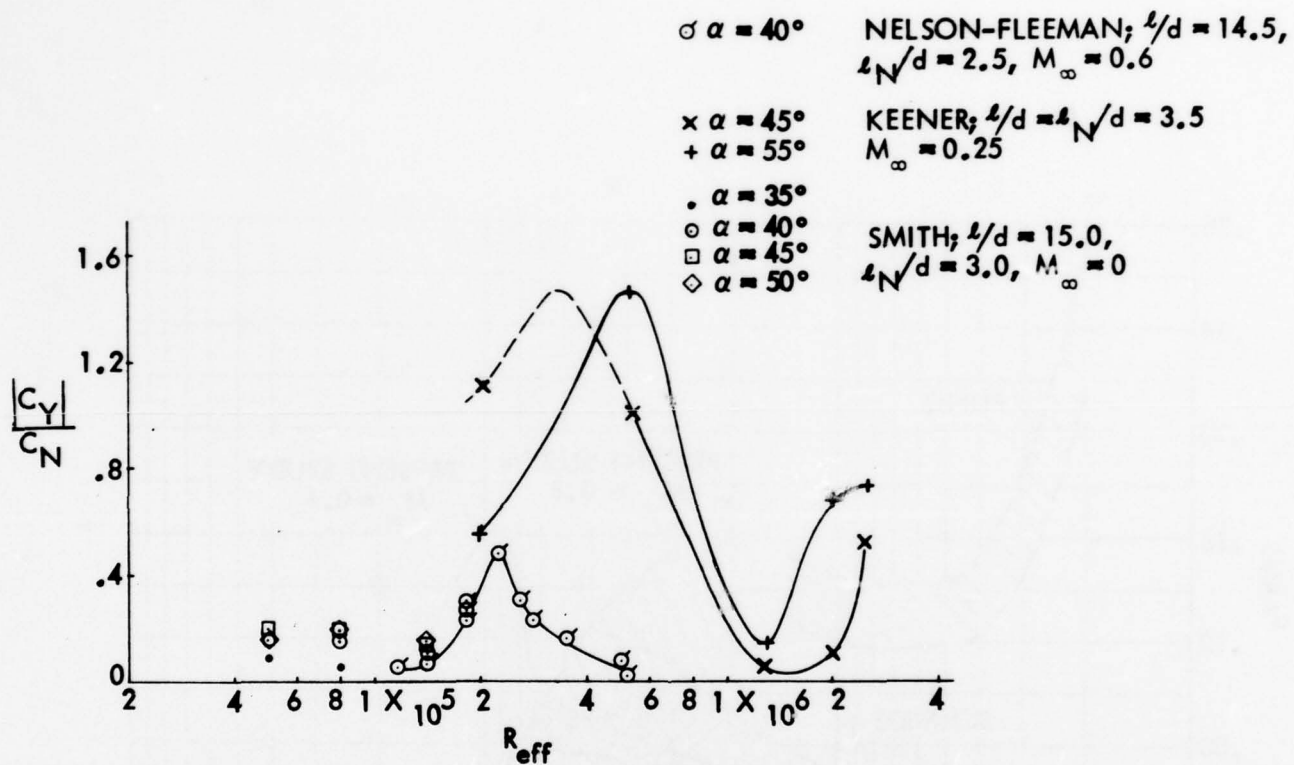
Fig. 47 Critical Reynolds Number for Maximum Vortex-Induced Side
Force

3-57
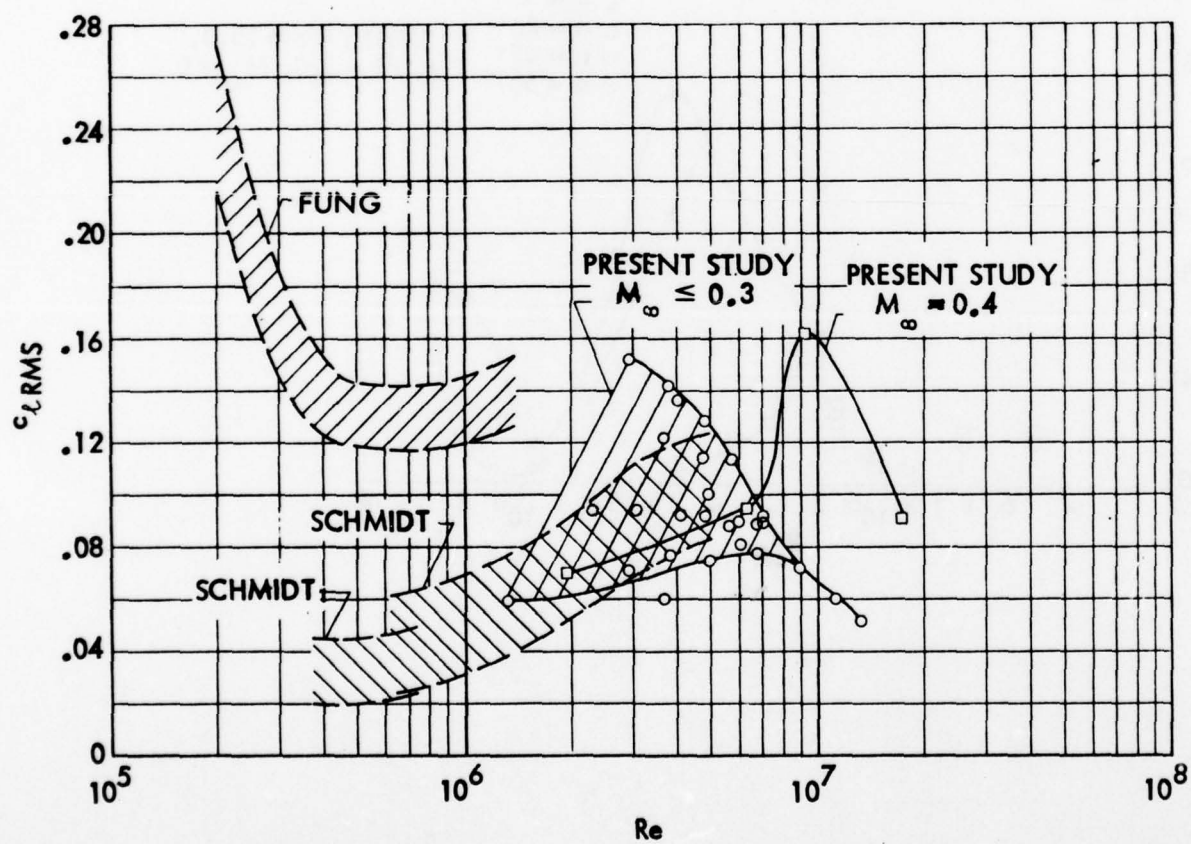
Fig. 48 Root Mean Square Lift Coefficient for a Circular Cylinder at
$2 \times 10^5 < R_d < 2 \times 10^7$ (Ref. 92)

3-2.1.1 <u>Effect of Roughness and Turbulence</u>. Considering the large effect
of Reynolds number one expects, of course, that surface roughness will have a
large effect; and it does, as the experimental results (Ref. 35) in Fig. 49
illustrate. Figs. 50a and 50b show other results from the same test. It is
apparent that the large effect of roll orientation (Fig. 50a) has its roots
in some form of nosetip imperfections (Fig. 50b). This effect of roll angle
was observed already by Gowen and Perkins (Ref. 5 and Fig. 51). It has since
then been observed by others (Refs. 14 and 26), and has been shown to be insen-
sitive to low roll-rates (Ref. 12 and Fig. 52).

All these results pointed rather strongly to model-asymmetry being the
source. However, Lamont and Hunt (Ref. 33) made a convincing case for wind
tunnel turbulence being an equally likely source. For that reason their tests
were repeated in a low turbulence (0.01 percent) wind tunnel (Ref. 41). The
results prove conclusively that wind tunnel turbulence did not cause the anoma-
lous effects of roll orientation. A very thorough investigation of the model
nose showed its roughness to be one order of magnitude below what the boundary
layer is expected to be able to feel. That seems to leave no clue to what
causes the observed effects of roll angle. However, one notes that the measured
roughness was compared with boundary layer characteristics for a local Reynolds
number of 10^5. At the very nosetip all roughness must be large compared to the
local boundary layer thickness. One wonders if not a nosetip much smaller than
the one shown in Fig. 50b would have given the same results.

Dynamic data for coning ogive-cylinders (Ref. 140) or pitching slender
delta wings (Ref. 141) show that the conditions at apex at time t_o determine
completely the downstream characteristics of the vortex (at later times, $t_o +$
Δt, where $\Delta t = x/\overline{U}$ with $\overline{U} \approx U_\infty$). The dominant influence of the apex conditions
are also reflected in the measured side force due to asymmetric vortex shed-
ding (Ref. 12 and Fig. 53). The fineness ratio is the same for the two nose
shapes. However, the apex angle for the tangent ogive nose is $\theta_A = 11.32^\circ$
and for the conic nose $\theta_A = 5.72^\circ$.

All results discussed so far speak loudly of the dominant influence of the
very tip of the nose. Having heard Morkovin describe how microscopic details
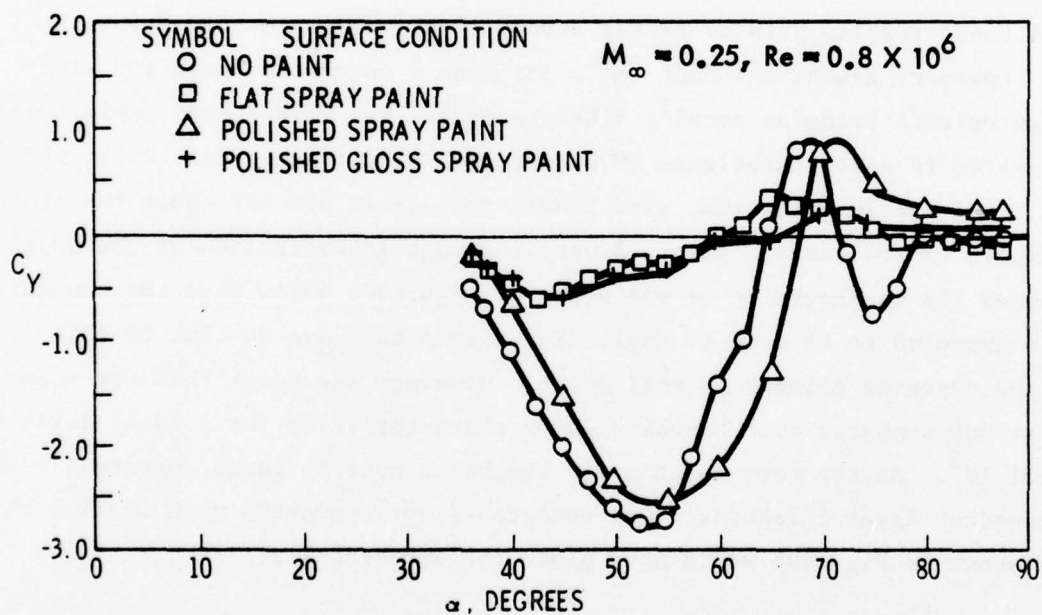
Fig. 49 Effect of Surface Finish on Vortex-Induced Side Force on a
$\ell/d = 3.5$ Ogive (Ref. 35)
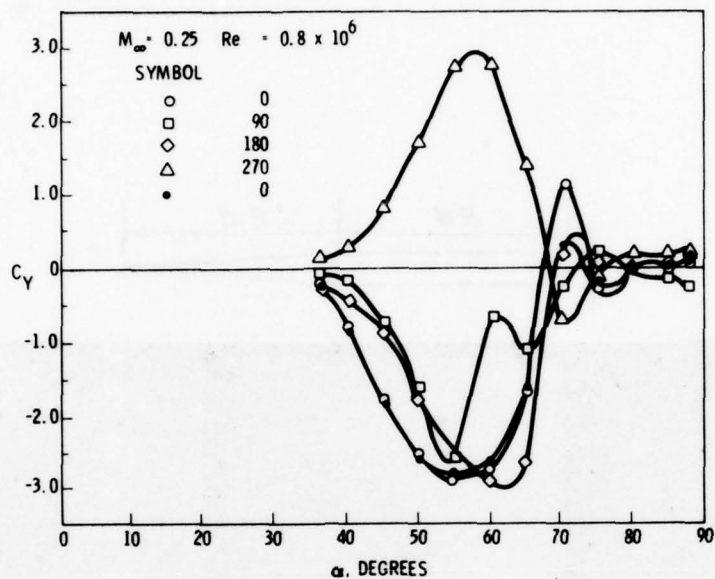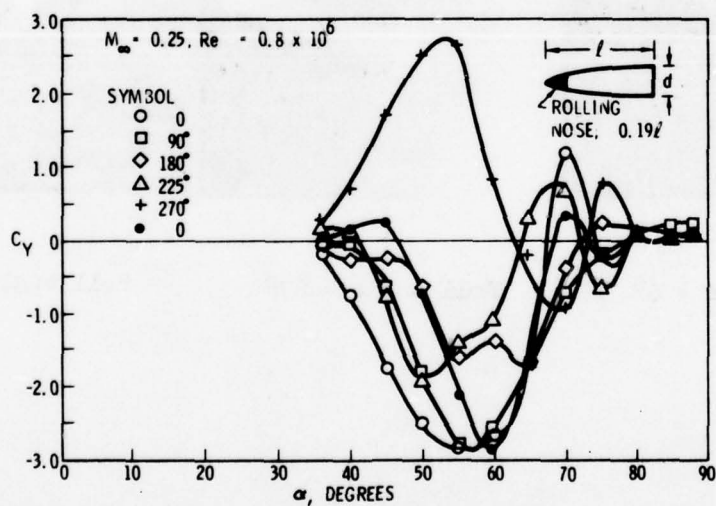
Fig. 50 Effect of Roll Angle on Vortex Induced Side Load on a
$l/d = 3.5$ Ogive (Ref. 35)
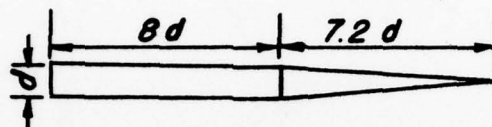
Roll angle = 0°   Roll angle = 67°   Roll angle = 139°

Fig. 51 Effect of Tip Rotation on Asymmetric Vortex Formation on
Cone-Cylinder at $\alpha/\theta_c = 3.75$ (Ref. 5)
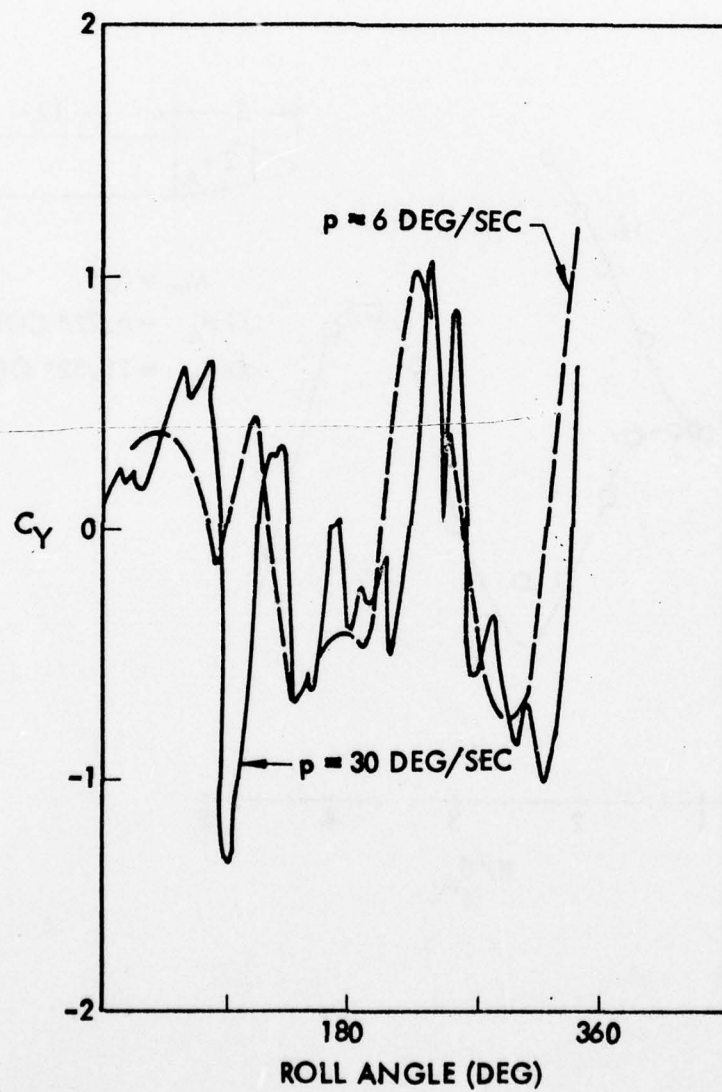
Fig. 52 Effect of Roll Angle and Low Roll Rate on Vortex-Induced
Side Force on a 5.8 Cone-Cylinder (Ref. 12)
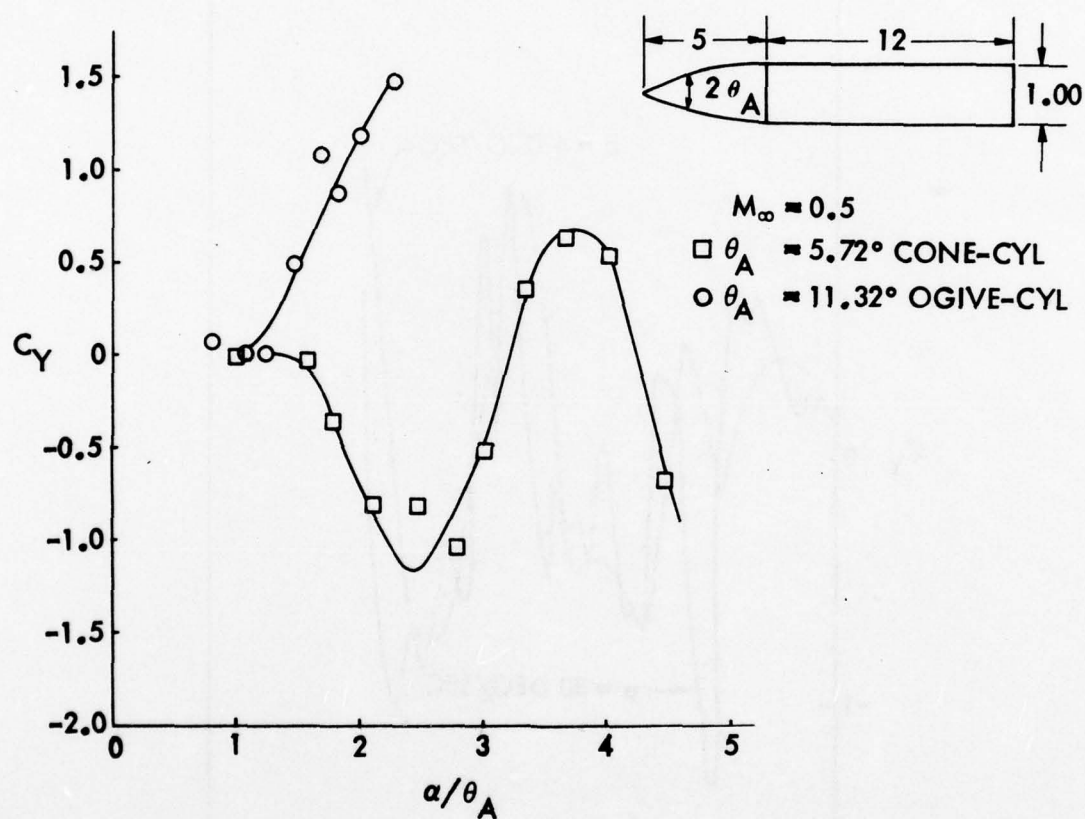
Fig. 53 Effect of Apex Half Angle on the Vortex-Induced Side Forces on Cylinders with Conical and Ogival Noses (Ref. 12)

at the birth of the vortex determine its complete downstream life (Ref. 142) the senior author has little difficulty believing in this apex dominance. If one accepts this dominance of the apex it is easy to understand why nose bluntness has such a large alleviating effect on asymmetric vortex loads (Ref. 14 and Fig. 54), and why apex rounding has a similarly strong effect on delta wing vortices (Ref. 143).

3-2.2 Effect of Mach Number

Wardlaw and Morrison recently reviewed the effect of Mach number on the vortex-induced maximum side force on cones, tangent-ogives and parabaloids (Ref. 53 and Fig. 55). Significant side forces have been measured on sharp cone-cylinders at $M_\infty = 2$ (Ref. 12) and on ogive-cylinder bodies even at $M_\infty = 5$ (Refs. 10 and 144). However, the latter results are very unreliable as they are affected greatly by support interference, which will be discussed later (Section 3-2.5). Fig. 56 shows the Wardlaw-Morrison data (Ref. 53) plotted against crossflow Mach number, $M_n = M_\infty \sin \alpha$. The Mach number trends show a certain similarity to those discussed earlier for two-dimensional flow (Fig. 22).

There is also a purely three-dimensional reason for the transonic C_Y "bucket" in Fig. 55, and that is nose-induced flow separation. It occurs on blunt-nosed bodies already at $\alpha = 0$ (Ref. 145 and Fig. 57) and will at angle-of-attack occur even on slender noses (Refs. 146, 147 and Fig. 58). This three-dimensional closed[*] separation bubble prevents the nose from generating the vortices associated with open[*] separation regions, which play such an important part in the vortex induced asymmetric (and symmetric) loads at lower subsonic Mach numbers. Thus, the vortices can only be generated by the aft body, and the generated side force will as a consequence be relatively small. The flow pattern observed at $M_\infty = 2.45$ on a flat-nosed cylinder at high angles of attack (Ref. 149 and Fig. 59) shows such nose induced flow separation followed by aftbody vortices, which first are symmetric and then become asymmetric, all in agreement with the vortex geometry specified by Thomson (Ref. 45). Very similar characteristics were observed for a hemisphere-cylinder (Ref. 149), and

---

[*]See Wang (Ref. 148) for details.
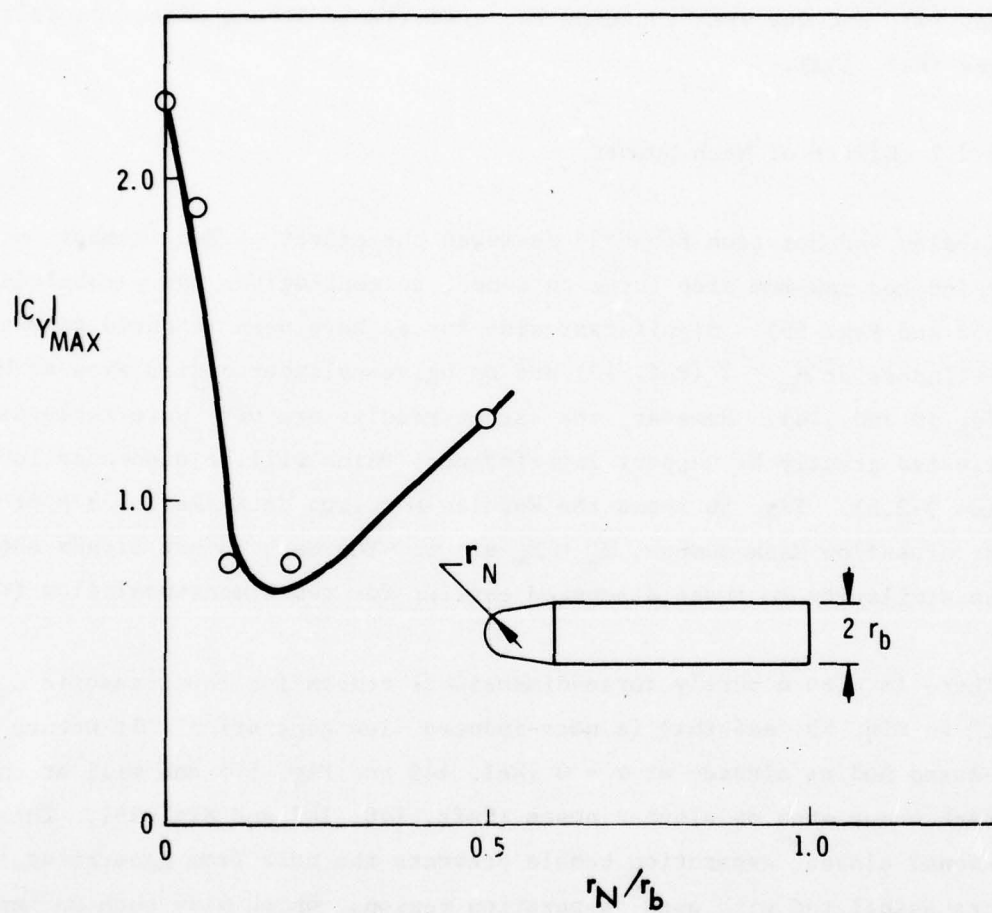
Fig. 54 Effect of Nose Bluntness on the Vortex-Induced Side Force
on an Ogive-Cylinder (Ref. 14)

Fig. 55 Effect of Mach Number on the Vortex-Induced Side Force on
Cones, Tangent-Ogives and Paraboloids (Ref. 53)
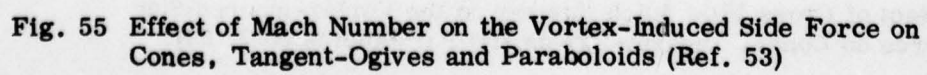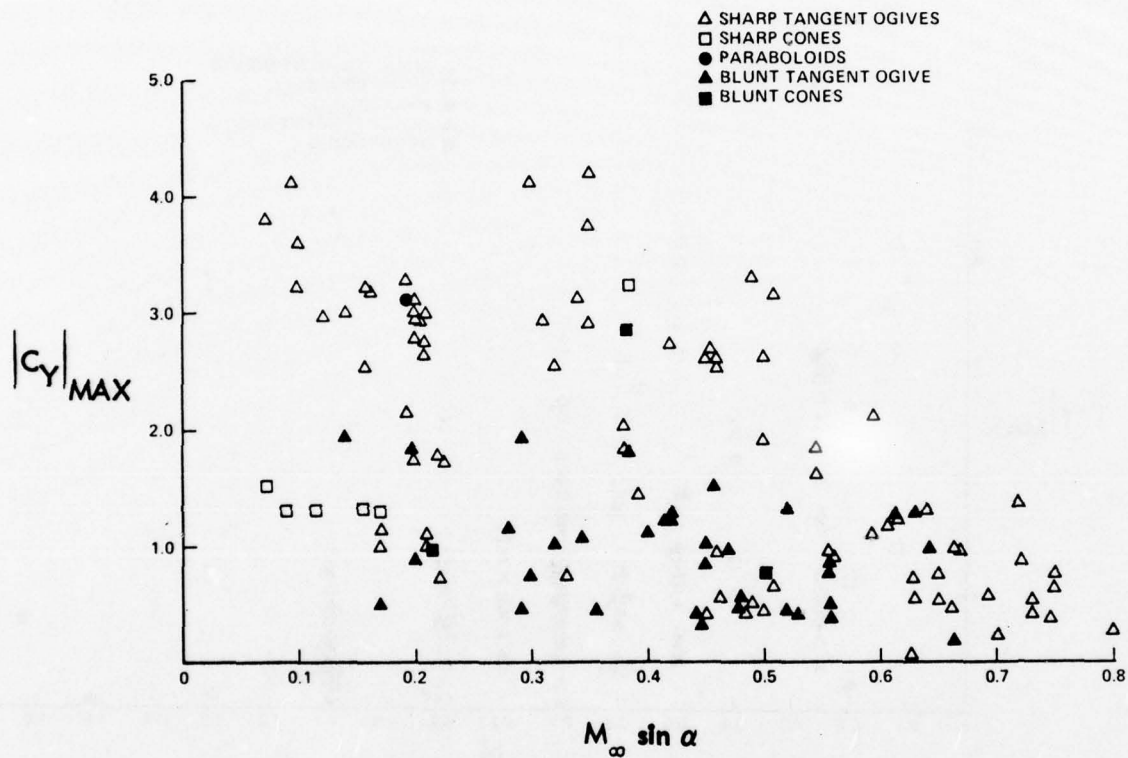
Fig. 56 Effect of Cross Flow Mach Number on the Vortex-Induced Side
Force on Cones, Tangent-Ogives and Paraboloids (Ref. 53)
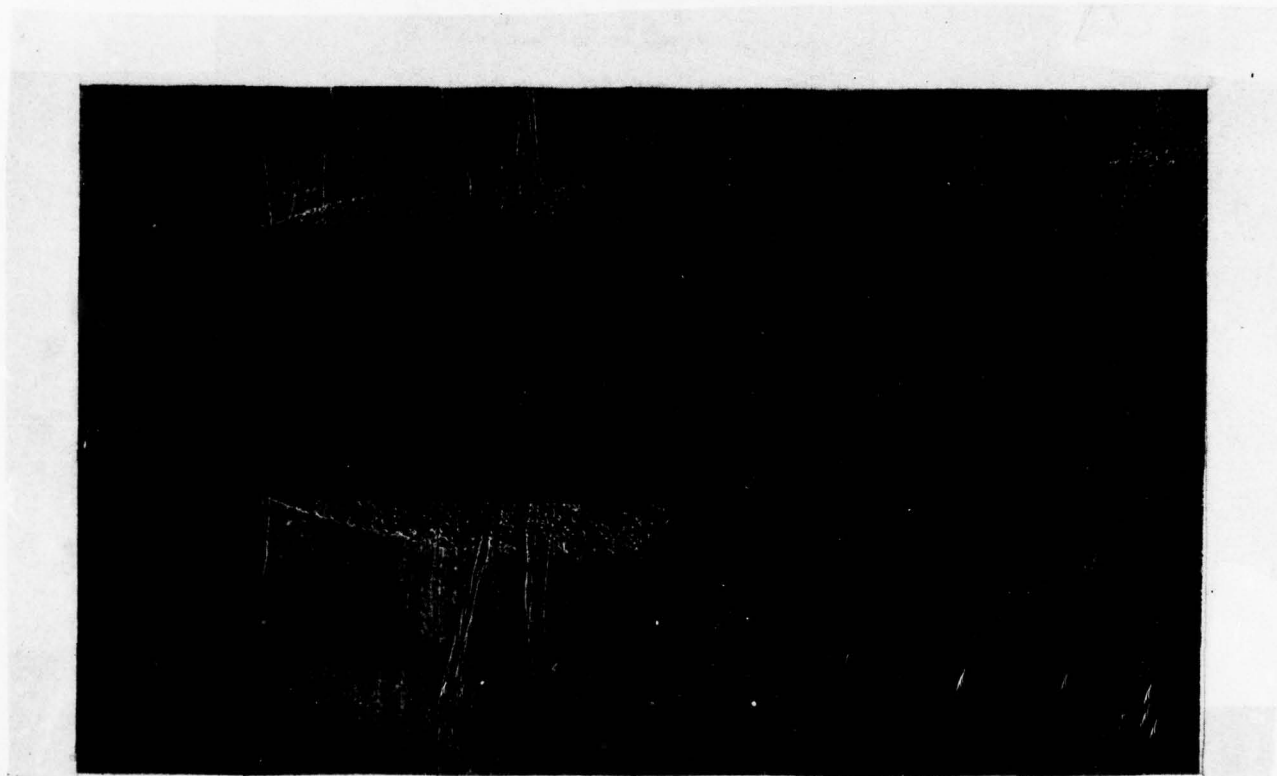
$\alpha = 0$

Fig. 57 Nose-Induced Flow Separation on a Blunt-Nosed Cylinder-Flare Body (Ref. 145)
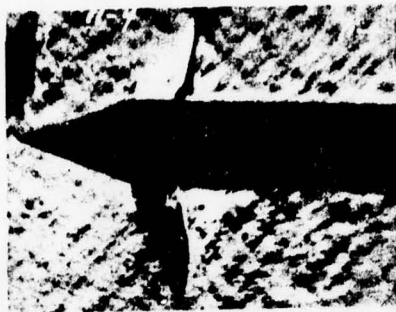
$M_\infty = 0.89, \ \alpha = 2°$
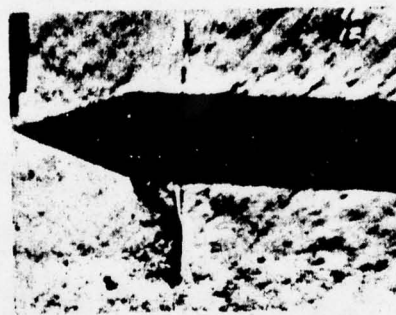
$M_\infty = 0.89, \ \alpha = 4°$
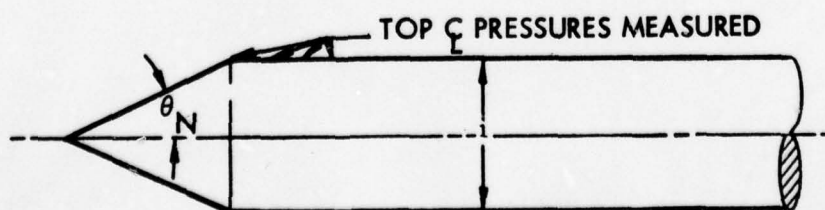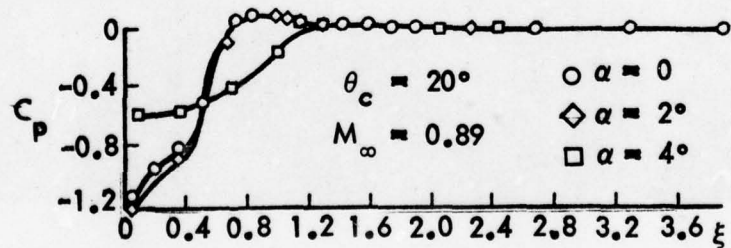
Fig. 58 Sudden Leeward Side Separation on Slender-Nosed Cone-Cylinder
Bodies at High Subsonic Speeds (Refs. 146 and 147)

Cross flow

Bow shock wave

Separated boundary layer from nose

Shock wave from beginning of vortex wake

A'

Cross-section of body

M_∞

Model

Shock waves in cross-flow

Separation bubble

Vortex wake

Vortices

A

Shock wave from reattachment

Shock waves (at high Mach number and incidence)

Separated boundary layer from nose
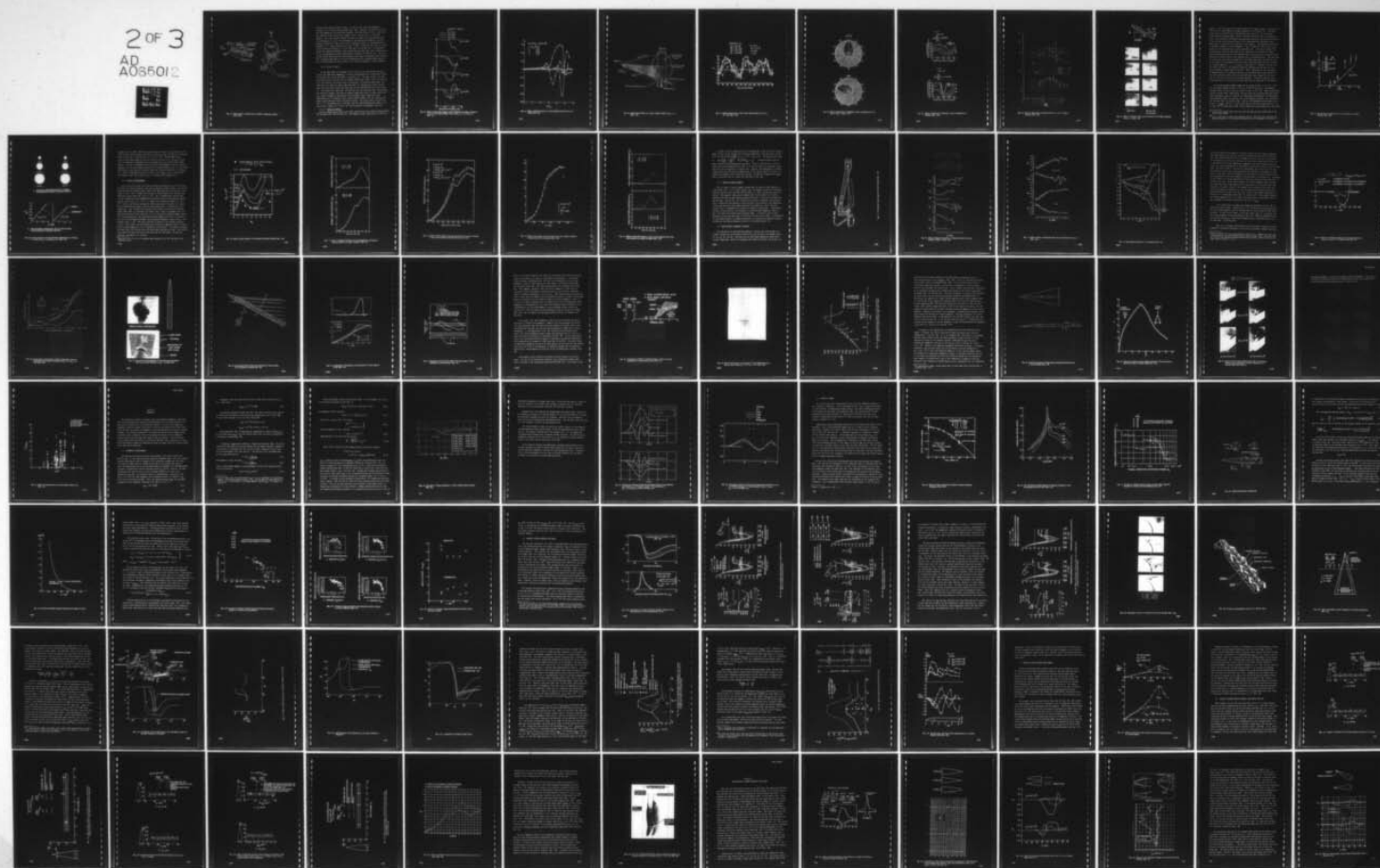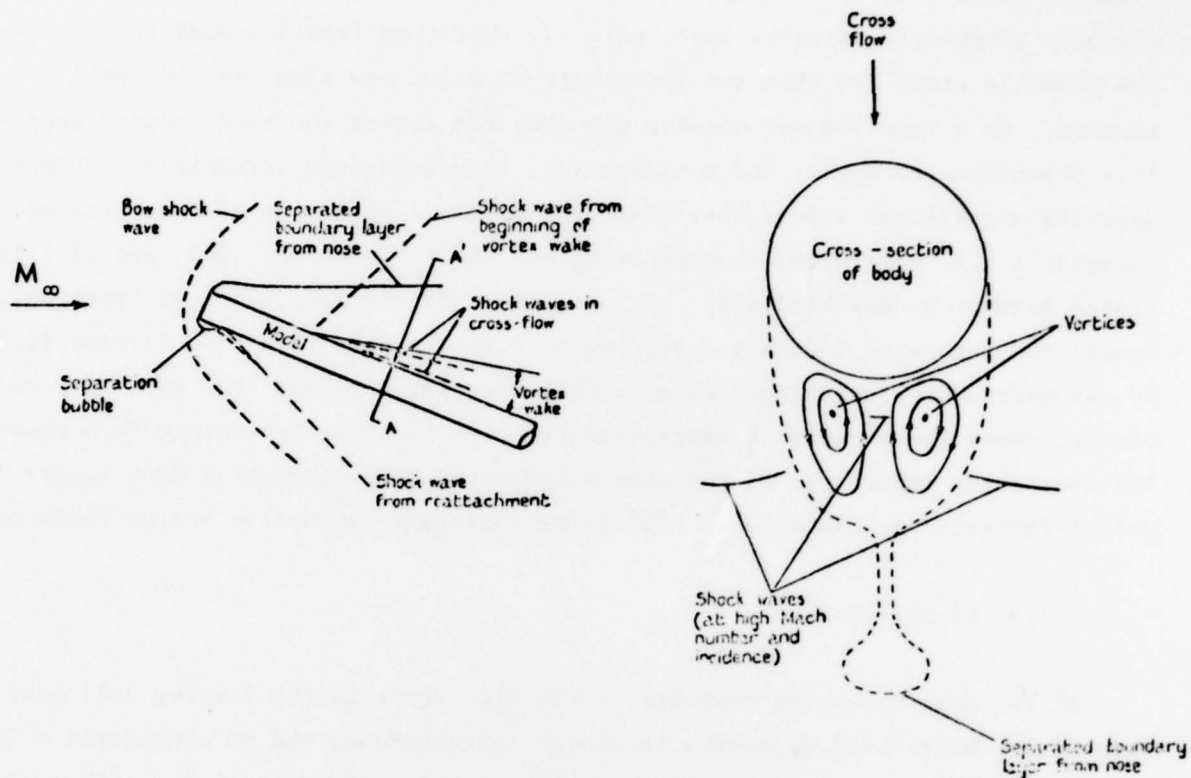
**Fig. 59 Wake Pattern on Blunt Nose Cylinder at Supersonic Speed
(Ref. 149)**

have also been seen by Schiff at $M_\infty = 1.4$ and $\alpha = 18^\circ$, when the hemisphere-cylinder is in a 10 cps coning motion (Ref. 150). However, in Schiff's case the aft body asymmetric vortices were unsteady, switching from one side to the other. The probable cause for this was thought to be a 10° yaw slop in the model support. On a very slender nosetip one does not expect the nose-induced separation phenomenon to occur, and consequently, nose-generated asymmetric vortices generate significant side forces also at supersonic speed, as is demonstrated by Atraghji's 5.7° cone-cylinder data at $M_\infty = 2$ (Ref. 12 and Fig. 60), and is illustrated further by Rainbird's 5° cone data (Ref. 63 and Fig. 61). At hypersonic speeds the separated boundary layer region from the nose (Fig. 59) is substituted by the nose-bluntness-induced entropy wake (see Ref. 151 and Fig. 62). For very slender noses there could be vortex-induced side loads at hypersonic Mach numbers. The increasing importance of the nose slenderness with increasing Mach number is well illustrated by the data in Fig. 5 for incipient asymmetric vortex shedding.

3-2.3 Effect of Spin

At low spin rates the response of the side force to the varying roll position of the body-fixed asymmetry is almost instantaneous and no consistent effect of the spin rate can be seen (Ref. 12 and Fig. 51). The data in Ref. 152 indicate that this is also the case at somewhat higher spin rates, up to 6-1/3 Hz, but still with surface velocities only a few percent of freestream speed (Fig. 63). There may be a sign of a small time lag effect in realizing the vortex induced side load, and such a phase lag effect may also be deduced from the data in Fig. 51. The results for cones (Ref. 153 and Fig. 64) and cylinders (Ref. 154 and Fig. 65) indicate, however, that one can expect higher spin rates to have a more decisive effect through its distortion of the boundary layer transition front. Measurements for a fineness ratio 7 ogive-cylinder (Refs. 155, 156, and Fig. 66) show a very nonlinear effect of angle-of-attack. The large effect of spin rate for $\alpha = 15^\circ$ is probably due to the fact that the crossflow Reynolds number is in the critical region, $Re = 0.15 \times 10^6$ (see discussion of 2D Magnus, Fig. 23).

3-2.3.1 Effect of Coning

How the coning motion affects free body vortices was first shown by Tobak, Schiff, and Peterson (Ref. 140 and Fig. 67). The symmetric nose vortex pair is tilted an
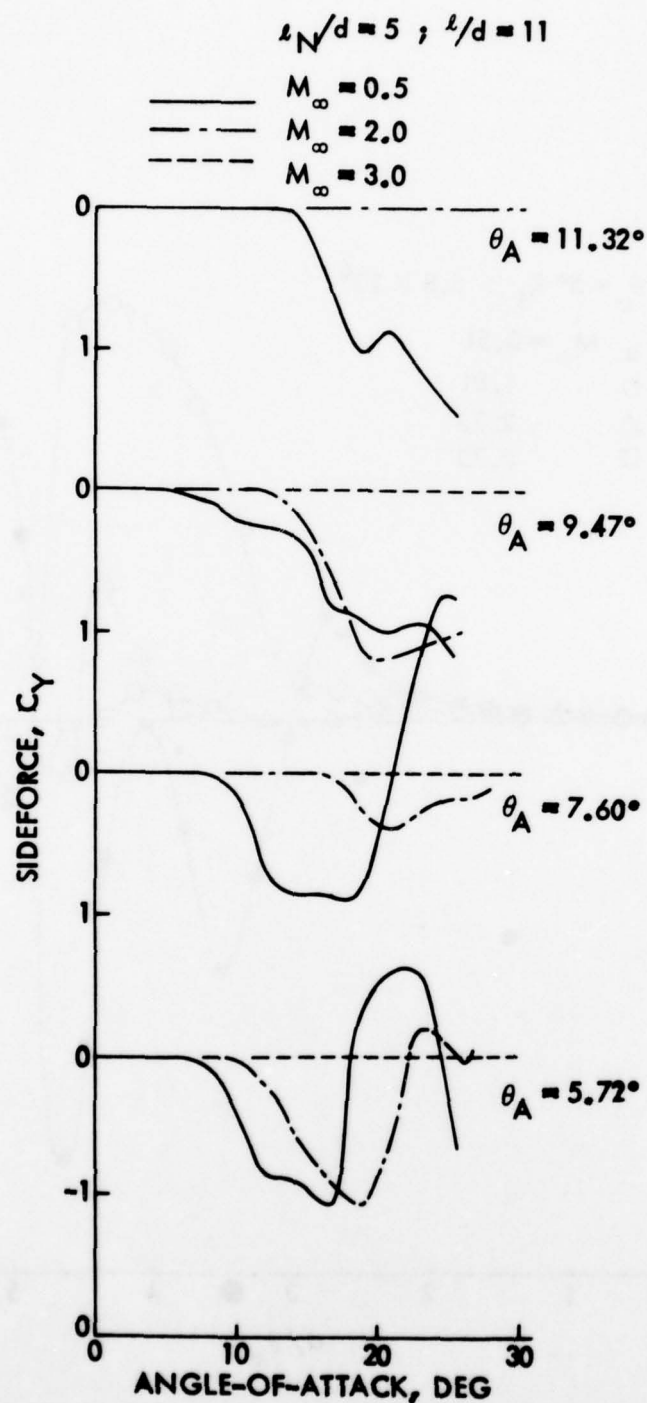
Fig. 60 Effect of Apex Half Angle of Cone Cylinders and Ogive Cylinders on the Vortex-Induced Side Force at M_∞ = 0.5, 2.0 and 3.5 (Ref. 12)

3–73
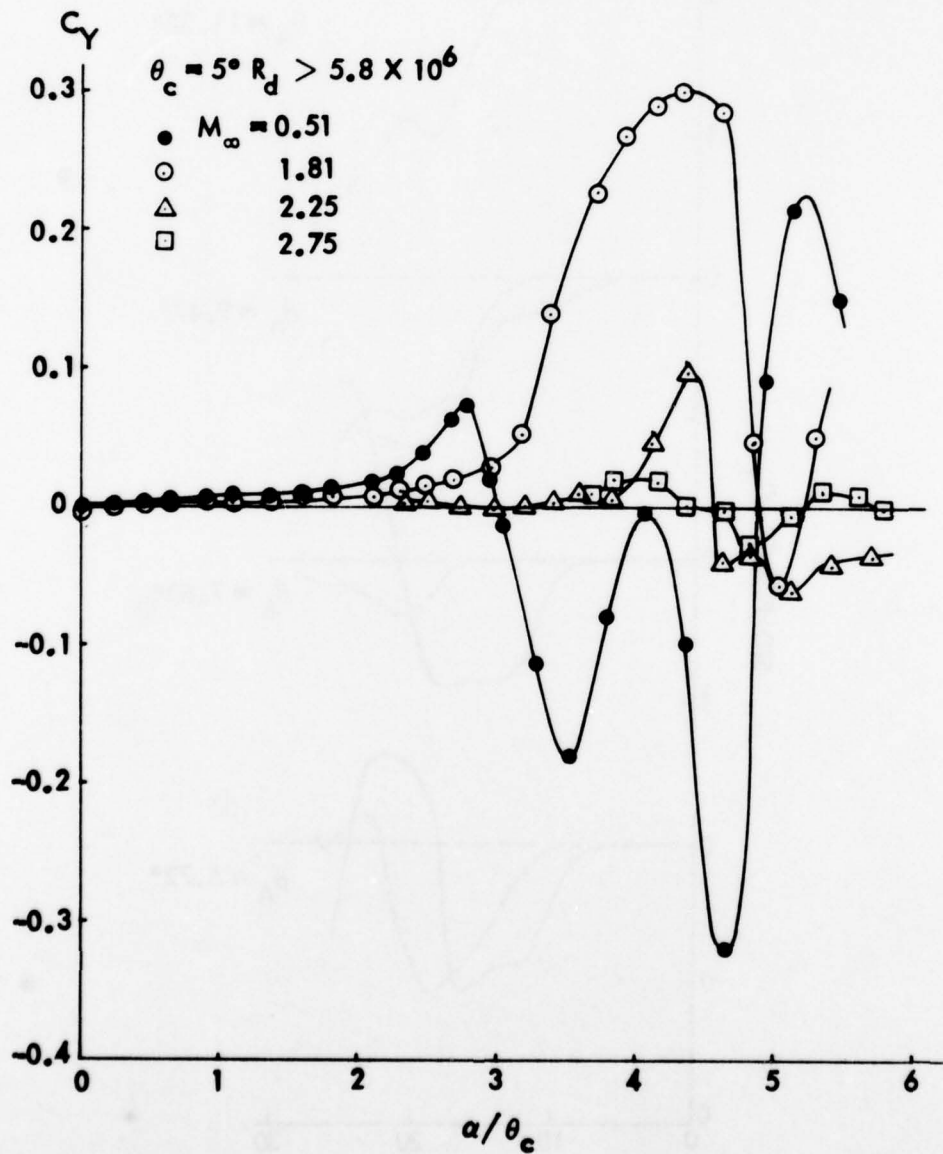
Fig. 61 Effect of Mach Number on Vortex-Induced Side Force on 5°
Cones (Ref. 63)
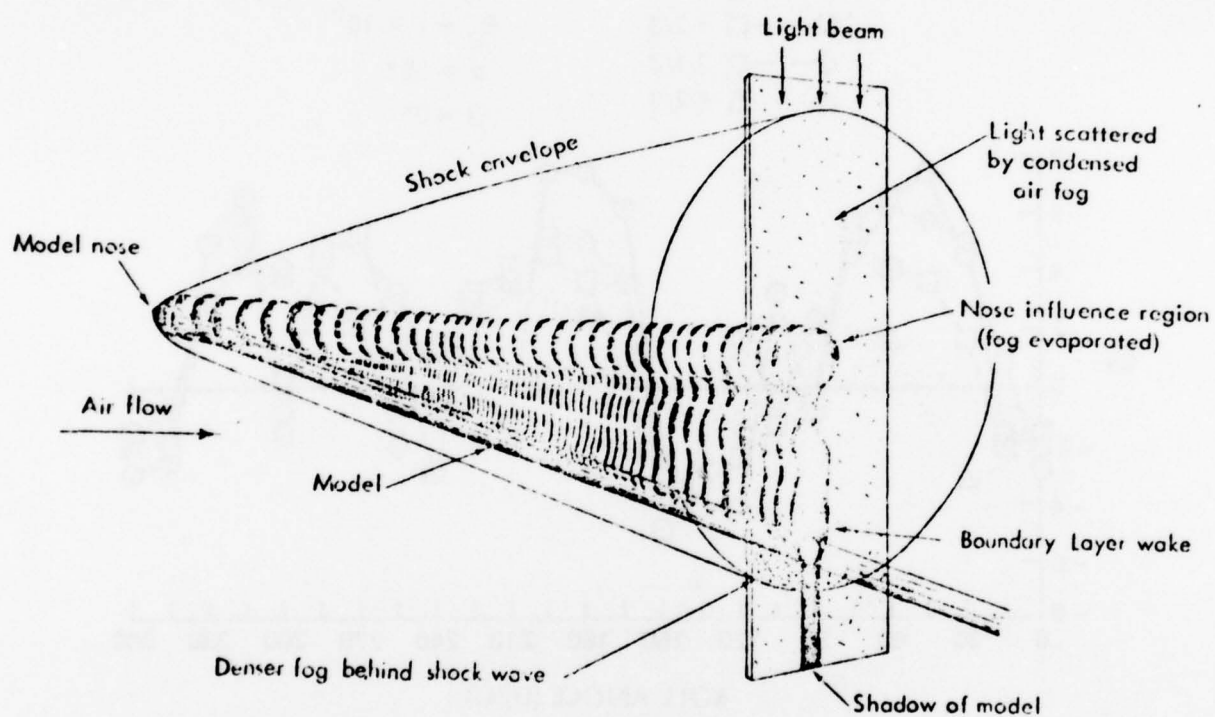
Fig. 62 Wake Flow Pattern on a Cone-Cylinder Body at $M_\infty = 7.5$ (Ref. 151)
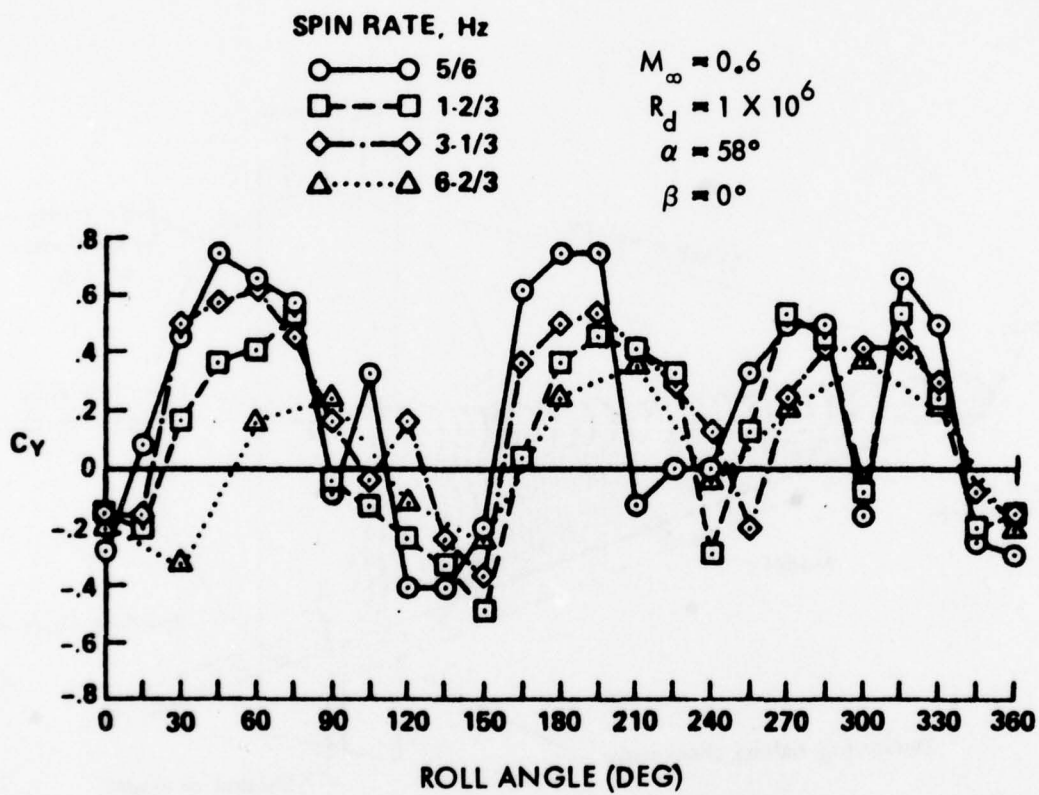
Fig. 63 Effect of Spin Rate on the Vortex-Induced Side Force on a
10° Cone (Ref. 152)
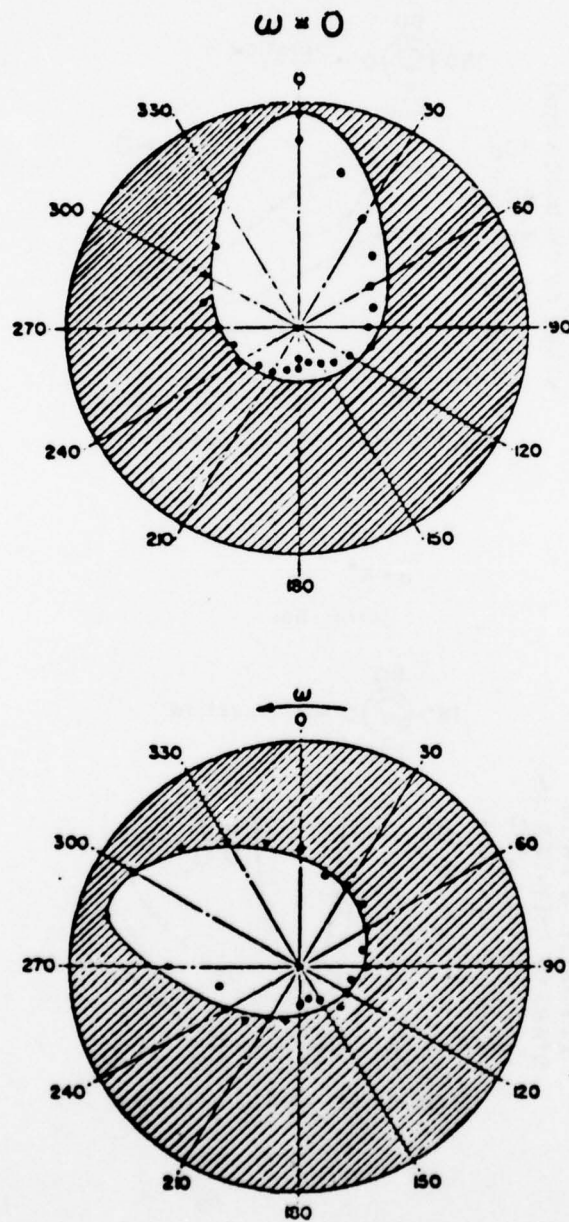
Fig. 64 Effect of Spin Rate on Boundary Layer Transition on a 10°
Cone at $M_\infty = 2$ (Ref. 153)
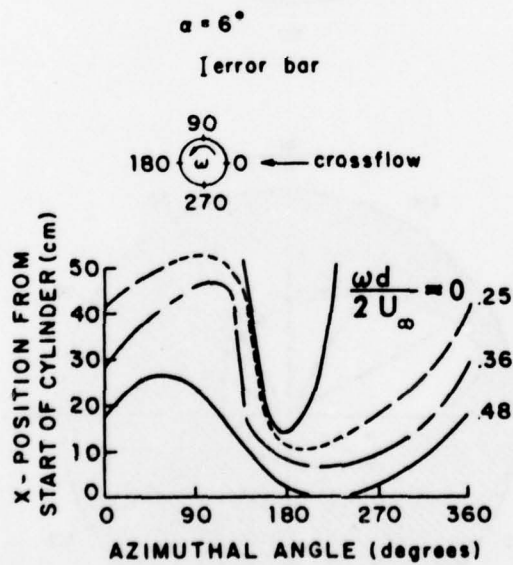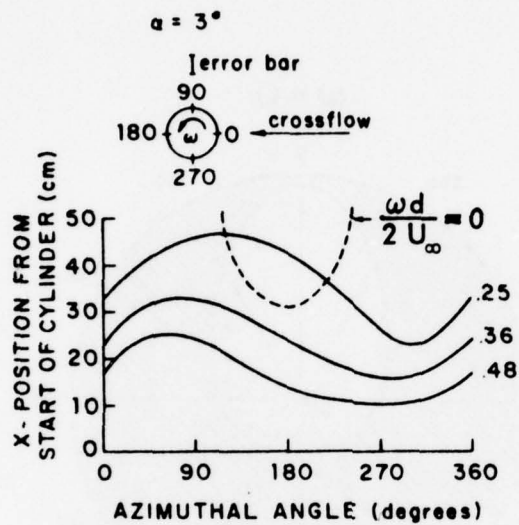
Fig. 65 Effect of Spin Rate on Boundary Layer Transition on a
Cylinder (Ref. 154)
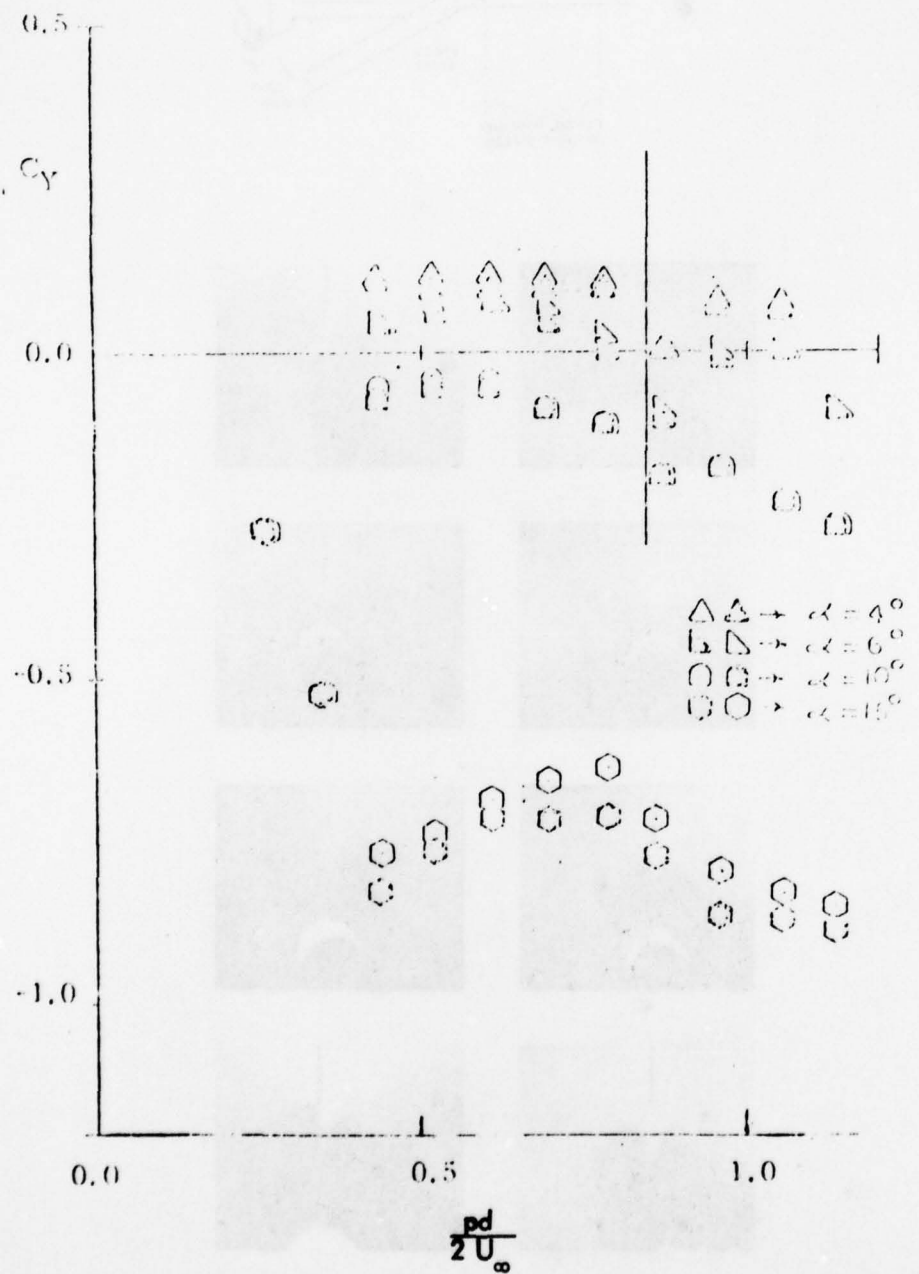
Fig. 66 Effect of Spin Rate on the Side Force of a $\ell/d = 7$ Ogive-Cylinder (Ref. 156)
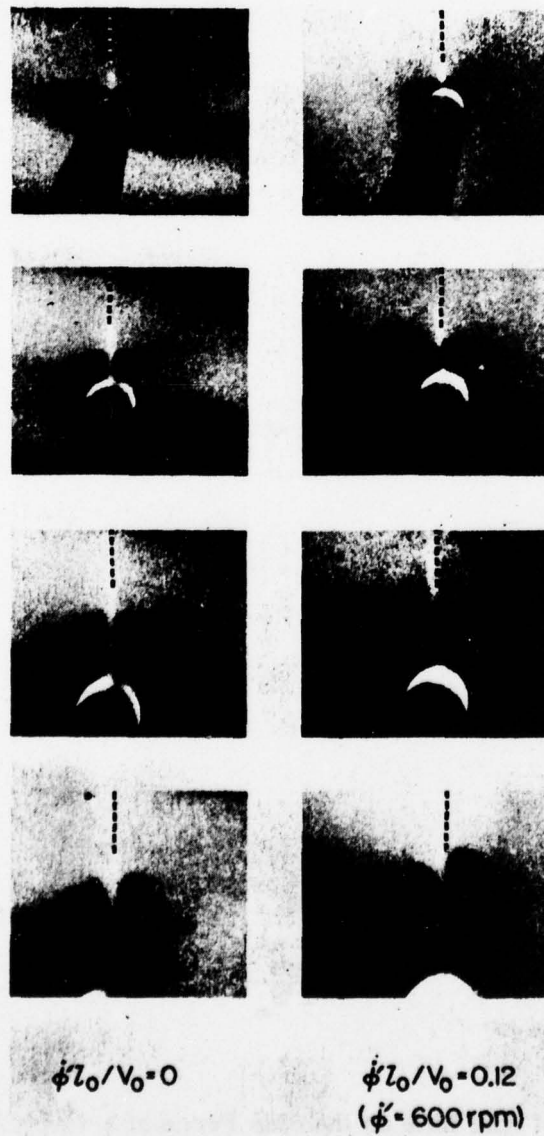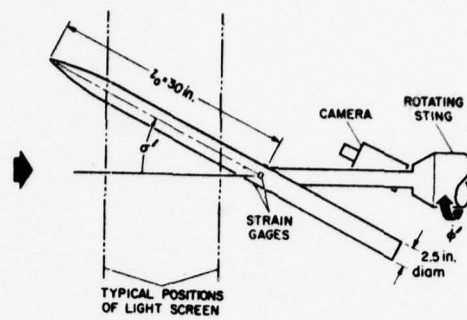
Fig. 67 Effect of Coning on the Vortex Geometry on an Ogive–Cylinder at $M_\infty = 1.4$ (Ref. 140)

angle $\gamma = \tan^{-1}(\dot{\phi}' \ell_o / U_\infty)$, the crosswind-induced tilt angle at apex. The angle the vortices are tilted remains the same regardless of x-station,[#] i.e., the apex conditions are controlling the downstream vortex location. By tilting the vortex-induced pitching moment vector, obtained from static tests, through the angle γ the predicted side moment characteristics shown in Fig. 68 were obtained. It can be seen that the main portion of the experimentally determined side moment due to coning rate is predicted in this manner. The remaining difference is probably induced by vortex asymmetry. Fig. 67 shows the vortex lobe to be larger on the advancing than on the retreating side. This can be explained by the moving wall effects discussed earlier (Section 3-1.3 and Fig. 23) which would promote separation on the advancing side, resulting in an increased vortex, whereas the effects would be the opposite for the retreating side. The same type of tests have later been performed for a $10°$ sharp cone (Ref. 157 and Fig. 69). We see again the experimental data deviating from predictions when the vortices can become asymmetric, i.e., for $\alpha/\theta_c > 2$ (see Fig. 5). However, in this case the deviation goes in the opposite direction from what was the case for the ogive-cylinder (compare Figs. 68 and 69). Why? Going back to the discussion of Magnus-effects in connection with Fig. 23 one would expect this reversal if the flow conditions were in the critical Reynolds number range for the cone test but not for the test with the ogive-cylinder. The much larger deviation from prediction in the case of the cone would also be explained in this manner.

The stated Reynolds number ranges for the tests are Re = 0.2 to 0.7 x 10^6 for the ogive-cylinder and Re = 1.0 to 2.4 x 10^6 for the cone. The maximum reversal effect in Fig. 23 was for curve m at Re = 0.35 x 10^6. Results published recently by Mack (Ref. 158 and Fig. 70) show that the transition Reynolds number could increase as much as a factor of 6 when going from Swanson's incompressible flow conditions (Ref. 112 and Fig. 23) to the present supersonic test conditions for the cone (Ref. 157 and Fig. 69). That is, the maximum reversal might occur at Re = 6 x 0.35 x 10^6 = 2.1 x 10^6, which falls in the test range used, Re = 1.2 to 2.8 x 10^6.[##] Going back to Fig. 23 one finds that purely subcritical conditions

---

[#] Later tests showed this to be true also for body stations downstream of the oscillation center.

[##] Re is used here to relate the different tests. How axial and crossflow components interact in the transition process will be discussed in Section 4-1.

3-81
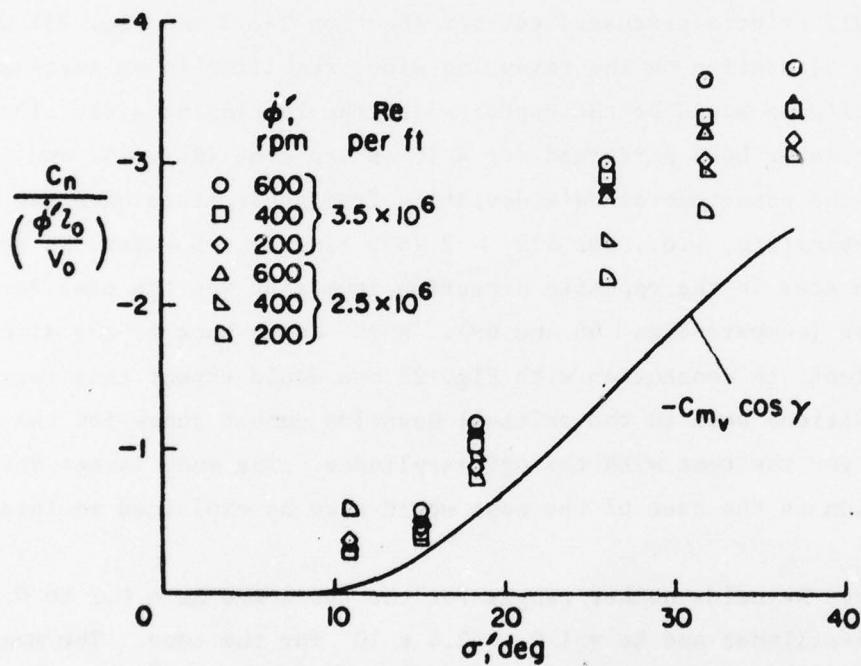
Fig. 68 Side Moment Coefficient due to Coning Motion of Ogive-
Cylinder (Ref. 140)
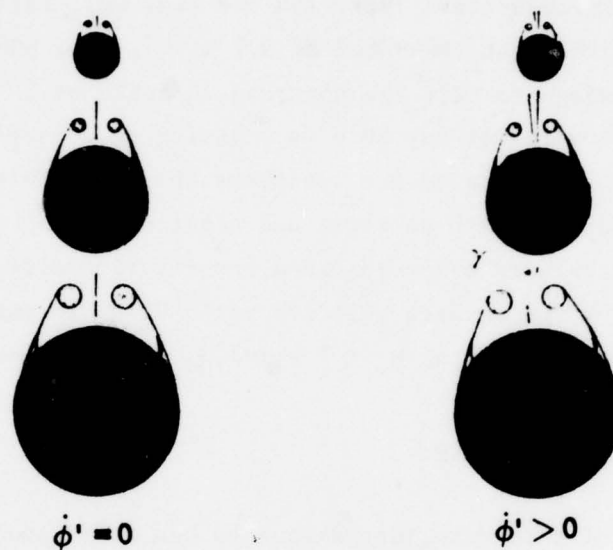
a. SCHEMATIC REPRESENTATION OF VORTEX DISPLACEMENT DURING CONING MOTION
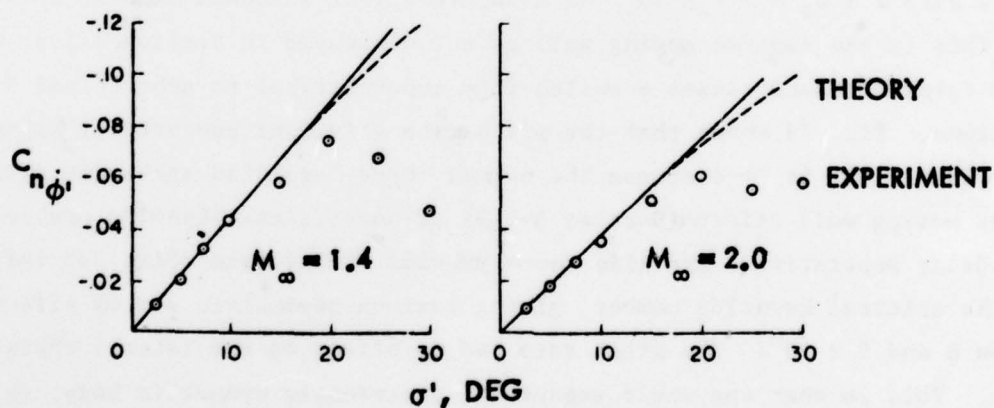
b. SIDE-MOMENT COEFFICIENT ON 10° HALF-ANGLE CONE CAUSED BY CONING MOTION

Fig. 69 Vortex Geometry and Side Moment Coefficient for a Coning 10° Cone at $M_\infty = 1.4$ and $M_\infty = 2.0$ (Ref. 157)

existed at Re = 0.358 x 10^6 (Curve a) which with a factor of 6 gives Re = 0.215 x 10^6 for the ogive-cylinder test (Ref. 140 and Fig. 68), falling in the Reynolds number range used in the test, Re = 0.2 to 0.7 x 10^6. The 600 RPM coning rate used was high enough to tilt the vortices an angle of $2°$ and would, there-fore, be expected to overpower any nose asymmetries on a carefully made model. However, in order to eliminate future questions about possible effects of model asymmetry the test was run with positive and negative coning rates. No noticeable differences in the data were observed (when the rotation direction is accounted for). Even at 600 RPM the surface velocity ratio U_W/U_∞ is small, being 0.007 and 0.0055 at apex for $\alpha = 30°$ at $M_\infty = 1.4$ and $M_\infty = 2.0$, respectively.

3-2.4 Effect of Pitch Rate

As in the case of spin rate just discussed one would expect that the effect of pitch rate could be large in the critical Reynolds number region. The results obtained by Smith and Nunn (Refs. 28 and 159) show that this is indeed the case (Figs. 71-73). Fig. 71 shows the increase in vortex-induced lift realized for subcritical flow conditions, Re = 5 x 10^4. Fig. 72 demonstrates how the sub-critical condition can be reached[#] by pitching the body at the constant reduced angular rate $\dot\alpha\ d/U_\infty = 2.7$ x 10^{-3} at a supercritical Reynolds number, Re = 8 x 10^4. This is the reverse moving wall effect discussed in Section 3-1.3, which delays transition and causes a switch from supercritical to subcritical flow conditions. Fig. 73 shows that the pitch rate effect at subcritical Reynolds number (Ref. 160) is to decrease the normal force, again in agreement with the regular moving wall effect (Section 3-1.3) at noncritical Reynolds number, which is to delay separation. The side force and side moment data (Fig. 74) indicate that the critical Reynolds number, giving maximum asymmetric vortex effect, lies between 8 and 5 x 10^4. The pitch rate had no effect on the lateral character-istics. This is what one would expect for a perfectly symmetric body, or, maybe, when the body-asymmetry is in an ineffective roll position. The results obtained by others (Ref. 25) indicate that the latter may have been the case. They rolled their model and found that pitch rate decreased the side moment for one roll position, increased it for another.

[#] Only data at $\alpha < 50°$ are of interest here because at $\alpha > 50°$ unsteady vortex shedding starts.

3-84
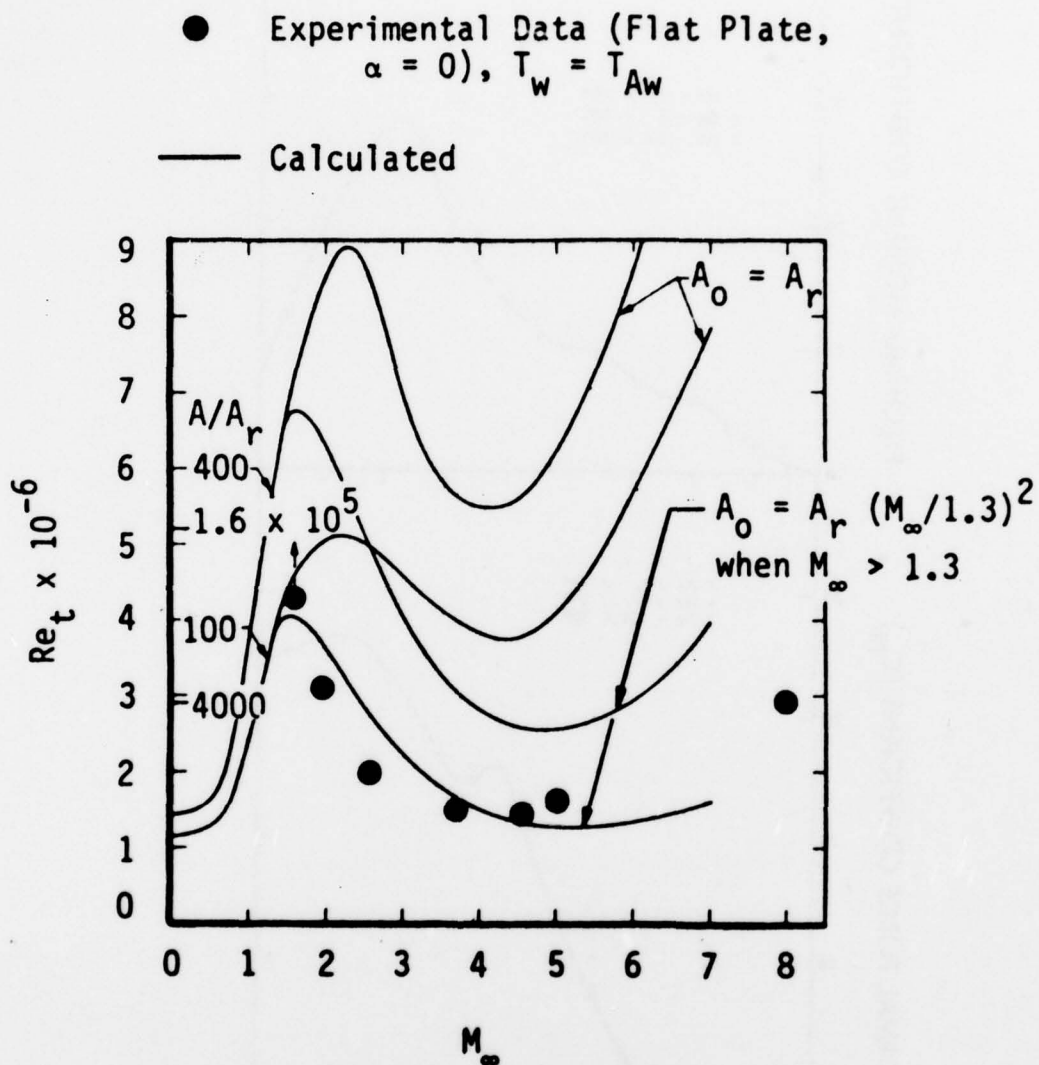
Fig. 70 Effect of Mach Number on Transition Reynolds Number (Ref. 158)
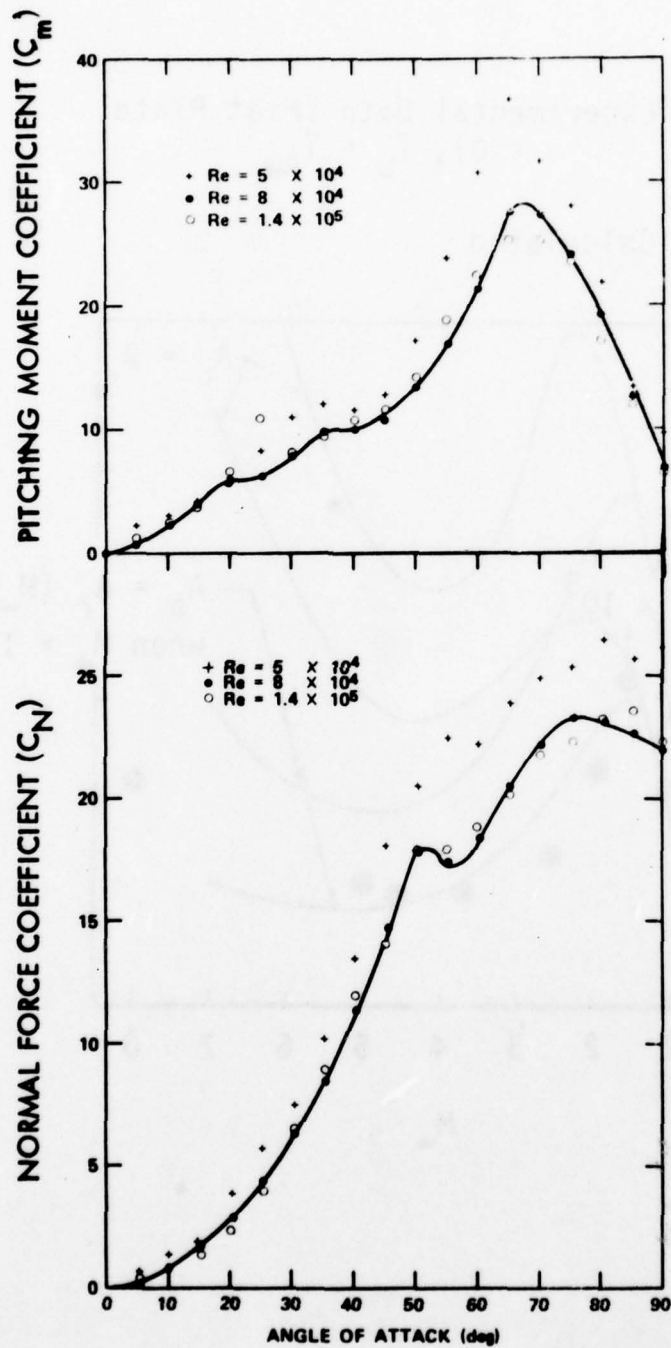
Fig. 71 Effect of Reynolds Number on the Longitudinal Aerodynamic
Characteristics of an Ogive-Cylinder (Ref. 28)
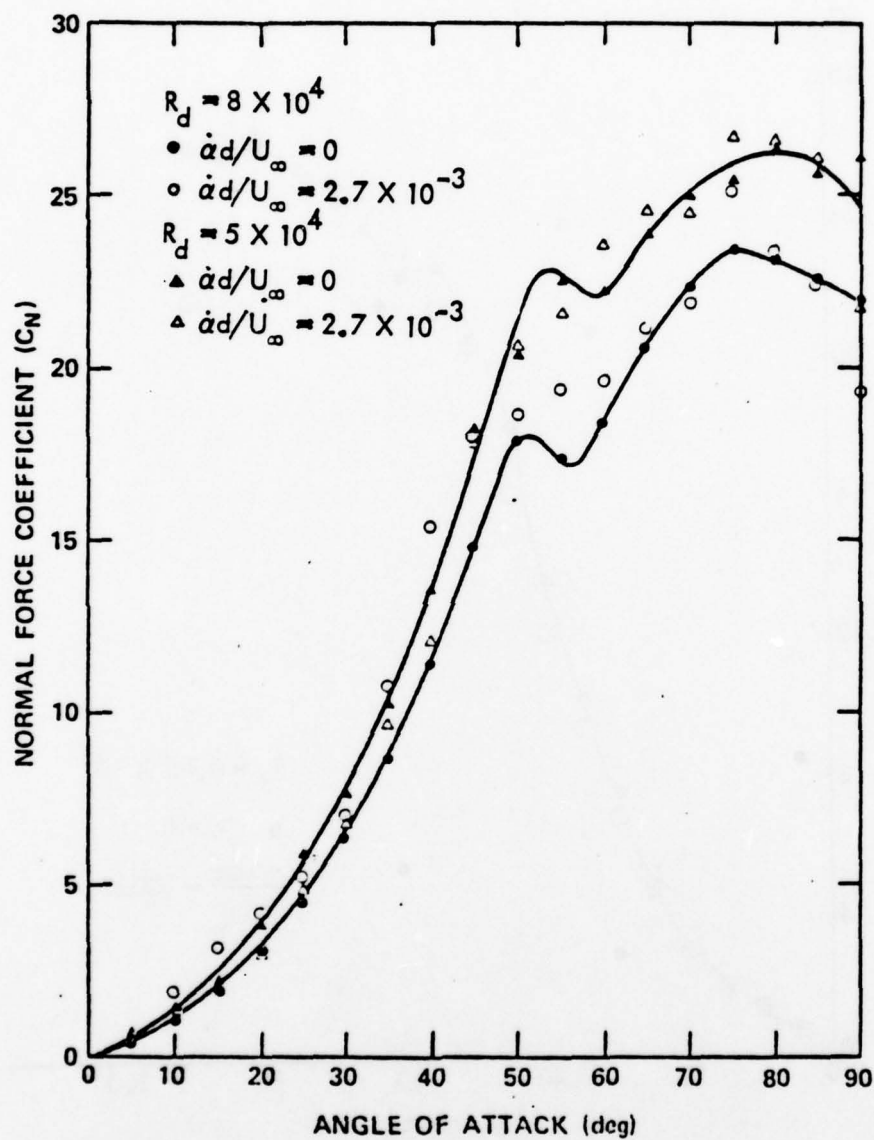
Fig. 72 Effect of Pitch Rate on the Normal Force of an Ogive-Cylinder
in the Critical Reynolds Number Region (Ref. 28)
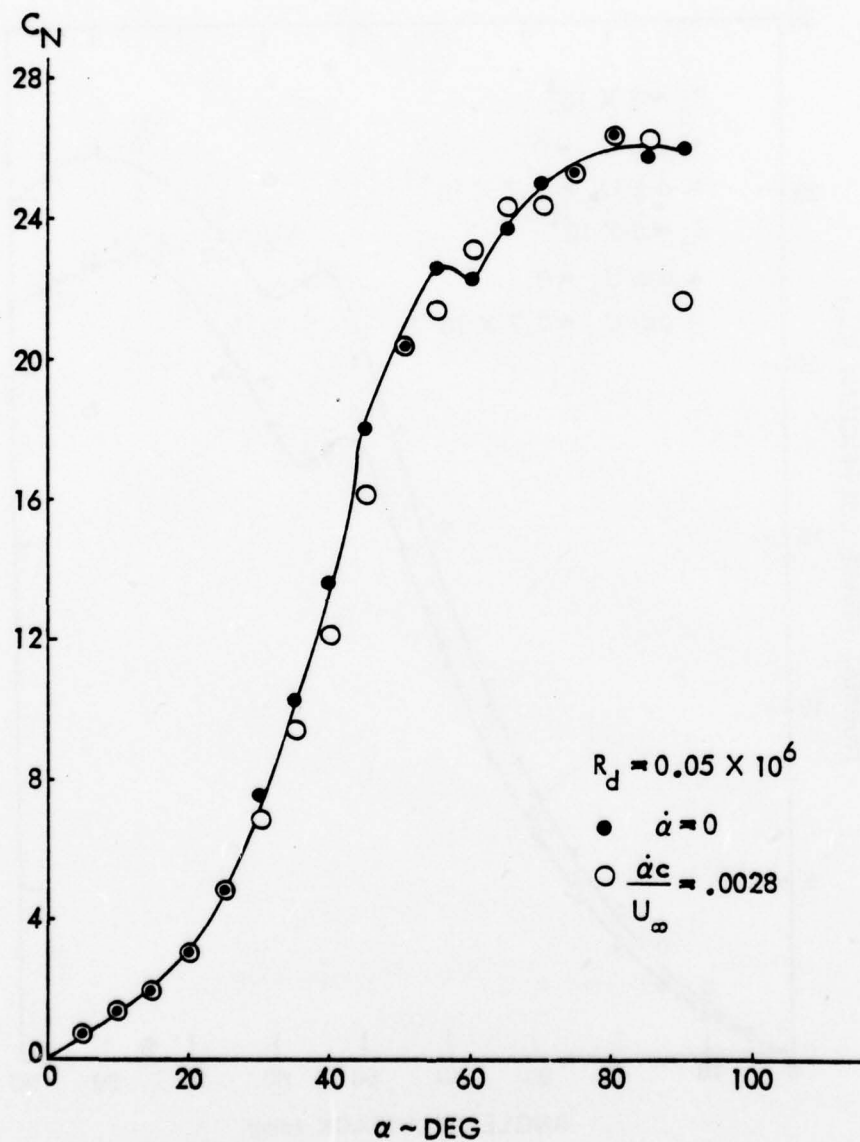
Fig. 73 Effect of Pitch Rate on the Normal Force of an Ogive-Cylinder at Subcritical Flow Conditions (Ref. 159)
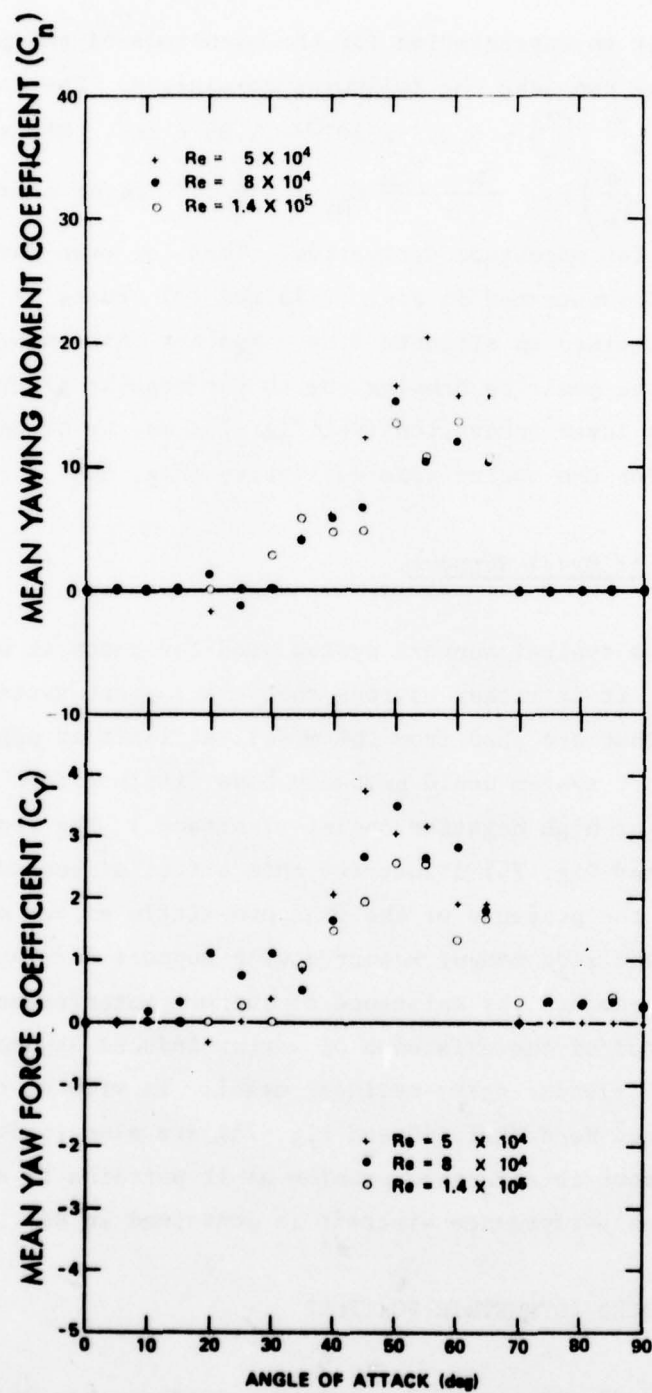
Fig. 74 Effect of Reynolds Number on the Vortex-Induced Side Force
and Moment on an Ogive-Cylinder (Ref. 159)

In order to get an appreciation for the magnitude of the pitch rate effects shown in Fig. 72 one can make the following comparison. The data give a normal force derivative $\partial C_N / \partial \left(\dfrac{c\dot\alpha}{U_\infty} \right) \approx 5/2.7 \times 10^{-3} = 1.85 \times 10^3$. The slender body value is $\quad dC_N / \partial \left(\dfrac{cq}{U_\infty} + \dfrac{c\dot\alpha}{U_\infty} \right) = - \dfrac{x_N - x_{CG}}{c} C_{N\alpha} \approx - \dfrac{\ell}{d}$. Using crossflow drag for high α gives a similar magnitude derivative. That is, even for $\ell/d = 10$ the pitch rate effect demonstrated in Fig. 72 is two (2) orders of magnitude larger than what can be obtained in attached flow. Against this background it becomes evident that also the positive damping due to the regular pitch rate effect, in absence of boundary layer transition (see Fig. 73), may be of appreciable magnitude, as was true for the coning rate derivative (Fig. 68).

3-2.5 Effect of Model Support

Fig. 75 shows a typical support system used for tests at high angles-of-attack (Ref. 161). It is rather obvious that the support system will interfere with the vortices that are shed from the model, at least at positive angles-of-attack. (The support system would probably have little effect on the nose-generated vortices at high negative angles-of-attack.) The results obtained by Uselton (Ref. 144 and Fig. 76) illustrate this effect of support interference. Fig. 77 shows that the presence of the fins had little effect on the magnitudes of the side force and side moment measured with support A. Thus, the data trend in Fig. 76 documents the existence of support interference. Consequently, one has no real proof of the existence of vortex-induced asymmetric loads at $M_\infty = 5$ on this very slender ogive-cylinder model. In view of this the data obtained by Curry and Reed (Ref. 10 and Fig. 78) are also in doubt. A discussion of this high-α support interference problem as it pertains to subscale testing of missiles and high performance aircraft is contained in Ref. 162.

3-3 NOSE-INDUCED ASYMMETRIC VORTICES

The importance of nose-induced asymmetric vortices has been brought out largely through the investigative efforts directed by Keener and Chapman (Refs. 27, 30, 32, 35, and 36). Not only are the side loads induced on noses alone of great magnitude, capable of exceeding the normal force (Ref. 30 and Fig. 6),

STRUT

$\alpha = 54$ deg

$\alpha' 0$
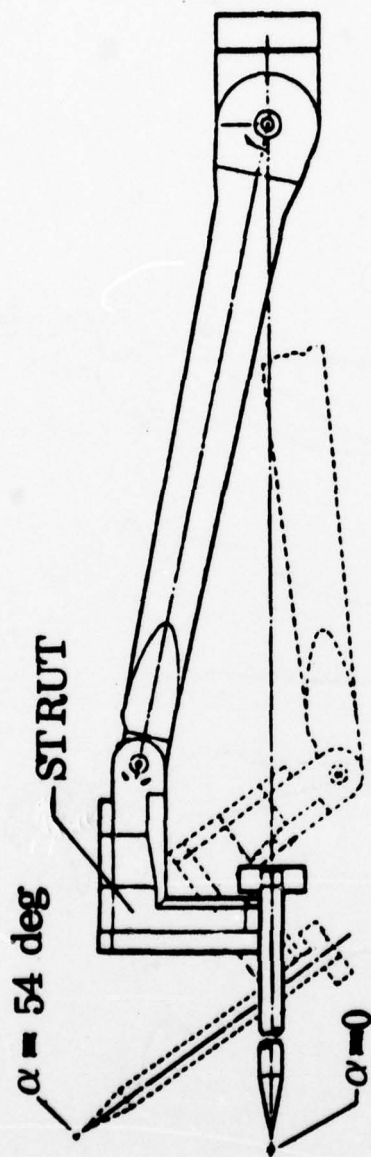
Fig. 75 Test Rig for High Angle of Attack Testing (Ref. 161)
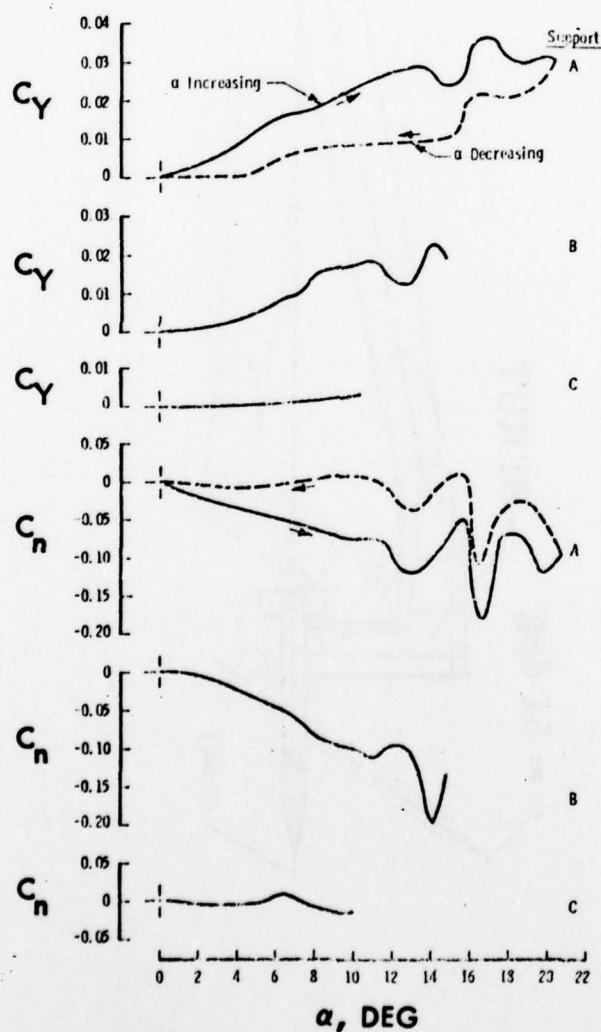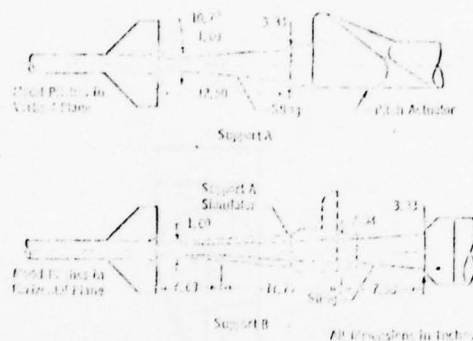
Fig. 76 Effect of Support Geometry on Measured Side Force and
Moment at $M_\infty = 5$ (Ref. 144)
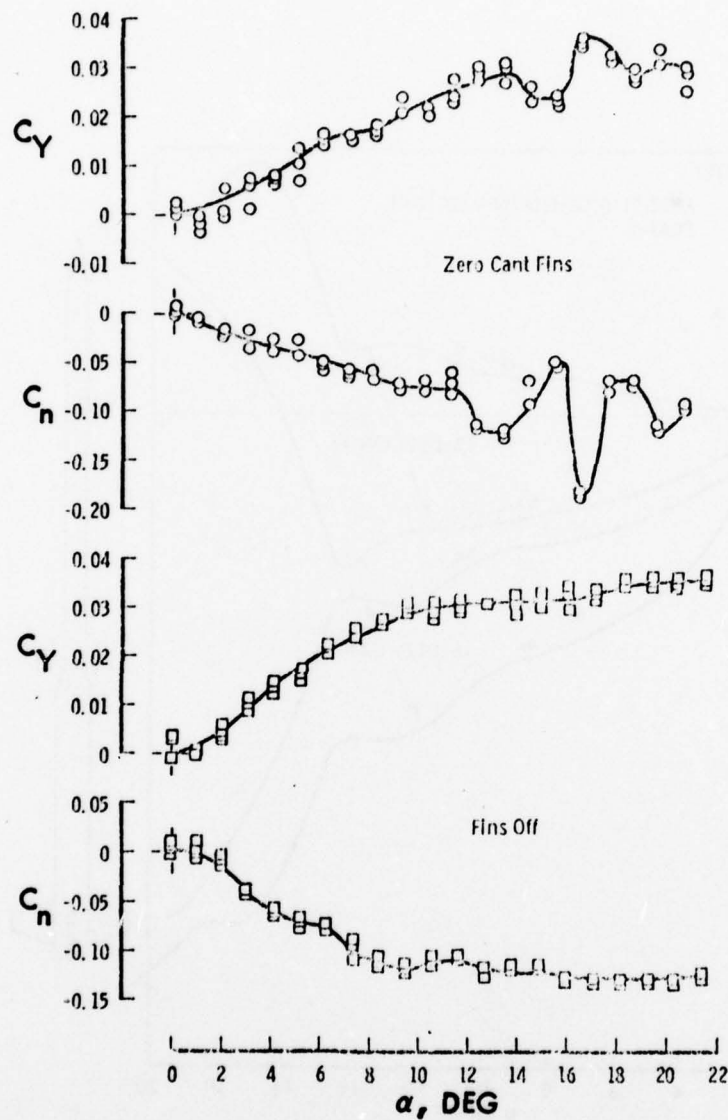
Fig. 77 Effect of Fins on Measured Side Force and Moment at $M_\infty = 5$ (Ref. 144)
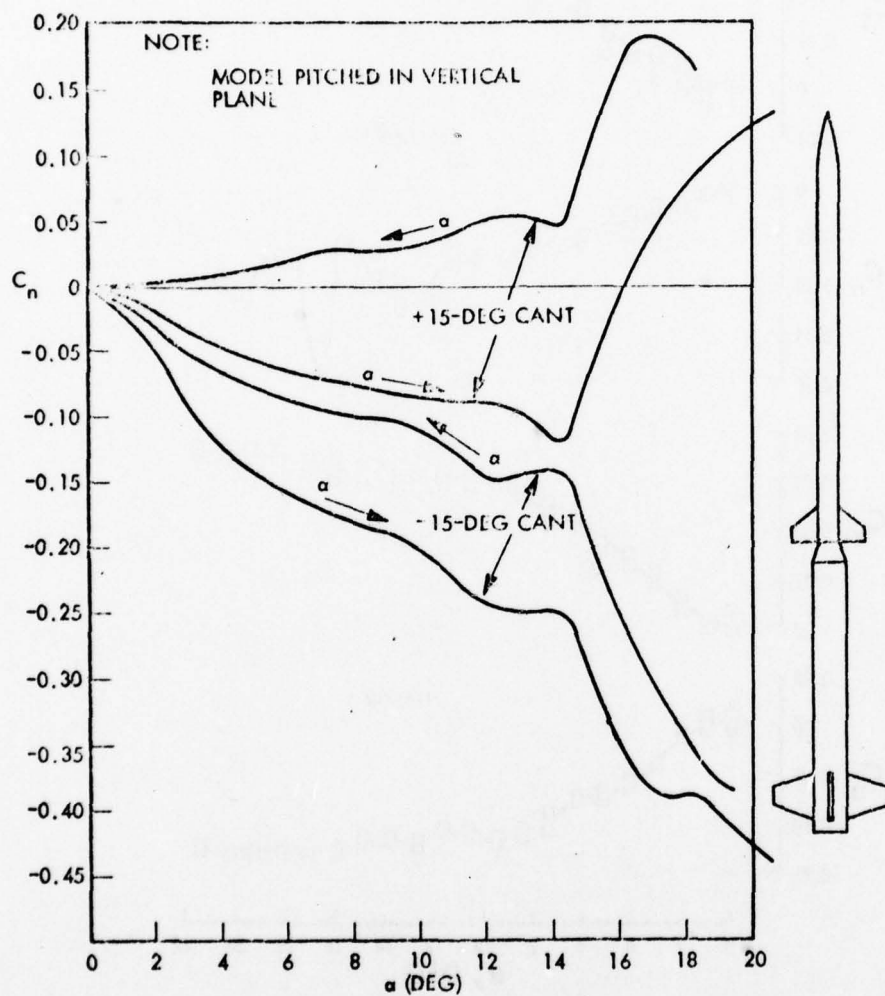
Fig. 78 Side Moment Measured on Tomahawk (Ref. 10)

but also on bodies with geometric features typical of many tactical missiles the nose-induced side load can often be the dominating load (Ref. 27 and Fig. 79). The results indicate that the asymmetric vortices on the aft body have no influence on the flow over the nose, but that they rather have to "line up" in the pattern set by the dominating asymmetric vortex pair generated by the nose, as is also demonstrated by the measured separation lines on a cone-cylinder (Ref. 163 and Fig. 80).[#] Vapor-screen photographs (Ref. 66 and Fig. 81) show the different vortex sizes associated with the difference in separation lines shown in Fig. 80). This nose-dominated vortex pattern is very different from that suggested for aft body asymmetric vortices (Ref. 45 and Fig. 82). According to the latter, the (local) generation of side force would be associated with a (local) lift loss. On the nose, however, the vortex asymmetry occurs because the separation moves from subcritical to supercritical on one side (Fig. 80). This will, of course, result in an increase of the vortex on this side (see earlier discussion in Section 3-1), and the generation of side force will be associated with lift gain, not lift loss. This is confirmed by experimental results for a tangent-ogive body (Ref. 26 and Fig. 83). The strakes eliminate the vortex asymmetry and, as a result, the normal force is decreased for $\alpha >$ α_{AV} (although the strakes increase the lift for $\alpha > \alpha_{AV}$).

It is interesting to compare the separation geometries in Fig. 80 for ogival and conical noses. Because $\alpha/\theta_A = 1.3$, and thus less than α_{AV}/θ_A (Fig. 5), the vortex asymmetry does not develop until on the aft body for the ogive-cylinder. For the cone-cylinder, on the other hand, $\alpha/\theta_A = 3.1 > \alpha_{AV}/\theta_A$, and the vortex asymmetry starts developing on the nose. When the angle-of-attack is increased ($\alpha \gg \alpha_{AV}$), appreciable asymmetry starts occurring also on the aft body (Ref. 12 and Fig. 84).

Thus, it is strongly indicated that the flow process leading to vortex asymmetry is radically differeent in the case of a pointed, slender nose from

---

[#]Further evidence of this is presented in Section 4-3. Compare the side load distribution on the nose-dominated sharp ogive-cylinder (Fig. 116) with that on the aft body dominated blunted ogive-cylinder (Figs. 104 and 105) for the same angle-of-attack, $\alpha = 50°$.
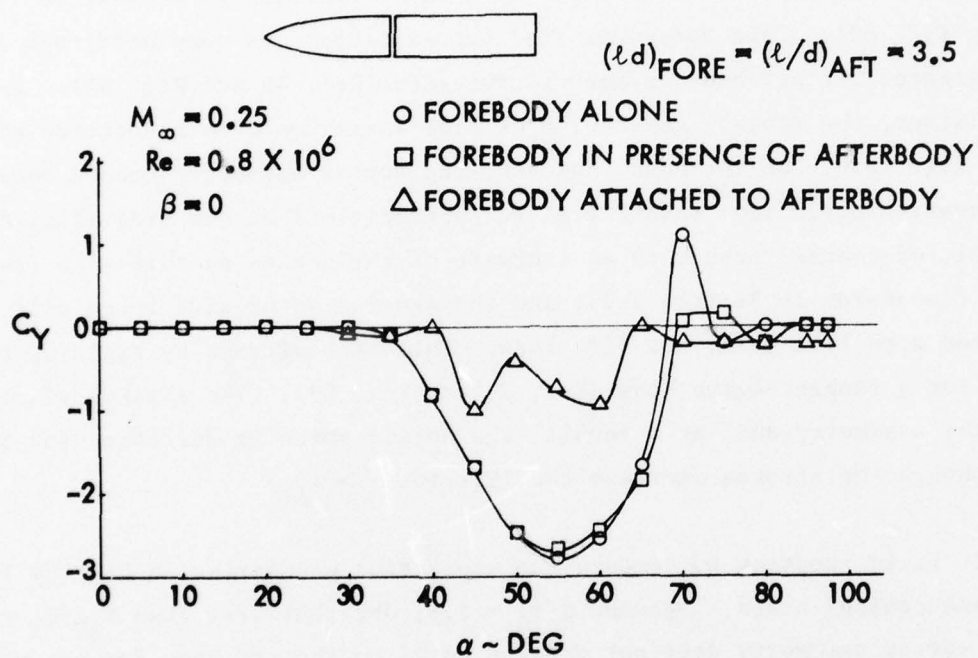
Fig. 79 Effect of Cylindrical Aftbody on Vortex-Induced Side
Force on an $\ell/d = 3.5$ Pointed Ogive (Ref. 27)
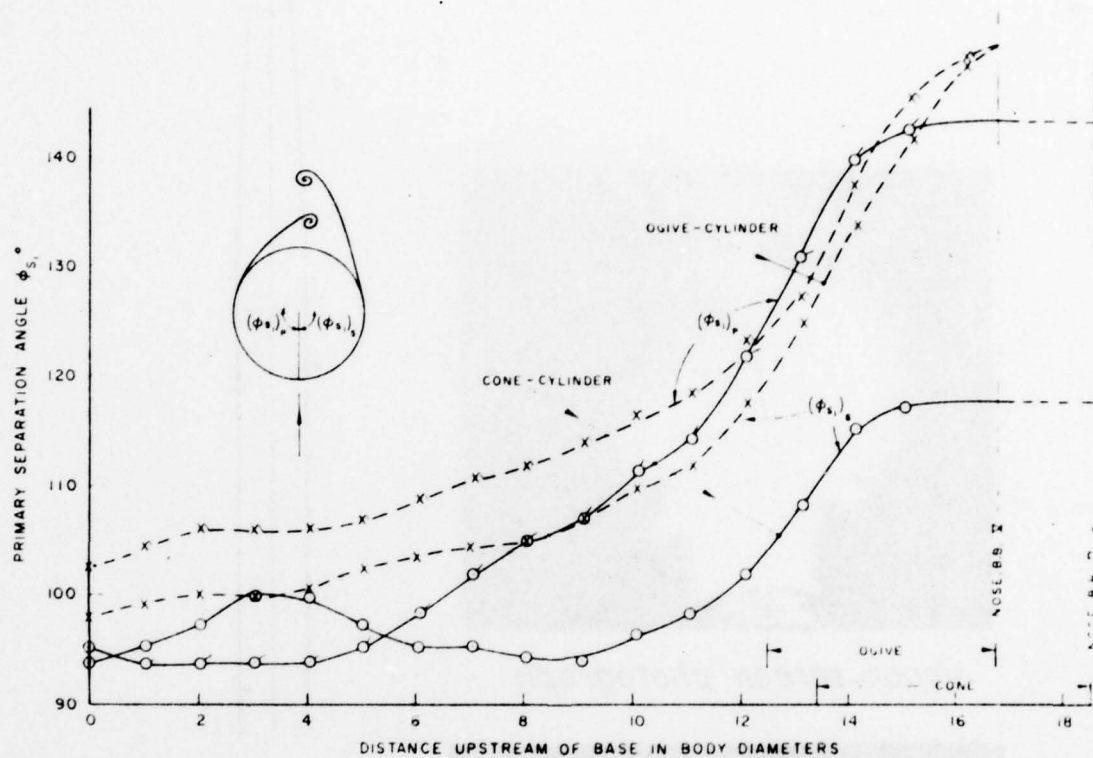
Fig. 80 Comparison of Asymmetric Primary Separation Lines on
Cone-Cylinder and Ogive-Cylinder at $M_\infty = 0.6$, $R_d = 1.9$
$\times 10^6$ (Ref. 163)

Vapor-screen photograph
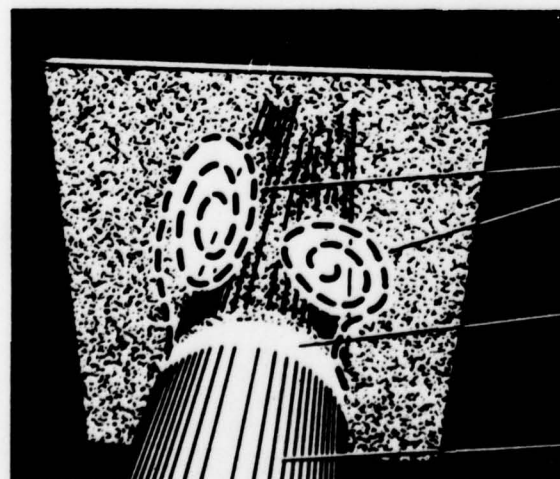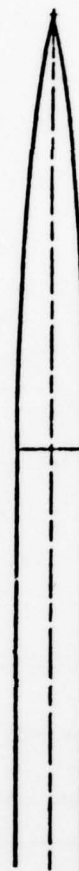
Light plane

Vortices

Intersection of
light plane
with body

Model

Fig. 81 Vapor-Screen Photographs of Nose-Induced Asymmetric
Vortices on Ogive-Cylinder at $M_\infty = 1.2$ (Ref. 66)
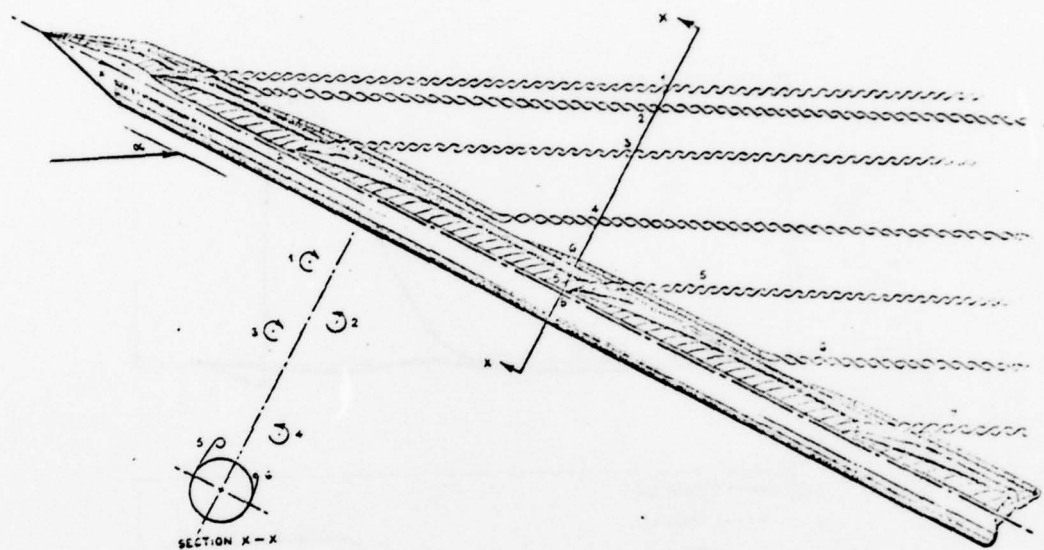
Fig. 82 Envisioned Vortex Array for Asymmetric Vortices Shed
from Cylindrical Aftbody (Ref. 45)
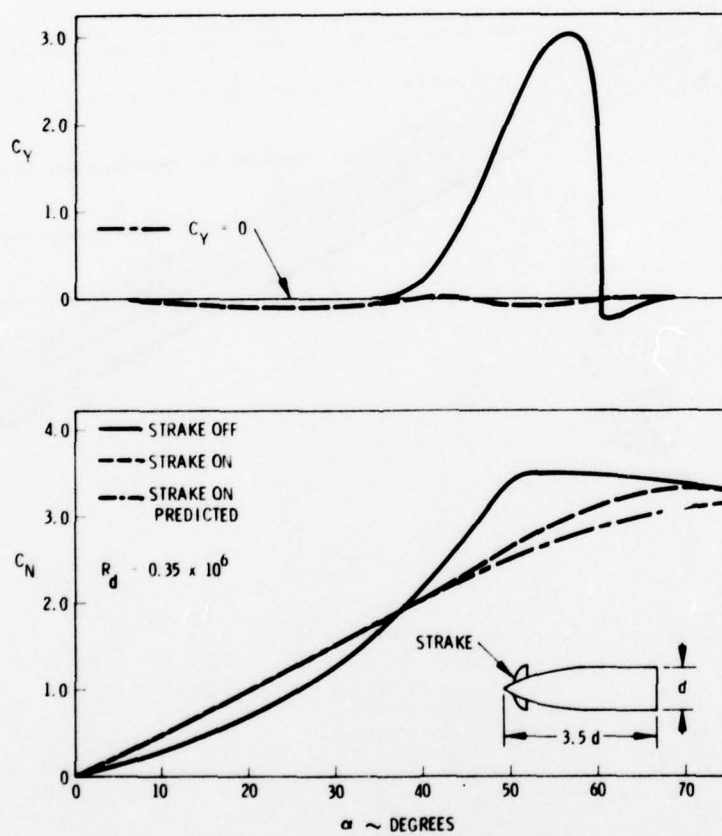
Fig. 83 Comparison of Symmetric and Asymmetric Vortex-Induced
Loads (Ref. 26)
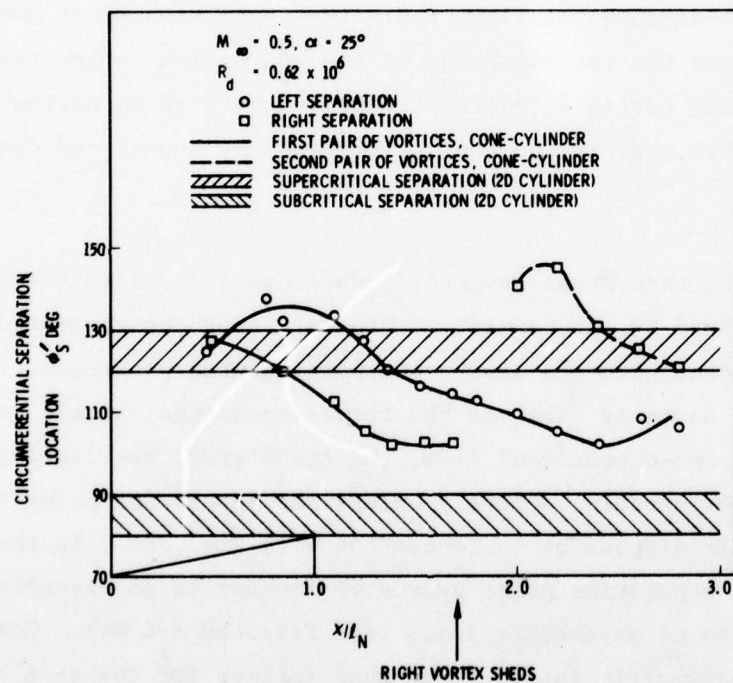
Fig. 84 Separation Geometry for Multi-Cell Asymmetric Vortex Shedding on Cone-Cylinder (Ref. 12)

what it is on the cylindrical aft body, the case which until now has received almost all attention, at least in theoretical investigations. It has been noted by Keener and Chapman (Ref. 164) that the α-boundaries for incipient asymmetric loads at zero sideslip are very similar for slender bodies (Ref. 27) and delta wings (Ref. 165) when plotted against the fineness ratio (Fig. 85). They suggest, therefore, that the vortex asymmetry in both cases is caused by a basic hydrodynamic instability that is very similar, resulting from the "crowding together" of the vortices. They further draw the conclusion that in that case the asymmetry in the separation points on a body of revolution would not necessarily be an essential feature of vortex asymmetry. This is, of course, in basic agreement with the conditions for the corresponding vortex asymmetry in two-dimensional flow, where the separation point movement is not a prerequisite for the establishment of the von Kármán vortex street (see Section 3-1). The tuft-grid pictures obtained by Bird on narrow delta wings (Ref. 166) tend to support the conclusion drawn by Keener and Chapman (see Fig. 86).

It is clear, then, that asymmetric vortices occur also when the separation point is fixed by the geometry. However, that the generated forces are very much dependent upon the separation point degree of freedom, both in the two-dimensional unsteady case and the three-dimensional steady case, is well documented. In two-dimensional flow, the translatory oscillations do not affect the vortex shedding strongly unless the separation point is free to move (see earlier discussion in connection with Fig. 39). In the three-dimensional case the separation point degree of freedom is an essential mechanism in the generation of asymmetric loads (see Figs. 80 and 84). One would expect the generated asymmetric forces to be much smaller for the case that the separation point was fixed by the geometry, in complete analogy with the subduing effect that a fixed separation point has on the two-dimensional response (Fig. 39).

A well-known vortex instability problem for delta wings is the vortex burst. In Fig. 87 the directional stability ($C_{\ell\beta}$) measured by Shanks (Ref. 165) is plotted in the normalized form derived in Ref. 167. Also shown is the

OGIVE CYLINDER BODIES, M=0.6

△ DELTA WINGS, LOW SPEED, SHANKS[16]

WINGS BODIES

.04 ⎡ 4

MAX |C_z| MAX |C_Y| β=0

.02   2

0   0

BODIES

WINGS   10°

WING SEMIAPEX ANGLE

20°   14°   12°

0   1   2   3   4   5
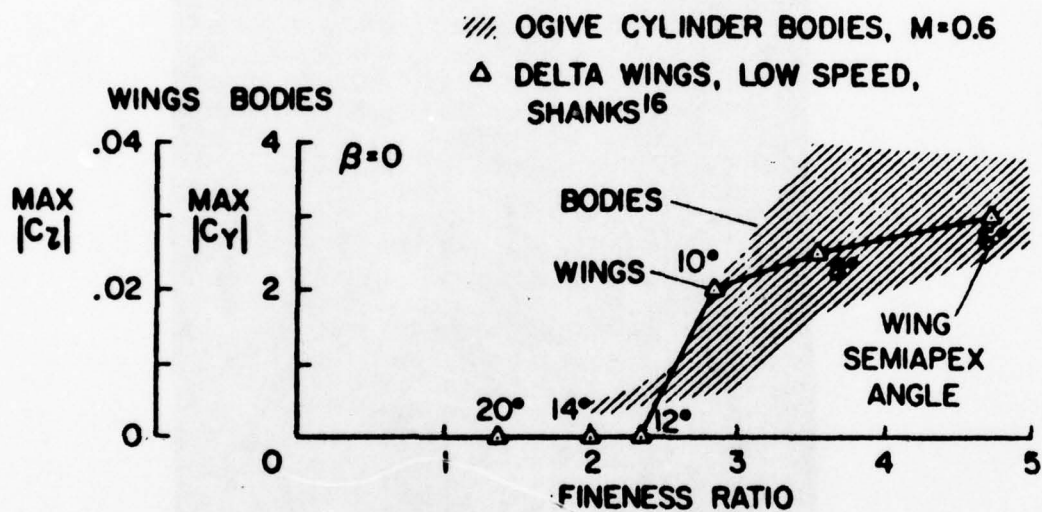
FINENESS RATIO

Fig. 85 Comparison of Effect of Fineness Ratio on Body and Wing
Asymmetric Vortex-Induced Loads (Ref. 27)
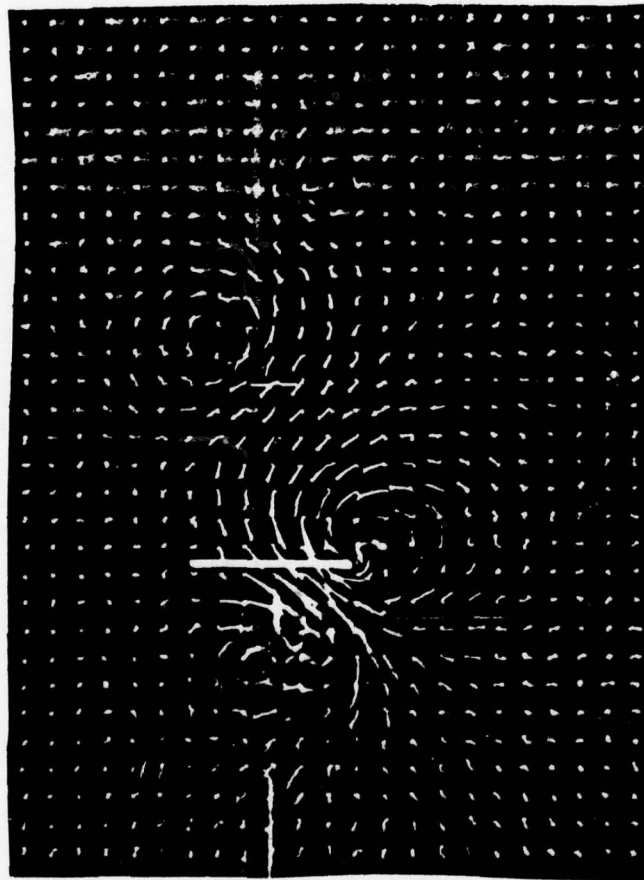
Fig. 86 Tuft-Grid Pictures of Asymmetric Vortex Shedding from a
Narrow Delta Wing ($\theta_A = 3.5°$) at $\alpha = 25°$ (Ref. 166)
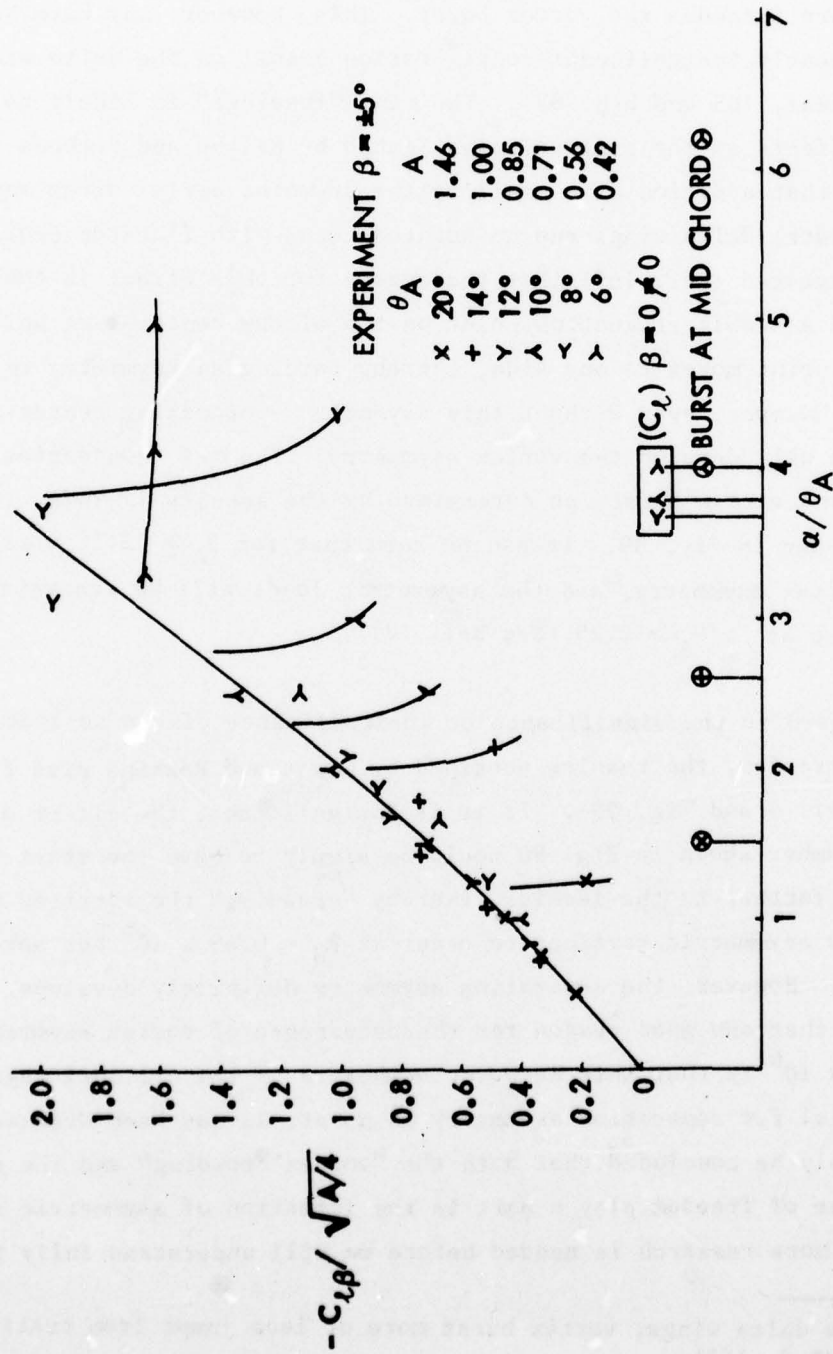
Fig. 87 Correlation of Directional Stability, Vortex Asymmetry and Vortex Burst for Slender Sharp-Edged Delta Wings

angle-of-attack at which significant rolling moment was measured at $\beta = 0$, indicating starting vortex asymmetry (Ref. 165), as well as the angle for which vortex burst occurs at midchord[#] (Ref. 168). It can be seen that a loss of directional stability precedes the occurrence of asymmetric vortices, which event in turn precedes the vortex burst. This, however, may have been influenced by an apparently insignificant configuration detail on the delta wings tested by Shanks (Ref. 165 and Fig. 88). The tiny "fuselage" is likely to have provided the same effects as the splines investigated by Maltby and Peckham (Ref. 4). They found that addition of a small spline promoted early vortex asymmetry both on (flat plate) delta wings and on pointed cones with flat-top cross-sections. We have suggested (Ref. 169) that the reason for this effect is that the flow cannot find a stable stagnation point on top of the center-line spline, but the stagnation point moves to one side, thereby forcing an asymmetry into the vortex geometry. However, even without this asymmetry - promoting center-spline narrow delta wings will develop the vortex asymmetry. The $\alpha - \theta_A$ boundaries for vortex asymmetry and vortex burst, as determined by the results in Refs. 166, 168, and 170, are shown in Fig. 89. It can be seen that for $\theta_A \geq 15.7°$ vortex burst will precede vortex asymmetry, and the asymmetric loads will be generated by asymmetric vortex burst at $\alpha/\theta_A > 2.25$ (see Ref. 171).

In regard to the significance or insignificance of the separation point degree of freedom, the results obtained by Gowen and Perkins give food for thought (Ref. 5 and Fig. 90). If it is insignificant, the effect of increasing Reynolds number shown in Fig. 90 would be simply to move the start of flow separation farther to the leeside, thereby "crowding" the vortices more, causing the asymmetric vortices to occur at $R_d = 0.69 \times 10^6$ but not at $R_d = 0.14 \times 10^6$. However, the separation asymmetry definitely develops. It appears, therefore, that one good reason for the occurrence of vortex asymmetry at $R_d = 0.69 \times 10^6$ is that this Reynolds number is in the critical regime, where the potential for separation asymmetry is great, as has been discussed earlier. It can safely be concluded that both the "vortex crowding" and the separation point degree of freedom play a part in the formation of asymmetric vortices. Obviously, more research is needed before we will understand fully the mechanism

---

[#]For narrow delta wings, vortex burst more or less jumps from trailing edge to midchord (Ref. 167).

1.53 R

2.91

.125
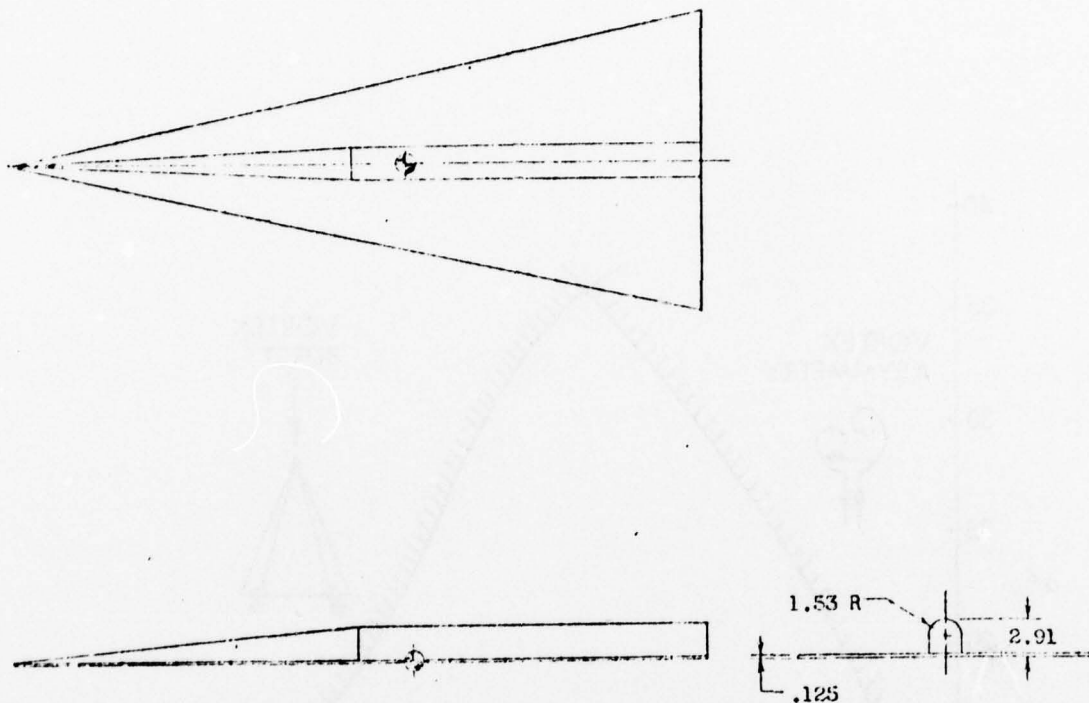
Fig. 88 Geometric Details of Delta Wing Producing Rolling Moment
at Zero Sideslip (Ref. 165)
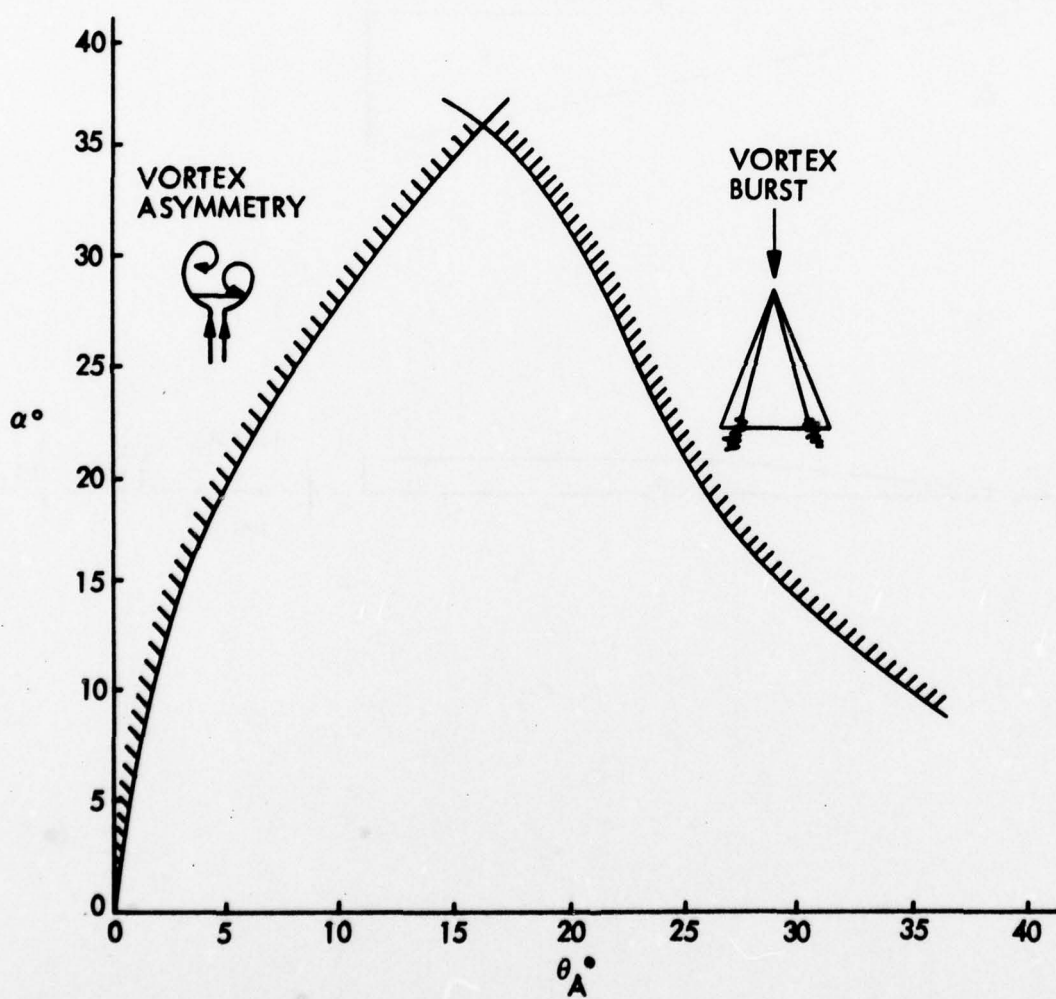
Fig. 89 Angles-of-Attack and Apex Angles Causing Vortex Asymmetry
and Vortex Burst on Delta Wings (Ref. 170)

(a) Re = 0.14 × 10⁶   (b) Re = 0.69 × 10⁶
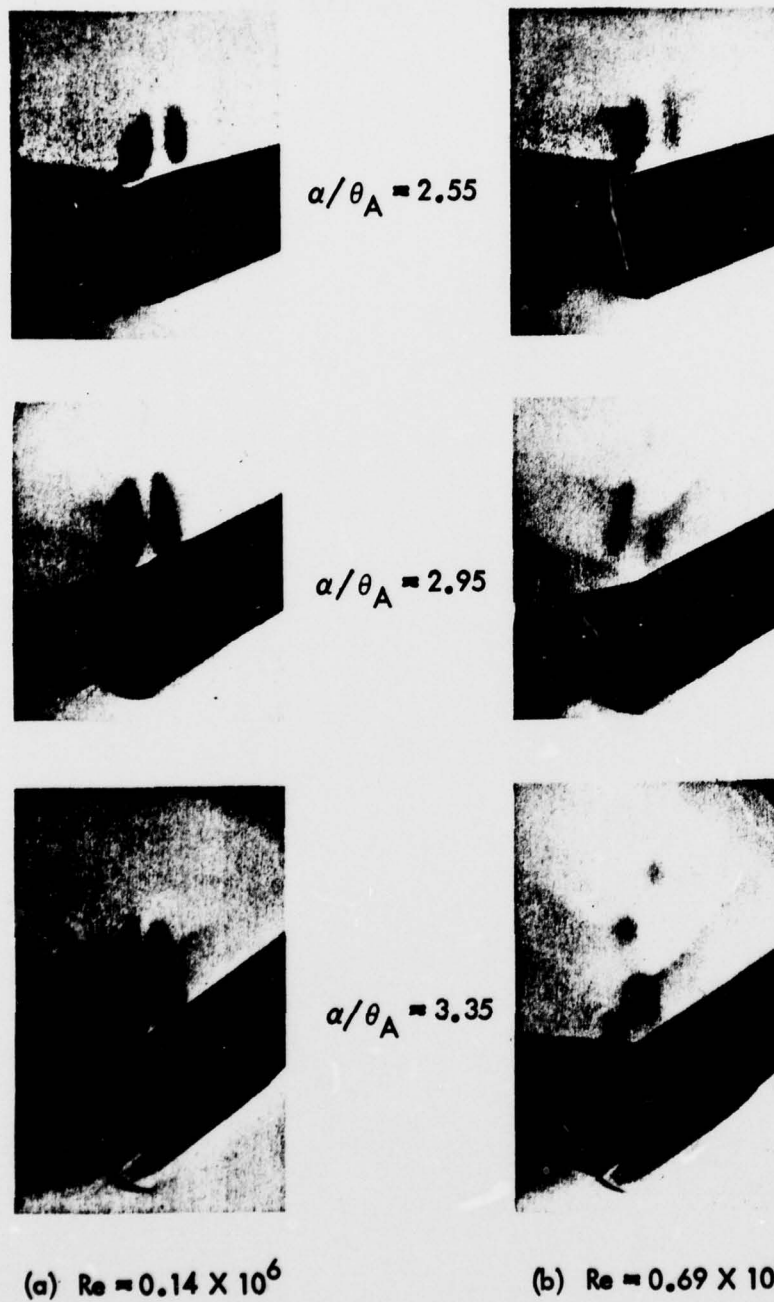
Fig. 90 Vapor-Screen Pictures Showing the Effect of Reynolds
Number on the Asymmetric Vortex Generation on a
Pointed-Ogive Nose (Ref. 5)

generating asymmetric vortices on slender, pointed forebodies. That this is
a problem that deserves attention is demonstrated by the data presentation
selected by Wardlaw and Morrison (Ref. 56 and Fig. 91).
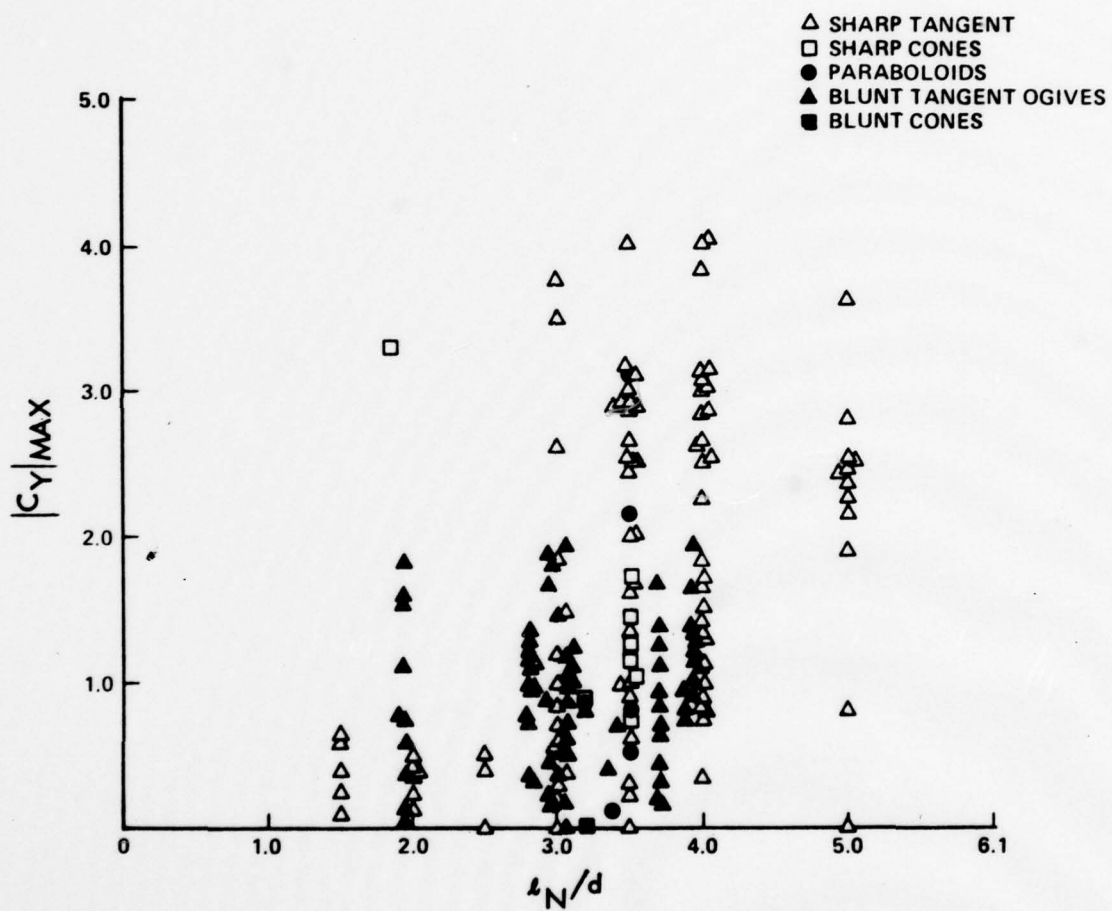
Fig. 91 Effect of Fineness Ratio on Nose-Induced Side Force
        (Ref. 56)

Section 4

ANALYSIS

All theoretical efforts to predict the vortex-induced asymmetric loads have until now been based upon inviscid flow modelling of the vortices generated for subcritical conditions on the cylindrical aftbody. In full scale flight the asymmetric loads of concern will occur at critical and supercritical flow conditions and will be produced by asymmetric vortices generated by a pointed, slender forebody. The evidence presented so far shows conclusively that boundary layer transition plays a dominant role in the generative process of the asymmetric vortices that cause the large side loads of special concern. In the analysis to be presented the dominating role played by boundary layer transition is recognized and analytic means are developed by which the upper limit for vortex-induced side loads can be predicted.

4-1 THEORETICAL DEVELOPMENT

The impulsively started cylinder flow analogy, first used by Allen and Perkins (Ref. 1), and described more recently by Sarpkaya (Ref. 172), who supplies detailed experimental data in support of his analysis, assumes that the crossflow plane is swept down the length of the body at the uniform rate $U_\infty \cos \alpha$. Thus, the developing flow in the crossflow plane is analogous to a two-dimensional cylinder in impulsively started flow with velocity $U_\infty \sin \alpha$. That is, the downstream distance from the start of the inclined cylinder is $x = U_\infty t \cos \alpha$. Sarpkaya's data (Ref. 172) indicate that for incompressible, subcritical flow ($Re < 1.2 \times 10^5$) the wake asymmetry first develops at $Ut/d = 4$, where $U = U_\infty \sin \alpha$ for the inclined cylinder. Thus, the angle-of-attack (α_{AV}) for incipient asymmetric vortex shedding, starting at the base ($x = \ell$), is

$$\alpha_{AV} = \tan^{-1}(4/\frac{\ell}{d}) \tag{4-1}$$

Sarpkaya's data also show that the first large vortex is shed at $Ut/d = 8.5$. This gives

$$\alpha_{peak} = \tan^{-1}(8.5/\tfrac{\ell}{d}) \qquad (4-2)$$

According to Wardlaw and Morrison (Ref. 53) these formulas can be applied to bodies with nonconstant cross section by substituting d by $\bar{d} = \int_0^1 d\, d(\tfrac{x}{\ell})$. For the sharp cone Eqs. (4-1) and (4-2) then give[#]

$$\alpha_{AV} = \tan^{-1}(4 \tan \theta_c) \approx 4\,\theta_c$$

and

$$\alpha_{peak} = \tan^{-1}(8.5 \tan \theta_c) \approx 8.5\,\theta_c$$

As we have seen (Fig. 5) experimental incompressible results define $\alpha_{AV} \approx 2\,\theta_c$ and show that $\alpha_{peak} = \alpha_{AV}$ for pointed noses (Fig. 46) even in presence of a cylindrical aftbody (Fig. 53).

Following a suggestion by Morkovin, Thomson and Morrison (Refs. 43 and 45) applied the time-space equivalence between the von Karman unsteady, asymmetric vortex wake in two-dimensional flow and the steady, asymmetric vortex array in three-dimensional flow (see Fig. 45). The period of the von Karman wake in the cross flow plane is

$$T = \frac{1}{f} = \frac{d}{S_{vo}U_\infty \sin\alpha} \qquad (4-3)$$

The geometry in Fig. 45 gives

$$T = \frac{1}{f} = \frac{2g}{U_\infty \cos\alpha} \qquad (4-4)$$

That is, the steady asymmetric vortex geometry in Fig. 45 is defined by Eqs. (4-3) and (4-4) as

$$g/d = (2\,S_{vo}\,\tan\alpha)^{-1} \qquad (4-5)$$

[#] If $\bar{d} = d$ were used, one would obtain $\alpha_{AV} \approx 2\,\theta_c$ in agreement with experiment. However, for pointed ogives with $\theta_A = 2\,\theta_c$ for the same ℓ/d one would still obtain $\alpha_{AV} \simeq 4\,\theta_A$ contrary to the experimental results $\alpha_{AV} \approx 2\,\theta_A$ (Refs. 27 and 32).

Using von Kàrmàn's vortex street theory (Ref. 71) the strength (Γ) of the shed vortices are given by (see Fig. 7)

$$\overline{U}_v/U_\infty = \frac{1}{2} \ (\Gamma/U \ d) \ (d/L) \ \tanh \ (\pi \ h/L) \qquad (4\text{-}6)$$

The geometry in Fig. 45 gives

$$\tan \xi = U \ (1 - \overline{U}_v/U)/U_\infty \ \cos \alpha \qquad (4\text{-}7)$$

and with $U = U_\infty \sin \alpha$ Eq. (4-7) gives

$$\left.\begin{aligned} \overline{U}_v/U &= 1 - \chi \\[2mm] \chi &= \tan \xi \ / \tan \alpha \end{aligned}\right\} \qquad (4\text{-}8)$$

The wake geometry in Fig. 45 gives

$$g/L = (2 \tan \xi)^{-1} \qquad (4\text{-}9)$$

Combining Eqs. (4-5) and (4-9) one obtains

$$\frac{d}{L} = \frac{S_{vo} \tan \alpha}{\tan \xi} = S_{vo} \ \chi^{-1} \qquad (4\text{-}10)$$

Eqs. (4-6), (4-8) and (4-10) together define the vortex strength

$$\Gamma /Ud = \Gamma /U_\infty \ d \ \sin \alpha$$

$$= \left[2 \ \chi \ (1 - \chi)/S_{vo} \right] \coth(\pi \ h/L) \qquad (4\text{-}11)$$

With χ measured from flow photographs, S_{vo} known from experiments (Fig. 10), and $h/L = 0.28$ according to von Kàrmàn's stability criterion (Ref. 71), the vortex strength (Γ) can be determined by Eq. (4-11). From their experiments Thomson and Morrison (Ref. 43 and 45) found that χ varied very little over the Mach number range $0 < M_\infty < 1.8$ (Fig. 92). Knowing the strength and position of the vortices there would seem to be no problem deriving the vortex-induced loads using any of the many available theoretical treatments (Refs. 44, 47, 49, 51, 172-175). In trying to apply Sarpkaya's method (Ref. 172) Thomson and Morrison found, however, that they did not know the vortex feeding sheets with the needed accuracy. This is the case with most vortex methods, which usually have to depend upon experiments for those details. Thomson and Morrison did not find any completely satisfactory method, as is demonstrated by the results in Fig. 93.
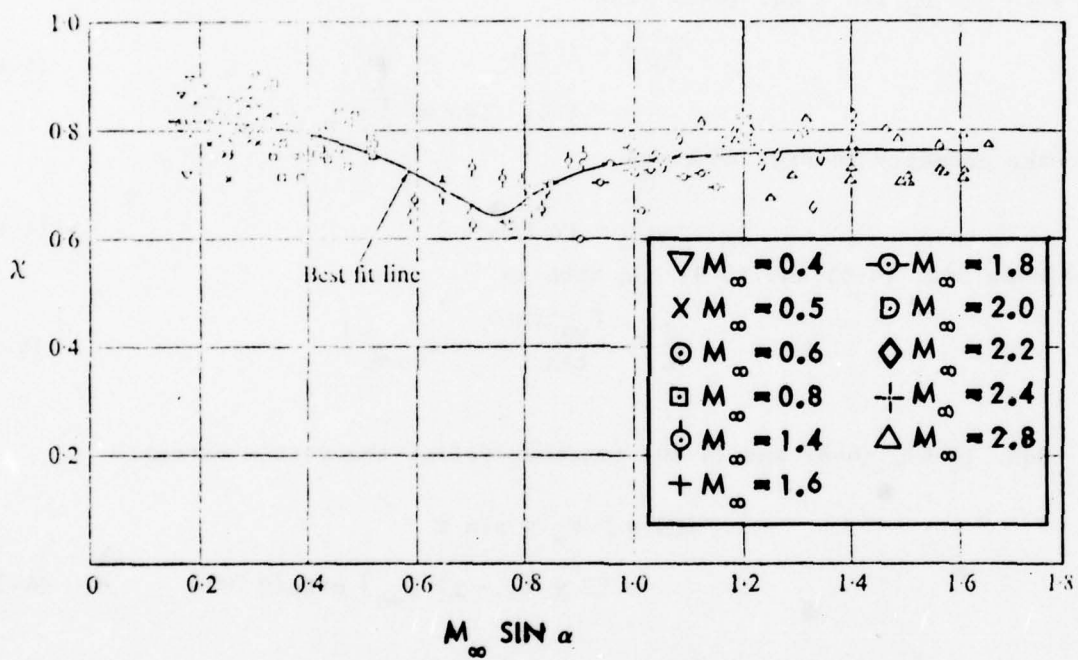
Fig. 92 Variation of Vortex Parameter χ with Crossflow Mach Number (Ref. 43)

The method designated a) assumes that once a vortex has been shed it ceases to have any influence on the body, while method b) assumes that all vortices appearing in the cross-section (see Fig. 82) influence the body.

Atraghji (Ref. 52) modified the Thomson-Morrison method (Refs. 43 and 45) by allowing the diameter (d) and wavelength (L) to vary with distance (x) along the body while keeping the ratio d/L constant. This d/L ratio is found by trial and error in matching the experimental data. Fig. 94 shows that even then it is not possible to match the experimental data.

The results shown in Figs. 93 and 94 are rather typical for the mismatch existing between present theory (Refs. 43-54) and experimental results (Refs. 24-42). The figures indicate where the problem lies, i.e., in neglecting the dominating influence that a pointed, slender nose has. The nose-induced asymmetric vortices do not start until $\alpha > 2 \theta_A$, whereas the theory predicts them to start much earlier (see Figs. 93 and 94).

In the present analysis two-dimensional unsteady characteristics for a circular cylinder are used to define upper limits for the static loads that can be induced by asymmetric vortices in three-dimensional flow. A critical link in this development is to be able to account correctly for the effect of sweep on the infinite cylinder characteristics.
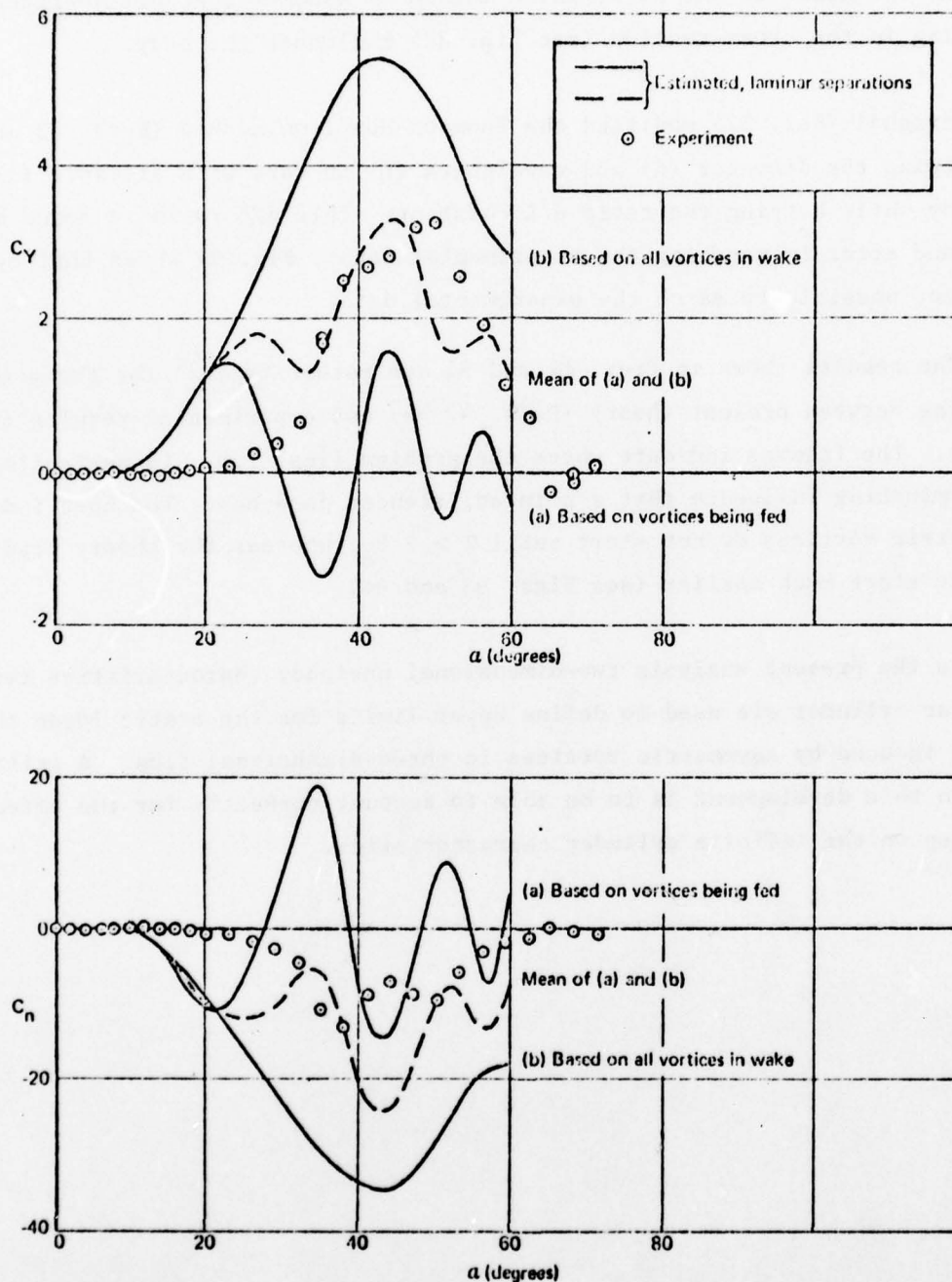
Fig. 93 Comparison Between Predicted and Experimental Vortex-Induced
Side Loads on a 10 Calibers Long 15° Cone-Cylinder at
$M_\infty = 0.5$ and $R_d \approx 0.09 \times 10^6$ (Ref. 45)
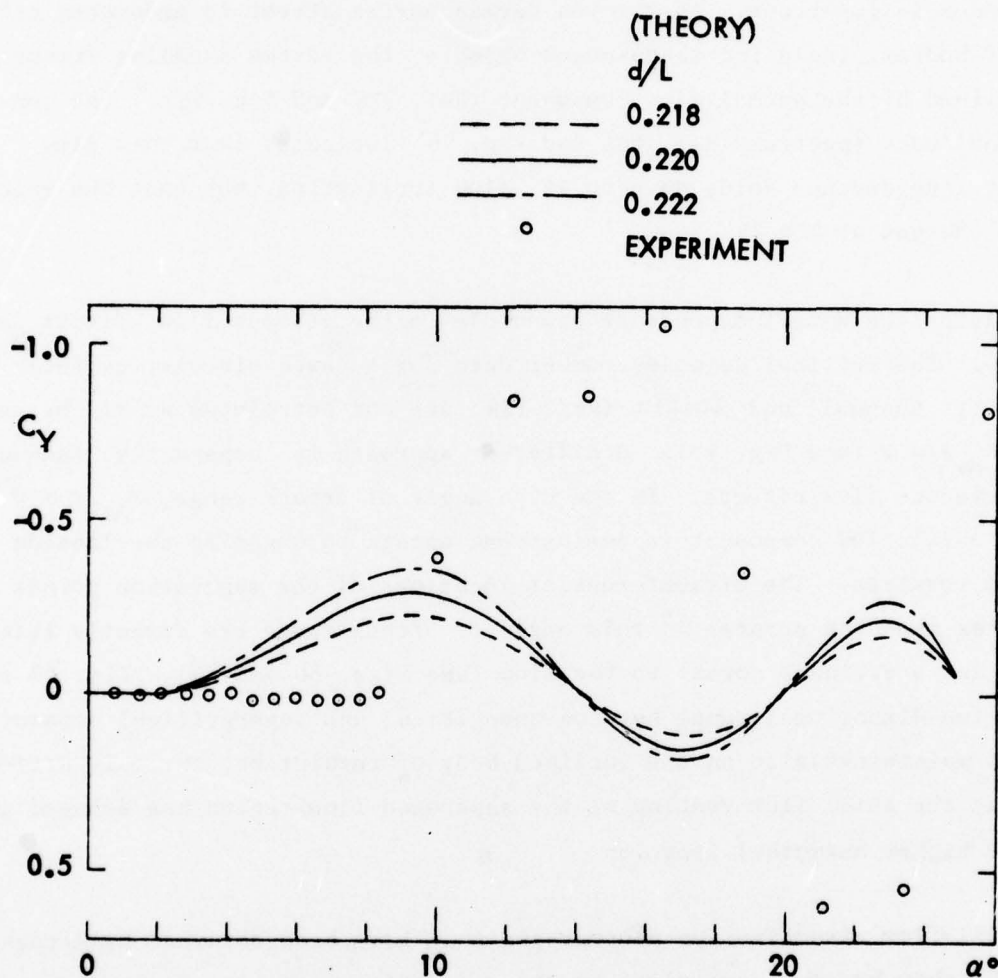
Fig. 94 Comparison Between Predicted and Experimental Side Force on
a 17 Calibers Long 3.7° Cone-Cylinder at $M_\infty = 0.5$ and
$R_d \approx 1.4 \times 10^6$ (Ref. 52)

4-2 EFFECT OF SWEEP

For the inviscid flow characteristics only the flow component normal to the cylinder is important. As the von Karman vortex street is generated behind all bluff bodies, including sharp-edged objects, the vortex shedding frequency is determined by the normal flow component (Ref. 176 and Fig. 95).[#] The non-dimensional wake spectrum (Ref. 177 and Fig. 96) indicates that this flow component independence holds down to $42°$ flow inclination, but that the spectrum has changed at $\alpha = 35°$.

Applying the same independence principle to the viscous flow effects fails miserably. The critical Reynolds number data for a yawed circular cylinder obtained by Bushnall and Loftin (Ref. 178) are not correlated at all by use of $R_n = R_d \sin \alpha$ (see Fig. 97). A different approach is apparently needed for the viscous flow effects. In the high angle of attack range, $\alpha_{AV} < \alpha < \alpha_{UV}$, the axial flow component is just strong enough to organize the leeside wake into vortices. The circumferential locations of the separation points (the vortex shedding points) in this angle of attack range are directly related to those for a cylinder normal to the flow (see Figs. 80 and 84). Fig. 84 shows that the two-dimensional range between subcritical and supercritical separation points is maintained also on the inclined body of revolution, the only difference being that the axial flow venting of the separated flow region has delayed separation to a higher azimuthal location.

The oil flow visualization photographs that have been obtained by Atraghji (Ref. 179) show how the streamline to the separation point is elevated above the freestream flow through an angle $(\sigma - \alpha)$ due to the acceleration of the cross-flow component around the body (Fig. 98). The condition of the boundary layer at the location of flow separation is determined by the viscous flow following this path. Aside from the initial "transient" the streamline is contained in the intersection between the cylinder and a plane at angle σ relative to the cylinder axis. The boundary layer edge conditions are determined by the inviscid flow streamline. For incompressible flow potential theory gives $\sigma = \tan^{-1}(2 \tan \alpha)$.

[#] The sweep angle is $\beta = 90° - \alpha$.
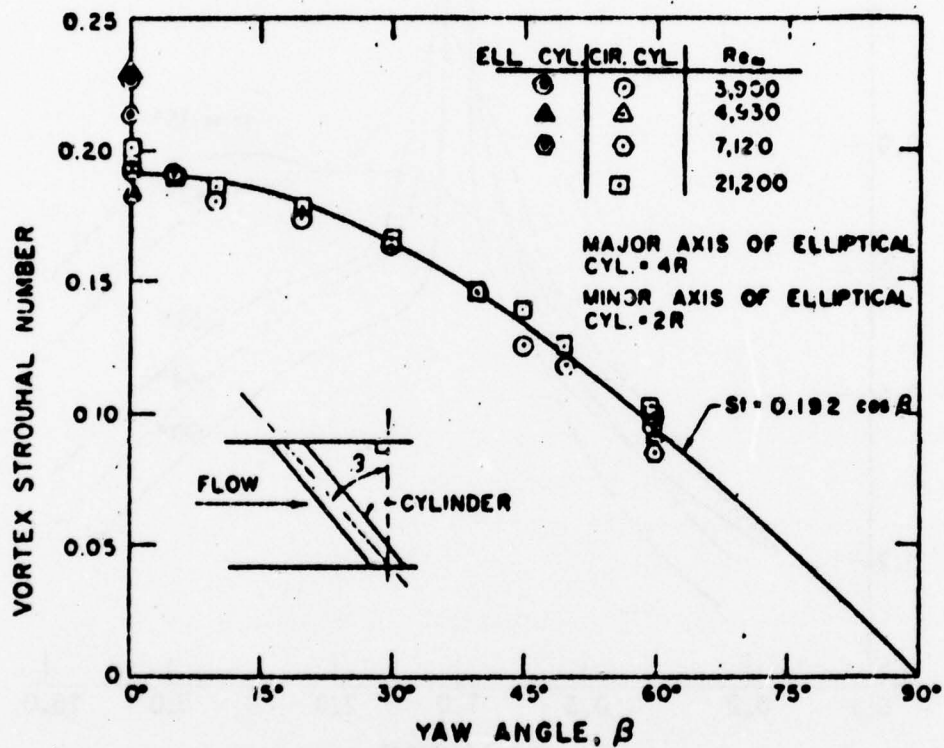
Fig. 95 Effect of Flow Inclination on Infinite Cylinder Shedding Frequency (Ref. 176)
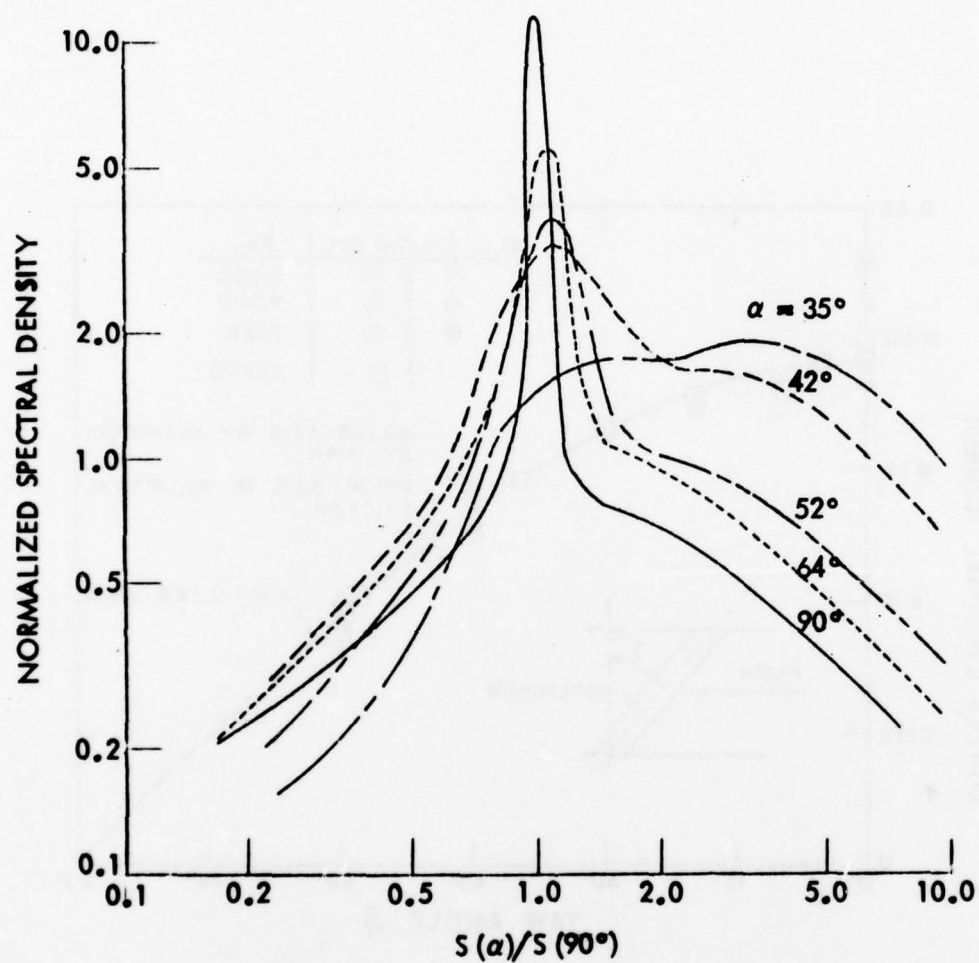
Fig. 96 Non-Dimensional Wake Spectra for Infinite Cylinder at Flow
Inclinations from 35 to 90° (Ref. 177)
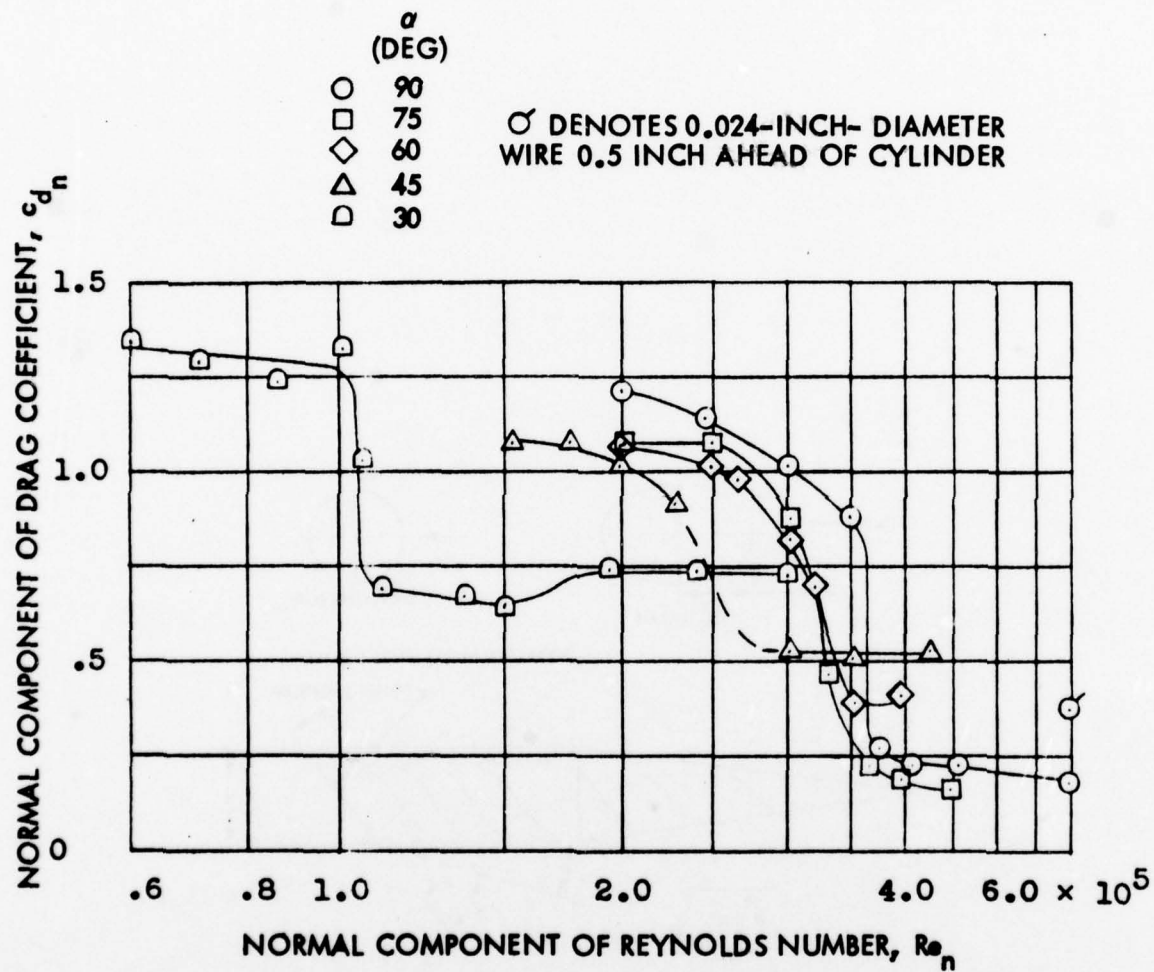
Fig. 97 Variation of Infinite Cylinder Drag with Crossflow Reynolds
Number for Various Flow Inclinations (Ref. 178)
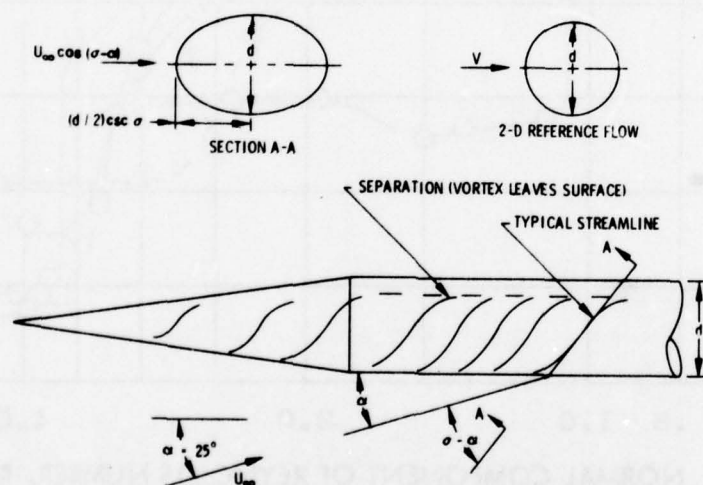
Fig. 98 Typical Streamline Trajectories

In subcritical flow the wetted length to separation is the quarter periphery of the elliptic cross-section in the σ-plane. For $\alpha > 30°$ the ellipse has an axis ratio that is less than 2 and we can approximate the wetted length as follows

$$\ell_{wet} = \frac{\pi d}{8} \ (1 + \mathrm{cosec} \ \sigma) \tag{4-12}$$

The corresponding Reynolds number is $R_{wet} = U_\infty \cos (\sigma - \alpha) \ \ell_{wet} / \nu_\infty$, i.e.,

$$R'_{wet} = \frac{U_\infty d}{\nu_\infty} \ \frac{\pi}{8} \ \frac{\cos \alpha \cot \alpha + 2 \sin \alpha}{2} \ \frac{1 + [1 + (\frac{1}{2} \cot \alpha)^2]^{\frac{1}{2}}}{[1 + (\frac{1}{2} \cot \alpha)^2]^{\frac{1}{2}}} \tag{4-13}$$

and the effect of flow inclination on the Reynolds number at the separation point is

$$\left[\frac{R(\alpha)}{R(90°)}\right]_{wet} = \frac{\cos \alpha \cot \alpha + 2 \sin \alpha}{2} \ \frac{1 + [1 + (\frac{1}{2} \cot \alpha)^2]^{\frac{1}{2}}}{[1 + (\frac{1}{2} \cot \alpha)^2]^{\frac{1}{2}}} \tag{4-14}$$

Eq. (4-14) can be used to relate the effective Reynolds number to the Reynolds number based upon diameter and freestream conditions, R_{eff}/R_d. The results are shown in Fig. 99. According to Ref. 180 the axial flow component can have an important effect on the boundary layer transition for $\alpha \leq 30°$. Thus, where the simplified two-dimensional analogy in Fig. 98 applies, i.e., for $\alpha > 30°$, one can according to Fig. 99 use the following approximation without causing more than 10% error

$$R_{eff} \approx R_d \tag{4-15}$$

Plotting the Bursnall-Loftin data (Ref. 178) against this effective Reynolds number, Eq. (4-14) gives the results shown in Fig. 100. It can be seen that with the exception of the borderline case, $\alpha = 30°$, the correlation is excellent in regard to the definition of the critical Reynolds number. The same conclusion has been reached by Clark (Ref. 37) who tried to correlate his crossflow drag using the different analytic models available: 1) The standard approach based upon the independence principle, i.e., $R_{eff} = R_d \sin \alpha$ (Fig. 101a). 2) The model suggested by Lamont and Hunt (Ref. 33), i.e., $R_{eff} = R_d/\sin \alpha$ (Fig. 101b). 3) The present model, Eq. (4-14), in the small angle approximation, $\sigma = 2\alpha$, presented
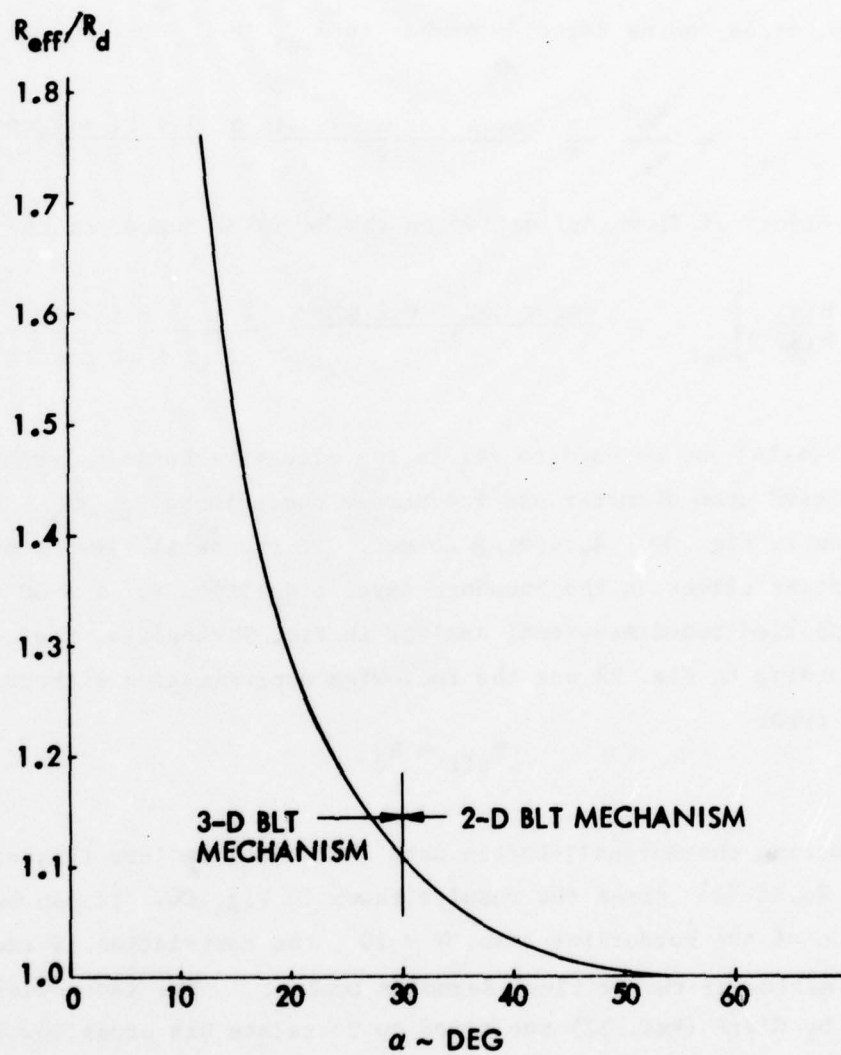
Fig. 99 Effective Reynolds Number Variation with Angle-of-Attack

earlier (Ref. 181), i.e., $R_{eff} = R_d / \sin 2\alpha$ (Fig. 101c). Fig. 101d, finally, shows that the correlation is improved further when using Eq. (4-14) without the small angle approximation. Following Wardlaw and Morrison (Ref. 53) for bodies with changing cross-sectional dimensions we define a mean diameter $\bar{d}$, based upon the projected planform area (see Nomenclature).

The crossflow drag in Ref. 178 and Fig. 97 was non-dimensionalized by use of $q_\infty \sin^2 \alpha$, in agreement with the independence principle for inviscid flow. Figs. 97 and 100 indicate that this works fine for the subcritical drag but not at all for the supercritical case. Hoerner (Ref. 182) shows that for an elliptic cross-section with axis ratio t/c the drag can be expressed as follows

$$
\left.
\begin{array}{l}
c_{de} = 2 \, (c_f)_{lam} \, (1 + c/t) + 1.1 \, t/c : Re < Re_{crit} \\[2ex]
c_{de} = (c_f)_{turb} \left[4 + 2 \, (c/t) + 120 \, (t/c)^2 \right] : Re > Re_{crit}
\end{array}
\right\} \qquad (4\text{-}16)
$$

where $(c_f)_{lam} = 1.328 \, Re^{-\frac{1}{2}} : (c_f)_{turb} = (3.46 \log Re - 5.6)^{-2}$

For our type of elliptic cross-sections, Fig. 98, where c/t > 0.5, the subcritical drag in Eq. (4-16) is dominated by the pressure drag component, 1.1 t/c, which in turn is determined largely by the inviscid flow. Consequently, the independence principle can be expected to work, which is in agreement with the results in Fig.100 (and Fig. 97). Eq. (4-16) shows that for the supercritical flow condition the drag is completely correlated by use of the turbulent skin friction $(c_f)_{turb}$. This indicates that the viscous flow conditions control the drag. Consequently, the normalizing dynamic pressure should be $q_\infty \cos^2 (\sigma - \alpha)$ according to Fig. 98, and the crossflow drag should be normalized as

$$
(c_{nc})_{eff} / (c_{nc})_\infty =
\begin{cases}
\csc^2 \alpha : Re < Re_{crit} \\[2ex]
\sec^2 (\sigma - \alpha) : Re > Re_{crit}
\end{cases}
\qquad (4\text{-}17)
$$

Fig.102 shows that Eq. (4-17) provides a satisfactory correlation of the sweep effect, considering the experimental data scatter (Ref. 178). The normalizing of the Bursnall-Loftin supercritical drag data (Ref. 62) attempted by Bootle (Ref. 183) gives as a result that the cross flow drag normalized with
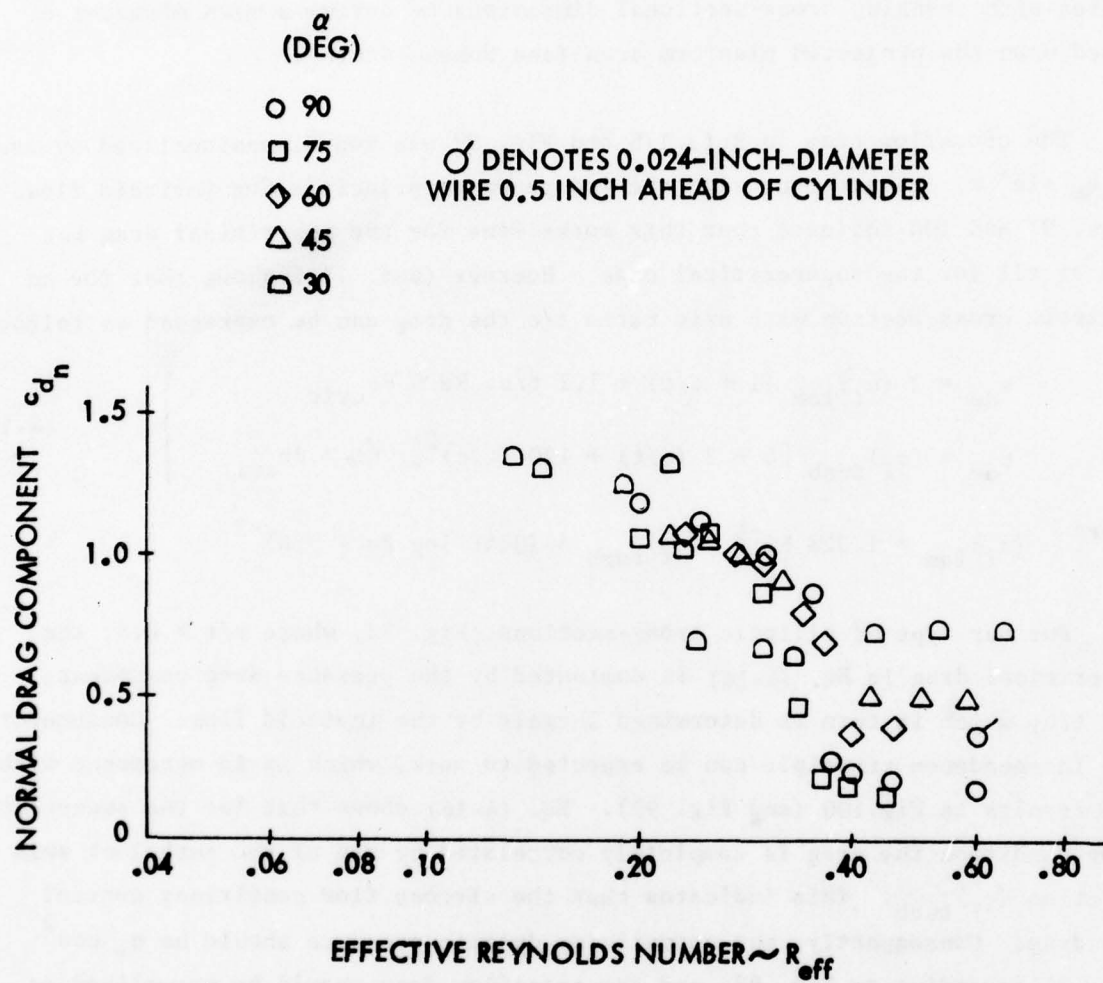
Fig. 100 Variation of Infinite Cylinder Drag with Effective Reynolds
Number for Various Flow Inclinations
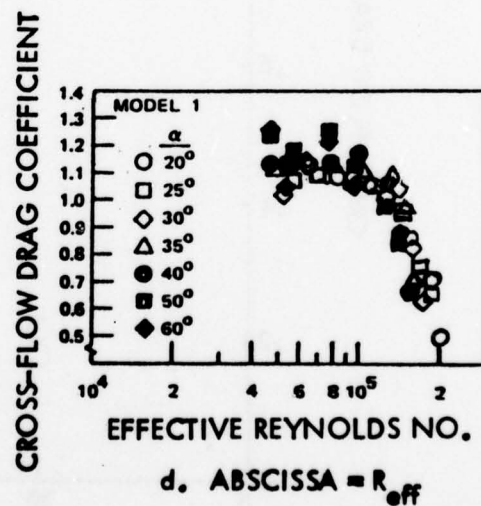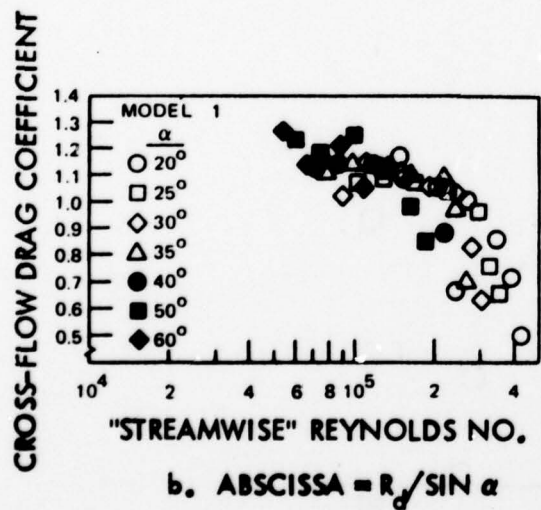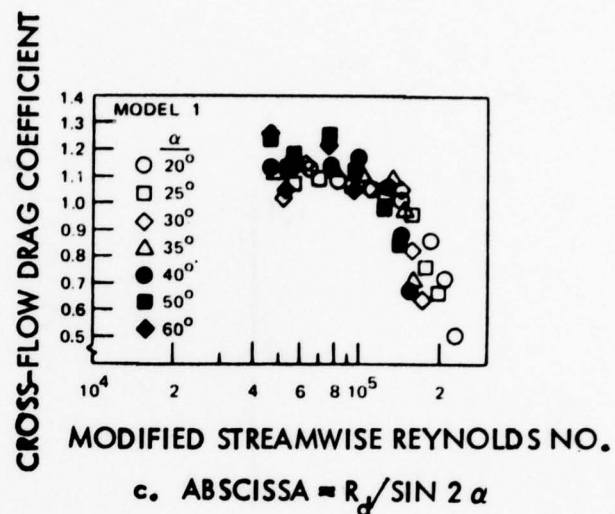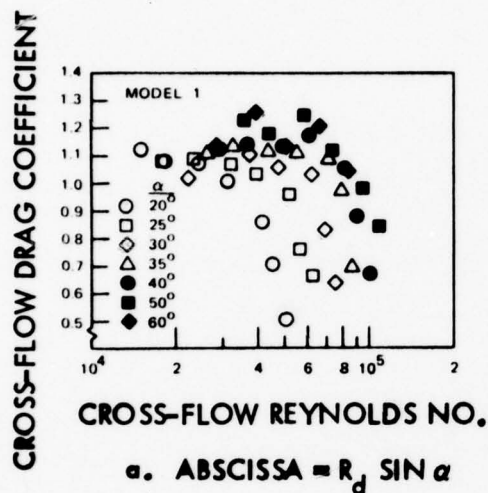
Fig. 101 Crossflow Drag Correlation with Reynolds Number Defined in Various Manners (Ref. 37)
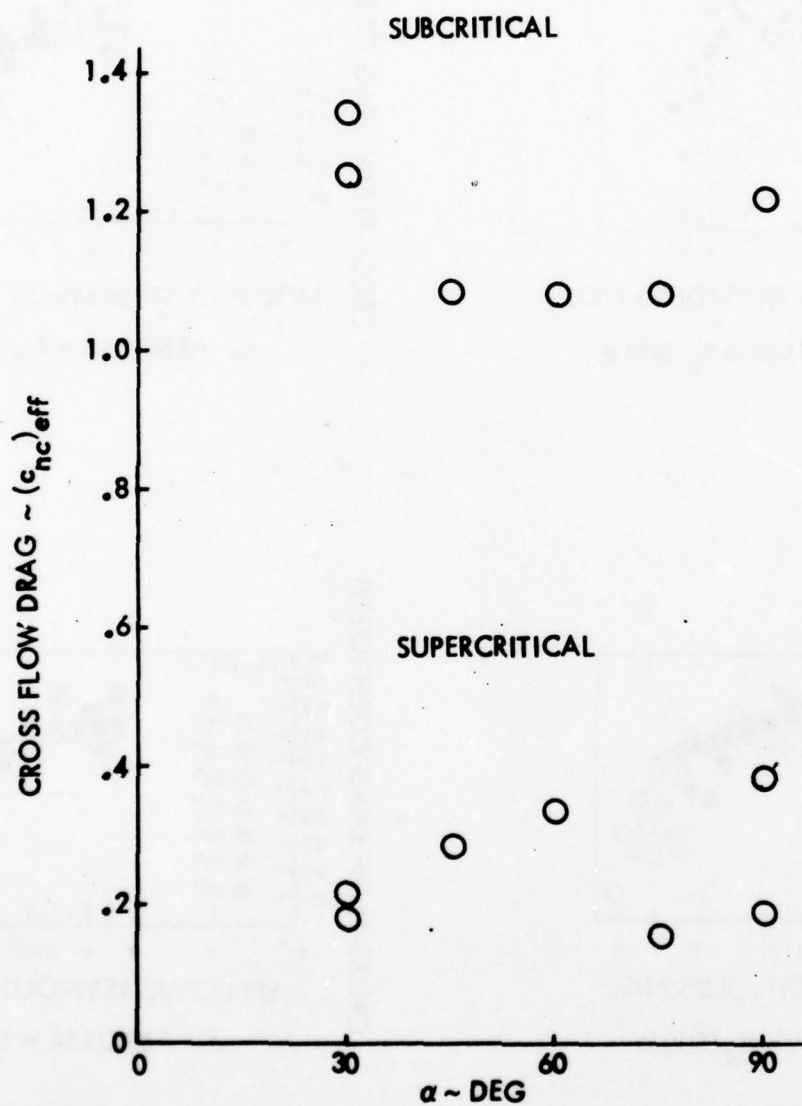
Fig. 102 Effective Crossflow Drag at Subcritical and Supercritical
Reynolds Number

$q_\infty \sin^2\alpha$ is equal to 120 $(c_f)_{turb}$, Eq. (11) in Ref. 183. As $(c_f)_{turb}$ varies little in the supercritical Reynolds number range of interest the prediction in Fig. 3 of Ref. 183 should essentially be a constant level around 0.4. How the shown variation from 0.63 at $\alpha = 30°$ to 0.25 at $\alpha = 90°$ was obtained is a complete mystery.

4-3 MAXIMUM VORTEX-INDUCED SIDE FORCE

All the data reviewed so far, both in two-dimensional and three-dimensional flow, have demonstrated that the largest aerodynamic loads are generated in the critical Reynolds number regime, where boundary layer transition exacts a dominating influence. This explains why the maximum side force measured by Nelson and Fleeman (Ref. 29) correlates, via the effective Reynolds number defined by Eq. (4-14), with the critical Reynolds number for a cylinder normal to the flow (Ref. 48 and Fig. 103). Recently obtained pressure data on a slender missile (Refs. 184, 185, and Fig. 104[**]) show conclusively that subcritical and super-critical separations can coexist, thus explaining why peak side forces are generated at the critical Reynolds number (Figs. 47 and 103). There is a broadening of the supercritical suction peak due to secondary vortex effects (to be discussed later) and a moderation of the subcritical suction pressure. Both combine to produce pressure differences across the inclined slender body that exceed the steady two-dimensional subcritical-supercritical flow separation model. However, as will be shown later, they are bounded by the unsteady, two-dimensional, subcritical-supercritical flow separation geometry.

The subcritical-supercritical separation pattern develops gradually with increasing angle-of-attack (Fig. 105). At $\alpha = 20°$ the pressure distribution at $x/d = 6.12$ is intermediate between that for inviscid, potential flow and the supercritical distribution. The vortex-induced side force is nonexistent and the normal force nearly negligible. At $\alpha = 30°$ the vortex-induced normal

---

[**] The use of $q_\infty \sin^2\alpha$ as the normalizing dynamic pressure for the inclined cylinder will account correctly for the sweep effect on the pressure distribution, with the exception of the supercritical base pressure (see earlier discussion in Section 4-1).

4-19
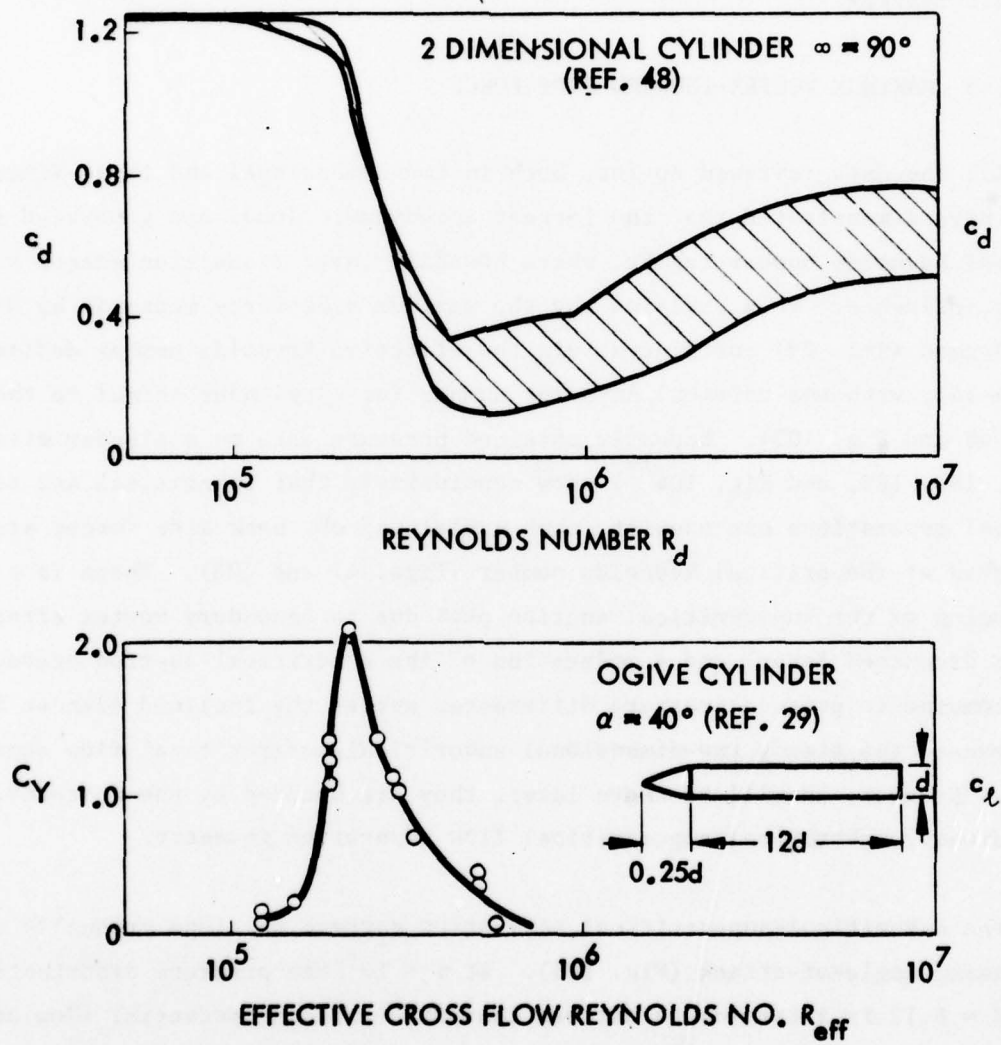
Fig. 103 Correlation of Critical Reynolds Number Effects in Two-
Dimensional and Three-Dimensional Flows
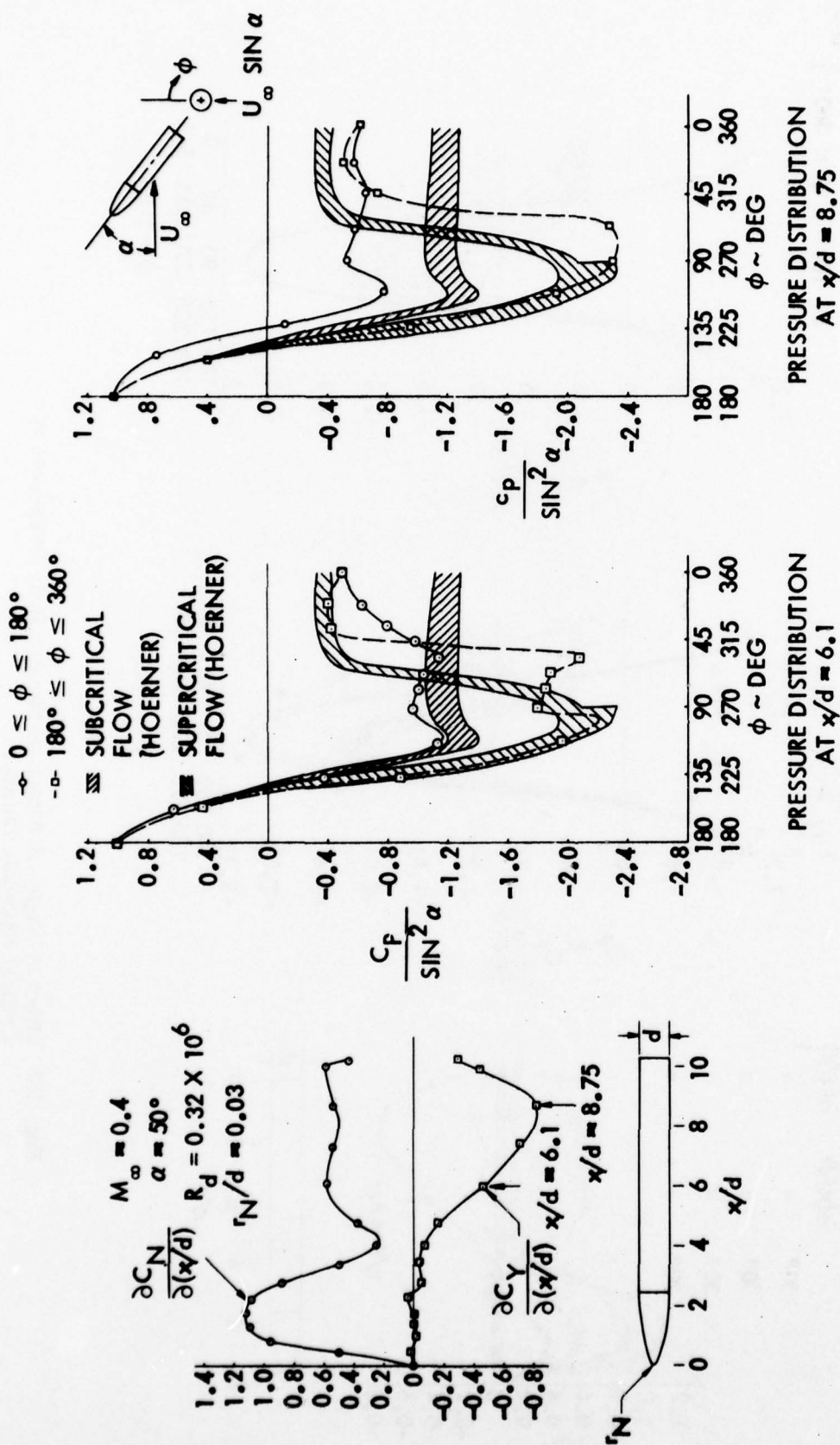
Fig. 104 Evidence of Supercritical/Subcritical Separation on a Slender
Body at Critical Reynolds Number
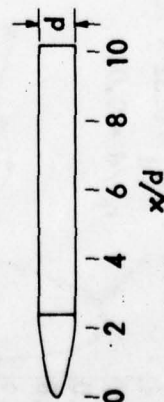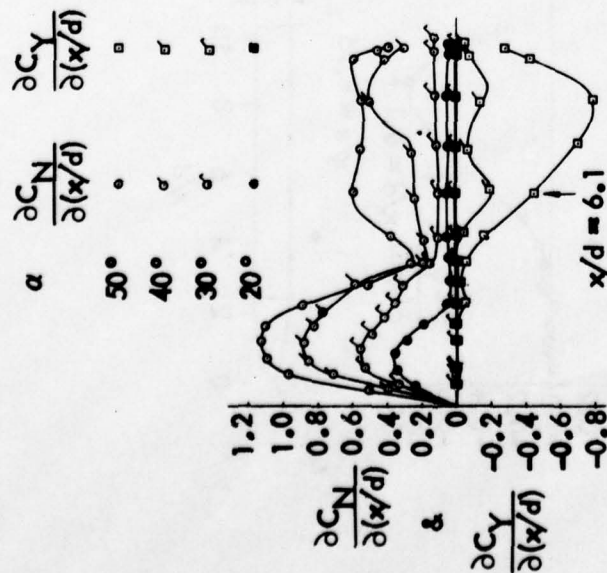
4-21
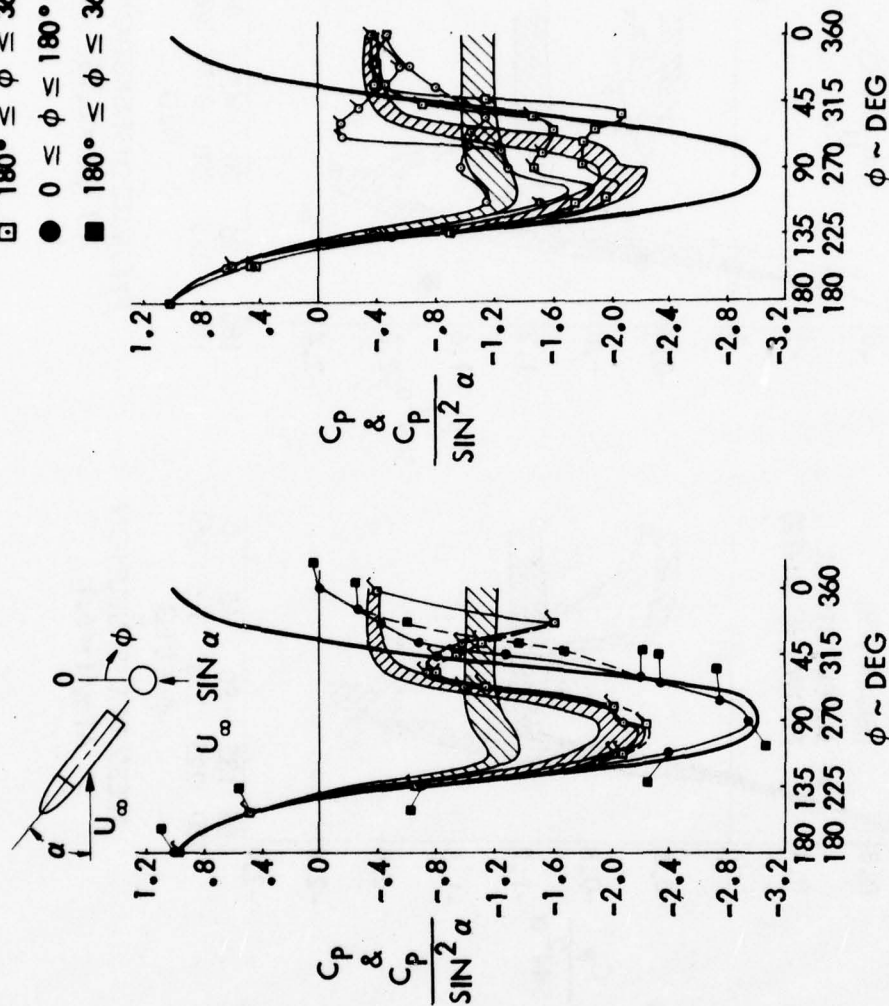
Fig. 105 Effect of Angle-of-Attack on Slender Body Pressures at Critical Reynolds Number

force begins to develop and a slight asymmetry is present in the supercritical pressure distribution, although not large enough to produce a significant side force. At $\alpha = 40°$, the asymmetric pressure distribution begins to produce a side force, and at $\alpha = 50°$ the full subcritical-supercritical separation pattern is realized with the result that both the vortex-induced side force and normal force are large.

The most noticeable difference between the static pressure distributions around the inclined slender body and the two-dimensional cylinder is the second suction peak that occurs on the leeside of the slender body (see Figs. 104 and 106). Rainbird (Refs. 58, 59, and 62) has shown this to be the result of separation of the recirculatory flow which rolls up into a secondary vortex pair. Of course, the secondary vortex is also present in the unsteady two-dimensional flow over a cylinder, e.g., for the impulsively started cylinder (Ref. 186 and Fig. 107). The secondary vortices make a significant contribution to the normal force (Fig. 106), which is reduced significantly when the secondary suction peak is lost. Actually, the secondary vortex moves outboard until its suction peak cannot be distinguished from the major, primary suction peak near the lateral meridian. The position of the secondary vortex is governed by the Reynolds number of the secondary flow, which develops on the leeside as a result of free stream air entrainment through the action of the primary vortices (Fig. 108). When transition occurs in the secondary flow (before roll up) the secondary vortex will move outboard, similarly to what happens on a delta wing (Ref. 187 and Fig. 109). The data in Fig. 106 show a loss of the vortex-induced side force as supercritical flow separation occurs on both sides. Thus, the pressure data for a slender missile configuration (Refs. 184, 185 and Figs. 104-106) verify that the largest vortex-induced side force occurs as a result of coexisting subcritical and supercritical flow separations.

The results in Figs. 104-106 show that the cross-flow load on the inclined, slender body can overshoot the two-dimensional values substantially. However, one can assume that the stationary, three-dimensional cross flow load cannot exceed the unsteady, two-dimensional load. This is, of course, in full
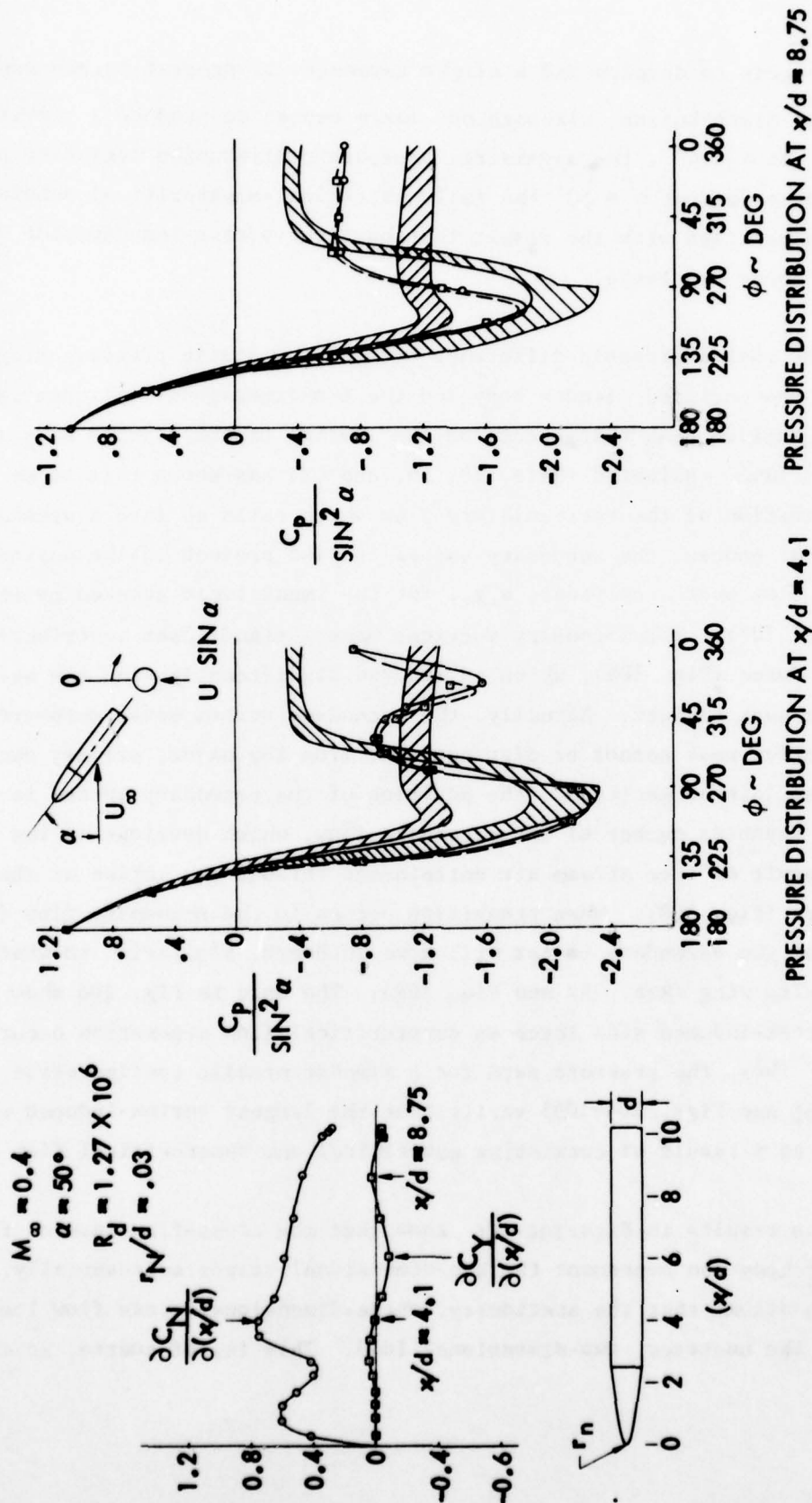
Fig. 106 Effect of Secondary Vortices on the Lift of a Slender Body at Supercritical Reynolds Number

a) $t = 1.64$ s, $\tau = 5.27 \times 10^{-4}$
b) $t = 3.52$ s, $\tau = 1.13 \times 10^{-3}$
c) $t = 5.20$ s, $\tau = 1.67 \times 10^{-3}$
d) $t = 6.88$ s, $\tau = 2.21 \times 10^{-3}$

Fig. 107 Secondary Vortices on Impulsively Started Cylinder (Ref. 186)
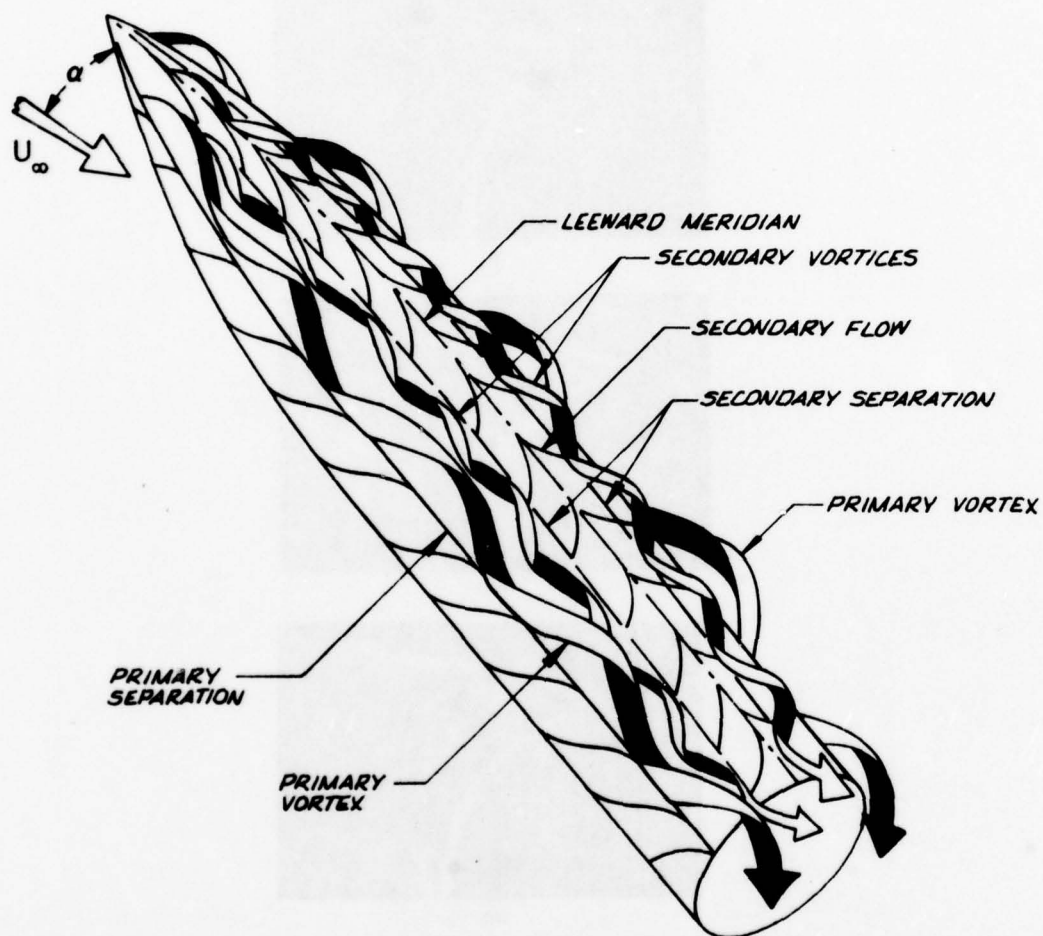
Fig. 108 Primary and Secondary Vortices on a Slender Body

SECTION A-A

$U_\infty \alpha \cos \alpha$

LAMINAR
SECONDARY
SEPARATION

A   A

$\alpha = 26.4$ DEG
$\beta = 15$ DEG
$\theta_A = 14$ DEG

TURBULENT
SECONDARY
SEPARATION
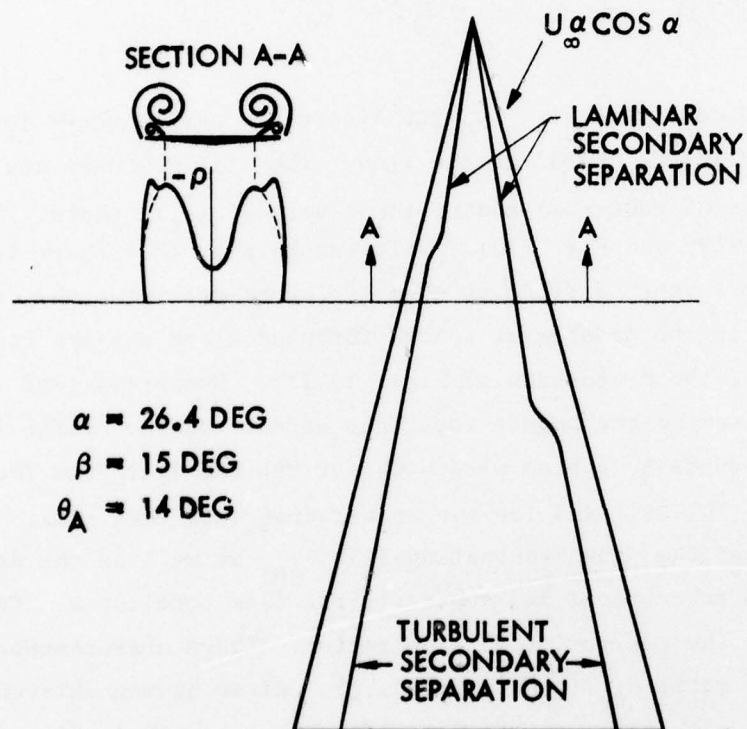
Fig. 109 Effect of Boundary Layer Transition on Secondary Separation
(Ref. 187)

4-27

accordance with the impulsively started cylinder anology (Ref. 172). Very
large dynamic overshoots of static loads have been recorded in the case of
dynamic lift stall of airfoils (Refs. 113, 188-190). Thus, the peak unsteady
lift on a two-dimensional cylinder represents the upper bound for the maximum
steady, out-of-plane force (the side force) in the three-dimensional case of
the inclined slender body. The normalizing in-plane forces for the two cases
are the steady mean drag and the normal force, respectively. Thus, the maxi-
mum sectional side force to normal force ratio for the inclined slender missile
is bounded by the ratio between peak unsteady lift and steady drag on a two-
dimensional cylinder

$$\frac{d|C_Y|_{max}}{dx} \bigg/ \frac{dC_N}{dx} = \frac{c_{\ell p}}{(\overline{c_\ell}^2)^{\frac{1}{2}}} \frac{(\overline{c_\ell}^2)^{\frac{1}{2}}}{c_d} = \frac{c_{\ell p}}{c_d} \qquad (4\text{-}18)$$

In order to determine $c_{\ell p}/c_d$ the literature was searched for unsteady
lift data of cylinders normal to the flow. The lift measurements were usually
presented in form of root-mean-square (RMS) values, $(\overline{c_\ell})^{\frac{1}{2}}$ (Refs. 79, 86, 90, 91,
94, 98, 100, 191-199 and Fig. 110). It can be seen that there is considerable
data scatter. A further difficulty when trying to determine the critical
Reynolds number is the problem of tunnel turbulence and surface roughness
(see Section 3-1, the discussion of Figs. 13-17). Humphreys (Ref. 91) has
attempted to determine the bounds for these effects on the critical Reynolds
number. These bounds have been used both for the RMS lift data (Refs. 79,96,90,
91, 94, 98, 100, 191-199) and for the static drag data (Ref. 48). Humphreys
(Ref. 91) measured the peak fluctuating lift $c_{\ell p}$, as well as the RMS value,
$(\overline{c_\ell}^2)^{\frac{1}{2}}$, for both subcritical and supercritical flow conditions. Fung (Ref. 94)
did the same for the supercritical flow region. These measurements are used
to determine the ratio $c_{\ell p}/(\overline{c_\ell}^2)^{\frac{1}{2}}$ (Fig. 111). After having shifted these
results to agree with the critical Reynolds number bounds in Fig. 110 they are
used on the data in Fig. 110 to obtain the peak lift $c_{\ell p}$ shown in Fig. 112.
This $c_{\ell p}$-curve, when divided by Jorgensen's drag data[#] (Ref. 48 and Fig. 113),

[#] The high Reynolds number wind tunnel data suffer from compressibility effects
since the velocity (thus the Mach number) must be increased to realize high
Reynolds number on small scale cylinders.
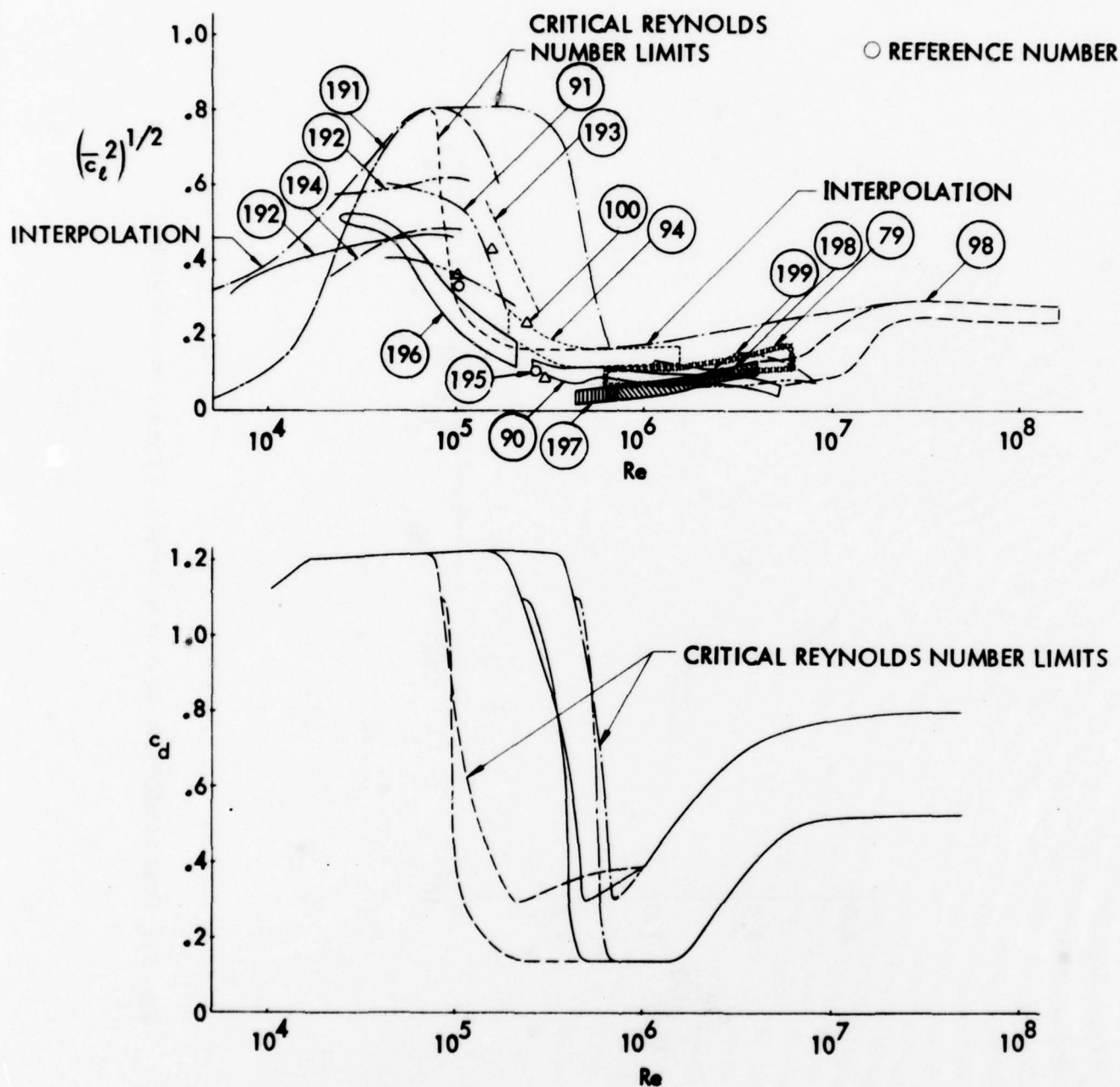
Fig. 110 Correlation of Root-Mean-Square Lift with Steady Drag for a Circular Cylinder in Crossflow
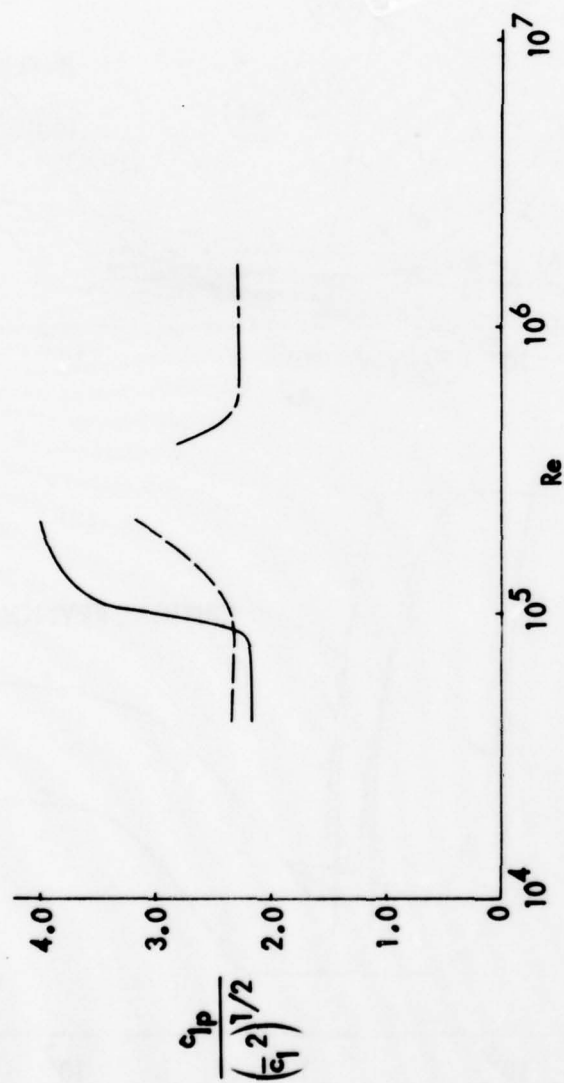
Fig. 111 Peak to RMS Lift Ratio on a Circular Cylinder in Crossflow
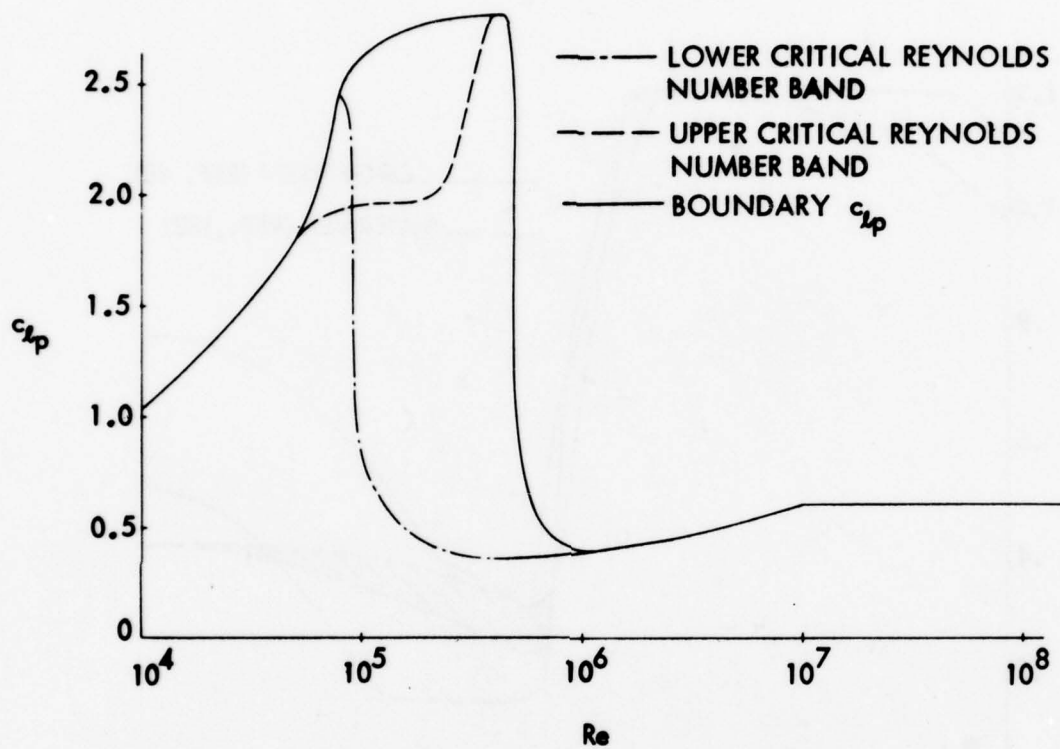
Fig. 112 Peak Sectional Lift Coefficient on a Circular Cylinder in Crossflow
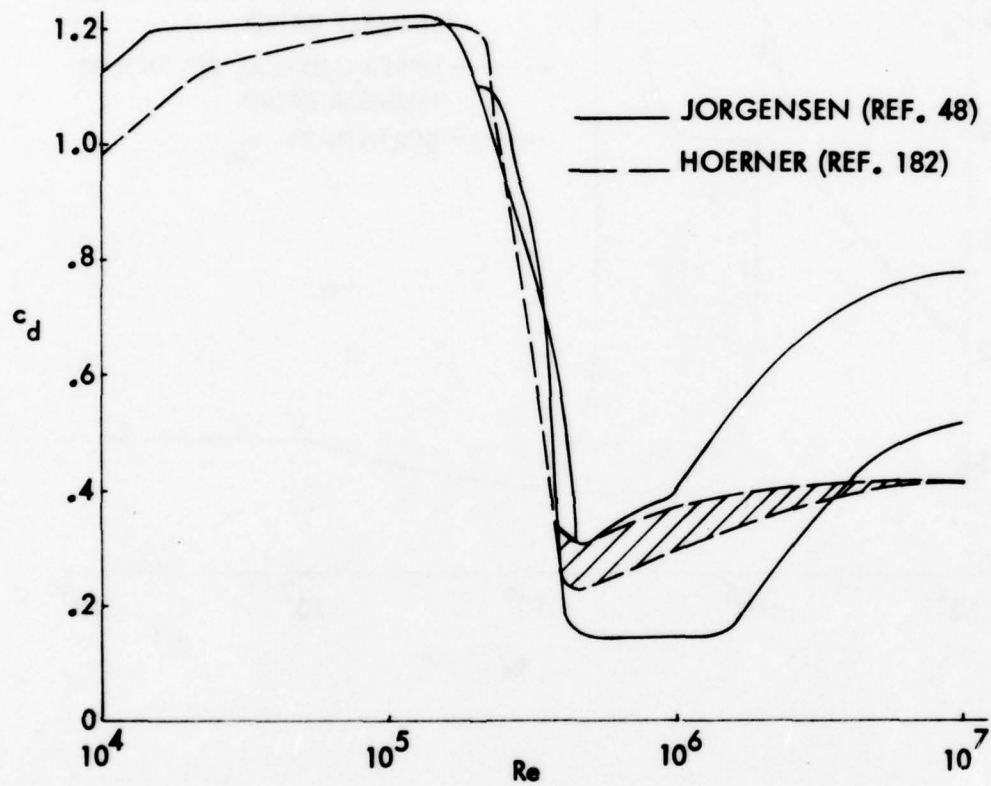
Fig. 113 Comparison of Cylinder Drag Curves

defines the bounds for the local vortex-induced side force to normal force ratio (Fig. 114). That this is indeed the upper boundary is indicated by the good agreement with Bearman's measured lift peak for a cylinder normal to the flow (Ref. 86). His flow visualization results indicated that a stationary supercritical-subcritical separation geometry had resulted due to the collapse of the laminar separation bubble on one side of the cylinder. The huge scatter in Jorgensen's drag data (Ref. 48 and Fig. 113) is undoubtedly due to the combined effects of roughness, turbulence and compressibility effects. In order to define the upper bound for the vortex-induced side force one must use incompressible data, because the maximum forces tend to diminish with increasing subsonic Mach number, both in two-dimensional (Fig. 22) and three-dimensional flow (Fig. 55). The low Mach number (incompressible) data tend to form the lower bound of the drag curve in the critical Reynolds number region (Ref. 48 and Fig. 113). Hoerner's drag data (Ref. 182) in this range, which agree well with the lower bound of Jorgensen's data (Fig. 113), are measured on large scale cylinders in atmospheric winds and are, therefore, not distorted by compressibility effects. Thus it is logical to use the lower bound of Jorgensen's drag curve to form the upper boundary for $c_{\ell p}/c_d$ (Fig. 114). It can be seen that this curve bounds a variety of sectional $|C_Y|_{max}/C_N$-measurements (Refs. 33, 35, and 184).

The application of this $c_{\ell p}/c_d$ ratio to $|C_Y|_{max}/C_N$ at Reynolds numbers above $R_d = 10^5$ tacitly assumes that the space-time equivalence existing at subcritical flow conditions applies also here. That is, the axial flow component existing in the wake of the inclined, slender body of revolution organizes the wake into a regular asymmetric vortex array. One way to organize the two-dimensional wake is through translatory oscillations, as was described in Section 3-1. The results obtained by Jones, et al. (Ref. 92 and Fig. 33) show that the RMS lift can be increased four-fold in the limit of large oscillations at Re = 6×10^6. Using this ratio for Re > 10^5 one obtains $c_{\ell p} = 4\sqrt{2} \cdot c_{\ell RMS}$, where $c_{\ell RMS}$ is the value for a stationary cylinder (Ref. 92 and Fig. 48). At Re = 3×10^6 the data for $M_\infty \leq 0.3$ show $0.06 \leq c_{\ell RMS} < 0.16$ whereas $c_{\ell RMS} = 0.08$ at Re = 8×10^6. Hoerner's drag curve in Fig. 113 gives $\dot{c}_d \approx 0.4$ at Re = 8×10^6. At Re = 3×10^6 the lower bound is $\dot{c}_d = 0.14$, which should apply to the super-
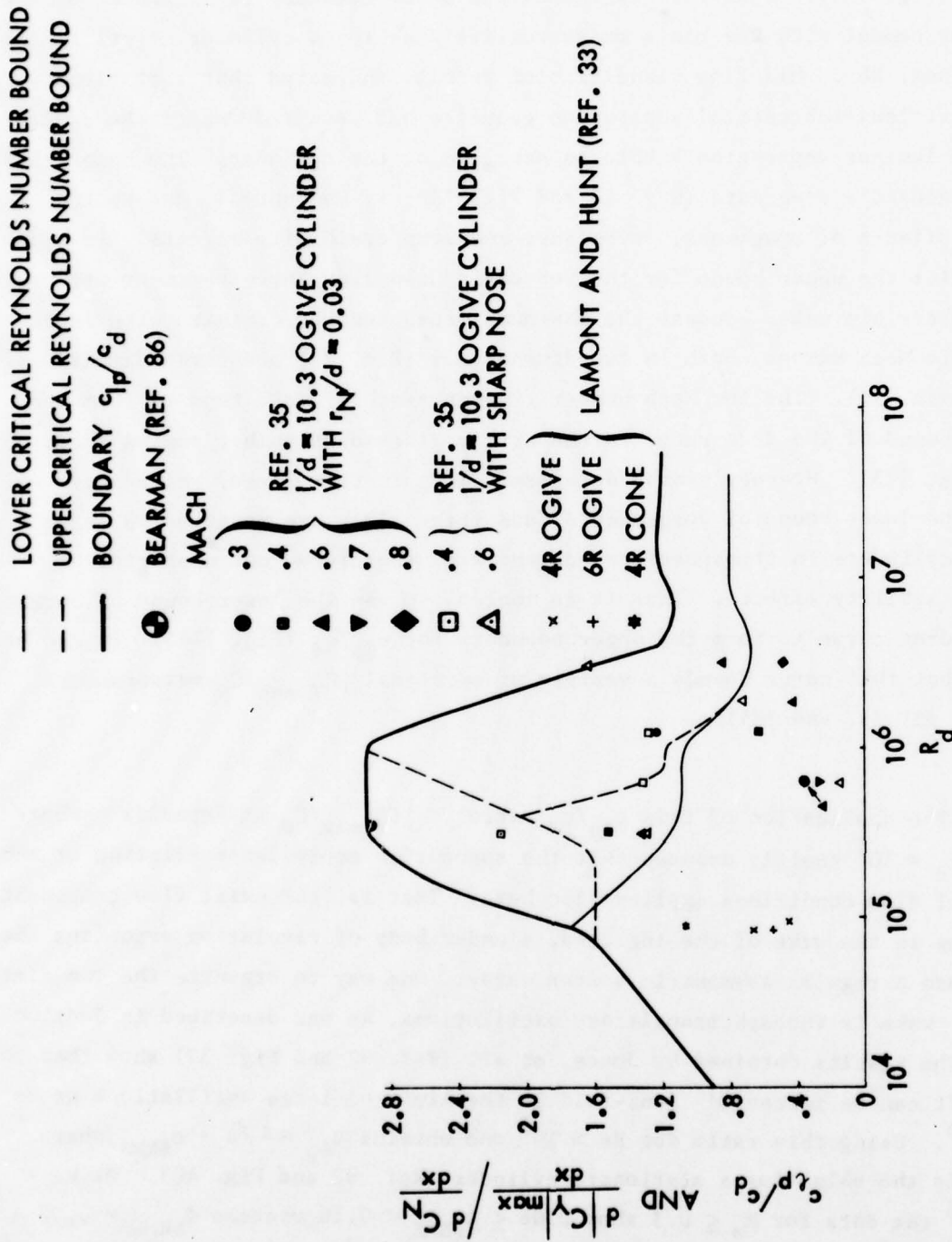
Fig. 114 Comparison of Peak Sectional Lift/Drag Ratio on a Circular Cylinder in Crossflow with the Peak Sectional Side Force/Normal Force Ratio on a Slender Body

critical flow conditions giving the lower bound $c_{\ell RMS} = 0.06$. Conversely, the maximum drag, $c_d = 0.30$, goes with the subcritical flow condition giving the upper lift bound, $c_{\ell RMS} = 0.16$. Combining the above data gives $2.3 \leq c_{\ell p}/c_d < 3.0$ for $R_d = 3 \times 10^6$ and $c_{\ell p}/c_d \leq 1.15$ at $R_d = 8 \times 10^6$. This is in excellent agreement with the boundary in Fig. 114, determined by other means, which shows $c_{\ell p}/c_d = 2.9$ and $c_{\ell p}/c_d = 1.2$ for critical and supercritical flow conditions, respectively.

The pressure data for the critical Reynolds number (Figs. 104 and 105) showed the vortex-induced normal force distribution on the cylinder to be of more or less rectangular shape whereas the side force had a triangular-like distribution. Thus, the overall vortex induced side force to normal force ratio is half of the maximum sectional ratio

$$\frac{\left| C_Y \right|_{max}}{C_N} = \frac{1}{2} \frac{c_{\ell p}}{c_d} \tag{4-19}$$

This boundary encloses all experimental $\left| C_Y \right|_{max}/C_N$ data known by us for which $\alpha > 30°$, i.e., where the two-dimensional analogue is valid (Refs. 8, 14, 26, 28, 30, 32, 35, 36, 49 and Fig. 115. The largest $\left| C_Y \right|_{max}/C_N$ ratio will be realized when only one asymmetric vortex pair exists over the entire length of the body. This occurs on relatively low fineness ratio, pointed[*] bodies (ogives, cones, etc.),where the vortex asymmetry begins to develop immediately and the side force starts to grow at the nosetip (Ref. 184 and Fig. 116).[#] This explains why the data for $\ell/d = 3.5$ and 5.0 ogives and for 8 and 10 degree cones fall close to the upper $\left| C_Y \right|_{max}/C_N$ boundary in Fig. 115.

It is unfortunate that very little wind tunnel data is available for supercritical Reynolds numbers, which are of most practical interest. At these Reynolds numbers the secondary separation effects discussed earlier may become

---

[*] Even a 3 percent nose bluntness is sufficient to suppress the nose-dominated vortex shedding (see Section 5).

[#] Note that the normal force and side force distributions on the pointed nose in Fig. 116 are consistent with rectangular and triangular "unit area distributions", respectively.
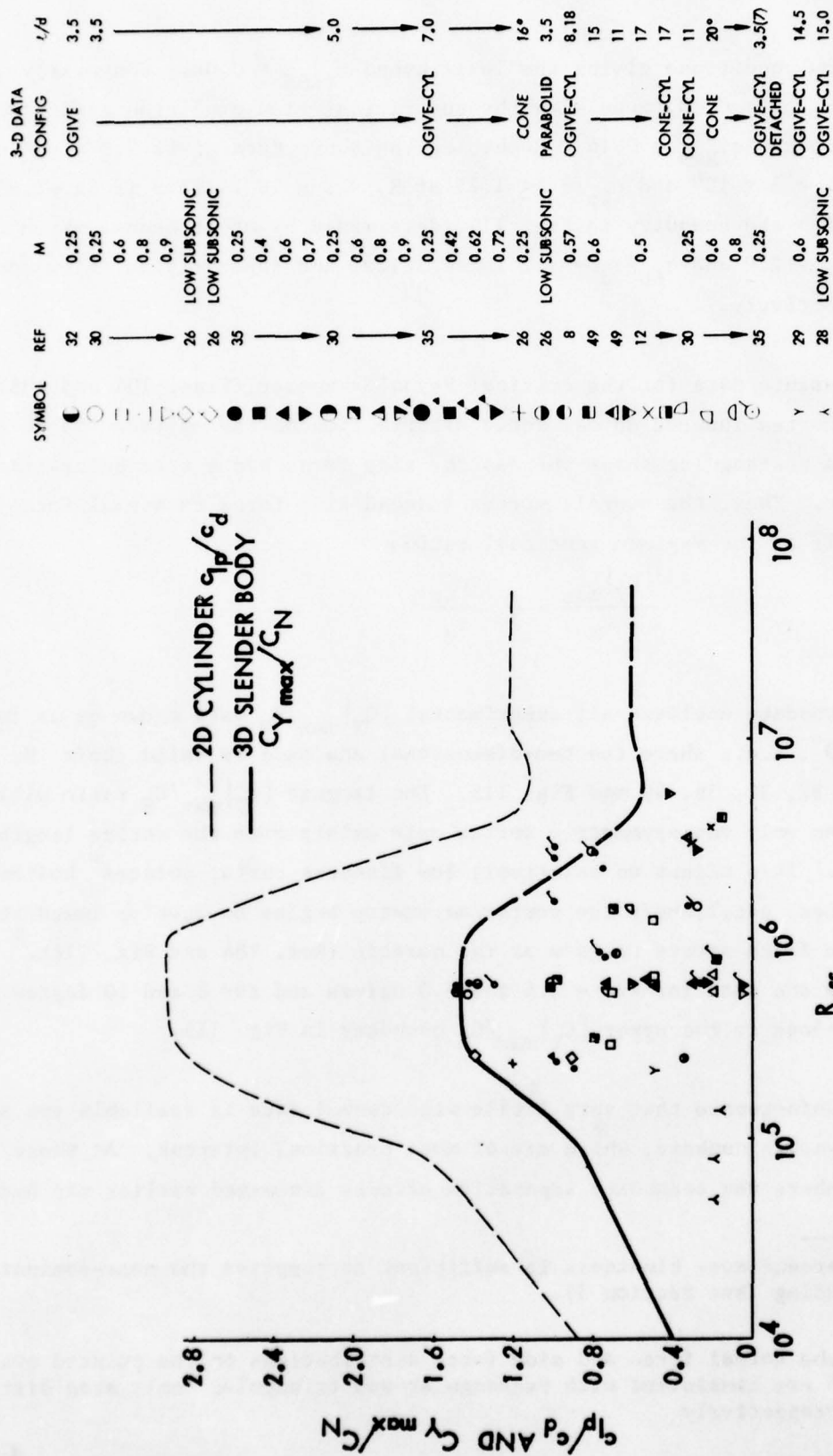
Fig. 115 Maximum Side Force/Normal Force Ratio
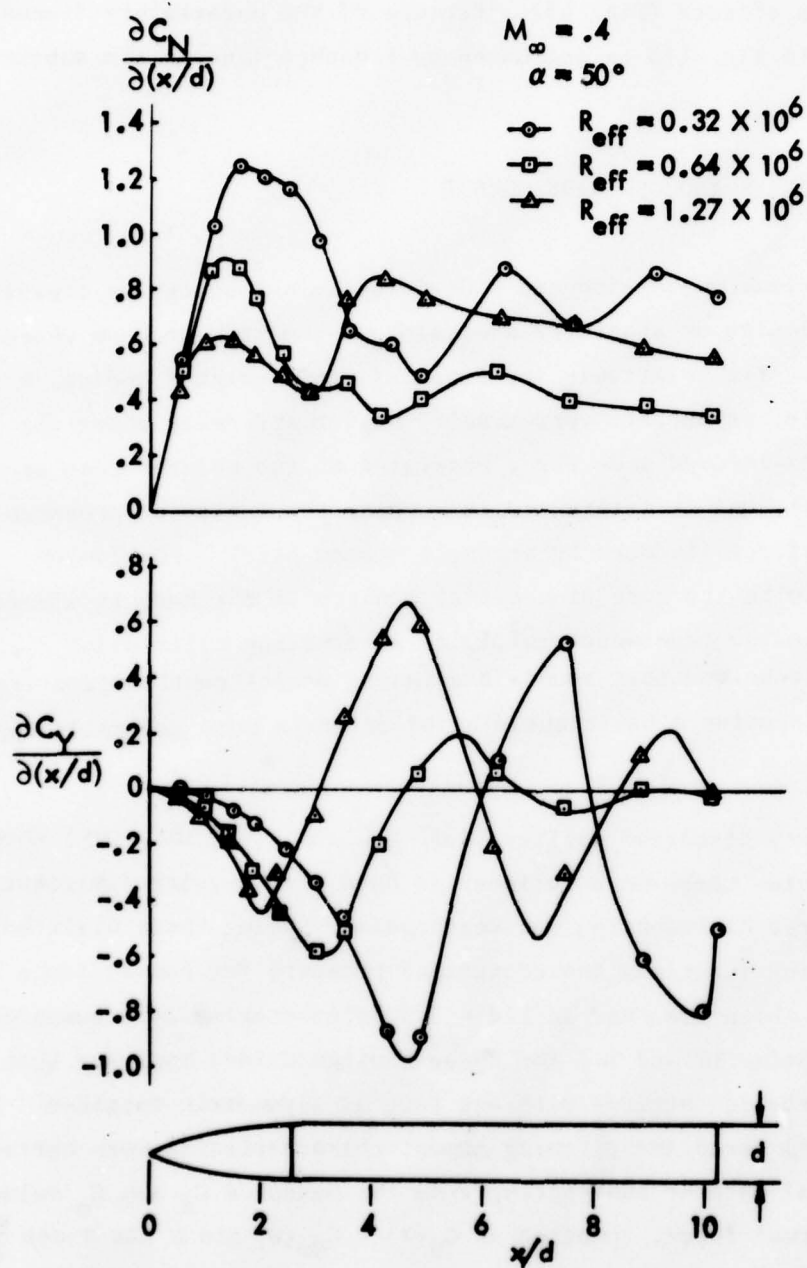
Fig. 116 Normal Force and Side Force Distributions on a Pointed
Slender Body (Ref. 184)

important. It will be necessary to obtain such supercritical flow data with natural boundary layer transition, since the vortex asymmetry is so sensitive to surface roughness effects (Fig. 49). Because of the uncertainty discussed above the boundary in Fig. 115 is indicated by a dashed line in the supercritical flow region.

4-4 MAXIMUM VORTEX-INDUCED SIDE MOMENT

Knowing the maximum vortex-induced side force is not enough by itself for control system design or stability analysis. One must also know where the side force acts. For relatively low fineness ratio pointed bodies, dominated by a single, asymmetric vortex pair, or for aircraft, where the concern is the vortex-induced side force generated on the pointed nose at high angles of attack, one is interested in knowing the center of pressure of the maximum side force (induced by a single vortex pair). For longer bodies this will also be the case of greatest concern if the nose is slender and pointed. Even in the case where multiple, alternating cells exist along the body, a technique that bounds the yawing moment contribution from the single cell can provide a basic building block for a more generally applicable method.

The pressure data discussed earlier (Ref. 184 and Figs. 104, 105) showed the vortex-induced side force on a cylinder to have a triangular distribution while the normal force distribution was rectangular. Using these distributions as unit area weighting functions the centers of pressure for normal force and side force on a 10° sharp cone and an $\ell/d = 3.5$ pointed ogive were computed. Experimental data (Refs. 30 and 36) for these configurations indicate that the maximum side force is obtained with one pair of asymmetric vortices. The vortex-induced normal force and pitching moment characteristics were extracted from the experimental data by subtracting from the measured C_N and C_m values the slender body normal force, computed as $C_N(\alpha) = C_{N\alpha}(0) \sin \alpha \cos \alpha \cos \frac{\alpha}{2}$ (adapting the method of Ref. 1) and the corresponding moment (see Fig. 117).

l/d = 3.5 OGIVE

M_∞ = 0.25

R_{eff} = 0.54 × 10^6

C_m ABOUT BASE

C_{ma}

ΔC_{mv}

α ~ DEG

C_N

ΔC_{Nv}

$C_{Na} = \dfrac{C_{N\alpha}}{2} \; \text{SIN} \; 2\alpha \; \text{COS} \; \dfrac{\alpha}{2}$

α ~ DEG
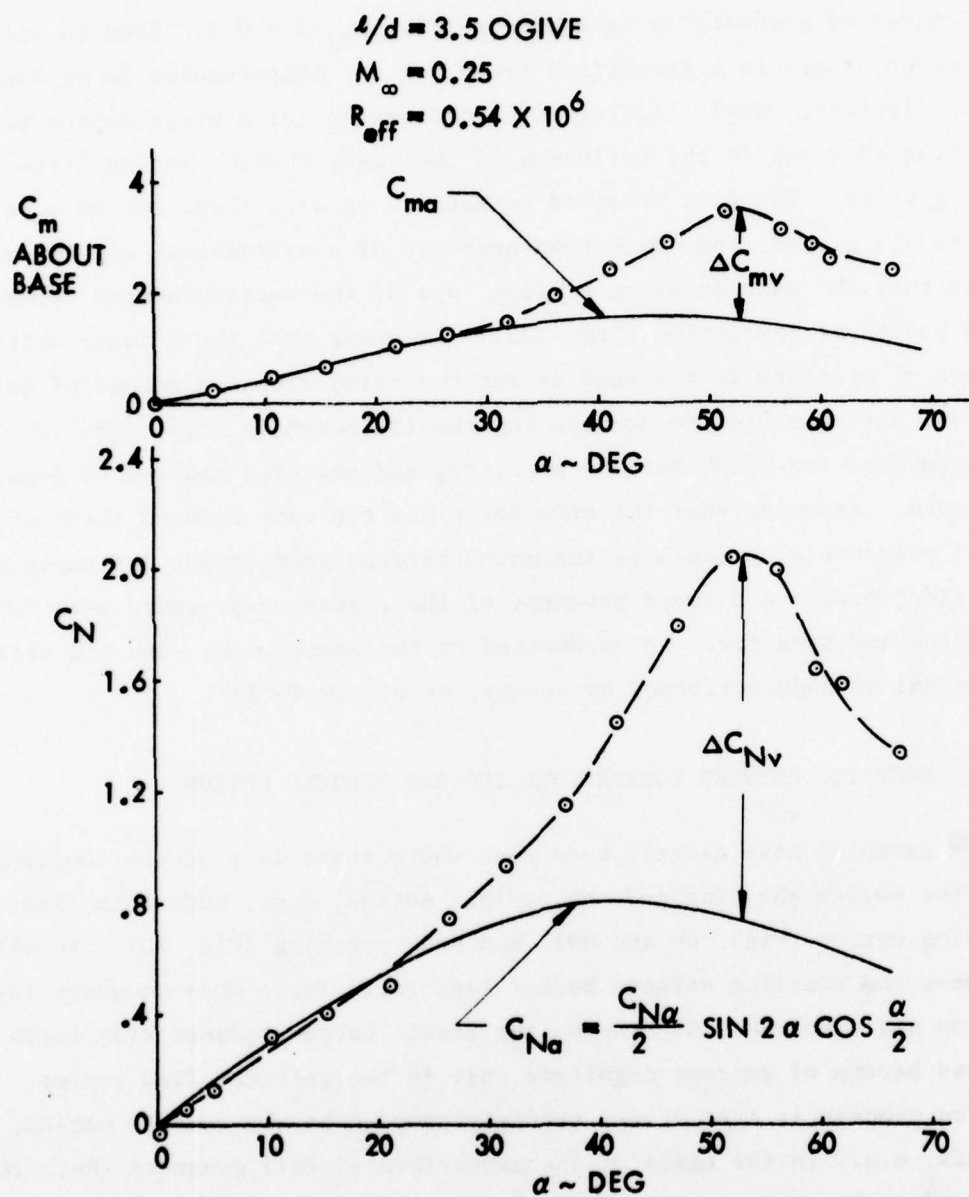
Fig. 117 Effect of Vortices on the Normal Force and Pitching Moment of a Pointed Ogive

Computed centers of pressure lie somewhat aft of the experimental values, for both the vortex-induced normal force and side force (Figs. 118-122). Repeat runs and comparisons between different tests indicate the data accuracy for the center of pressure to be approximately $\Delta x_{CP}/d = 0.3$. Even in view of that, however, there is a persistent trend for the measurements to be forward of the predictions. Why? Leading edge vortices on delta wings depart before the trailing edge due to the influence of the wake, thereby losing lift-generating power. The data obtained by Keener, et al., (Ref. 36) on a pointed ogive with and without the downstream presence of a cylindrical afterbody indicates that the wake causes a similar loss of the vortex-induced normal force on bodies of revolution (Fig. 123). Assuming that the forward shift of the center of pressure is the same as for the delta wing the method of Refs. 167 and 200 has been used to compute the results shown in Figs. 118-122. It can be seen that the match between predicted and measured centers of pressure has improved. Assuming that the side force has the same forward shift of the center of pressure also improves the match between predictions and experiment for the side force. A forward movement of the center of pressure both for normal force and side force is documented by the measurement with and without a cylindrical aftbody performed by Keener, et al. (Ref. 36).

4-5 COUPLING BETWEEN VORTEX SHEDDING AND VEHICLE MOTION

Some examples have already been seen where there is a strong coupling between the vortex shedding and the vehicle motion, e.g., body spin (Fig. 64), body coning motion (Figs. 68 and 69), and body pitching (Fig. 72). In all these cases the coupling effects became especially large when boundary layer transition was involved. Of course, the static vortex-induced side loads themselves become of extreme magnitude only in the critical flow regime. The transition process is itself very strongly coupled to the vehicle motion, at all speeds, e.g., in the cases of incompressible airfoil dynamics (Ref. 201), shock-boundary layer interaction at transonic speeds (Refs. 202 and 203), or reentry body dynamics at hypersonic velocities (Refs. 204-206). It is, therefore, no surprise that the effect of spin or coning motions on the generation of asymmetric vortices and associated side loads become especially large when
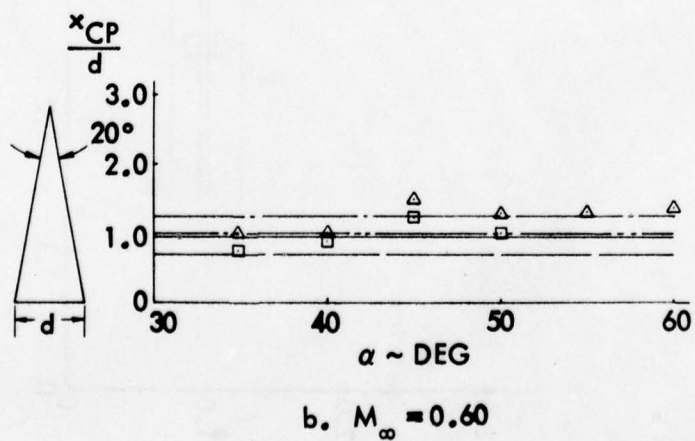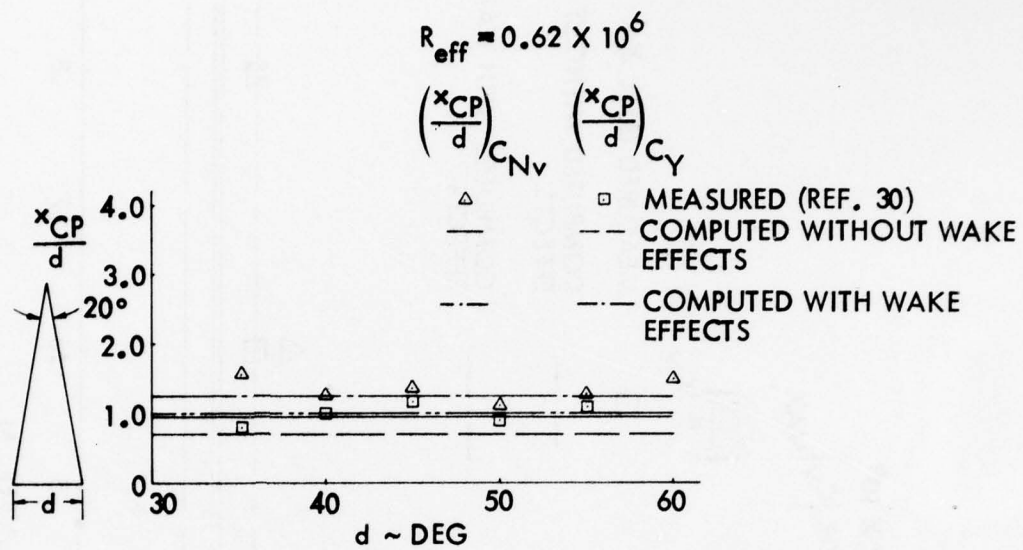
Fig. 118 Centers of Pressure of the Vortex-Induced Loads on a 10° Cone
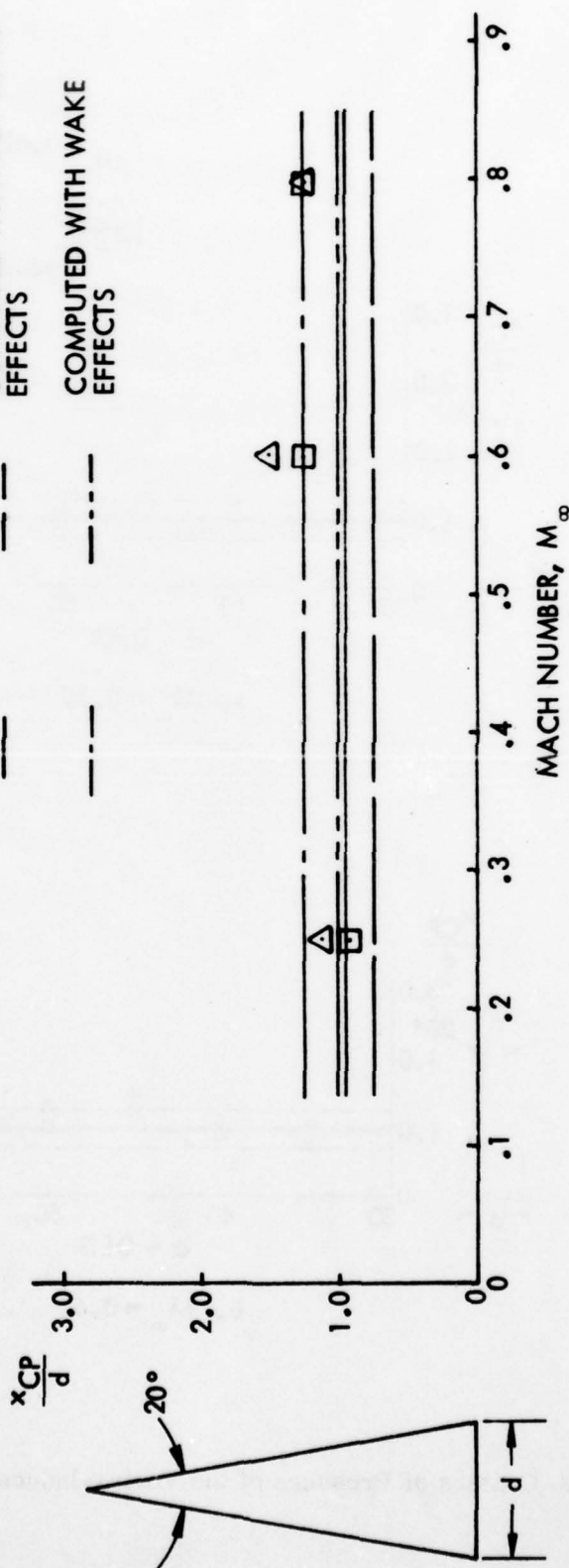
Fig. 119 Effect of Mach Number on the Centers of Pressure of the Vortex-Induced Loads on a 10° Cone When the Side Force is Maximum
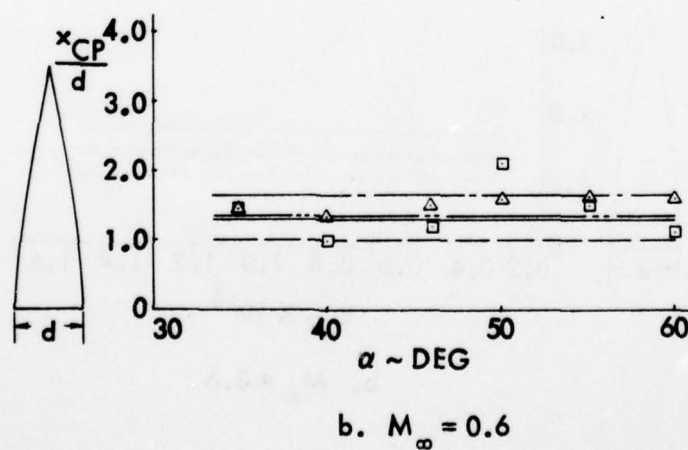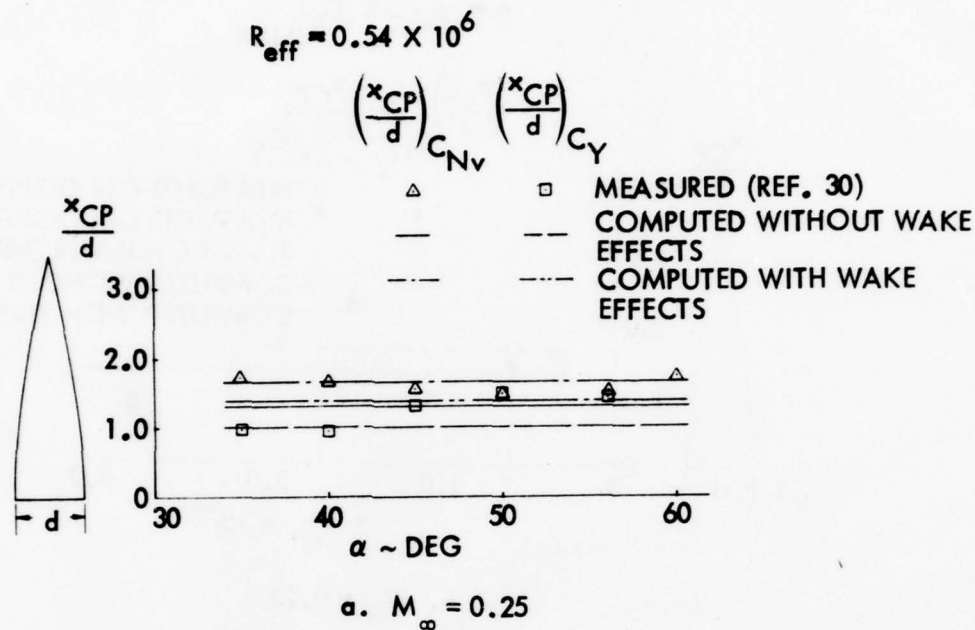
a. $M_\infty = 0.25$

b. $M_\infty = 0.6$

Fig. 120 Centers of Pressure of the Vortex-Induced Loads on an
$\ell/d = 3.5$ Ogive

Fig. 121 Effect of Reynolds Number on the Centers of Pressure of the Vortex-Induced Loads on an $l/d = 3.5$ Ogive at $M_\infty = 0.25$ when the Side Force is Maximum
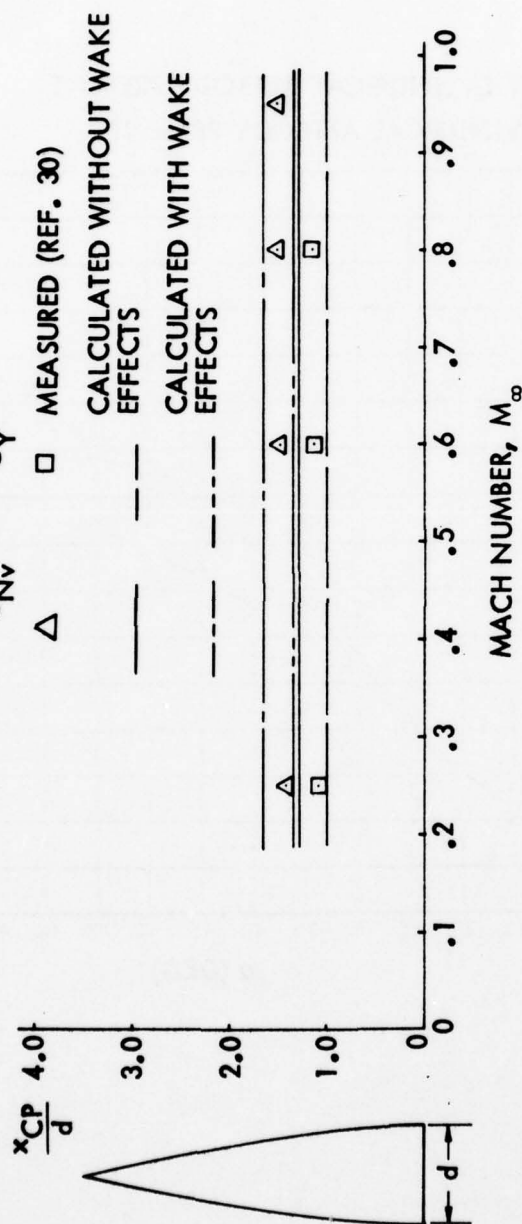
Fig. 122 Effect of Mach Number on the Centers of Pressure of the Vortex-Induced Loads on an $\ell/d = 3.5$ Ogive when the Side Force is Maximum

O WITHOUT CYLINDRICAL AFTBODY PRESENT
□ WITH CYLINDRICAL AFTBODY PRESENT
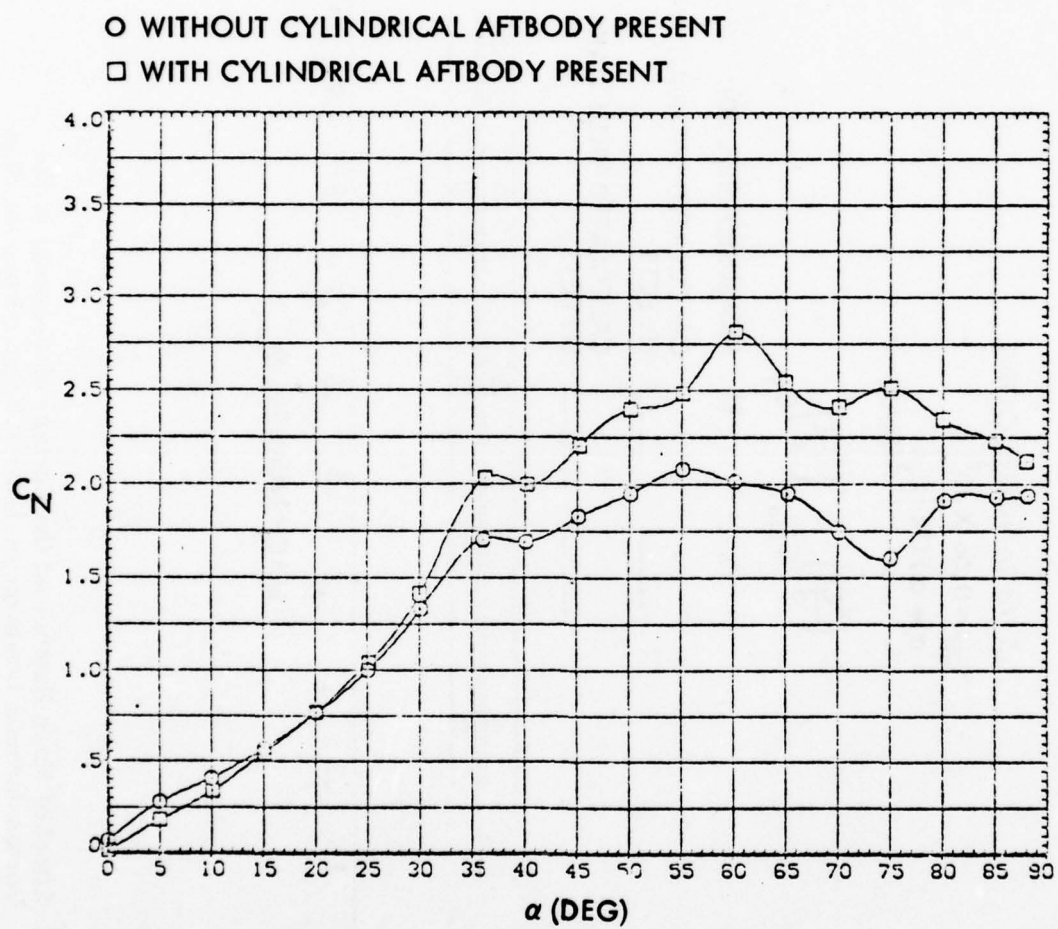
Fig. 123 Effect of Aftbody Presence on the Normal Force of an $\ell/d = 3.5$ Ogive (Ref. 36)

transition is one of the flow mechanisms involved. This strong coupling between vehicle motion and transition complicates dynamic testing, as no boundary layer tripping device can be used (Refs. 203 and 207).

Bearman's "frozen" subcritical-supercritical separation geometry on a cylinder normal to the flow (Ref. 86), which produced the maximum sectional load (Fig. 114) along the full length of the cylinder, resulted because the laminar separation bubble was for some reason "wiped out" on one side of the cylinder. We have suggested that the large dynamic overshoot of static $c_{\ell \text{ MAX}}$ on a pitching airfoil occurs because the wall-jet effect of the upward moving leading edge wipes out the laminar separation bubble (Ref. 208). Recent experiments have confirmed that this is really what happens (Ref. 209). There is no good reason to believe that the same thing cannot happen on the cylinder, especially in view of the effects that translatory and longitudinal oscillations have on the two-dimensional wake (Figs. 30-33 and Fig. 40). This means that a certain vehicle motion might be able to "lock-in" this maximum separation asymmetry over an extended part of the vehicle, thereby generating the maximum side load (Fig. 114), rather than the otherwise expected total load (Fig. 115). Furthermore, the results obtained by Jones, et al., (Ref. 92) show that the laminar separation bubble is present even at $R_d = 1.73 \times 10^6$ (Fig. 124), indicating that this "lock-in" to the maximum side-load could occur even at transcritical Reynolds numbers, the flow regime where many full-scale vehicles will fly.

One very important effect of the asymmetric vortices is the coupling mechanism they provide between longitudinal and lateral degrees of freedom. Forebody pitching generates side loads on downstream missile body and tail surfaces. As these cross-coupling effects are large, highly nonlinear, often discontinuous and associated with hysteresis effects, and have especially powerful effects on the vehicle dynamics, they have recently become of great concern to missile and aircraft industry (Ref. 210). A summary of our present capability (or lack thereof) in handling these new problems is given in Ref. 162.
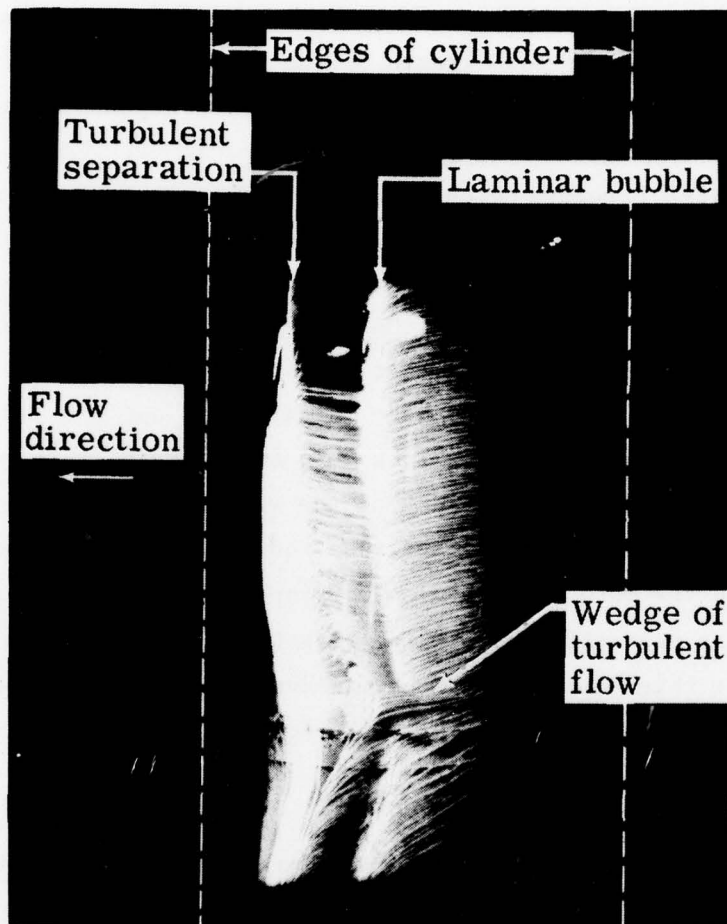
Fig. 124 Oil Flow Photograph Showing Laminar Separation Bubble on a
Circular Cylinder in Crossflow at $R_d = 1.73 \times 10^6$ (Ref. 92)

Section 5
ALLEVIATION OF VORTEX-INDUCED SIDE LOADS

After all the discussions earlier in the text about the dominating influence
that the apex has on the generation of free body vortices, it is rather obvious
what would be one certain way of reducing the vortex-induced side loads, i.e.,
removing the pointed apex. Gowen and Perkins (Ref. 5) did exactly that. They
removed the first 14 percent of their sharp cone and substituted it with a hemi-
spherical nosetip thereby accomplishing "the desired change in the wake vortex
configuration from asymmetric to symmetric." Pick found in his investigation
(Ref. 14 and Fig. 54) that small nose bluntness (< 25 percent) had a dramatic-
ally alleviating effect on the side load, but that large nose bluntness (50 per-
cent in his case) brought back the large side loads. This effect of large nose
bluntness has also been observed on *slender-nosed* aircraft (Ref. 16 and Fig.
125). The results obtained by Coe et al. (Ref. 26 and Fig. 126) also show this
beneficial effect of nose bluntness. The pointed paraboloid has as large a
side force as the tangent ogive according to the results in Ref. 32. The results
in Ref. 27 show that the large side force on the pointed ogive can be eliminated
almost completely by the use of 4.2, 8.4 or 16.7 percent hemispherical nose
bluntness, and also by adding a nose boom (Fig. 127). The effect of the nose
boom may be to "bury" the pointed apex in a "locally thick" boundary layer
thereby eliminating its microscopic creativeness (Ref. 142). The data in Fig.
127 seem to support this supposition. They show that increasing the Reynolds
number decreases the boom's effectiveness as a side load alleviator. The
effect of nose bluntness is similar to that of apex rounding (Ref. 143), that
is, it is the planform roundness that counts, at least this is what the results
obtained by Titiriga and Skow indicate (Ref. 23 and Fig. 128).

Strakes have, of course, long been known to reduce the asymmetric loads
induced by nose vortices (Refs. 5, 6, 16, 22, 26, 27, 35). The design used by
Coe, et al. (Ref. 26) seems to work well for the l/d = 3.5 tangent ogive (Fig.

DIMENSIONS IN: INCHES (CENTIMETERS)
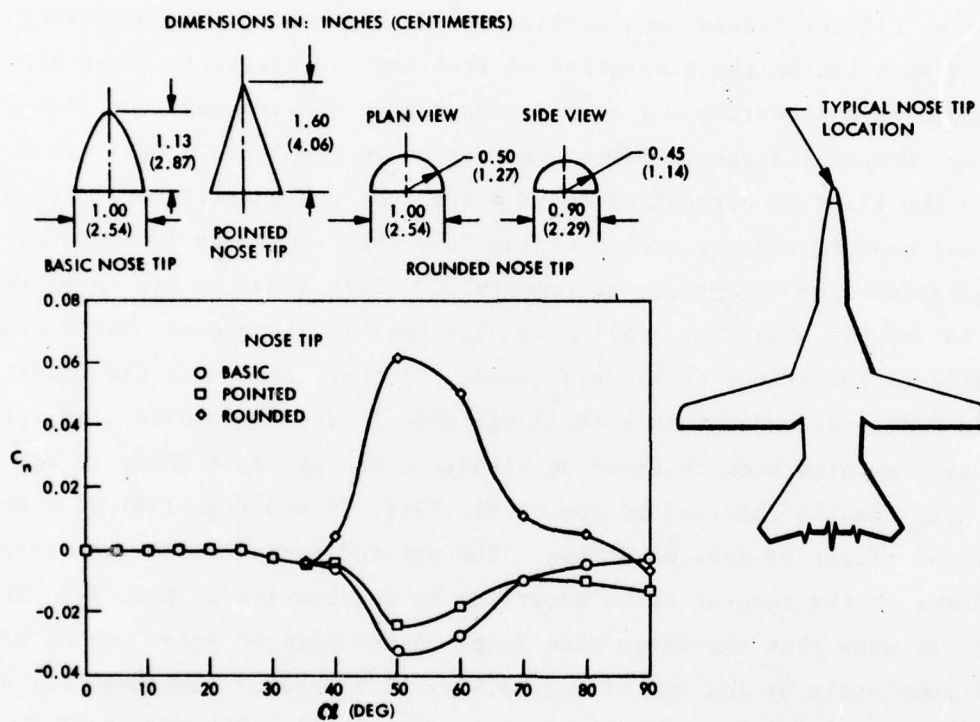
Fig. 125 Effect of Nosetip Shape on Side Moment of a High Performance
Aircraft at Zero Yaw (Ref. 16)
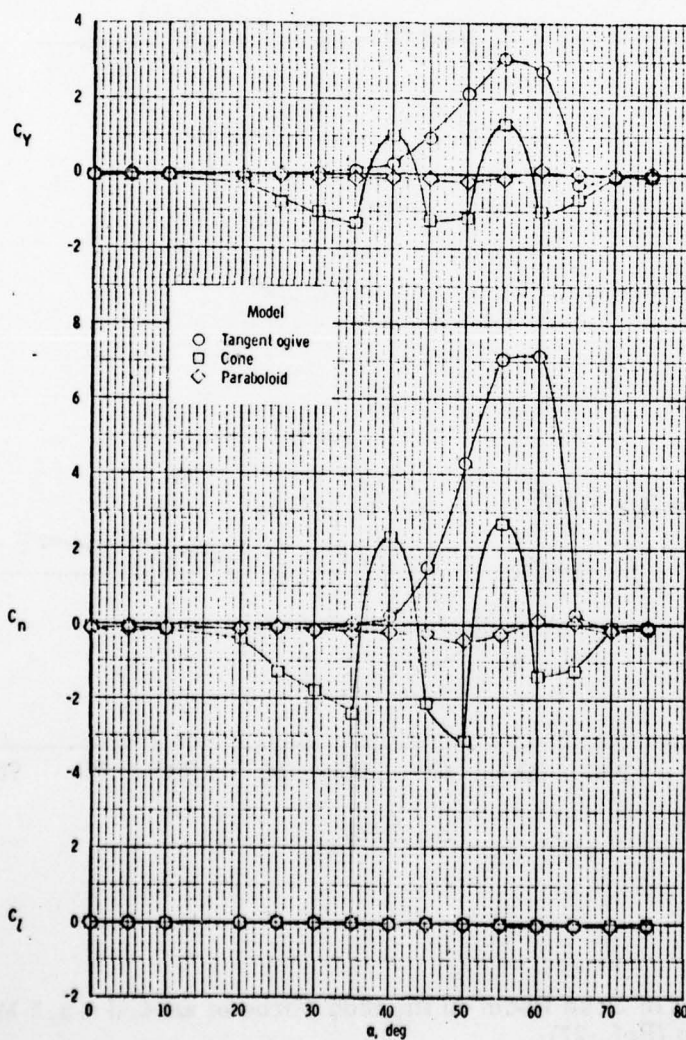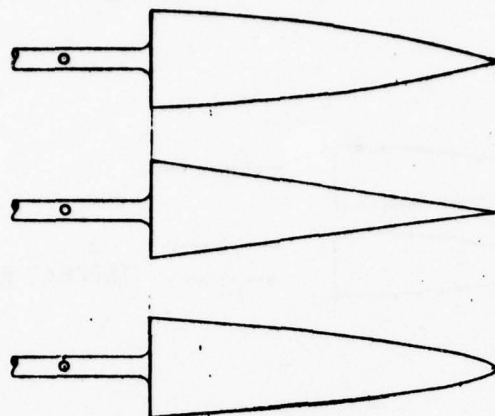
Fig. 126 Comparison of the Lateral-Directional Aerodynamic Characteristics of the Tangent-Ogive Model, Cone, and Paraboloid at Zero Yaw and $R_d = 0.35 \times 10^6$ (Ref. 26)
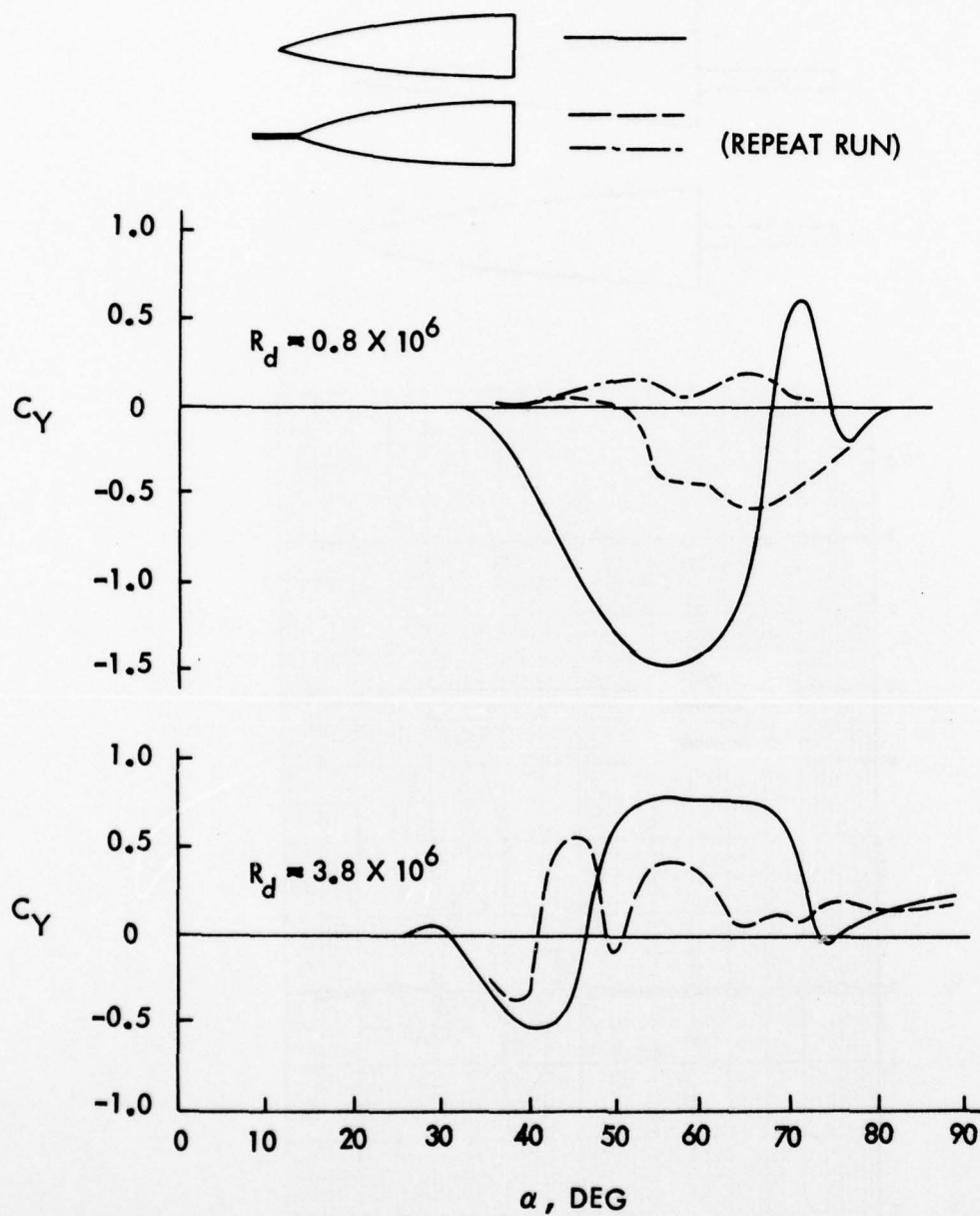
Fig. 127 Effect of Nose Boom on the Side Force of an $l/d = 3.5$ Pointed Ogive (Ref. 27)
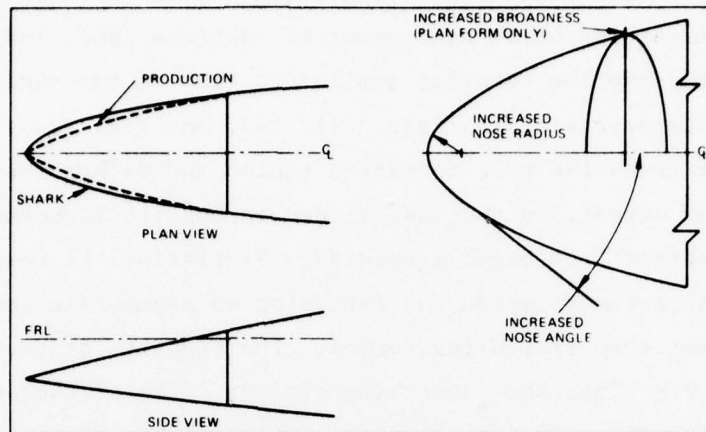
Shark Nose Geometry

$C_n\,(\alpha)$ for $\beta = 0$
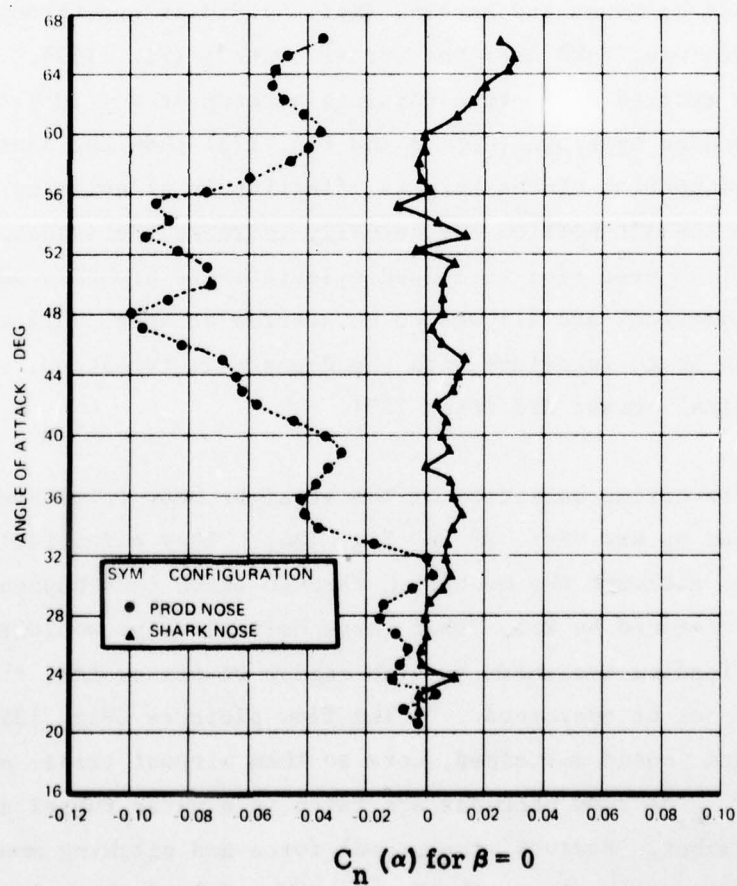
Fig. 128 Effect of Nose Planform Change on Vortex–Induced Side Moment (Ref. 23)

83) but to be somewhat less effective on a cone with its smaller apex
angle (Fig. 129). The strake does not extend all the way to the tip, thus
leaving room for the birth of asymmetric vortices (Ref. 142). The action of
the strake may then be somewhat similar to that of too short a splitter plate
in the two-dimensional case (Refs. 211, 212, and Fig. 130). The splitter
plate only extends the wake formation region and delays the start of the von
Karman vortex street, in this manner decreasing its frequency but not preventing
the vortex street from being generated. Similarly, the results in Fig. 129
show that the strakes impede the formation of asymmetric vortices somewhat but
do not prevent them from being formed. The results for the X-15 airplane
(Ref. 7 and Fig. 134) show something similar. The strakes do not go all the
way to the nosetip, and, consequently, the left strake (△) does not have any
larger effect than an invisible body asymmetry (o)(in the apex region). The
strakes used by Gowen and Perkins (Ref. 5) did extend through to the apex and
could, therefore, take over the vortex control (Fig. 132). Thus, at a 7° roll
angle they started asymmetric vortices already at $\alpha \leq 10^{\circ}$. The strakes or
body trips used by Brown (Ref. 8 and Fig. 133) show the same trend, i.e., only
the forward portion of the trip is effective in alleviating vortex-induced side
loads, and the aft portion may actually increase the loads. The relative
failure of the nose ring as a load alleviator is probably again due to the
fact that vortices are allowed to be started at apex. All that the nose ring
then can do is to interfere with the downstream formation, similarly to what
the "set-back" strake did (Fig. 129).

An interesting variation of the straight body trips are the helical trips
investigated by Rao (Ref. 39 and Fig. 134). They effectively eliminate the
side force, although the mechanism through which that happens hardly can be
the one envisioned by Rao, "that these helical trips would so disrupt the
vorticity feeding mechanism at high angles of attack that the primary vortex
pair could not be sustained..." The flow pictures (Fig. 135) indicate that the
vortices are indeed sustained, more so than without trips, as no vortices
break away. The flow pictures are taken in a water tunnel at an unspecified
Reynolds number. However, the normal force and pitching moment data (Fig. 136)
tell the same story, i.e., the vortex-induced loads have increased, not
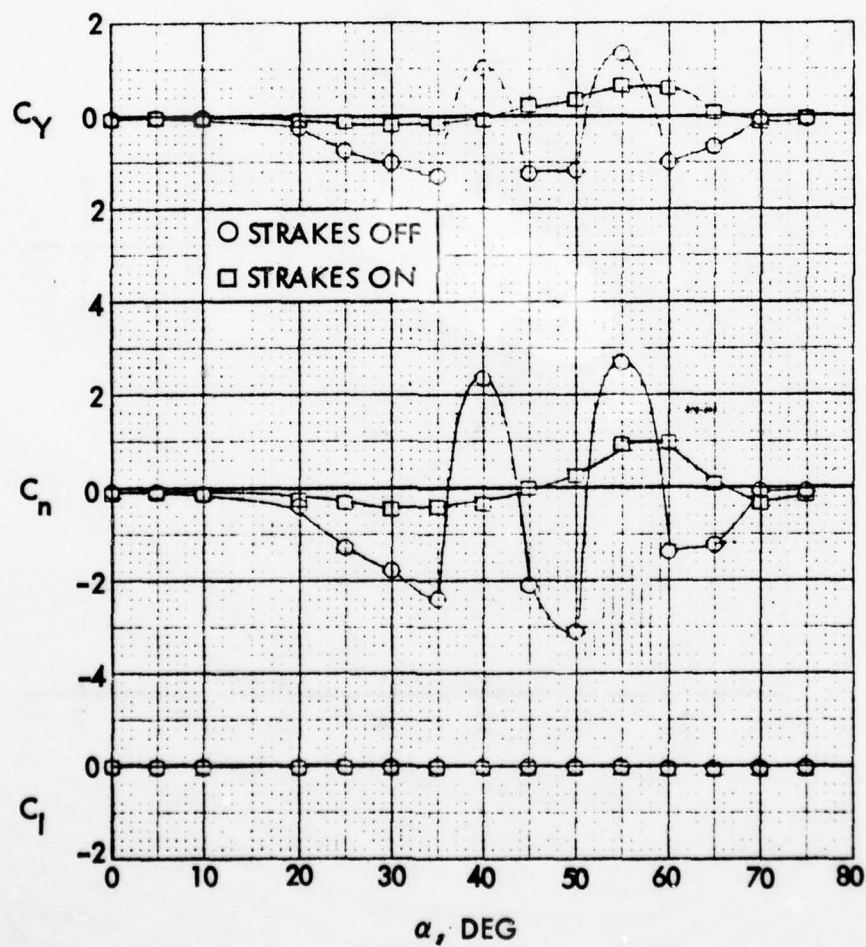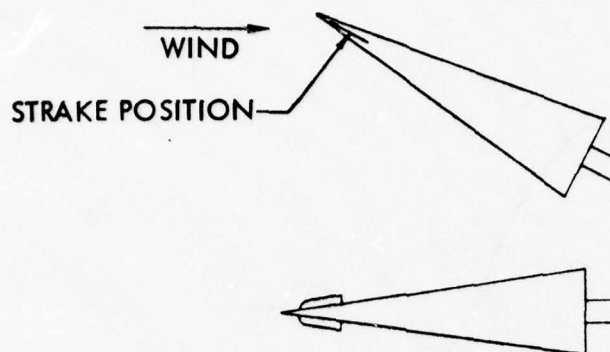
Fig. 129 Effect of Nose Strakes on the Vortex-Induced Side Force of a Cone (Ref. 26)
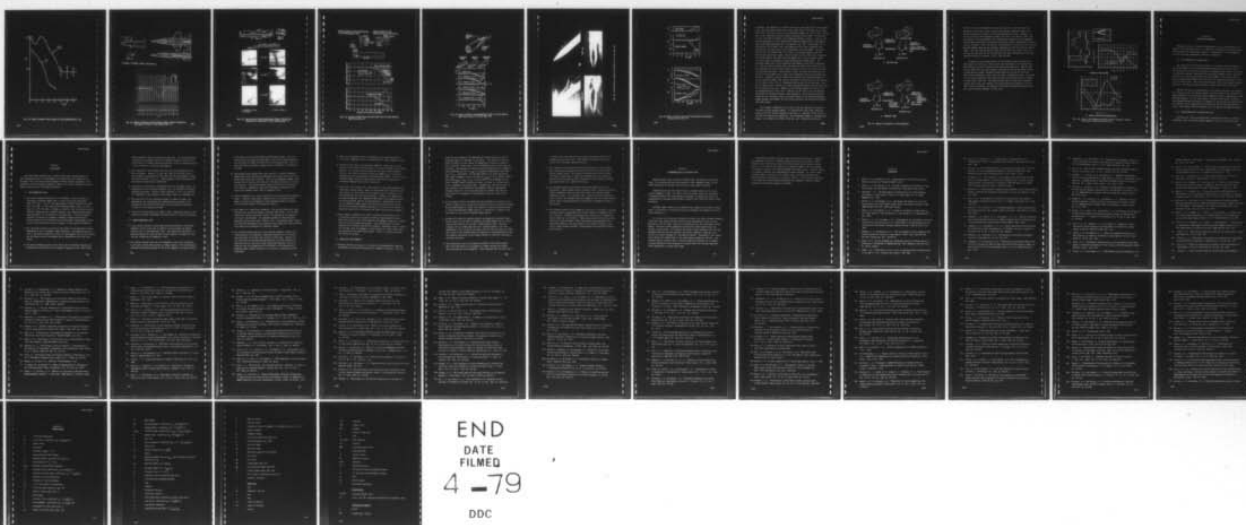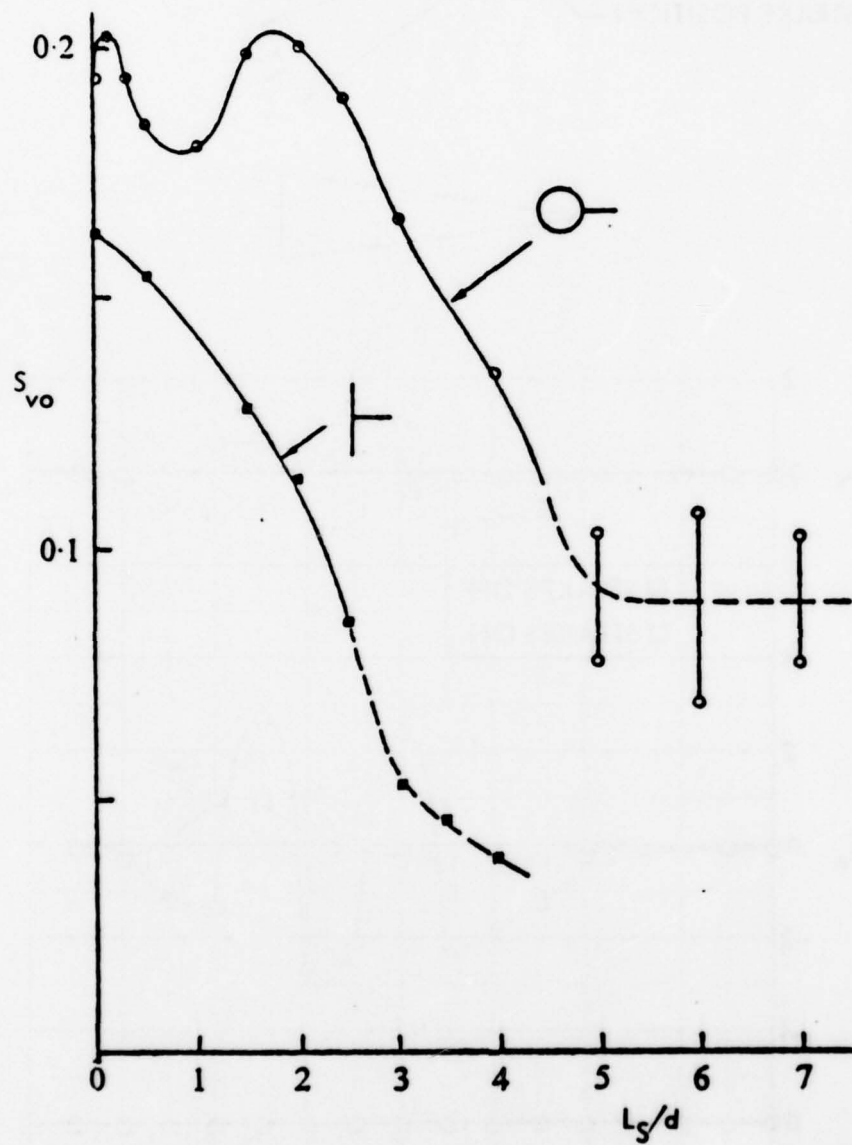
Fig. 130 Effect of Splitter Plate Length on Vortex Shedding (Ref. 212)
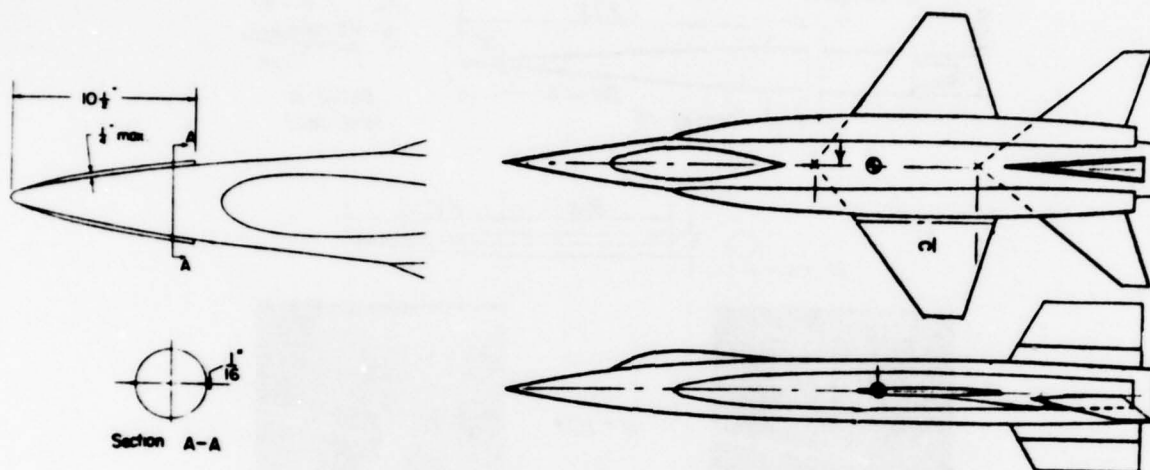
Fuselage forebody strake installation
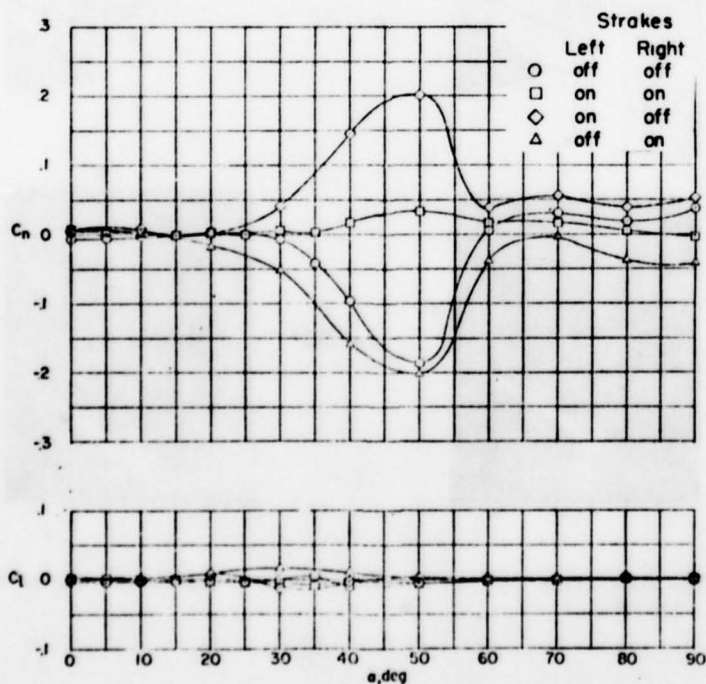
Fig. 131 Effect of Strakes on the Variation of Static Lateral Coefficients
with Angle-of-Attack at Zero Sideslip (Ref. 6)

5-9
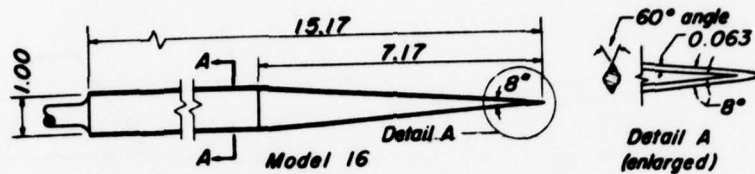
(a) Separation strips
    horizontal

(b) Model rotated 7°

Fig. 132 Vapor-Screen Pictures Showing the Effect of Strake Roll
Orientation on Asymmetric Vortex Shedding (Ref. 5)

CROSS SECTION AND DIMENSIONS
OF LONGITUDINAL TRIP
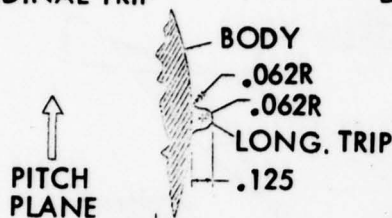
CROSS SECTION AND
DIMENSIONS OF NOSE RING

BODY
.062R
.062R
LONG. TRIP
.125

PITCH
PLANE

NOSE RING BODY
0.125
.125
1.00

NOSE
RING
1.00
30.535

SIDE-FORCE COEFFICIENT

FULL LENGTH TRIP

$M_\infty = 0.57$
$R_d = 1.35 \times 10^6$

FORWARD
HALF
CENTER
THIRD

NO
TRIP

AFT HALF

NOSE RING TRIP

NO TRIP

ANGLE OF ATTACK, DEGREES
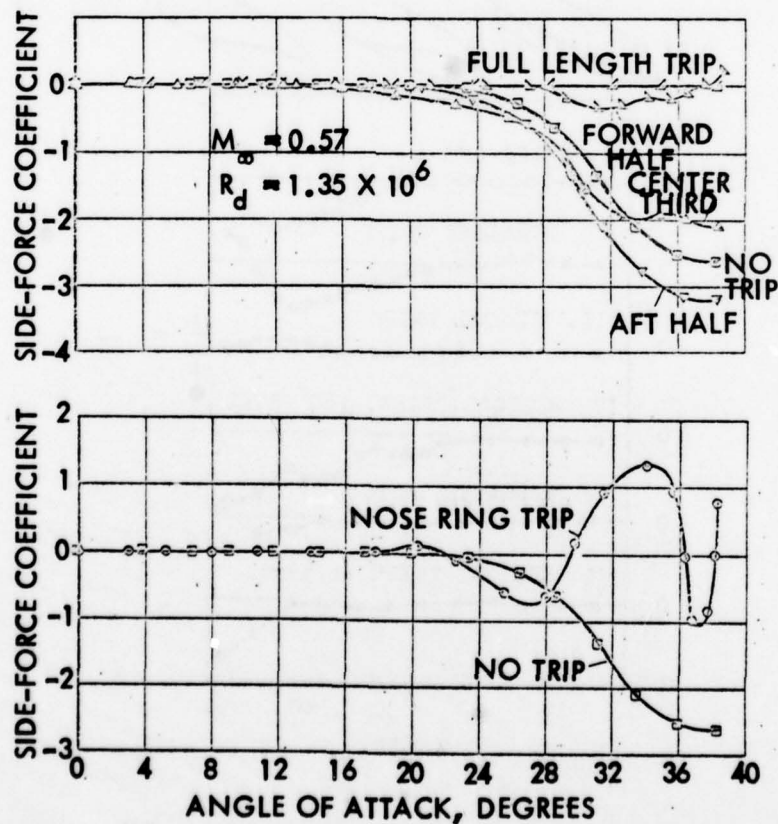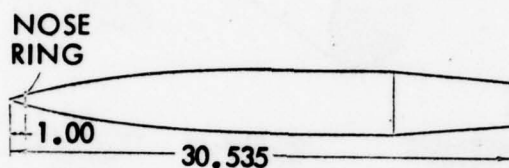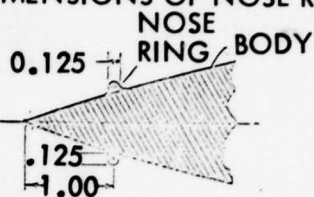
Fig. 133 Effects of Body Trips and Nose Ring Trip on Vortex-Induced
Side Force (Ref. 8)

5-11
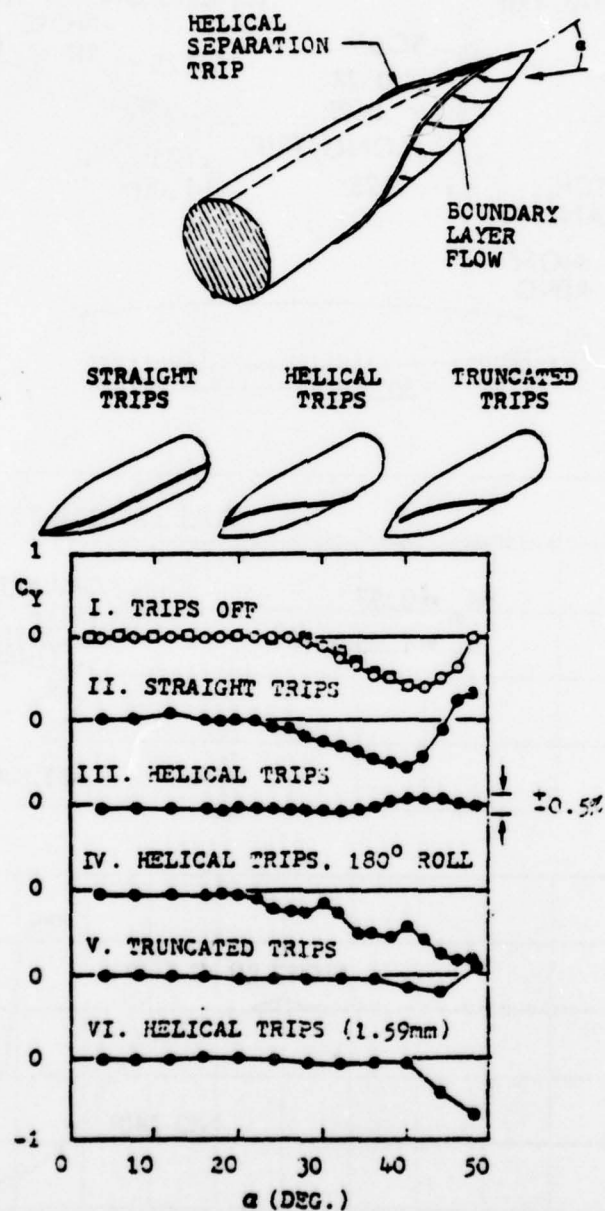
Fig. 134 Effect of Helical and Straight Body Trips on Vortex-Induced
Side Force at $R_d = 0.47 \times 10^6$ (Ref. 39)
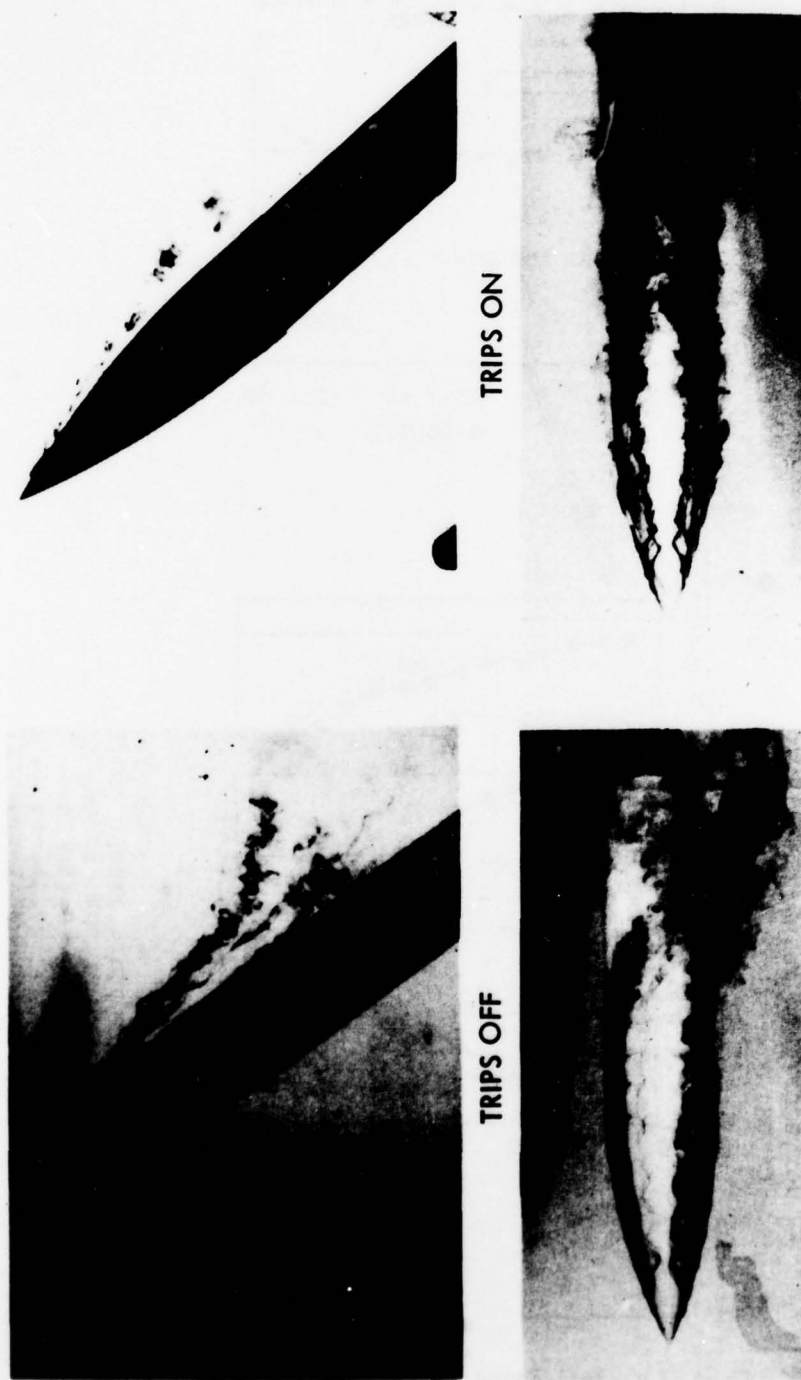
Fig. 135 Flow Pictures of Helical Trip Effect at $\alpha = 50°$ (Ref. 39)

5-13
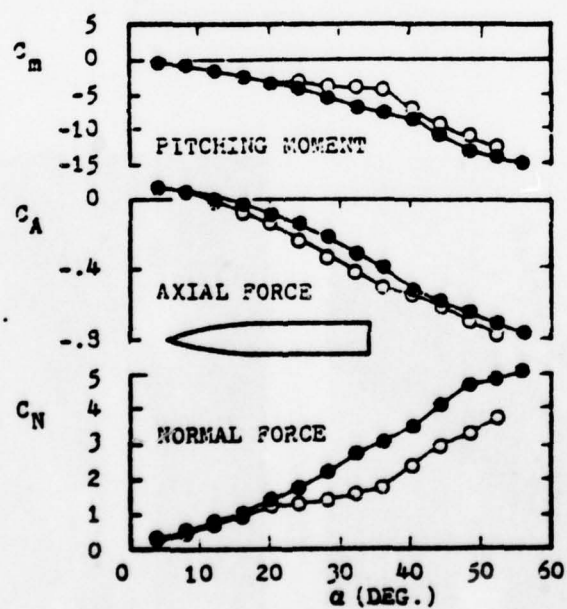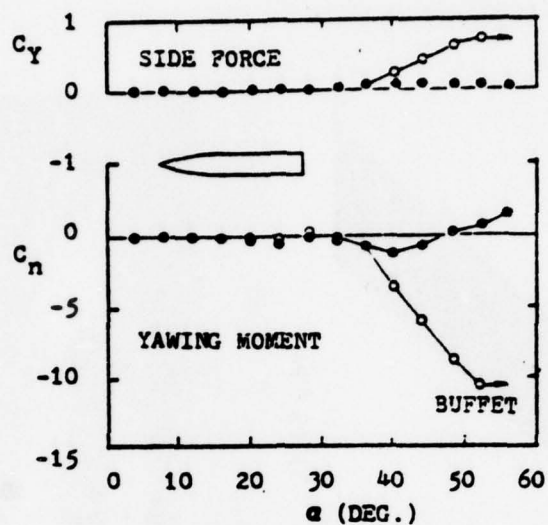
Fig. 136 Effect of Helical Trips on Vortex-Induced Aerodynamic
Characteristics (Ref. 39)

decreased. The question is: Why do the helical trips work, while the straight trips, who have proven effective in other tests (Ref. 8 and Fig. 133), do not (Fig. 134)? The clue lies in the test Reynolds number, $R_d = 0.47 \times 10^6$. Going back to the transition reversal effects discussed earlier (Ref. 112 and Figs. 23, 24), one finds that Rao's test conditions belong to Group 3. That is, the test was performed at a low supercritical Reynolds number where a disturbance such as the upstream moving wall in Swanson's case (Ref. 112 and Fig. 23) or the helical trip in Rao's case, can change the local flow conditions from supercritical to subcritical if the disturbance is large enough. The force data in Fig. 136 confirm that the helical trip indeed changes conditions towards the subcritical region. Not only does the trip effectively eliminate the vortex-induced side force and side moment but it also increases normal and axial forces and generates a more stabilizing pitching moment. The increased normal force (with associated improvement of the static stability) is a result of the increased cross flow drag for subcritical conditions (see Fig. 100 and 102), and the axial force increase is due to the loss of suction on the pointed forebody. The sketches in Figs. 137a and 137b illustrate why the helical trip might work at these test conditions, while the straight trip does not. Without a trip the supercritical-subcritical conditions expected at this Reynolds number (Fig. 105) are sketched in the left part of the figures. At the right in Fig. 137a is illustrated how the helical trip may work. Forward of Section A-A it works as a regular separation device, forcing separation to take place at the trip. However, at and behind Section A-A it acts as a pre-separation device (Ref. 213). However, in this case it is not delaying separation but delaying boundary layer transition. The effective Reynolds number of the reattaching flow is lessened because of the shortened approach length between reattachment and the lateral meridian, and subcritical separation takes place.

The straight, longitudinal trip (Fig. 137b) was ineffective because of the near critical Reynolds number. In supercritical flow, when transition occurs aft of the lateral meridian on one side the addition of the trip will only fix the subcritical separation. If the Reynolds number is substantially higher, as in Brown's test (Ref. 8 and Fig. 133), transition occurs well
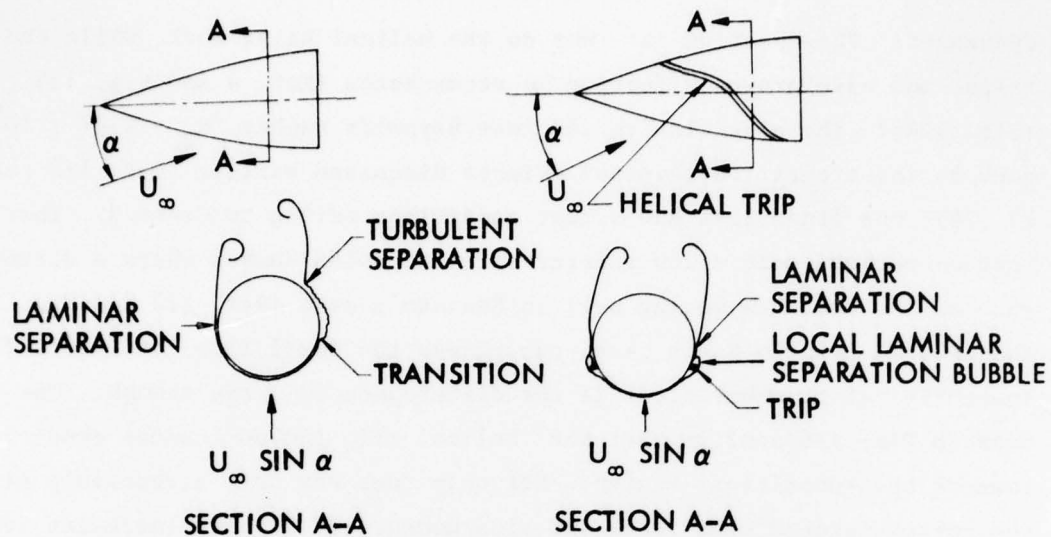
a. HELICAL TRIP
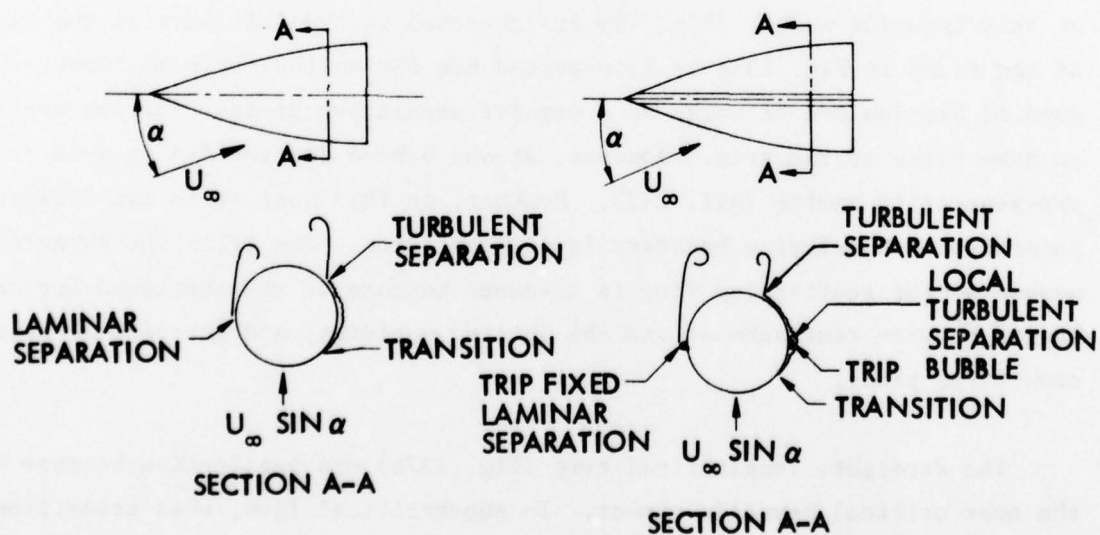
b. STRAIGHT TRIP

Fig. 137 Sketch of Trip Effect on Flow Separation

forward of the lateral meridian and the trip causes a local turbulent pre-separation, which only serves to delay the turbulent separation (Ref. 213), thereby reducing the potential for vortex-induced side forces. However, at the near critical test condition of Rao's test (Ref. 39 and Fig. 137b), the trip helps in the establishment of a supercritical-subcritical flow geometry, fixing laminar separation on one side and causing delayed supercritical separation on the other. Thus, the helical trip may work as a fix only in the critical Reynolds number range and the straight, longitudinal trip only outside of this range. That the inverted helical trips did not work (Fig. 134) is not surprising, as they more or less lined up with the local streamlines at the high angles-of-attack of interest, $\alpha > 25^\circ$ (see Fig. 98).

In regard to the relative merits of the various devices for side-load alleviation one notices, of course, that nose bluntness is the simplest and works whether or not the vehicle flies coordinated maneuvers. Daniels (Ref. 40) has shown that the nose bluntness effectiveness can be amplified by downstream diameter changes (backward facing steps and cylindrical cavities). Nose surface roughness is also likely to have a significant effect. For fixes such as strakes and body trips there may often be penalties to pay in regard to directional stability. Titiriga and Skow (Ref. 23) show that although a regular nose strake can eliminate the vortex-induced side moment as well as their shark-nose design, the former will degrade directional stability while the latter actually enhances it (Fig. 138).
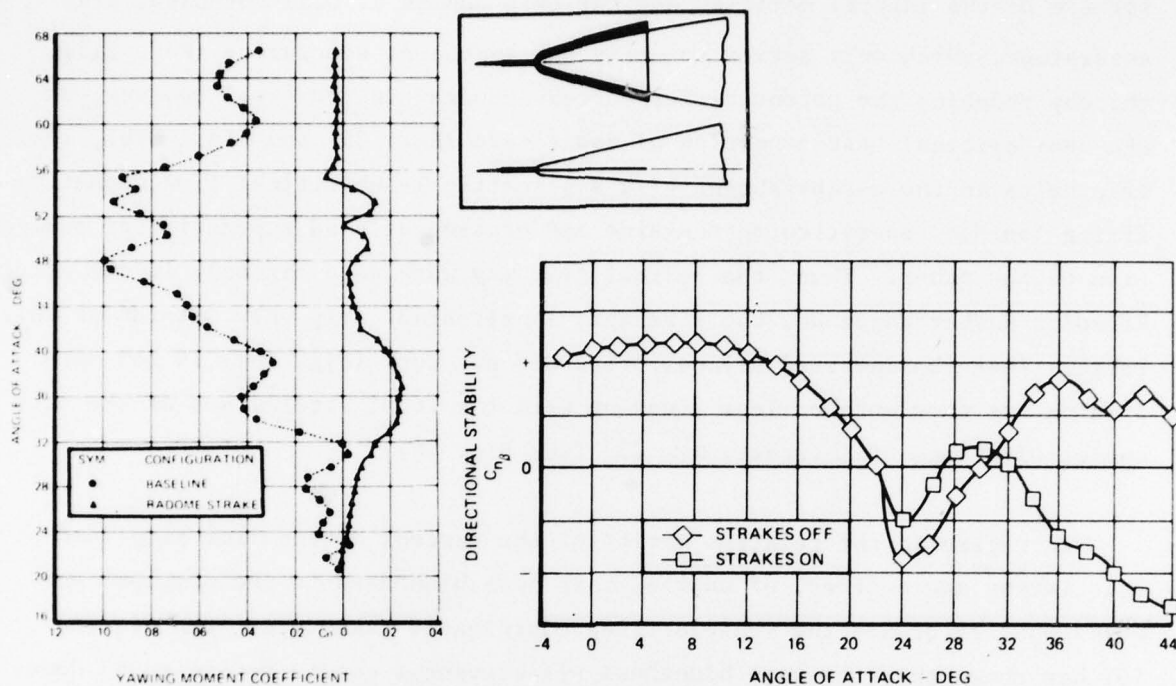
a. Effect of Nose Strake
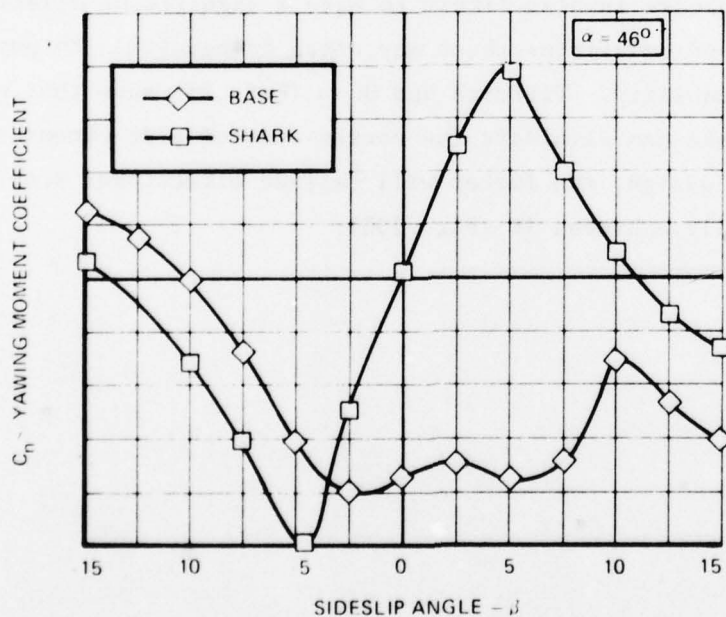
b. Effect of Shark Nose Modification

Fig. 138 Effect of Nose Strakes and Body Planform Change on Lateral
Aerodynamic Characteristics (Ref. 23)

Section 6
PROPOSED EXPERIMENTS

During the review of available experimental results, deficiencies were found in the existing data base. In addition, the analysis pointed out some new directions for experimental research. Consequently, it is recommended that the following experimental efforts be undertaken:

6-1 TWO-DIMENSIONAL CYLINDER DATA

The review of the existing data base for a circular cylinder normal to the stream showed that for the high Reynolds numbers of practical interest the results were of limited use because of compressibility effects. New tests are needed to separate compressibility and Reynolds number effects from each other in the critical and supercritical flow regimes. This can be done in the new high Reynolds number facilities that are presently available, or will be in the near future. The tests should measure steady and unsteady pressures and forces, and should whenever possible include flow visualization data.

Besides filling in an existing gap in the present data base, the results are of direct use in the present analysis for prediction of less conservative upper boundaries for the vortex-induced asymmetric loads at compressible cross-flow Mach numbers. For the same reason, it would be of interest to obtain new information about the effect of roughness in the critical and supercritical flow regimes, where compressibility effects have not had the opportunity to distort the roughness effects (together with the effects of Reynolds number).

6-2 THREE-DIMENSIONAL INCLINED BODY DATA

Also here the review of existing data revealed that there is a lack of information about the vortex-induced asymmetric loads in the critical and

supercritical flow regimes of practical interest. The problem of separating compressibility and Reynolds number effects from each other is the same as in the two-dimensional case. Therefore, tests are needed in present and future high Reynolds number test facilities in which static pressure distributions and six degrees of freedom balance data will be obtained, as well as flow visualization data, whenever possible.

More investigative efforts are needed to define in more detail the flow near apex. The cone data in Fig. 80 show that tests on models that include only a small portion of the cone or ogive body aft of the apex could reveal flow details otherwise not obtainable because of model size and Reynolds number limitations. The effect of roughness in the apex region would be of practical interest. Not only flight hardware type of roughness should be tested but also extreme roughness of the Jimsphere type. If extreme roughness would bring the separation lines of the cone-cylinder in Fig. 80 toward those of the ogive-cylinder, extreme roughness would be a means of eliminating the large side loads. It is, of course, also possible that flight hardware type roughness may be extreme in relation to body and boundary layer dimensions near apex. In that case tests of subscale models with polished nosetips would be totally misrepresentative of full scale flight conditions.

In regard to fixes for the vortex-induced side loads, Fig. 80 points out one possibility, i.e., substituting the tip of the conic nose ($\theta_A = 5.8°$) by that of the ogival nose ($\theta_A = 13.8°$). One has reason to believe that this would cause the large nose-induced vortex-asymmetry to disappear. Fig. 54 shows that for spherical nose bluntness the maximum benefit is obtained with 10 to 15 percent nose bluntness on ogival noses. Bi-conic and bi-ogival nose shapes may be more effective in reducing the vortex-induced side loads as they would cause less increase in drag.

In regard to strakes and body trips the present data base should be extended in view of the apex dominance indicated by the review of existing data. That is, small strakes and trips, located over the first few percent of the pointed nose, should be investigated. Among the trips to be tested should, of course, be Scruton's helical trips, for which the optimum number may be different on a cone from what it was on his cylindrical smoke stacks (Ref. 214).

According to the results available (Ref. 35) the effect of a nose boom is to eliminate or greatly reduce the vortex-induced side loads for pointed noses, and to insignficantly influence the beneficial effect of nose bluntness. What needs to be investigated is to what extent boom vibrations (on top of support and model vibrations in a subscale test) affect the boom effectiveness. One could envision that the vibrations would effectively enlarge the shear layer that is "burying" the micro-asymmetries at apex.

Finally, tests need to be performed to find out more about support interference and the possibility of minimizing if not eliminating it. The interference may come from bulky supports for wake probing instrumentation as well as from the model support itself. This problem can no longer be ignored as there is evidence indicating that much of the presently available experimental results for missiles and aircraft at high angles of attack is distorted by support interference (Ref. 162). Because of our complete dependence on experiments in this flight regime the problem of support interference must be solved before meaningful progress can be made.

Section 7

CONCLUSIONS

The study which consisted of a review of pertinent two-dimensional and three-dimensional data, the development of analytic means for prediction of the upper limit for vortex-induced asymmetric loads, and the assessment of the importance of vortex-induced asymmetric loads on the vehicle dynamics has given results leading to the following conclusions:

7-1 TWO-DIMENSIONAL FLOW

- The vortex shedding frequency for a stationary, circular cylinder is defined by a Strouhal number that is close to 0.20 for subcritical flow, $10^3 < R_d < 2 \times 10^5$, and approximately 0.28 for supercritical flow $R_d > 3.5 \times 10^6$. In the transcritical Reynolds number range, $2 \times 10^5 \leq R_d \leq 3.5 \times 10^6$, the wake is random in character, and the various measured discrete frequencies are caused by peculiar test conditions and measurement techniques, as is discussed in the main text. Using von Karman's stability criterion the changes in shedding frequency taking place between subcritical and supercritical flow and due to Mach number effects can be predicted from the occurred changes in flow separation geometry.

- On a spinning cylinder the wall-jet-like effect of the moving wall delays separation as well as boundary layer transition. The measured positive lift at subcritical conditions as well as the negative lift in the critical and low supercritical flow regions can be explained by this "wall-jet" effect.

- The vortex shedding process can be driven off its Strouhal frequency by translatory oscillations at near resonant frequencies, the effect being

highly dependent upon the translatory amplitude. The coupling between translatory oscillations and vortex shedding leading to self-excited oscillations is strongly affected by whether or not the separation point is free to move or is fixed by the geometry.

- Also longitudinal oscillations can drive the vortex shedding off its basic frequency. However, in this case "lock-in" does not occur at near resonant frequencies but first when the forcing frequency exceeds the second harmonic, $f > 2 f_{vo}$. There appears to be no mechanism for self-excited longitudinal oscillations.

- Translatory oscillations at frequencies near the odd number super- and subharmonics of the resonant frequency will also influence the vortex shedding appreciably. Similar strong coupling is also to be expected for longitudinal oscillations at even number super- and subharmonics.

- The selectivity of the locking-on process in regard to super- and subharmonics for translatory and longitudinal oscillations can be explained by the wall-jet-like effect of the moving wall discussed in detail for the spinning cylinder.

- Side walls and end plates are found to have a significant effect on the steady and unsteady aerodynamic characteristics of a circular cylinder.

7-2 THREE-DIMENSIONAL FLOW

- A blunt-nosed cylinder at high angle-of-attack generates a stationary asymmetric vortex array that is similar to the unsteady von Karman vortex street in two-dimensional flow. This space-time equivalence is possible because the vortices have an axial degree of freedom for their lift-off to make up the asymmetric array.

- On a pointed slender body the first asymmetric vortex pair originates at the apex and the above analogy no longer applies. The fluid mechanic instability mechanism leading to the vortex asymmetry is instead likely

7-2

to be similar to the one existing on narrow delta wings. As in the case of the delta wings the apex angle is the correct normalizing unit for the effect of angle-of-attack on the vortex generation. This is true also when the pointed, slender nose is followed by a cylindrical aft body.

- The maximum vortex-induced side force occurs at a critical Reynolds number where fully subcritical conditions are reached on one side and fully supercritical on the other. This critical Reynolds number varies between test facilities, and also with the angle-of-attack in the same test facility. This occurs because every facility has its own noise and turbulence topography, where the disturbances generated by the tunnel wall boundary layers play an important role.

- Surface roughness has a large influence on the vortex-induced asymmetric loads. Invisible, microscope irregularities in the nosetip region appear to control the asymmetric vortex shedding process, according to the observed effects of rolling the nosetip.

- Mach number is a significant parameter. The vortex-induced side loads decrease with increasing subsonic crossflow Mach number. At transonic speeds nose-induced separation inhibits the generation of asymmetric vortices on the forebody. At hypersonic speeds the nose-bluntness-generated entropy wake plays a similar role. For pointed noses, however, the available experimental data indicates that significant vortex-induced side loads can be generated at supersonic speeds.

- On a pointed slender body the vortex-induced asymmetric loads can be reduced greatly and sometimes eliminated completely by use of small nose bluntness, nose boom, nose strakes or body trips. Whereas the two first devices have general applicability, the nose strakes are effective only for vehicles flying coordinated maneuvers, and to be effective the trip design has to be different in the transcritical Reynolds number region from what it is at sub- or supercritical flow conditions.

- Spin has a significant effect on boundary layer transition which in turn plays a dominant role in the generation of large asymmetric loads.

- Coning has the effect of tilting the symmetric vortex pair an angle equal to the relative side wind angle at the apex (induced by the coning motion). At an angle-of-attack near the one where vortex asymmetry occurs in the static case the vortices go asymmetric in a direction determined by the coning motion and the Reynolds number. In the critical Reynolds number region the same reversal observed in regard to two-dimensional Magnus effects occurs also here.

- Pitch rate, like coning, has a large effect on the vortex shedding and associated in-plane loads. There are indications that also the out-of-plane loads, the side loads, may be affected, but the evidence is so far insufficient for any firm conclusions. However, the longitudinal unsteady aerodynamics are completely dominated by the coupling between the pitching motion and the vortex generation. As expected, in the critical Reynolds number region the pitch rate effects are reversed. The resulting negative damping contribution can be up to two orders of magnitude larger than the attached flow (body alone) positive damping.

- Model support interference is often a problem in wind tunnel tests. It is especially difficult in tests of bodies at high angles-of-attack, where the vortices, which often generate the dominant loads on the model, interact with the downstream support. This problem has so far been ignored both by missile and aircraft industry. Available results indicate that in many cases the asymmetric loads measured on a wind tunnel model are generated by the downstream support. This is a difficult problem that cannot be ignored.

7-3 ANALYTICAL DEVELOPMENTS

- Existing theories can usually not predict the experimentally observed aerodynamic characteristics generated by asymmetric vortices. They can

often not even repredict the experimental results which were used to determine empirical constants in the theory. The reason for this sad state of affairs is that almost all geometries of practical interest have a pointed, slender nose, and the assumptions used in the theory do not apply. The impulsively started cylinder analogy predicts asymmetric vortex shedding to start at $\alpha_{AV} \approx 4 \theta_A$ whereas experimental data show $\alpha_{AV} \approx 2 \theta_A$. Furthermore, the analogy predicts the vortex generating the largest asymmetric load to be shed at $\alpha_{peak} \approx 8.5 \theta_A$, whereas experiments show $\alpha_{peak} = \alpha_{AV} = 2 \theta_A$. In the case of the von Karman vortex street analogy similar difficulties exist, as there is no means available to represent the pointed nose. Consequently, the nose is more or less ignored in the theoretical developments, whereas experimental evidence shows that it not only generates the largest side load but also controls the asymmetric vortex geometry that can exist on the aftbody.

- In the present study a new method has been developed to account for the effect of sweep on the viscous flow characteristics on a circular cylinder. The developed method is found to be superior to other available methods in correlating Reynolds number effects, in particular in regard to the definition of the critical Reynolds number region.

- Through this effective Reynolds number two-dimensional unsteady experimental results can be used to determine the upper bounds for the vortex-induced side loads on an inclined, slender missile body. The peak unsteady lift to steady drag ratio on a cylinder normal to the (two-dimensional) flow is used as the upper limit for the side force to normal force ratio of the inclined body of revolution in three-dimensional flow. The boundary determined in this manner bounds all available experimental sectional load data.

- The distribution over the cylindrical aftbody of the vortex-induced side force was found to be triangular in shape, whereas the normal force distribution was rectangular. This indicated that the side force

to normal force ratio for the total loads could only be half of the
maximum sectional load ratio. The boundary determined in this way
encloses all available experimental data.

- The triangular and rectangular load distributions over the cylinder
  were used as area weighting functions for the vortex-induced loads on
  pointed slender noses. The centers of pressure for the nose loads,
  calculated in this manner, agree with experimental results when the
  effect of the base wake has been accounted for using analytic methods
  developed earlier for slender delta wings.

- The coupling between vehicle motion and vortex generation is very
  significant. When boundary layer transition occurs, causing the vortex-
  induced asymmetric loads to reach their peak, the coupling becomes
  especially strong. It is possible that a particular vehicle maneuver
  could "lock-in" the maximum crossflow asymmetry over an extended portion
  of the vehicle thereby potentially increasing the asymmetric loads by
  100 percent.

- One important effect of the asymmetric vortices is to provide a coupling
  mechanism between longitudinal and lateral degrees of freedom, even at
  zero sideslip. Forebody pitching generates side forces on downstream
  missile body and tail surfaces. These cross-coupling effects have been
  found to be very nonlinear, often discontinuous and associated with
  hysteresis effects, with large impact on the vehicle dynamics. They
  are for these reasons presently causing missile and aircraft designers
  great concern.

Section 8

RECOMMENDATIONS FOR FURTHER STUDY

Among the many areas in need of further study, uncovered by the present study, the following are mentioned because of their immediate impact on the flight operations of missiles and aircraft at high angles-of-attack.

Compressibility has been found to have a profound effect on the vortex-induced asymmetric loads. In view of this the present method for estimation of maximum possible side loads should be extended to include the effects of compressibility, thereby providing more realistic load limits for actual flight conditions.

Reynolds number effects in the supercritical region are in need of further study, in particular in conjunction with the secondary flow separation and the loads induced by it.

It is clear that theoretical efforts to predict the vortex induced asymmetric loads have been failing because they have been concentrated on the vortices generated on the aft body, which are of importance only for blunt-nosed slender bodies. Practical missile geometries and aircraft noses usually have very slender, pointed noses. The evidence available clearly indicates that the nose-generated vortices not only generate the largest asymmetric loads but also control the vortex shedding on a cylindrical aftbody. Consequently, new theoretical efforts are needed aimed at the nose-induced asymmetric vortices. Preliminary results indicate that a fruitful theoretical approach is to compare the apex dominated vortex shedding on a pointed body with the apex dominated vortex generation on narrow delta wings.

Experimental evidence indicates that the generative process of symmetric and asymmetric vortices is strongly coupled with the vehicle motion. When boundary layer transition is one of the fluid mechanical processes involved, which it is at critical and supercritical Reynolds numbers, the flow regimes of practical interest, the coupling becomes especially strong. Analytic efforts are needed to improve our understanding of these problems. In a first effort limiting loads, as derived in the present report, could be determined for vehicle motions and maneuvers of practical interest. Of particular importance is to define the cross-coupling provided by the asymmetric vortices between longitudinal and lateral degrees of freedom.

Section 9
REFERENCES

1. Allen, H. J. and Perkins, E. W., "Characteristics of Flow Over Inclined Bodies of Revolution," NACA RM A50L07 (1951).

2. Allen, H. J. and Perkins, E. W., "A Study of Effects of Viscosity on Flow Over Slender Inclined Bodies of Revolution," NACA Report 1048 (1951).

3. Gapcynski, J. P., "An Experimental Investigation of the Flow Phenomena Over Bodies at High Angles of Attack at a Mach Number of 2.0," NACA RML55H29, Oct. 1955.

4. Maltby, R. L. and Peckham, D. H., "Low Speed Flow Studies of the Vortex Patterns Above Inclined Slender Bodies Using a New Smoke Technique," RAE-AERO-TN-2482, March 1957, ARC Great Britain.

5. Gowen, F. E. and Perkins, E. W., "A Study of the Effect of Body Shape on the Vortex Wakes of Inclined Bodies at a Mach Number of 2," NACA RM A53I17, Dec. 1958.

6. Hassel, J. L., Jr. and Hewes, D. E., "Investigation of the Subsonic Stability and Control Characteristics of a 1/7 Scale Model of the North American X-15 Airplane With and Without Fuselage Forebody Strakes," NASA TM X-210, Feb. 1960.

7. Thomson, K. D. and Morrison, D. F., "On the Asymmetric Vortex Shedding from Slender Cylindrical Bodies at Large Angles of Yaw," Tech. Note HSA 106, May 1965, Weapon Res. Est., Australia.

8. Brown, R. C., "On the Asymmetrical Aerodynamic Forces of Slender Bodies of Revolution," Proceedings of BOWACA Meeting, 1965, McDonnell Aircraft Corp., St. Louis, Missouri.

9. Ohman, L. H., "Some Results of W.T. Tests on Sounding Rocket Configurations in the NAE 5 x 5 Ft. Trisonic Wind Tunnel," CASI 1966.

10. Curry, W. H. and Reed, J. F., "Measurements of Magnus Effects on a Sounding Rocket Model in a Supersonic Wind Tunnel," AIAA Paper No. 66-754, Sept. 1966.

11. Fiechter, M., "Uber Wirbelsysteme an schlanken Rotationskörpern und ihren Einfluss auf die aerodynamischen Beiwerte," Bericht 10166, Dec. 1966, Deutsch-Französisches Forchungsinstitut, Saint Louis, France.

12. Atraghji, E. G., "The Influence of Mach Number, Semi-Nose Angle and Roll Rate on the Development of the Forces and Moments over a Series of Long Slender Bodies of Revolution at Incidence," NAE Data Report 5 x 5/0020, 1967, National Research Council, Ottawa, Canada.

13. Fiechter, M., "Wirbelsysteme schlanker Rotationskörper und die Aerodynamische Kräfte," Jahrbuch der Deutschen Gesellschaft für Luft-und Raumfahrt, 1969, pp. 77-85.

14. Pick, G. S., "Investigation of Side Forces on Ogive-Cylinder Bodies at High Angles of Attack in the M = 0.5 to 1.1 Range," AIAA Paper No. 71-570, June 1971.

15. Castell, G. R. and Weyl, C. J., "A Design Approach to Provide Satisfactory Spin Characteristics for a Modern Fighter Aircraft," AIAA Paper No. 70-928, July 1970.

16. Chambers, J. R., Anglin, E. L., and Bowman, J. B., Jr., "Effects of Pointed Nose on Spin Characteristics of a Fighter Airplane Model Including Correlation with Theoretical Calculations," NASA TN-D5921, Sept. 1970.

17. Chambers, J. R. and Bowman, J. S., Jr., "Recent Experience with Techniques for Prediction of Spin Characteristics of Fighter Aircraft," Journal of Aircraft, Vol. 8, No. 7, July 1971, pp. 548-553.

18. McElroy, G. E. and Sharp, P. S., "An Approach to Stall/Spin Development and Test," AIAA Paper No. 71-772, July 1971.

19. Jorgensen, L. H. and Nelson, E. R., "Experimental Aerodynamic Characteristics for a Cylindrical Body of Revolution with Various Noses at Angles of Attack from 0 to 58° and Mach Numbers from .6 to 2.0," NASA TM X-3128, Dec. 1974.

20. Jorgensen, L. H. and Nelson, E. R., "Experimental Aerodynamic Character-
istics for Bodies of Elliptic Cross Section at Angles of Attack from 0 to
$58°$ and Mach Numbers from .6 to 2.0," NASA TM X-3129, Feb. 1975.

21. Kao, H. C., "Side Forces on Unyawed Slender Inclined Aerodynamic Bodies,"
Journal of Aircraft, Vol. 12, No. 3, March 1975, pp. 142-150.

22. Chapman, G. T., Keener, E. R. and Malcolm, G., "Asymmetric Aerodynamic
Forces on Aircraft Forebodies at High Angles of Attack - Some Design Guides,"
Paper No. 16, AGARD Meeting on Stall/Spin Problems of Military Aircraft,
Ames Res. Ctr., Moffett Field, Calif., Nov. 18-21, 1976.

23. Titiriga, A. and Skow, A. M., "Analytical and Experimental Techniques to
Predict Aircraft Dynamic Characteristics at High Angles of Attack," Paper
No. 19, AGARD Meeting on Dynamic Stability Parameters, Athens, Greece,
May 22-24, 1978.

24. Chambers, J. R., Gilbert, W. P., and Nguyen, L. T., "Results of Piloted
Simulator Studies of Fighter Aircraft at High Angles of Attack," Paper
No. 33, AGARD Meeting on Dynamic Stability Parameters, Athens, Greece,
May 22-24, 1978.

25. Briggs, M. M., Clark, W. H., and Peoples, J. R., "Occurrence and Inhibition
of Large Yawing Moments During High Incidence Flight of Slender Missile
Configurations," J. Spacecraft and Rockets, Vol. 10, No. 8, Aug. 1973,
pp. 510-519.

26. Coe, P. L., Jr., Chambers, J. R., and Letko, W., "Asymmetric Lateral-
Directional Characteristics of Pointed Bodies of Revolution at High
Angles of Attack," NASA TN D-7095, Nov. 1972.

27. Keener, E. R. and Chapman, G. T., "Onset of Aerodynamic Side Forces at
Zero Sideslip on Symmetric Forebodies at High Angles of Attack," AIAA
Paper No. 74-770, Aug. 1974.

28. Smith, L. H., "Aerodynamic Characteristics of an Axisymmetric Body Under-
going a Uniform Pitching Motion," Ph.D. Thesis, Naval Postgraduate School,
Monterey, Calif., Dec. 1974.

29. Nelson, R. C. and Fleeman, E. L., "High Angle-of-Attack Aerodynamics on a

Slender Body with a Jet Plume," J. Spacecraft and Rockets, Vol. 12, No. 1, pp. 12-16, Jan. 1975.

30. Keener, E. R. and Taleghani, J., "Wind Tunnel Investigations of the Aerodynamic Characteristics of Five Forebody Models at High Angles of Attack at Mach Numbers from 0.25 to 2," NASA TM X-73,076, Dec. 1975.

31. Clark, W. C. and Nelson, R. C., "Body Vortex Formation on Missiles at High Angles of Attack," AIAA Paper No. 76-65, Jan. 1976.

32. Keener, E. R., Chapman, G. T. and Kruse, R. L., "Effects of Mach Number and Afterbody Length on Onset of Asymmetric Forces on Bodies at Zero Sideslip and High Angles of Attack," AIAA Paper No. 76-66, Jan. 1976.

33. Lamont, P. J. and Hunt, B. L., "Pressure and Force Distributions on a Sharp-Nosed Circular Cylinder at Large Angles of Inclination to a Uniform Subsonic Stream," J. Fluid. Mech., Vol. 76, Part 3, Aug. 1976, pp. 519-559.

34. Uselton, B. L. and Jenke, L. M., "Test Mechanism for Obtaining Dynamic Stability Characteristics of High Fineness Ratio Bodies at Angles of Attack up to 90 Degrees," Proceedings of the AIAA 9th Aerodynamic Test. Conf., Arlington, Texas, June 7-9, 1976, pp. 76-90.

35. Keener, E. R., Chapman, G. T., Cohen, L., and Taleghani, J., "Side Forces on a Tangent-Ogive Forebody with a Fineness Ratio of 3.5 at High Angles of Attack and Mach Numbers from 0.1 to 0.7," NASA TMX-3437, Feb. 1977.

36. Keener, E. R., Chapman, G. T., Cohen, L., and Taleghani, J., "Side Forces on Forebodies at High Angles of Attack and Mach Numbers from 0.1 to 0.7. Two Tangent Ogives, Parabolid and Cone," NASA TMX-3438, Feb. 1977.

37. Clark, W. H., "Body Vortex Formation on Missiles in Incompressible Flows," AIAA Paper No. 77-1154, Aug. 1977.

38. Faherty, J. I., "Experimental and Analytical Investigation of High Angle of Attack Missile Aerodynamics," AIAA Paper No. 77-1156, Aug. 1977.

39. Rau, D. M., "Side-Force Alleviation on Slender, Pointed Forebodies at High Angles of Attack," AIAA Paper No. 78-1339, Aug. 1978.

40. Daniels, P., "Ogive Cylinder Modified for Near Minimum Side Moment,"

Paper 37, 11th Navy Symposium on Aeroballistics, NADC, Warminster, Penn., Aug. 1978

41. Hunt, B. L. and Dexter, P. C., "Pressures on a Slender Body at High Angle of Attack in a Very Low Turbulence Level Airstream," Paper No. 17, AGARD Symposium on High Angle of Attack Aerodynamics, Sandefjord, Norway, 4-6 October, 1978.

42. Peake, D. J., Owen, F. K., and Higuchi, H., "Symmetrical and Asymmetrical Separations about a Yawed Cone," Paper No. 16, AGARD CP-247, AGARD Symposium on High Angle of Attack Aerodynamics, Sandefjord, Norway, 4-6 Oct. 1978.

43. Thomson, K. D. and Morrison, D. F., "The Spacing, Position and Strength of Vortices in the Wake of Slender Cylindrical Bodies at Large Incidence," J. Fluid. Mech., Vol. 50, Part 4, 1971, pp. 751-783.

44. Fiechter, M., "Kegelpendelung, Autorotation und Wirbelsysteme schlanker Flugkörper," Z. Flugwiss, Vol. 20, No. 8, Aug. 1972, pp. 281-292.

45. Thomson, K. D., "The Estimation of Viscous Normal Force, Pitching Moment, Side Force and Yawing Moment on Bodies of Revolution at Incidences up to 90°," WRE-Report-782, Oct. 1972, Australia.

46. Lamont, P. J. and Hunt, B.L., "Out-of-Plane Force on a Circular Cylinder at Large Angles of Inclination to a Uniform Stream," Aeronautical Journal, Vol. 69, Jan. 1973, pp. 41-45.

47. Wardlaw, A. B., Jr., "Prediction of Normal Force, Pitching Moment, and Yawing Force on Bodies of Revolution at Angles of Attack up to 50 Degrees Using a Concentrated Vortex Flow-Field Model," NOL TR 73-209, Oct. 1973.

48. Jorgensen, L. H., "Prediction of Static Aerodynamic Characteristics for Space Shuttle Like and Other Bodies at Angles of Attack from 0° to 180°," NASA TN D-6996, Jan. 1973.

49. Kubin, J. S., "An Analysis of Steady Asymmetric Vortex Shedding from a Missile at High Angles of Attack," AD-774390, Nov.1973, Air Force Inst. of Tech.

50. Wardlaw, A. B., Jr., "Prediction of Yawing Force at High Angle of Attack," AIAA Journal, Vol. 12, No. 8, Aug. 1974, pp. 1142-1144.

51. Fidler, J. E. and Bateman, M. C., "Asymmetric Vortex Effects on Missile Configurations," J. Spacecraft and Rockets, Vol. 12, No. 11, Nov. 1975, pp. 674-681.

52. Atraghji, E., "A Method for Estimating the Loading Distribution on Long Slender Bodies of Revolution at High Incidence in Incompressible Flow," Paper No. 14, AGARD CP-204, AGARD Symposium on Prediction of Aerodynamic Loading, Ames Research Center, Moffett Field, Calif., Sept. 1976.

53. Wardlaw, A. B., Jr. and Morrison, A. M., "Induced Side Forces at High Angles of Attack," NSWC/WOL/TR 75-176, Nov. 1975.

54. Lamont, P. J. and Hunt, B. L., "Prediction of Aerodynamic Out-of-Plane Forces on Ogive-Nosed Circular Cylinders," J. Spacecraft and Rockets, Vol. 14, No. 1, Jan. 1977, pp. 38-44.

55. Anderson, C. A., "Stall/Post-Stall Characteristics of the F-111 Aircraft," Paper 18, AGARD CP-102, AGARD Conference on Fluid Dynamics of Aircraft Stalling, Lisbon, Portugal, 25-28 April, 1972.

56. Wardlaw, A. B., Jr. and Morrison, A. M., "Induced Side Forces at High Angles of Attack," J. Spacecraft and Rockets, Vol. 13, No. 10 Oct. 1976, pp. 589-593.

57. Hunt, B. L. and Lamont, P. J., "Comment on Induced Side Forces at High Angles of Attack," J. Spacecraft and Rockets, Vol. 14, No. 5, May 1977, p. 319.

58. Rainbird, W. J., "Turbulent Boundary-Layer Growth and Separation on a Yawed Cone," AIAA Journal, Vol. 6, No. 12, Dec. 1968, pp. 2410-2416.

59. Rainbird, W. J., Crabbe, R. S., and Jurewicz, L. S., "A Water Tunnel Investigation of the Flow Separation About Circular Cones at Incidence," Aero Report LR-385, Sept. 1963, Nat. Res. Council, Ottawa, Canada.

60. Tracy, R. R., "Hypersonic Flow Over a Yawed Circular Cone," CIT/GAL No. 69, Aug. 1963, California Inst. of Tech., Pasadena, California.

61. Stetson, K. J. and Ojadana, E. S., "Hypersonic Laminar Boundary Layer Separation on a Slender Cone at Angle of Attack," AIAA Journal, Vol. 10, No. 5, May 1972, pp. 642-648.

62. Rainbird, W. J., "The External Flow Field About Yawed Circular Cones," Paper 19, AGARD CP-30, AGARD Meeting on Hypersonic Boundary Layers and Flow Fields, May 1-3, 1968, London, England.

63. Rainbird, W. J., "Private Communication of Unpublished Data on Vortex-Induced Asymmetric Loads on a 5° Cone at Mach Numbers from 0.51 to 4.27," April 5, 1968.

64. Nebbeling, C. and Bannink, W. J., "Experimental Investigation of Supersonic Flow Past a Slender Cone at High Incidence," Journal of Fluid Mechanics, Vol. 87, Part 3, Aug. 1978, pp. 475-496.

65. Thomson, K. D., "Subsonic Wing-Body Interference for Missile Configurations at Large Angles of Attack," Aer. Quart., Aug. 1977, pp. 163-175.

66. Mead, M. H., "Observations of Unsteady Flow Phenomena for an Inclined Body Fitted with Stabilizing Fins," NACA RM A51K05, Jan. 1952.

67. Gowen, F. E., "Buffeting of a Vertical Tail on an Inclined Body at Supersonic Mach Numbers," NACA RM A53A09, March 1953.

68. Morkovin, M. V., "Flow Around a Circular Cylinder - A Kaleidoscope of Challenging Fluid Phenomena," Symposium on Fully Separated Flows, Edited by A. G. Hansen, ASME, May 1964, pp. 102-118.

69. Wille, R., "On Unsteady Flows and Transient Motions," Progress Aer. Sci., Ed. D. Küchemann, Perganon Press, London, Vol. 7, 1966, pp. 195-207.

70. Berger, E. and Wille, R., "Periodic Flow Phenomena," 1972.

71. V. Karman, Th. and Rubach, H., "Über den Mechanismus des Flüssigkeits - und Luftwiderstands," Phys. Zeitschrift, Vol. 13, 1912, pp. 49-59.

72. Young, J. O. and Hall, J. W., "Effects of Cavitation on Periodic Wakes Behind Symmetric Wedges," J. Basic Eng., ASME Paper No. 65-FE-15 (1965).

73. Asher, J. A. and Dosanjh, D. S., "An Experimental Investigation of the Formation and Flow Characteristics of an Impulsively Started Vortex Sheet," J. Basic Eng., Dec. 1968, pp. 596-606.

74. Roshko, A., "On the Development of Turbulent Wakes from Vortex Sheets," NACA Report 1191, 1954.

75. Roshko, A., "Experiments on the Flow Past a Circular Cylinder at Very High Reynolds Numbers," J. Fluid, Mech., Vol. 10, 1960, pp. 345-356.

76. Kistler, A. L. and Chen, W. S., "The Fluctuating Pressure Field in a Supersonic Turbulent Boundary Layer," TR 32-277, Aug. 1962, Jet Prop. Lab., Calif. Inst. of Tech., Pasadena, Calif.

77. Roshko, A., "Structure of Turbulent Shear Flows: A New Look," 1976 Dryden Research Lecture, AIAA Paper No. 76-78, Jan. 1976.

78. Achenbach, E., "Distribution of Local Pressure and Skin Friction Around a Circular Cylinder in Cross-Flow Up to Re = 5×10^6," J. Fluid. Mech., Vol. 34, Part 4, 1968, pp. 625-639.

79. Van Nunen, J.W.G., Persoon, A. J., and Tijdeman, H., "Analysis of Steady and Unsteady Pressure and Force Measurements on a Circular Cylinder at Reynolds Numbers up to 7.7×10^6" NLR TR 69102, May 1971, NLR, Netherlands.

80. Szechenyi, E. and Loiseau, H., "Portances Instationnaires sur un Cylindre Vibrant dans un Ecoulement Supercritique," La Recherche Aérospatiale, Jan.-Feb., 1975, pp. 45-57.

81. Delany, N. K. and Sorensen, N. E., "Low-Speed Drag of Cylinders of Various Shapes," NACA TN-3038, Nov. 1953.

82. Theisen, J. G., "Vortex Periodicity in Wakes," AIAA Paper No. 67-34, Jan. 1964.

83. DiSilvio, G., Angrillo, F. and Zanardo, A., "Fluidelastic Vibrations: Mathematical Model and Experimental Result," Mechanica, Dec. 1975, pp. 269-279.

84. Modi, V. J. and Dikshit, A. K., "Near-Wakes of Elliptic Cylinders in Subcritical Flow," AIAA Journal, Vol. 13, No. 4, April 1975, pp. 490-497.

85. Birhoff, G. D., "Formation of Vortex Streets," J. Appl. Phys., Vol. 24, No. 1, 1953, pp. 98.

86. Bearman, P. W., "On Vortex Shedding from a Circular Cylinder in the Critical Reynolds Number Regime," J. Fluid Mech., Vol. 37, Part 3, 1969, pp. 577-585.

87. Relf, E. F. and Simmons, L.G.F., "The Frequency Generated by the Motion of Circular Cylinders Through A fluid," ARC R&M No. 917 (1924), Aircraft Res. Council, Great Britain.

88. Drescher, H., "Messung der auf querangeströmte Zylinder ausgeübten zeitlich veränderten Drücke," Z. Flugwiss, Vol. 4, Heft 112, 1956, pp. 17-21.

89. Varga, J. and Sebestyen, G. Y., "Determination of the Frequencies of Wakes Shedding from Circular Cylinders," Acta Technica Academiae Sci. Hungaricae 53 (1966), pp. 91-108.

90. Loiseau, H. and Szechenui, E., "Analyse Experimentale des Portances sur un Cylindre Immobile Soumis a un Ecoulement Perpendiculaire a son Axe a des Nombres de Reynolds Eleves," La Recherche Aérospatiale, Sept.-Oct., 1972, pp. 279-291.

91. Humphreys, J. S., "On a Circular Cylinder in a Steady Wind at Transition Reynolds Numbers," J. Fluid Mech., Vol. 9, Part 4, 1960, pp. 603-612.

92. Jones, G. W., Jr., Cincotta, J. C., and Walker, R. W., "Aerodynamic Forces on a Stationary and Oscillating Circular Cylinder at High Reynolds Numbers," NASA TR R-300, Feb. 1969.

93. Blenk, H. F., Fuchs, D., and Liebers, F., "Über Messungen von Wirbelfrequenzen," Luftfahrtforschung 12 (1935), pp. 38-41.

94. Fung, Y. C., "Fluctuating Lift and Drag Acting on a Cylinder in a Flow at Supercritical Reynolds Numbers," Journal Aero. Sci., Vol. 27, No. 11, Nov. 1960, pp. 801-814.

95. Dyment, A. and Gryson, P., "Etude d'Ecoulements Turbulents Subsoniques et Supercritiques par Visualization Ultra-Rapide," Paper 28, AGARD CP-227, AGARD Symposium on Unsteady Aerodynamics, Ottawa, Canada, 26-28 Sept. 1977.

96. Gerrard, J. H., "The Mechanics of the Formation Region of Vortices Behind Bluff Bodies," J. Fluid Mech. - Vol. 25, Part 2, 1967, pp. 401-413.

97. Fage, A. and Warsap, "The Effects of Turbulence and Surface Roughness on the Drag of a Circular Cylinder," ARC R&M No. 1283 (1930).

98. Schechenyi, E., "Supercritical Reynolds Number Simulation for Two-Dimensional Flow Over Circular Cylinders," J. Fluid Mech., Vol. 70, Part 3, 1975, pp. 529-542.

99. Güven, O., Patel, V. C. and Farrel, C., "A Model for High-Reynolds-Number Flow Past Rough-Walled Circular Cylinders," J. Fluids Eng., Sept. 1977, pp. 487-494.

100. Schlinker, R. H., Fink, M. R., and Amiet, R. K., "Vortex Noise from Non-Rotating Cylinder and Airfoils," AIAA Paper No. 76-81, Jan. 1976.

101. Joubert, P. N. and Hoffman, E. R., "Drag of a Circular Cylinder with Vortex Generators," J. Royal Aero. Soc., Vol. 77, July 1962, pp. 456-457.

102. Gerrard, J. H., "A Disturbance-Sensitive Reynolds Number Range of the Flow Past a Circular Cylinder," J. Fluid Mech. Vol. 22, Part 1, 1965, pp. 187-196.

103. Murthy, V. S. and Rose, W. C., "Detailed Measurements on a Circular Cylinder in Cross Flow," AIAA Journal, Vol. 16, No. 6, June 1978, pp. 542-550.

104. Naumann, A. and Pfeiffer, H., "Über die Grenzschichtablösung am Zylinder bei hohen Geschwindigkeiten," Advances in Aero. Sci., Pergamon Press, N. Y., Vol. 3, 1962, pp. 185-206.

105. Ericsson, L. E. and Reding, J. P., "Stall Flutter Analysis," J. Aircraft, Vol. 10, No. 1, Jan. 1973, pp. 5-13.

106. Ericsson, L. E. and Reding, J. P., "Unsteady Airfoil Stall and Stall Flutter," NASA CR-111906, June 1971.

107. Thomson, K. D., "The Estimation of the Drag of Circular Cylinders at Sub-critical Reynolds Numbers and Subsonic Speeds," The Aeronautical Journal, Vol. 74, Sept. 1970, pp. 762-763.

108. Thomann, H., "Measurements of the Recovery Temperature in the Wake of a

Cylinder and a Wedge at Mach Numbers Between 0.5 and 3"," FFA Report 84, 1959, The Aer. Res. Institute of Sweden.

109. Macha, J. M., "Drag of Circular Cylinder at Transonic Mach Number," J. Aircraft, Vol. 14, No. 6, June 1977, pp. 605-607.

110. Jacobson, I. D., "Magnus Characteristics of Arbitrary Rotating Bodies," AGARD-AG-171, Nov. 1973.

111. Kelly, H. R. and van Aken, R. W., "The Magnus Effect at High Reynolds Numbers," Aero. Sci., Nov. 1956, pp. 1053-1054.

112. Swanson, W. M., "The Magnus Effect: A Summary of Investigations to Date," J. Basic Eng., Sept. 1961, pp. 461-470.

113. Ericsson, L. E. and Reding, J. P., "Dynamic Stall Analysis in Light of Recent Numerical and Experimental Results," J. Aircraft, Vol. 13, No. 4, April 1976, pp. 248-255.

114. Miller, M. C., "A Technique to Measure The Pressure Distribution on the Surface of Spinning Wind Tunnel Models," Proceedings of AIAA 9th Aerodynamic Testing Conference, June 1976, pp. 91-99.

115. Parkinson, G. V. and Ferguson, N., "Amplitude and Surface Pressure Measurements for a Circular Cylinder in Vortex-Excited Oscillation at Subcritical Reynolds Numbers," Paper 18, Meeting on Ground Wind Loads, Problems in Relation to Launch Vehicles, Langley Res. Ctr., June 7-8, 1966.

116. Ferguson, N. and Parkinson, G. V., "Surface and Wake Flow Phenomena of the Vortex-Excited, Oscillation of a Circular Cylinder," J. Eng. for Industry, Nov. 1967, pp. 831-838.

117. Stansby, P. K., "The Locking-On of Vortex Shedding due to Cross-Stream Vibration of Circular Cylinders in Uniform and Shear Flows," J. Fluid Mech., Vol. 74, Part 4, 1976, pp. 641-665.

118. Koopman, G. H., "The Vortex Wakes of Vibrating Cylinders at Low Reynolds Numbers," J. Fluid Mech., Vol. 28, Part 3, 1967, pp. 501-512.

119. Mei, V. C. and Currie, I. G., "Flow Separation on a Vibrating Circular Cylinder," The Physics of Fluids, Vol. 12, No. 11, Nov. 1969, pp. 2248-2254.

120. Schindel, L. and Zartarian, G., "Some Water Table Experiments on Oscillating Cylinders," Paper 17, Meeting on Ground Wind Load Problems in Relation to Launch Vehicles, Langley Res. Ctr., June 7-8, 1966.

121. Cincotta, J. C., Jones, G. W., and Walker, R. W., "Experimental Investigation of Wind Induced Oscillation Effects on Cylinders in Two-Dimensional Flow at High Reynolds Numbers," Paper 20, Meeting on Ground Wind Load Problems in Relation to Launch Vehicles, Langley Res. Ctr., June 7-8, 1966.

122. Landl, R., "A Model for Flow Induced Vibrations," ESROTT-125, Jan. 1975. (Original Rpt. DLR-FB 74-42, 1974).

123. Hartlen, R. T., Baines, W. D., and Currie, I. G., "Vortex-Excited Oscillations of a Circular Cylinder," Tech. Publ. UTME-TP 6809, Nov. 1968, U. Toronto, Canada.

124. Sallet, W. D., "The Drag and Oscillatory Transverse Force on Vibrating Cylinders due to Steady Fluid Flow," Eng. Archiv, Vol. 44, 1975, pp. 113-122.

125. Mody, V. J. and Slater, J. E., "Unsteady Aerodynamics and Vortex Induced Aeroelastic Instability of a Structural Angle Section," AIAA Paper No. 77-160, Jan. 1977.

126. Marris, A. W., "A Review of Vortex Streets, Periodic Wakes, and Induced Vibration Phenomena," J. Basic Eng., June 1964, pp. 185-196.

127. Tanida, Y., Okajima, A., and Watanabe, Y., "Stability of a Circular Cylinder Oscillating in a Uniform Flow or in a Wake," J. Fluid Mech., Vol. 61, Part 4, 1973, pp. 769-784.

128. Ericsson, L. E. and Reding, J. P., "Aerodynamic Effects of Bulbous Bases," NASA CR-1339, Aug. 1969.

129. Ericsson, L. E. and Reding, J. P., "Re-Entry Capsule Dynamics," J. Spacecraft and Rockets, Vol. 8, No. 6, June 1971, pp. 575-586.

130. Hatfield, H. M. and Morkovin, M. V., "Effect of an Oscillating Free Stream on the Unsteady Pressure on a Circular Cylinder," J. Fluids Eng., June 1973, pp. 249-254.

131. Chen, C. F. and Ballengee, D. B., "Vortex Shedding from Circular Cylinders in an Oscillating Freestream," AIAA Journal, Vol. 9, No. 2, Feb. 1971, pp. 340-342.

132. Durgin, W. W., March, P. A. and Lefebvre, P. J., "Lower Mode Response of Circular Cylinders in Cross Flows," ASME Winter Annual Meeting, San Francisco, 11-15 Dec., 1978, Nonsteady Fluid Dynamics Volume, pp. 193-200.

133. Ericsson, L. E. and Reding, J. P., "Dynamic Stall Simulation Problems," J. Aircraft, Vol. 8, No. 7, July 1971, pp. 579-583.

134. Ericsson, L. E., "Supersonic Interference Flow Effects on Finned Bodies," AIAA Journal, Vol. 14, No. 9, Sept. 1976, pp. 1342-1343.

135. Stansby, P. K., "The Effect of Endplates on the Base Pressure Coefficient of a Circular Cylinder," Aeromechanical Journal, Vol. 78, Jan. 1974, pp. 36-37.

136. Pollock, N., "The Aerodynamic Behavior of a Two-Dimensional Airfoil Fitted with Semicircular and Square Blunt Bases at Mach Numbers up to 1.20," Report ARL/A 336, June 1972, Australia.

137. Wood, C. J., "The Effect of Lateral Vibrations on Vortex Shedding from Blunt-Based Airfoils," J. Sound and Vibration, Vol. 14(1), 1971, pp. 91-102.

138. Pate, S. R., "Dominance of Radiated Aerodynamic Noise on Boundary Layer Transition in Supersonic and Hypersonic Wind Tunnels, Theory and Application," AEDC TR-77-107, March 1978.

139. Spangler, J. G. and Wells, C. S., Jr., "Effects of Free Stream Disturbances on Boundary-Layer Transition," AIAA Journal, Vol. 3, March 1968, pp. 543-545.

140. Tobak, M., Schiff, L. B., and Peterson, V. L., "Aerodynamics of Bodies of Revolution in Coning Motion," AIAA Journal, Vol. 7, No. 1, Jan. 1969, pp. 95-99.

141. Ericsson, L. E. and Reding, J. P., "Unsteady Aerodynamics of Slender Delta Wings at Large Angles of Attack," J. Aircraft, Vol. 12, No. 9, Sept. 1975, pp. 721-729.

142. Morkovin, M. V., Prepared Comment to "Some Sources of Ground-Wind Loads in Launch Vehicles," AIAA Fifth Annual Structures and Materials Conference, April 1-3, 1964, Palm Springs, California.

143. Whitehead, A. H., Jr. and Bertram, M. H., "Alleviation of Vortex-Induced Heating on the Lee Side of Slender Wings in Hypersonic Flow," AIAA Journal, Vol. 9, Oct. 1971, pp. 1870-1872.

144. Uselton, J. C., "Aerodynamic Characteristics of High Fineness Ratio Model with Various Spin Rates at M = 3.0 and 5.0," AEDC TR 66-177, Sept. 1966.

145. Ericsson, L. E., "Unsteady Aerodynamics of Separating and Reattaching Flow on Bodies of Revolution," Recent Research on Unsteady Boundary Layers, Vol. 1, IUTAM Symposium, Laval U. Quebec, May 24-28, 1971, pp. 481-512.

146. Robertson, J. E. and Chevalier, H. L., "Characteristics of Steady-State Pressures on the Cylindrical Portion of Cone-Cylinder Bodies at Transonic Speeds," AEDC TDR 63-104, Aug. 1963.

147. Ericsson, L. E., "Loads Induced By Terminal-Shock Boundary-Layer Interaction on Cone-Cylinder Bodies," J. Spacecraft and Rockets, Vol. 7, No. 9, Sept. 1970, pp. 1106-1112.

148. Wang, K. C., "Separation of Three-Dimensional Flow," MML TR-76-54C, Aug. 1976, Martin-Marietta Laboratories.

149. Hall, I. M., Rogers, E. W. E., and Davies, B. M., "Experiments With Inclined Blunt-Nosed Bodies at M = 2.45," ARC R&M No. 3128, Aeronautical Research Council, Great Britain.

150. Schiff, L. B., Private Communication of Unpublished Results, April 5, 1968.

151. Kaye, A. S. and Williams, M. J., "Experimental Studies of the Wake Behind Long, Yawed Cone-Cylinders at Mach 7.5," Note ARL/AERO 353, Sept. 1974, Aeronautical Res. Lab., Australia.

152. Kruse, R. L., "Influence of Spin Rate on Side Force of an Axisymmetric Body," AIAA Journal, Vol. 16, No. 4, April 1978, pp. 415-416.

153. Jacobson, I. D., "Contribution of Wall Shear Stress to Magnus Effect on Nose Shapes," AIAA Journal, Vol. 12, No. 7, July 1969, pp. 1003-1005.

154. Morton, J. B., Jacobson, I. D., and Saunders, S., "Experimental Investigation of the Boundary Layer on a Rotating Cylinder," AIAA Journal, Vol. 14, No. 10, Oct. 1976, pp. 1458-1463.

155. Martin, J. M. and Ingram, C. W., "Experimental Correlation Between the Flow and Magnus Characteristics of a Spinning Ogive-Nose Cylinder," AIAA Journal, Vol. 11, No. 7, July 1973, pp. 901-902.

156. Martin, J. M., "A Correlation Between the Flow and Magnus Characteristics of a Spinning Ogive-Nose Cylinder," PhD. Dissertation, Aug. 1971, U. Notre Dame.

157. Schiff, L. B. and Tobak, M., "Results from a New Wind-Tunnel Apparatus for Studying Coning and Spinning Motions of Bodies of Revolution," AIAA Journal, Vol. 8, No. 11, Nov. 1970, pp. 1953-1958.

158. Mack, L. M., "Linear Stability Theory and The Problem of Supersonic Boundary-Layer Transition," AIAA Journal, Vol. 13, No. 3, March 1975, pp. 278-289.

159. Smith, L. H. and Nunn, R. H., "Aerodynamic Characteristics of an Axisymmetric Body Undergoing a Uniform Pitching Motion," J. Spacecraft and Rockets, Vol. 13, No. 1, Jan. 1976, pp. 8-14.

160. Nunn, R. H. and Smith, L. H., "Private Communication of Unpublished Data," 6 Oct., 1978.

161. Orlik-Rückemann, K. J., "Dynamic Stability Testing in Wind Tunnels," Paper No. 1, AGARD CP-235, AGARD Meeting on Dynamic Stability Parameters, Athens, Greece, Sept. 25-28, 1978.

162. Ericsson, L. E., "A Summary of AGARD FDP Meeting on Dynamic Stability Parameters," Paper 2, AGARD Symposium on Stability and Control, Ottawa, Canada, 25-28 Sept., 1978.

163. Rainbird, W. J., Crabbe, R. S., Peake, D. J. and Meyer, R. F., "Some Examples of Separation in Three-Dimensional Flows," Canadian Aero. and Space Journal, Vol. 12, No. 10, Dec. 1966, pp. 409-423.

164. Keener, E. R. and Chapman, G. T., "Similarity in Vortex Asymmetries Over Slender Bodies and Wings," AIAA Journal, Vol. 15, No. 9, Sept. 1977, pp. 1370-1372.

165. Shanks, R. E., "Low Subsonic Measurements of Static and Dynamic Stability Derivatives of Six Flat-Plate Wings Having Leading Edge Sweep Angles of 70° to 84°," NASA TND-1827, July 1963.

166. Bird, J. D., "Tuft-Grid Surveys at Low Speeds for Delta Wings," NASA TND-5045, Feb. 1969.

167. Ericsson, L. E. and Reding, J. P., "Approximate Nonlinear Slender Wing Aerodynamics," J. Aircraft, Vol. 14, No. 12, Dec. 1977, pp. 1197-1204.

168. Wendtz, W. H. and Kohleman, D. L., "Vortex Breakdown on Slender Sharp-Edged Delta Wings," AIAA Paper 69-778, July 1969.

169. Reding, J. P. and Ericsson, L. E., "Review of Delta Wing Space Shuttle Vehicle Dynamics," NASA CR-115357, Oct. 1971.

170. Polhamus, E. C., "Predictions of Vortex-Lift Characteristics by a Leading-Edge Suction Analogy," J. Aircraft, Vol. 8, No. 4, April 1971, pp. 193-199.

171. Lowson, M. V., "Some Experiments with Vortex Breakdown," J. Royal Aeronautical Society, Vol. 68, May 1964, pp. 343-346.

172. Sarpkaya, T., "Separated Flow About Lifting Bodies and Impulsive Flow About Cylinders," AIAA Journal, Vol. 4, March 1966, pp. 414-420.

173. Schindel, L. H., "Effects of Vortex Separation on the Lift Distribution on Bodies of Elliptic Cross Section," J. Aircraft, Vol. 6, Nov.-Dec., 1969, pp. 537-543.

174. Schindel, L. H., "Separated Flow About Lifting Bodies," MIT/AL TR-80, Sept. 1973.

175. Fidler, J. E., Nielsen, J. N. and Schwind, R. G., "An Investigation of Slender Body Wake Vortices," AIAA Journal, Vol. 15, No. 12, Oct. 1977, pp. 1736-1741.

176. Chin, W. S. and Lienhard, J. H., "On Real Fluid Over a Yawed Circular Cylinder," J. Basic Eng., Dec. 1967, pp. 851-857.

177. Surry, J. and Surry, D., "The Effect of Inclination on the Strouhal Number and Other Wake Properties of Circular Cylinders at Subcritical Reynolds Numbers," UTIA TN 116, Aug. 1967.

178. Bursnall, W. J. and Loftin, L. K., Jr., "Experimental Investigation of the Pressure Distribution About a Circular Cylinder in the Critical Reynolds Number Range," NACA TN 2463, Sept. 1951.

179. Atraghji, E. G., "Pressure Distribution Over a Family of Inclined Long Slender Bodies of Revolution at M = 0.5, 2.0 and 3.5," NAE Data Report 5 x 5/0029, 1968, National Research Council, Ottawa, Canada.

180. Clarkson, M. H., Malcolm, G. N. and Chapman, G. T., "A Subsonic, High-Angle-of-Attack Flow Investigation at Several Reynolds Numbers," AIAA Journal, Vol. 16, No. 1, Jan. 1978, pp. 53-60.

181. Reding, J. P. and Ericsson, L. E., "Maximum Vortex-Induced Side Forces on Slender Bodies," High Angle of Attack Aerodynamic Working Group Meeting, Redstone Arsenal, Ala., March 16-17, 1977.

182. Hoerner, S. F., "Fluid-Dynamic Drag," 1958.

183. Bootle, W. J., "Forces on an Inclined Circular Cylinder in Supercritical Flow," AIAA Journal, Vol. 9, No. 3, March 1971, pp. 514-516.

184. Dahlem, V. and Shereden, D., "Private Communication of Unpublished MX Wind Tunnel Data," 2 May, 1978, and 20 Aug. 1978.

185. Dahlem, V., "Semi-Empirical Prediction Method for Induced Side Forces on Missiles at High Angles of Attack," Paper 38, 11th Navy Symposium on Aeroballistics, Aug. 1978. NADC, Warminster, Penn.

186. Honji, H. and Taneda, S., "Unsteady Flow Past a Circular Cylinder," J. Phys. Soc. Japan, Vol. 77, Dec. 1969, pp. 1668-1677.

187. Hummel, D., "Experimentelle Untersuchnng der Strömung auf der Saugseite eines Schlanken Deltaflügels," Z. f. Flugwiss, Vol. 13, July 1965, pp. 247-252.

188. Ericsson, L. E. and Reding, J. P., "Spilled Leading Edge Vortex Effects on Dynamic Stall Characteristics," J. Aircraft, Vol. 13, No. 4, April 1976, pp. 313-315.

189. Ericsson, L. E. and Reding, J. P., "Further Consideration of Spilled Leading Edge Vortex Effects on Dynamic Stall," J. Aircraft, Vol. 14, June 1977, pp. 601-603.

190. Ericsson, L. E. and Reding, J. P.,"Quasi-Steady and Transient Dynamic Stall Characteristics," Paper 24, AGARD CP-204, AGARD Symposium on Prediction of Aerodynamic Loading, Moffet Field, Calif. USA, Sept. 27-29, 1976.

191. Gerrard, J. H., "An Experimental Investigation of the Oscillatory Lift and Drag of a Circular Cylinder Shedding Turbulent Vortices," J. Fluid Mech., Vol. 11, Part 2, Sept. 1961, pp. 244-256.

192. Keefe, R. T., "An Investigation of the Fluctuating Forces Acting on a Stationary Circular Cylinder in a Subsonic Stream and of the Associated Sound Field," U. Toronto, Rept. UTIA No. 76, Sept. 1961.

193. Goldman, R. L., "Karman Vortex Forces on Vanguard Rocket," Shock and Vibr. Bull., Pt. 11, Naval Res. Lab., Washington, D. C., 1958.

194. McGregor, D. M., "An Experimental Investigation of the Oscillatory Pressures on a Circular Cylinder in a Fluid Stream," U. Toronto, Inst. of Aerophysics, Tech. Note 14, 1957.

195. Batham, J. P., "Pressure Distributions on Circular Cylinders of Critical Reynolds Number," J. Fluid Mech., Vol. 57, 1973, pp. 209-228.

196. Kacker, S. C., Pennington, B., and Hill, R. S., "Fluctuating Lift Coefficient for a Circular Cylinder in Cross Flow," J. Mech. Eng. Sciences, Vol. 16, No. 9, 1974, pp. 215-224.

197. Schmidt, L. V., "Measurements of Fluctuating Air Loads on a Circular Cylinder," J. Aircraft, Vol. 2, No. 1, 1965, pp. 49-55.

198. Schmidt, L. V., "Fluctuating Force Measurements Upon a Circular Cylinder at Reynolds Numbers up to 5×10^6," Paper No. 19, Meeting on Ground Wind Load Problems, Relation to Launch Vehicles, NASA TM X-57779, 1966.

199. Jones, G. W., Jr., "Unsteady Lift Forces Generated by Vortex Shedding About a Large, Stationary, and Oscillating Cylinder at High Reynolds Numbers," ASME Symposium on Unsteady Flow at the Fluids Engineering Conference, Philadelphia, Penna., May 6-9, 1968.

200. Ericsson, L. E. and Reding, J. P., "Unsteady Aerodynamic Analysis of Space

Shuttle Vehicles, Part II, Steady and Unsteady Aerodynamics of Sharp-Edged Delta Wings," NASA CR-124423, Aug. 1973.

201. Ericsson, L. E. and Reding, J. P., "Dynamic Stall of Helicopter Blades, J. American Helicopter Society, Vol. 17, No. 1, Jan. 1972, pp. 10-19.

202. Ericsson, L. E., "Dynamic Effects of Shock-Induced Flow Separation," J. Aircraft, Vol. 12, No. 2, Feb. 1975, pp. 86-92.

203. Ericsson, L. E. and Reding, J. P., "Scaling Problems in Dynamic Tests of Aircraft-Like Configurations," Paper 25, AGARD CP-227, AGARD Conference on Unsteady Aerodynamics, Ottawa, Canada, 26-28 Sept., 1977.

204. Ericsson, L. E., "Effects of Boundary Layer Transition on Vehicle Dynamics," J. Spacecraft and Rockets, Vol. 6, No. 12, Dec. 1969, pp. 1404-1409.

205. Ericsson, L. E., "Transition Effects on Slender Vehicle Stability and Trim Characteristics," J. Spacecraft and Rockets, Vol. 11, No. 1, Jan. 1974, pp. 3-11.

206. Ericsson, L. E., "Correlation of Attitude Effects on Slender Vehicle Transition," AIAA Journal, Vol. 12, No. 4, April 1974, pp. 523-529.

207. Ericsson, L. E. and Reding, J. P., "Reynolds Number Criticality in Dynamic Tests," AIAA Paper No. 78-166, Jan. 16-18, 1978.

208. Ericsson, L. E. and Reding, J. P., "Analytic Prediction of Dynamic Stall Characteristics," AIAA Paper No. 72-682, June 1972.

209. Carr, L. W., McAllister, K. W. and McCroskey, W. J., "Analysis of the Development of Dynamic Stall Based on Oscillating Experiments," NASA TN D-8382, Jan. 1977.

210. Many Authors, AGARD FDP Meeting on Dynamic Stability Parameters, AGARD CP-235, Athens, Greece, 22-24 May, 1978.

211. Apelt, C. J., West, G. S. and Szewczk, A. A., "The Effects of Wake Splitter Plates on the Flow Past a Circular Cylinder in the Range $10^4 < R < 5 \times 10^4$," J. Fluid, Mech. Vol. 61, Part 1, 1973, pp. 197-198.

212. Apelt, C. J. and West, G. S., "The Effects of Wake Splitter Plates on Bluff-Body Flow in the Range $10^4 < R < 5 \times 10^4$, Part 2," J. Fluid. Mech., Vol. 71, Part 1, 1975, pp. 145-160.

213. Ericsson, L. E., "Aeroelastic Instability Caused by Slender Payloads," J. Spacecraft and Rockets, Vol. 4, No. 1, Jan. 1967, pp. 65-73.

214. Scruton, C. and Walshe, D. E., "A Means for Avoiding Wind-Excited Oscillations of Structures with Circular or Nearly Circular Cross-Sections," NPL-Aero-335, Oct. 1957, Aer. Res. Council, Great Britain.

Appendix A
NOMENCLATURE

a   oscillation amplitude

A   axial force, coefficient $C_A = A/\rho_\infty U_\infty^2/2)S$

A   aspect ratio

b   wing span

c   reference length, c = d

c   cross-sectional chord length

d   maximum diameter for body of revolution

$\bar{d}$ mean diameter $\bar{d} = \int_0^1 d \, d\frac{x}{\ell}$.

d_{max} maximum cross-sectional dimension

d   sectional drag; coefficient $c_d = d/(\rho_\infty U_\infty^2/2)c$

f   sectional friction drag, coefficient $c_f = f/(\rho_\infty U_\infty^2/2)c$

f   frequency of oscillating body

f_v frequency of vortex shedding

f_{vo} f_v for stationary flow conditions

g   3-D vortex wake parameter (Fig. 45)

h   width of vortex wake (Fig. 7)

ℓ body length

ℓ sectional lift, coefficient $c_\ell = \ell/(\rho_\infty U_\infty^2/2) \, c$

ℓ rolling moment: coefficient $C_\ell = \ell/(\rho_\infty U_\infty^2/2) \, \bar{S}b$

L   wavelength of vortex wake (Fig. 7)

L_S length of splitter plate (Fig. 133)

M	Mach number
M_p	pitching moment: coefficient $C_m = M_p/(\rho_\infty U_\infty^2/2)\,Sc$
n	yawing moment, coefficient $C_n = n/(\rho_\infty U_\infty^2/2)\,Sc$
$(nc)_\infty$	crossflow drag, coefficient $(c_{nc})_\infty = (nc)_\infty/(\rho_\infty U_\infty^2/2)\,c$
N	normal force, coefficient $C_N = N/(\rho_\infty U_\infty^2/2)\,S$
p	roll rate
p	static pressure: coefficient $C_p = (p - p_\infty)/(\rho_\infty U_\infty^2/2)$
q	pitch rate
q_∞	dynamic pressure, $q_\infty = \rho_\infty U_\infty^2/2$
r	radius
Re	Reynolds number based on d_{max} and freestream conditions Usually $Re = R_d$
R_d	Reynolds number, $R_d = U_\infty d/\nu_\infty$
S	Strouhal number, $S = f\,d_{max}/U_\infty$
S	reference area, $S = \pi\,d^2/4$
$\bar{S}$	reference area (= projected wing area)
t	cross-sectional maximum thickness
t	time
Δt	timelag
U	horizontal velocity
$\bar{U}$	convection velocity
x	axial body-fixed coordinate (distance from apex)
Y	side force, coefficient $C_Y = Y(\rho_\infty U_\infty^2/2)\,S$
z	translatory coordinate
$\bar{z}$	dimensionless amplitude, $\bar{z} = z_{max}/d_{max}$

α	angle of attack
β	sideslip angle
γ	rotation of plane of symmetry of forebody vortices (Fig. 67)
Γ	vortex strength
δ	roughness height
ξ	3-D vortex inclination (Fig. 45)
χ	vortex parameter, Eq. (4-8)
θ_c	cone half angle
θ_A	apex half angle
θ_s	separation angle on 2-D cylinder
ρ	air density
ϕ	roll angle
ϕ'	coning angle (Fig. 67)
ϕ_s	3-D separation angle (Fig. 80)
σ	surface upwash angle (Fig. 98)
σ'	total angle of inclination (Fig. 67)
ν	kinematic viscosity

Subscripts

A	apex
AV	asymmetric vortices
b	base
c	cone
CG	center of gravity
CP	center of pressure
e	ellipse

A-3

eff	effective
lam	laminar flow
max	maximum
n	normal to body axis
N	nose
p or peak	peak amplitude
rel	relative
RMS	root mean square value
s	separated flow
S	splitter plate
SV	symmetric vortices
turb	turbulent
UV	unsteady vortices
v	2-D vortices from oscillating cylinder
vo	2-D vortices from stationary cylinder
W	wall
wet	wetted length
∞	freestream conditions

Superscripts

$([\overline{}]^2)^{\frac{1}{2}}$ root-mean-square value

$[\overline{}]$ a bar, e.g. $[\overline{d}]$, indicates integrated mean parameter value

Differential Symbols

$\dot{\alpha}$ $= \partial\alpha/\partial t$

$C_{m\alpha}$ $= \partial C_m/\partial\alpha; C_{\ell\beta} = \partial C_\ell/\partial\beta$